

Methods and algorithms for undifferenced multi-GNSS global network processing and applications to satellite geodesy

Inauguraldissertation

der Philosophisch-naturwissenschaftlichen Fakultät

der Universität Bern

vorgelegt von

Emilio José Calero Rodríguez

aus Spanien

Leiter der Arbeit

Prof. Dr. Adrian Jäggi¹

Ko-Leiter der Arbeit

Prof. Dr. Rolf Dach¹

Dr. Arturo Villiger²

¹Astronomisches Institut der Universität Bern

²Bundesamt für Landestopografie swisstopo



This work is licensed under a
Creative Commons Attribution 4.0 International License
<https://creativecommons.org/licenses/by/4.0/>

Methods and algorithms for undifferenced multi-GNSS global network processing and applications to satellite geodesy

Inauguraldissertation

der Philosophisch-naturwissenschaftlichen Fakultät

der Universität Bern

vorgelegt von

Emilio José Calero Rodríguez

aus Spanien

Leiter der Arbeit

Prof. Dr. Adrian Jäggi¹

Ko-Leiter der Arbeit

Prof. Dr. Rolf Dach¹

Dr. Arturo Villiger²

¹Astronomisches Institut der Universität Bern

²Bundesamt für Landestopografie swisstopo

Von der Philosophisch-naturwissenschaftlichen Fakultät angenommen.

Der Dekan:

Bern, July 8, 2024

Prof. Dr. Marco Herwegh

University of Bern - Faculty of Science - Astronomical Institute

Abstract

Methods and algorithms for undifferenced multi-GNSS global network processing and applications to satellite geodesy

by Emilio José Calero Rodríguez

The constant monitoring of the Earth is a key factor to understand the physical processes that our planet undergoes. For many of such processes, the scientific community agrees on their human-induced nature, and preventing (or, ultimately, reacting to) them is vital to keep the human footprint under control (or, at least, to avoid catastrophic hazards).

The global geodetic techniques play an important role in this context, as they permit us to observe the Earth as a whole, beyond political barriers. In particular, observations from artificial satellites have become a mayor contribution in this domain, being the Global Navigation Satellite System (GNSS) constellations the backbone for most of the scientific satellite geodetic missions, since they help to define the terrestrial frame upon which the Earth measurements are referred to. Such an important contribution to metrology is entangled with the GNSS contribution to geodesy through the provision of coordinates for fiducial sites (Earth's shape) as well as the orientation of the Earth in space.

The present dissertation gives, on the one hand, an exhaustive description of the implemented GNSS processing strategy using undifferenced observations, including a tailor-made algorithm to cope with the so-called carrier phase ambiguity resolution problem. The reader will find this novel algorithm especially useful when large networks of ground stations are involved. On the other hand, there are some chapters intended to give a deep insight into the GNSS capabilities in geodesy, with particular focus on geodynamics. Especially, geocenter motion, Earth's orientation and long-wavelength time-variable gravity field recovery. This latter subject has received very little attention in the dedicated literature and, hence, grants scientific value to the present work.

The comprehensive characterization of the GNSS capabilities in geodesy is a mandatory preceding step for a more ambitious objective: To rigorously combine observations from different geodetic techniques, leveraging their individual advantages, while diminishing their lacks. Particularly, the estimation of common geodynamic parameters (Earth's rotation, geocenter motion and time-variable gravity field) during the reduction of all the satellite-based observations could act as a global tie, strengthening the geodetic solution, which, in turn, closes the cycle by stabilizing the terrestrial frame.

Acknowledgements

The research conducted in the frame of this dissertation would not have been possible without third parties, to which I must express my gratitude.

First of all, this dissertation was financially supported by the European Research Council under the grant agreement no. 817919 (project SPACE TIE).

UBELIX (<http://www.id.unibe.ch/hpc>), the HPC cluster at the **University of Bern**, has to be acknowledged since the most demanding calculations were performed on it. It has also to be acknowledged that the MATLAB open-source LAMBDA toolbox provided by the Delft University of Technology (Verhagen et al., 2012) was used for some tests during the development of the carrier phase ambiguity resolution strategy. Credit has to be given to **Flaticon.com** too, since some figures include images from that website.

More importantly, this dissertation was carried out at the **Astronomical Institute** of the **University of Bern**. I shall be thankful to Prof. Dr. Adrian Jäggi, who trusted me to work on the Space Tie Project. I shall also be thankful to Prof. Dr. Rolf Dach and Dr. Arturo Villiger, who guided me through the use of the Bernese Software, the primary tool used in the frame of this project. For our discussions, viewpoints, and shared moments over beers, I extend my gratitude to Dr. Julián Rodríguez.

Dissertation Overview

The present dissertation has been envisaged to equally distribute theory, state-of-the-art review and practical aspects within the following seven chapters:

Chapter 1: Introduction to the concepts underpinning satellite geodesy

An introduction to the principles of satellite geodesy, contextualizing this dissertation and including basic ideas of time, Earth's rotation, gravity field and satellite orbits. These discussions aim at understanding the results presented in the remaining chapters from a fundamental point of view.

Chapter 2: Theory of parameter estimation for GNSS processing

This chapter introduces the basis of parameter estimation, pointing out very specific results which are of special interest in the frame of this work.

Chapter 3: Global network GNSS solutions using undifferenced observations

Here, we provide an overall view of the GNSS technologies. Special attention is paid to the different terms that make up the observation model and their parameterization. Additionally, we describe the adopted GNSS processing schemes, which are based on undifferenced observations. The derived results are evaluated and discussed.

Chapter 4: Global GNSS ambiguity resolution for undifferenced processing

This chapter describes a novel ambiguity resolution strategy developed and implemented in the context of this dissertation. The chapter begins with some basic theoretical and practical notions and elaborates on the implemented algorithm for global ambiguity resolution, along with its validation and technical considerations.

Chapter 5: Review of the GNSS capabilities to derive geodynamic parameters

This chapter provides an overview of the current multi-GNSS capabilities for estimating geodynamic parameters. It begins by presenting the ideas and findings from existing literature and then exemplifies them through numerous exercises.

Chapter 6: The role of the time-variable gravity field in GNSS network solutions

This chapter quantifies the influence of the time-variable gravity field in GNSS orbits throughout various experiments. It includes the estimation of GNSS-based long-wavelength gravity signals, as well as the general impact that these signals have over the geodetic network solutions.

Chapter 7: Summary, conclusions and outlook

This chapter concludes the dissertation, stressing the achievements along with the present challenges.

Contents

Abstract	iii
Acknowledgements	v
Dissertation Overview	vii
1 Introduction to the concepts underpinning satellite geodesy	1
1.1 Introduction	1
1.2 Geodetic community	2
1.3 Understanding time	5
1.4 An insight into the Earth's rotation	7
1.4.1 Dynamic equations	7
1.4.2 Kinematic equations	9
1.4.3 A qualitative view of the motion	10
1.5 Description of the Earth's gravitational potential	12
1.5.1 Spherical harmonics	12
1.5.2 Geoid and reference ellipsoid	15
1.5.3 Surface mass variations	16
1.6 Orbit representation	17
1.6.1 Equations of motion	17
1.6.2 Osculating elements and precession of the ascending node . . .	18
1.6.3 Variational equations	19
1.7 Summary	20
2 Theory of parameter estimation for GNSS processing	23
2.1 Introduction	23
2.2 Estimation principles	24
2.3 The fundamental differencing theorem	25
2.4 A posteriori parameter constraining	27
2.5 Manipulation of normal equations	28
2.5.1 Stacking of normal equations	28
2.5.2 Linear transformations of parameters	28
2.5.3 Pre-eliminating parameters	29
2.6 Computation of long-arc solutions	30
2.7 Summary	32
3 Global network GNSS solutions using undifferenced observations	35
3.1 Introduction	35
3.2 General aspects of the navigation systems	36
3.3 GNSS observation model	39
3.3.1 GNSS attitude model	42

3.3.2	Range contribution	42
3.3.3	PCO and PCV contributions	47
3.3.4	Clock corrections	47
3.3.5	Ionospheric delay	48
3.3.6	Tropospheric delay	49
3.3.7	Phase wind-up effect	49
3.3.8	Pseudorange biases	49
3.3.9	Phase ambiguities and biases	51
3.4	General aspects of the processing strategy	52
3.5	Validation of the results	55
3.5.1	UD-based against DD-based solutions: Controlled test case	55
3.5.2	UD-based solution against CODE MGEX products	57
3.6	TRF update: From ITRF2014 to ITRF2020	58
3.7	Galileo SRP model based on satellite metadata	58
3.8	SLR-based evidence of second-order relativistic effect on Galileo clocks	61
3.9	Summary	62
4	Global GNSS ambiguity resolution for undifferenced processing	65
4.1	Introduction	65
4.2	Theoretical framework	67
4.3	AR strategy based on HMW/IF observations	68
4.4	Inspection of real-valued ambiguities	68
4.4.1	Ambiguity parameterization	69
4.4.2	Ambiguity clustering	71
4.4.3	Mixed-integer model property	74
4.4.4	Inspection of WL ambiguities	75
4.5	Metrics for quality control	76
4.6	Technical considerations	78
4.6.1	Integer-cycle-conform products for PPP-AR	78
4.6.2	Boundary effect	79
4.6.3	Implications of orbit corrections	79
4.6.4	Phase jumps	80
4.6.5	Diverging clock estimates	81
4.6.6	Influence of the network size	82
4.7	Summary	83
5	Review of the GNSS capabilities to derive geodynamic parameters	85
5.1	Introduction	85
5.2	Main difficulties estimating ERP and GCC	86
5.3	GNSS-based ERP and GCC results	87
5.3.1	ERP and GCC solutions in accord with ITRF2014	88
5.3.2	Sub-daily polar motion background model update	90
5.3.3	ERP and GCC solutions in accord with ITRF2020	91
5.3.4	Influence of the TRF datum definition	92
5.3.5	Influence of the Galileo SRP model on the ERP and GCC solutions	94
5.4	Summary	94

6	The role of the time-variable gravity field in GNSS network solutions	97
6.1	Introduction	97
6.2	Processing strategy	99
6.3	Estimability of degree-2 Stokes' coefficients using GNSS orbits	100
6.3.1	Sensitivity to the time-variable gravity field	100
6.3.2	Collinearity between length of day and Earth's oblateness	101
6.3.3	Arc length selection	102
6.3.4	Data accumulation	103
6.3.5	Constraining of stochastic pulses	104
6.3.6	GNSS-based degree-2 gravity solutions	106
6.4	GNSS-specific estimation of degree-2 gravity signals	106
6.5	Higher order GNSS-derived gravity signals	109
6.6	GNSS network solutions based on time-variable gravity field models	111
6.7	Mapping of the relativistic orbit precession into the Earth's oblateness	114
6.8	Summary	115
7	Summary, conclusions and outlook	117
A	GNSS processing strategy	121
	Bibliography	123
	Curriculum vitae	133
	List of publications	137
	Declaration of Originality	139

List of Abbreviations

AC	Analysis Center
AIUB	Astronomical Institute of the University of Bern
ANTEX	ANTenna EXchange format
AOD1B	Atmosphere and Ocean De-aliasing level-1B
AR	Ambiguity Resolution
ARP	Antenna Reference Point
BSW	Bernese GNSS SoftWare
CDMA	Code Division Multiple Access
CIP	Celestial Intermediate Pole
CODE	Center for Orbit Determination in Europe
COST-G	COmbination Service for Time-variable Gravity fields
CRF	Celestial Reference Frame
DD	Double-Difference
DORIS	Doppler Orbitography and Radiopositioning Integrated by Satellite
ECOM	Empirical CODE Orbit Model
EGM	Earth Gravitational Model
ERP	Earth Rotation Parameters
EWH	Equivalent Water Height
FDMA	Frequency Division Multiple Access
FOC	Full Operational Capability
FSM	Fitted Signal Model
GCC	Geocenter Coordinates
GF	Geometry-Free
GIM	Global Ionospheric Maps
GLONASS	<i>GLObal'naya NAVigatsionnaya Sputnikovaya Sistema</i>
GNSS	Global Navigation Satellite System
GPS	Global Positioning System
GRACE	Gravity Recovery and Climate Experiment
GRACE-FO	Gravity Recovery and Climate Experiment Follow-On
HMW	Hatch–Melbourne–Wubben
IAG	International Association of Geodesy
IAU	International Astronomical Union
ICRF	International Celestial Reference Frame
IERS	International Earth Rotation and Reference Systems Service
IF	Ionospheric-Free
IGS	International GNSS Service
ILRS	International Laser Ranging Service
ILS	Integer Least Squares

IRC	I nteger R ecovery C lock
ITRF	I nternational T errestrial R eference F rame
LAMBDA	L east-squares A MBiguity D ecorrelation A djustment
LEO	L ow E arth O rbital
LOD	L ength O f D ay
LOS	L ine O f S ight
LS	L east S quares
MGEX	M ulti- G NSS E Xperiment
NEQ	N ormal E quations
NL	N arrow- L ane
NNR	N o- N et- R otation
NNT	N o- N et- T ranslation
O-C	O bserved minus C omputed
OSB	O bservable S pecific B ias
PCO	P hase C enter O ffset
PCV	P hase C enter V ariations
PM	P olar M otion
PHM	P assive H ydrogen M aser
PPP	P recise P oint P ositioning
PPP-AR	P recise P oint P ositioning with A mbiguity R esolution
RINEX	R eceiver I Ndependent E Xchange format
RMS	R oot M ean S quare
SIS	S ignal I n S pace
SLR	S atellite L aser R anging
SRP	S olar R adiation P ressure
STD	S Tandard D eviation
TAI	<i>Temps Atomique International</i>
TCB	<i>Temps Coordonnée Barycentrique</i>
TCG	<i>Temps Coordonnée Géocentrique</i>
TN-14	T echnical N ote 14
TT	T errestrial T ime
TRF	T errestrial R eference F rame
UD	U n D ifferenced
UT1	U niversal T ime 1
UTC	U niversal T ime C oordinate
VLBI	V ery L ong B aseline I nterferometry
VMF1	V ienna M apping F unction 1
WL	W ide- L ane

Introduction to the concepts underpinning satellite geodesy

1.1 Introduction

The history of geodesy (KC and Acharya, 2023) starts around 600 BC with Thales of Miletus, who conjectured the Earth as a flat disc floating in an infinite ocean. Unfortunately for the flat Earth society, that view did not last long, since Pythagoras and his school (580-500 BC) hypothesized a spherical Earth, for which Eratosthenes of Alexandria (250 BC) was able to quantify its radius by looking into the shadow cast by a vertical rod in two distant cities located at the same meridian. Centuries of scientific development, borne by the brightest minds, especially after the modern era, have forged today's definition of geodesy, which is customarily introduced by quoting the German geodesist Friedrich Robert Helmert: "Geodesy is the science of the measurement and mapping of the Earth's surface". The mapping of the Earth's surface directly translates into the knowledge of the Earth's shape, which depends on its mass distribution, i.e., its gravity field. Additionally, a global view of the Earth is only possible w.r.t. an external (extraterrestrial) reference (e.g., quasars), for which the Earth's orientation is needed. In short, it is said that the three pillars of geodesy are the shape, gravity field and orientation of the Earth (Fig. 1.1, Plag and Pearlman, 2007).

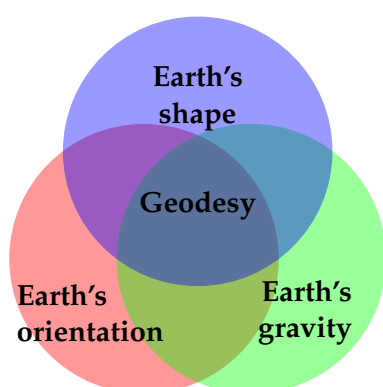


FIGURE 1.1: Components of geodesy

Geodesy itself belongs to the domain of basic sciences and there is a multitude of textbooks compiling its principles (e.g., Hofmann-Wellenhof and Moritz, 2006). On the other hand, satellite geodesy comprises geodetic solutions which are derived from measurements of artificial satellites and, depending on how we approach to the subject, it may belong to the domain of basic and/or applied sciences. In particular, if we focus on the description of the orbits from the basis of orbital mechanics, then it belongs to the former group (e.g.,

Kaula, 2013). Likewise, if we pay more attention to the processing of the observations, then it belongs to the latter group (e.g., Seeber, 2003), which is closely aligned to the work carried out throughout this dissertation. Consequently, this chapter has been envisaged to give a wider, more fundamental, context to the results presented in subsequent chapters.

Satellite geodesy is in the scope of space geodesy, which includes all those techniques whose observations are derived from any extraterrestrial source (e.g., the Moon or extragalactic quasars). These techniques give an external view of the Earth and are thus employed to realize the most precise global terrestrial frames upon which global measurements of all the Earth sciences (navigation, hydrography, oceanography, etc.) are referred to. Despite the fact that terrestrial frames are defined by the coordinates of a number of fiducial sites (shape of the Earth), the reduction of space geodetic observations generally requires the orientation of the Earth and, for the processing of satellite data, its gravity field. Therefore, the boundary between terrestrial frames and geodesy itself faints.

This chapter has been divided into a total of seven sections, including this introduction. The following section describes some of the infrastructure and services used by the geodetic community and stresses its present and future challenges. The treatment of time for high precision applications (such as satellite geodesy) is a topic that often leads to confusion and, hence, it is convenient to revisit some of its notions in section 1.3. Afterwards, sections 1.4 and 1.5 succinctly deal with the fundamentals of the Earth's rotation and gravitational potential, covering the minimum underlying theory needed to contextualize the results presented in chapter 5 and chapter 6, respectively. Since the trajectory of any satellite is best described by orbital mechanics, some insight into this matter is given in section 1.6. The seventh section concludes the chapter.

1.2 Geodetic community

The International Association of Geodesy (IAG), whose origin dates back to 1862, is the scientific organization devoted to the advancement of geodesy (Altamimi and Gross, 2017). It is an association of the International Union of Geodesy and Geophysics (IUGG) and fulfills its objectives by means of different operating components, including services to process observations from the four main space geodetic techniques, namely (see Fig. 1.2):

- The Global Navigation Satellite System (GNSS) technique, whose associated service is the International GNSS Service (IGS, Johnston et al., 2017). It has an important space segment consisting of several satellite constellations transmitting radio frequency signals. These signals are tracked by (either ground, airborne, or spaceborne) dedicated receivers that correlate them against internal signal replicas, resulting in a one-way signal transfer time measurement.
- The Satellite Laser Ranging (SLR) technique, whose associated service is the International Satellite Ranging Service (ILRS, Pearlman et al., 2019). Its ground segment consists of a number of laser ranging stations. The fundamental observable is the round trip time of flight of a transmitted laser pulse emitted by one of these stations and reflected back by a target satellite.
- The Doppler Orbitography and Radiopositioning Integrated by Satellite (DORIS) technique, whose associated service is the International DORIS Service (IDS, Willis et al., 2016). Its ground segment consist of a number of well-distributed stations transmitting radio frequency signals towards space. When these signals are collected by dedicated receivers equipped on some orbiting satellites, a doppler-shift measurement is generated.

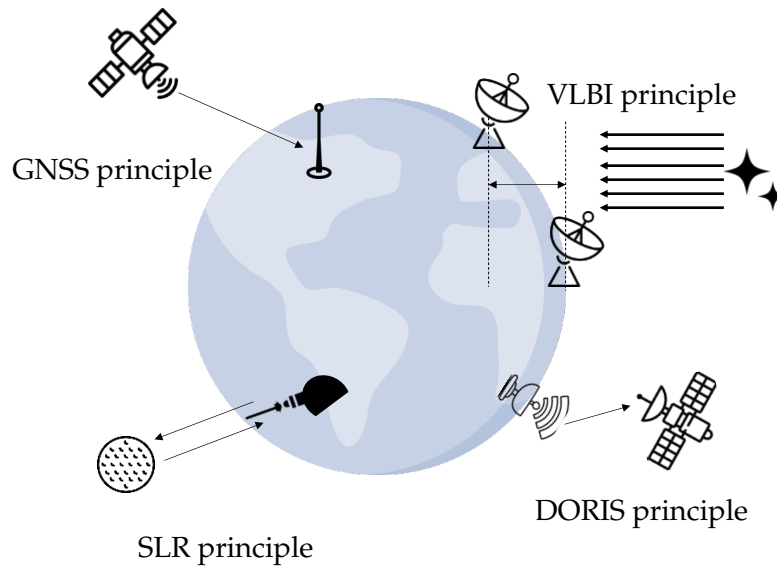


FIGURE 1.2: Geodetic techniques representation

- The Very Long Baseline Interferometry (VLBI) technique, whose associated service is the International VLBI Service (IVS, Nothnagel et al., 2017). This technique relies on a number of ground stations tracking radio frequency signals emitted from distant extraterrestrial sources (such as quasars). When two stations separated thousands of kilometers apart track the same source, the difference in signal propagation time between them can be measured, which results in the fundamental observable of this technique.

The activities of the different services are performed by analysis centers (ACs). In particular, it deserves special mention the Center for Orbit Determination in Europe (CODE), which is the IGS AC hosted by the Astronomical Institute of the University of Bern (AIUB), where this dissertation has been carried out.

The Global Geodetic Observing System (GGOS) component of the IAG gives a common framework for the many IAG services, hence forming a unified observing instrument. It coordinates international geodetic activities, promotes the improvement of the geodetic infrastructure, bridges the scientific activities with society, and serves as the expertise hub in the field.

Each of the aforementioned techniques has its own advantages and drawbacks. VLBI, for instance, is the only one linking the celestial reference frame (CRF)¹, defined by the coordinates of some fundamental quasars, and the terrestrial reference frame (TRF), defined by the coordinates of fiducial sites, from a geometrical point of view. Because of that, VLBI is able to locate the Earth's pole w.r.t. the inertial space, but it cannot sense the geocenter motion or the gravity field. In contrast, these properties can

¹Although it is not completely rigorous, in this context we will interchangeably use celestial frame of reference and inertial frame of reference. It is also important to point out here the difference between reference coordinate systems and reference coordinate frames: The former refer to the theoretical definition of its fundamental properties (e.g., scale, origin and orientation, in case of terrestrial systems), whereas the latter to its practical realization.

be derived to a certain extent by the other techniques, which are satellite techniques connected to inertial space by means of the laws of celestial mechanics. Nonetheless, they only have a limited access to those parameters (depending on the orbital regime and geometry) and are insensitive to the absolute orientation of the Earth around its rotation axis. Additionally, every technique is subject to technique-specific systematic errors.

To seize the individual strengths of the different geodetic techniques, combined inter-technique solutions are used for the realization of the International Terrestrial Reference Frame (ITRF, which is the (most precise) internationally accepted standard for a TRF²), maintained by another IAG service: The International Earth Rotation and Reference Systems Service (IERS³). The most recent realizations of this frame are ITRF2008 (Altamimi et al., 2011), ITRF2014 (Altamimi et al., 2016) and ITRF2020 (Altamimi et al., 2023), where the last four digits indicate the year corresponding to the latest assimilated observations. The IERS also provides conventions (the so-called IERS Conventions, Petit, Luzum, et al., 2010) to guarantee the consistency between the many different products generated by the community. They include definitions, background models and procedures to describe the Earth's rotation, the gravitational potential and the propagation of signals, among others. Of course, the content of the IERS Conventions and the references thereof exceed by far the theoretical aspects that are treated in the following sections and should be considered as the basis for any practical implementation in geodesy.

The technique-specific solutions involved in the ITRF realization consist of time series of the coordinates of fiducial sites and parameters describing the orientation of the Earth. During the combination process, local ties (i.e., measurements between instrument reference points of independent geodetic techniques, derived from local surveys), local constraints in the velocity field of nearby stations, as well as a global ties for the rotation of the Earth are introduced to connect the different techniques. Some fundamental frame properties are, however, defined by technique-specific solutions: The scale is aligned to the SLR and VLBI solutions (although Villiger et al., 2020 show that the scale can be derived from GNSS solutions, too), and the origin to the SLR solutions. On the other hand, the orientation is defined by imposing no-net-rotation w.r.t. the previous ITRF realization. Altogether, Altamimi et al., 2023 stipulate that the uncertainty of the frame origin and its temporal evolution are about 5 mm and 0.5 mm/yr, respectively. In spite of such a good performance, it does not suffice the requirements defined by the community of 1 mm for the frame positions and 0.1 mm/yr for its velocities, as demanded by scientific studies of sea level change (Plag and Pearlman, 2007). To homogeneously enlarge the SLR and VLBI networks, as well as to develop new technologies could improve the performance of future ITRF realizations.

Besides those costly investments, there are still fundamental open points that, if properly addressed, could also convey enhancements to the ITRF realization. They are related to the combination process itself, which misses important physical ties common to the various techniques. For example, Herrera Pinzón, 2023 explores local tropospheric and clock ties between co-located GNSS and VLBI sites. It could be even more interesting to also consider global ties, such as the geocenter motion and the gravity field, which are common to the satellite techniques.

A prerequisite for such a rigorous combination that accounts for those global ties is to fully characterize the capabilities of the different techniques in the different

²Analogously, the International Celestial Reference Frame (ICRF) is the most precise internationally accepted standard for a CRF. It is maintained by the International Astronomical Union (IAU).

³<http://www.iers.org>

domains, which justifies the effort that this dissertation devotes to the understanding of GNSS-based geocenter motion and time-variable gravity field solutions in [chapter 5](#) and [chapter 6](#), respectively. Additionally, many scientific satellites (typically placed at low Earth orbits, or, LEO) are equipped with geodetic (high-performance) GNSS receivers, allowing to integrate them as orbiting stations in the global GNSS processing. Since these satellites are seen as stand-alone stations (i.e., it is not common to form baselines between them), it is preferred to develop GNSS processing schemes based on undifferenced observations, being this the driving element for [chapter 3](#) and [chapter 4](#).

The geodetic community is aware of the necessity to connect all the space geodetic techniques together. This is the reason why it has been planned the mission GENESIS (Delva et al., 2023), which will co-locate the instruments for those techniques into a satellite platform. Thanks to the availability of very precise calibrations between their reference points, it is expected to gain an unprecedented insight into the inter-technique biases and systematics.

1.3 Understanding time

The necessity to precisely measure time is a prerequisite for most of the sciences (including, of course, satellite geodesy) in order to link the observational data with physical events. Intuitively, time can be measured by counting the cycles of a periodic process w.r.t. a given reference. The stability of such a periodic process will thus define the stability of the time scale.

The topic of time has been covered by countless authors. In particular, an easy-to-follow introduction can be found in Montenbruck et al., 2002, chapter 5, being the primary reference on which the definitions presented in the sequel are based. On the other hand, the reader may find an exhaustive insight into time and clock technologies, with special focus on GNSS, in Beard and Senior, 2017 and the references thereof.

There are several time scales that are of interest in satellite geodesy:

- The sidereal time uses the Earth's rotation as reference, so that it maps any rotated angle with a lapse of time. The length of day (LOD) is defined as one complete revolution. Sidereal time is realized by the Greenwich Mean Sidereal Time (GMST), which gives the Greenwich hour angle w.r.t. the vernal equinox.
- The universal time, whose time scale realization is known as UT1, also uses the Earth's rotation as reference, but differs from sidereal time in the definition of the LOD: One day is measured as two consecutive transits of the same Earth's meridian w.r.t. the Sun (see Fig. 1.3). This implies a longer LOD and, consequently, the conversion factor from universal time into sidereal time is greater than one (about 1.0027).

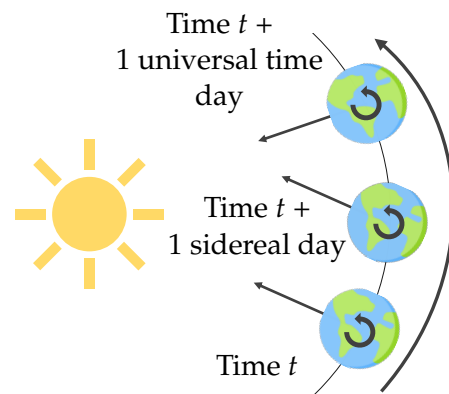


FIGURE 1.3: Sidereal and universal time representation

- Since the Earth's rotation is somewhat irregular, the time scales that it defines do not qualify to label precise astronomy observations. To overcome this limitation, the IAU introduced the ephemeris time (ET) in 1956. It is an ideal time scale based on the uniform and absolute time that appears as the independent variable in the formulation of classical mechanics. If the trajectories of the Earth and Moon were propagated considering all the perturbing effects, it would be possible to know their relative position at any future time, and hence any Earth-to-Moon observation could be tagged with a temporal label. The actual application of the method is, however, unpractical due to the absurdly long observational intervals required to precisely find those time labels.
- Atomic time is based on the low-energy transitions that an atom undergoes when it is coherently excited. Today's atomic clocks are mainly based on hydrogen, rubidium or cesium, and they provide the most stable commercially available time scales. In particular, some cesium-based clocks are stable at the second level within more than 100 million years. Not in vain, the cesium atom participates in the definition of second (as unit of time) established by the *Système International* (SI; BI, 2006): "[...] the duration of 9192631770 periods of the radiation corresponding to the transition between the two hyperfine levels of the ground state of the cesium 133 atom". The International Atomic Time (known as TAI due to its French abbreviation) is the practical realization of a uniform time scale based on atomic standards.
- A variant of TAI is the Universal Time Coordinate (UTC), which is present in our daily lives. It follows TAI in rate, but includes some one-second discontinuities (known as leap seconds) to accommodate the difference between TAI and UT1. Since the rotation of the Earth is slowing down due to some dissipative processes, the difference between UTC and TAI is negative.

We shall point out that the different GNSS ground segments also maintain their own atomic-based time scales to accomplish their operational purposes.

Once the theories of special and general relativity became widely accepted, an additional layer of complexity was added to the handling of time. In contrast to the classical belief that time flows at a constant pace equal for the entire universe, this new theoretical framework poses the idea that time is the fourth coordinate of a four-dimensional manifold defining space-time (Bambi, 2018), for which different observers use different times to label the same event. In order to cope with the scenarios imposed by today's scientific missions, the community has established three main coordinate times:

- Barycentric Coordinate Time (known as TCB due to its French abbreviation) is the coordinate time of a coordinate system with origin at the barycenter of the solar system.
- Geocentric Coordinate Time (known as TCG due to its French abbreviation) is the coordinate time of a coordinate system with origin at the center of the Earth.
- Terrestrial Time (TT) is a rescaled version of TCG that follows the rate of a clock located on the surface of the Earth. Its practical realization is TAI (plus a 32.184 s bias).

The TCB is conveniently used to describe interplanetary trajectories and it relates with TCG through the position and time of the studied body. On the other hand, TCG

and TT relates through the linear relationship

$$\Delta\text{TT} := (1 - L_G)\Delta\text{TCG}, \quad \text{where } L_G := 6.969290134 \cdot 10^{-10}.$$

It has to be stressed that a GNSS ground station tags the observational data according to TT, which is, on the other hand, the independent variable used for the equations of motion governing the geocentric GNSS orbits. The time sensed by an orbiting satellite differs, however, from TT, and its correct interpretation requires to account for relativistic effects (sections 3.3.4 and 3.8).

1.4 An insight into the Earth's rotation

1.4.1 Dynamic equations

The rotational dynamic of the Earth is governed by the law of conservation of angular momentum, which links the time derivative of the total angular momentum vector, \mathbf{l}^4 , expressed in an inertial system (in this case, realized by the ICRF) with the sum of external torques, $\boldsymbol{\tau}$, exerted on the Earth

$$\frac{d\mathbf{l}_{\mathcal{I}}}{dt} = \boldsymbol{\tau}_{\mathcal{I}} \quad (1.1)$$

Let us consider \mathbf{R} as the rotation matrix that converts terrestrial coordinates (in this case, expressed in the ITRF) into inertial coordinates, so that

$$\mathbf{R}^\top \frac{d(\mathbf{R}\mathbf{l}_{\mathcal{T}})}{dt} = \frac{d\mathbf{l}_{\mathcal{T}}}{dt} + \mathbf{R}^\top \frac{d\mathbf{R}}{dt} \mathbf{l}_{\mathcal{T}} = \mathbf{R}^\top \boldsymbol{\tau}_{\mathcal{I}} = \boldsymbol{\tau}_{\mathcal{T}} \quad (1.2)$$

Computing the time derivative of $\mathbf{R}^\top \mathbf{R} = \mathbf{I}$ (with \mathbf{I} the identity matrix), we see that the term $\mathbf{R}^\top \frac{d\mathbf{R}}{dt}$ is represented by a skew-symmetric matrix,

$$\mathbf{R}^\top \frac{d\mathbf{R}}{dt} = \begin{pmatrix} 0 & -\omega_{z\mathcal{T}} & \omega_{y\mathcal{T}} \\ \omega_{z\mathcal{T}} & 0 & -\omega_{x\mathcal{T}} \\ -\omega_{y\mathcal{T}} & \omega_{x\mathcal{T}} & 0 \end{pmatrix} \quad (1.3)$$

and $\mathbf{R}^\top \frac{d\mathbf{R}}{dt} \mathbf{l}_{\mathcal{T}}$ can thus be expressed as $\boldsymbol{\omega}_{\mathcal{T}} \times \mathbf{l}_{\mathcal{T}}$, being $\boldsymbol{\omega} = (\omega_x \ \omega_y \ \omega_z)^\top$ the angular velocity vector of the terrestrial system. Hence, equation (1.2) leads to the more compact form

$$\frac{d\mathbf{l}_{\mathcal{T}}}{dt} + \boldsymbol{\omega}_{\mathcal{T}} \times \mathbf{l}_{\mathcal{T}} = \boldsymbol{\tau}_{\mathcal{T}} \quad (1.4)$$

For a rigid body, the angular momentum is computed as the product between the inertia tensor and the angular velocity vector, i.e, $\mathbf{l} = \mathbf{I} \cdot \boldsymbol{\omega}$. However, the Earth behaves as a rigid body only to a first order approximation and, consequently, the so-called relative (to the terrestrial system) angular momentum, \mathbf{h} , shall be added to account for some small departures. All in all, equation (1.4) becomes the Liouville equation

$$\frac{d}{dt}(\mathbf{I}_{\mathcal{T}} \cdot \boldsymbol{\omega}_{\mathcal{T}} + \mathbf{h}_{\mathcal{T}}) + \boldsymbol{\omega}_{\mathcal{T}} \times (\mathbf{I}_{\mathcal{T}} \cdot \boldsymbol{\omega}_{\mathcal{T}} + \mathbf{h}_{\mathcal{T}}) = \boldsymbol{\tau}_{\mathcal{T}} \quad (1.5)$$

Since the Earth resembles a revolution ellipsoid (whose principal moments of inertia are A and C , with $A < C$) and rotates at an almost constant rate (denoted

⁴We will make use of the subscripts \mathcal{I} and \mathcal{T} to appoint to the components of a vector/tensor expressed in the inertial and terrestrial reference systems, respectively.

by Ω), it is preferred to closely align the terrestrial reference system to the Earth's rotation pole, such that

$$\boldsymbol{\tau}_{\mathcal{T}} = \Omega^2 \mathbf{C} (\tau_x \ \tau_y \ \tau_z)^\top \quad (1.6)$$

$$\mathbf{h}_{\mathcal{T}} = \Omega \mathbf{C} (h_x \ h_y \ h_z)^\top \quad (1.7)$$

$$\boldsymbol{\omega}_{\mathcal{T}} = \boldsymbol{\omega}_{0\mathcal{T}} + \Omega \mathbf{m}_{\mathcal{T}} = (0 \ 0 \ \Omega)^\top + \Omega (m_x \ m_y \ m_z)^\top \quad (1.8)$$

$$\mathbf{I}_{\mathcal{T}} = \mathbf{I}_{0\mathcal{T}} + \mathbf{C} \mathbf{I}_{\mathcal{T}} = \begin{pmatrix} A & 0 & 0 \\ 0 & A & 0 \\ 0 & 0 & C \end{pmatrix} + \mathbf{C} \begin{pmatrix} I_{xx} & I_{xy} & I_{xz} \\ I_{xy} & I_{yy} & I_{yz} \\ I_{xz} & I_{yz} & I_{zz} \end{pmatrix} \quad (1.9)$$

with $\tau_{(\cdot)} \ll 1$, $h_{(\cdot)} \ll 1$, $m_{(\cdot)} \ll 1$ and $I_{(\cdot)} \ll 1$. Note that the subscript \mathcal{T} has been omitted on purpose from the vector/tensor components to simplify the notation. Replacing (1.6-1.9) into (1.5) and keeping only first order terms, we readily get (e.g., Gross, 2007)

$$\frac{1}{\sigma} \frac{dm_x}{dt} + m_y = -\frac{1}{\Omega} \frac{d\phi_x}{dt} + \phi_y + \frac{C}{C-A} \tau_x \quad (1.10)$$

$$\frac{1}{\sigma} \frac{dm_y}{dt} - m_x = -\frac{1}{\Omega} \frac{d\phi_y}{dt} - \phi_x + \frac{C}{C-A} \tau_y \quad (1.11)$$

$$\frac{1}{\Omega} \frac{dm_z}{dt} = -\frac{1}{\Omega} \frac{d\phi_z}{dt} + \tau_z \quad (1.12)$$

where $\sigma = \Omega(C-A)/A$, and the $\phi_{(\cdot)}$ terms (known as excitation functions)

$$\phi_x = \frac{C}{C-A} (h_x + I_{xz}) \quad (1.13)$$

$$\phi_y = \frac{C}{C-A} (h_y + I_{yz}) \quad (1.14)$$

$$\phi_z = h_z + I_{zz} \quad (1.15)$$

It has to be noted that (1.10-1.15) are linear equations, being conveniently exploited when looking for solutions. More specifically, we split different contributions of $\tau_{(\cdot)}$, $h_{(\cdot)}$ and $I_{(\cdot)}$ into two different $\mathbf{m}_{(\cdot)}$ solutions: The so-called precession-nutation (subscript n) and polar motion (subscript p) solutions, such that

$$\begin{aligned} \boldsymbol{\omega}_{\mathcal{T}} &= \boldsymbol{\omega}_{0\mathcal{T}} + \Omega \mathbf{m}_{n\mathcal{T}} + \Omega \mathbf{m}_{p\mathcal{T}} = \\ &= (0 \ 0 \ \Omega)^\top + \Omega (m_{xn} \ m_{yn} \ m_{zn})^\top + \Omega (m_{xp} \ m_{yp} \ m_{zp})^\top \end{aligned} \quad (1.16)$$

It is noteworthy that the magnitude⁵ of the angular velocity vector can be approximated as

$$\omega \approx \Omega (1 + m_{zn} + m_{zp}) \quad (1.17)$$

Nonetheless, we can advance that the precession-nutation solution primary accounts for external torques (subsection 1.4.3), which do not induce variations in the third terrestrial component of the angular velocity vector for an ideal axisymmetric Earth (i.e., $m_{zn} \approx 0$, see Beutler, 2004a, equation (3.125)), and then

$$\omega \approx \Omega (1 + m_{zp}) \quad (1.18)$$

⁵Here we appoint to the magnitude of a vector, $\|\mathbf{a}\|$, by simply using non-bold font, i.e., a .

1.4.2 Kinematic equations

The orientation of the terrestrial system w.r.t. inertial space (in practice, the orientation of the ITRF w.r.t. the ICRF) is mathematically realized by the rotation matrix \mathbf{R} , such that

$$\mathbf{r}_{\mathcal{I}} = \mathbf{R}\mathbf{r}_{\mathcal{T}} \quad (1.19)$$

for any vector \mathbf{r} . This rotation is decomposed as

$$\mathbf{R} = \mathbf{N}(\psi, \epsilon, s)\mathbf{R}_z(-\Omega t)\mathbf{P}(p_x, p_y, p_z) \quad (1.20)$$

where \mathbf{N} and \mathbf{P} are rotation matrices associated to the precession-nutation and polar motion solutions, respectively, and can be further decomposed as

$$\mathbf{N} = \mathbf{R}_z(-\psi)\mathbf{R}_x(\epsilon)\mathbf{R}_z(-s) \quad (1.21)$$

$$\mathbf{P} = \mathbf{R}_z(-p_z)\mathbf{R}_y(p_x)\mathbf{R}_x(p_y) \quad (1.22)$$

Recall that the matrices $\mathbf{R}_{(\cdot)}$ represent basic rotations:

$$\mathbf{R}_x(\alpha) = \begin{pmatrix} 1 & 0 & 0 \\ 0 & +\cos(\alpha) & +\sin(\alpha) \\ 0 & -\sin(\alpha) & +\cos(\alpha) \end{pmatrix} \quad (1.23)$$

$$\mathbf{R}_y(\alpha) = \begin{pmatrix} +\cos(\alpha) & 0 & -\sin(\alpha) \\ 0 & 1 & 0 \\ +\sin(\alpha) & 0 & +\cos(\alpha) \end{pmatrix} \quad (1.24)$$

$$\mathbf{R}_z(\alpha) = \begin{pmatrix} +\cos(\alpha) & +\sin(\alpha) & 0 \\ -\sin(\alpha) & +\cos(\alpha) & 0 \\ 0 & 0 & 1 \end{pmatrix} \quad (1.25)$$

According to the empirical evidence, $p_{(\cdot)}$, as well as the time derivatives of the angles appearing in (1.20) are small, and so the application of (1.3) to (1.20) approximately results in

$$\boldsymbol{\omega}_{\mathcal{T}} = \begin{pmatrix} 0 \\ 0 \\ \Omega \end{pmatrix} + \begin{pmatrix} -\sin(\epsilon)\sin(\Omega t + s)\frac{d\psi}{dt} - \cos(\Omega t + s)\frac{d\epsilon}{dt} \\ -\sin(\epsilon)\cos(\Omega t + s)\frac{d\psi}{dt} + \sin(\Omega t + s)\frac{d\epsilon}{dt} \\ \cos(\epsilon)\frac{d\psi}{dt} + \frac{ds}{dt} \end{pmatrix} + \begin{pmatrix} +\Omega p_x - \frac{dp_y}{dt} \\ -\Omega p_y - \frac{dp_x}{dt} \\ +\frac{dp_z}{dt} \end{pmatrix} \quad (1.26)$$

Comparing with (1.16), it can be identified

$$\Omega \mathbf{m}_{n\mathcal{T}} = \begin{pmatrix} -\sin(\epsilon)\sin(\Omega t + s)\frac{d\psi}{dt} - \cos(\Omega t + s)\frac{d\epsilon}{dt} \\ -\sin(\epsilon)\cos(\Omega t + s)\frac{d\psi}{dt} + \sin(\Omega t + s)\frac{d\epsilon}{dt} \\ \cos(\epsilon)\frac{d\psi}{dt} + \frac{ds}{dt} \end{pmatrix} \quad (1.27)$$

$$\Omega \mathbf{m}_{p\mathcal{T}} = \begin{pmatrix} +\Omega p_x - \frac{dp_y}{dt} \\ -\Omega p_y - \frac{dp_x}{dt} \\ +\frac{dp_z}{dt} \end{pmatrix} \quad (1.28)$$

Equations (1.27) arise in multitude of applications and are referred to as Euler's kinematic equations. Equations (1.28), on the other hand, define more specific relations for the Earth's rotation problem and have been previously derived by several other authors (e.g., Gross, 1992).

We have to note that, for the sake of clarity, the decomposition (1.20) does not fully agree with the one employed by the IERS Conventions, although it still preserves the underlying ideas.

1.4.3 A qualitative view of the motion

The ecliptic and Earth's equator planes are the fundamental references to orient the Earth in space. These planes are inclined about 23.5° w.r.t. each other, and, because of perturbing dynamical interactions, they undergo some temporal variations. It is necessary then to freeze those planes at a given epoch (by convention, the beginning of the year 2000) for the definition of a suitable inertial system. In such a case, the pole (third axis) of the celestial system is perpendicular to the frozen ecliptic, its first axis follows the intersection between the frozen ecliptic and Earth's equator towards the vernal equinox, and the second axis is such that the resulting coordinate system is orthogonal and right-handed. The terrestrial system can be simply defined through the rotation (1.20). Note that the angles ϵ and $-\Omega t$ have a straightforward interpretation: The former approximates the 23.5° tilted angle, so that the third axis of the terrestrial system is nearly the Earth's pole, whereas the latter accounts for a nominal rotation rate in order for the terrestrial system to closely rotate with the Earth.

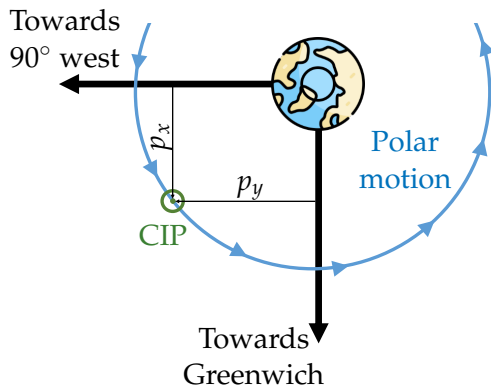


FIGURE 1.5: Polar motion

owe to the retrograde motion of the Moon orbital node, periodic variations in ψ (i.e., lunisolar nutation in longitude) and ϵ (i.e., lunisolar nutation in obliquity) arise. These variations are responsible of a prograde motion, characterized by a 18.6-year period and an amplitude of about 11 as, of the Earth's pole w.r.t. inertial space.

The homogeneous solution for (1.10-1.15) is simply

$$m_x = \rho_0 \cos(\sigma t - \sigma_0) \quad (1.29)$$

$$m_y = \rho_0 \sin(\sigma t - \sigma_0) \quad (1.30)$$

$$m_z = 0 \quad (1.31)$$

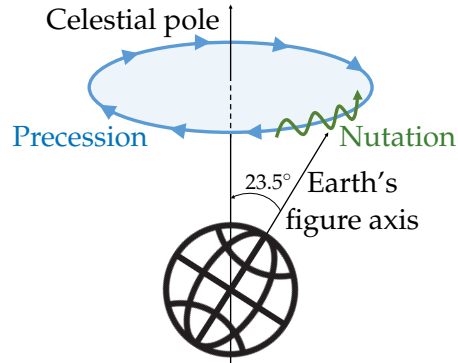


FIGURE 1.4: Precession-nutation motion

The solution for (1.10-1.15), complemented by (1.27) and considering that the only external torques acting upon a perfect ellipsoidal rigid Earth are exerted by the Sun and Moon, will provide the precession-nutation motion of the Earth. Its dominant long-term features are depicted in Fig. 1.4 and can be explained by the variations of ψ and ϵ (Beutler, 2004b, pages 44-45): On the one hand, a secular drift in ψ (i.e., lunisolar precession in longitude) of about 50.5 as/yr. This drift causes a retrograde complete rotation of the Earth's pole around the celestial pole in about 26.000 years. On the other hand,

and it exhibits the most distinctive characteristic of the polar motion: As seen from the terrestrial frame, the Earth's pole traces a prograde rotation with amplitude $\rho_0 \approx 0.2$ as and period of $2\pi/\sigma \approx 303$ days. If we neglect $\frac{1}{\Omega} \frac{dp_{(\cdot)}}{dt}$, then $p_{(\cdot)}$ equals $m_{(\cdot)}$ by virtue of (1.28). This is only a coarse approximation and, rather than the location of the Earth's pole, it is said that the angles $p_{(\cdot)}$ (particularly, p_x and p_y) give the location of the so-called Celestial Intermediate Pole (CIP) as seen from a left-handed terrestrial coordinate system (Fig. 1.5). Because of this geometrical interpretation, p_x and p_y are known as polar motion (abbreviated as PM) coordinates.

Although for the polar motion scenario presented before $p_z = 0$, as soon as Earth irregularities are considered (i.e., $h_z \neq 0$ and $I_{zz} \neq 0$), that statement no longer holds and we have to properly discuss the p_z interpretation. Its geometrical interpretation is simply a rotation around the CIP according to (1.20-1.22). More interesting is its dynamical explanation: Equations (1.18, 1.28) indicate that $\frac{dp_z}{dt}$ induces small excursions to the nominal rotation rate of the Earth. Considering the defining relations for UT1 and ΔLOD (i.e., departure from nominal LOD)

$$\Omega d\text{UT1} = \omega dt \quad (1.32)$$

$$\Omega \text{LOD} = \omega (\text{LOD} + \Delta\text{LOD}) \quad (1.33)$$

where t represents absolute time, which can be realized by UTC, we obtain the fundamental relation

$$-\frac{\Delta\text{LOD}}{\text{LOD}} \approx \frac{d(\text{UT1} - \text{UTC})}{dt} = \frac{1}{\Omega} \frac{dp_z}{dt} \quad (1.34)$$

The IERS Conventions generalize precession-nutation and polar motion according to the frequencies of the motion of the CIP (see Fig. 1.6), disregarding their physical origin:

- Precession-nutation includes all those terms with frequencies between -0.5 cpsd (cycles per sidereal day) and 0.5 cpsd as seen from the ICRF.
- Polar motion includes all those terms with frequencies below -1.5 cpsd and above 0.5 cpsd as seen from the ITRF.

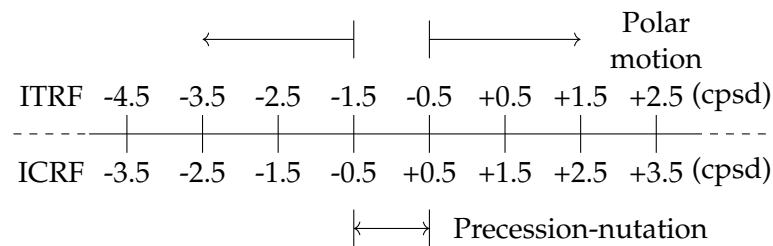


FIGURE 1.6: Conventional frequency-based distinction between precession-nutation and polar motion

The background models provided by the IERS Conventions build on external lunisolar and planetary torques as well as internal processes caused by ocean tides. The rotation of the Earth depends, however, on many other physical effects, and hence the IERS also reports observation-based tabular corrections to complement those models. For instance, by using the Poincaré's Earth Model (rigid Earth with liquid core), Beutler, 2004b (pages 114-115) shows that the unobservable initial state of the core induces long-period signals in nutation, causing the so-called Free Core Nutation

(FCN), for which the otherwise well-predicted precession-nutation model requires corrections. Likewise, the non-rigidity of the Earth, surficial fluid processes as well as internal processes, including different mechanisms for angular momentum exchange between the mantle and the core, produce polar motion variations at different time scales. Among those variations, the most significant are: A linear trend towards 79° west at a 3.5 mas/yr rate, and a different period for the main polar motion wobble of about 433 days⁶, instead of the 303 days previously noted. This difference is attributed to the elastic response of the Earth and the empirical evidence actually suggests that it is a multi-modal motion (Beutler et al., 2020). An exhaustive insight into these and more long-term polar motion variations can be found in Gross, 2007.

It must be stressed that the satellite geodetic techniques participate in the generation of the aforementioned IERS corrections for the polar motion model (note that corrections for the precession-nutation model are only accessible with VLBI). This is achieved by computing corrections over the kinematic $p_{(\cdot)}$ angles (section 3.3.2), which are referred to as earth rotation parameters (ERP), and whose GNSS-based derivation is at the heart of chapter 5. By means of (1.28) and (1.10-1.15), such parameters allow to infer and evaluate physical models for the Earth's processes, and so they become a valuable scientific asset for the community.

1.5 Description of the Earth's gravitational potential

1.5.1 Spherical harmonics

The gravitational potential (or geopotential, when referred to the Earth) at a point \mathbf{r} , $V(\mathbf{r})$, caused by a massive body equals the integral of the contributions associated to every infinitesimal mass of the body, dm_0 , located at \mathbf{r}_0 , i.e.,

$$V(\mathbf{r}) = \int_{m_0} \frac{Gdm_0}{\|\mathbf{r} - \mathbf{r}_0\|} = \frac{G}{r} \sum_{l=0}^{\infty} \int_{m_0} \left(\frac{r_0}{r}\right)^l P_l(\cos \gamma) dm_0 \quad (1.35)$$

where G is the gravitational constant, γ the angle formed by \mathbf{r} and \mathbf{r}_0 (see Fig. 1.7), and P_l the Legendre polynomial of degree l ⁷. The second equality in (1.35) directly follows from the expansion of $\|\mathbf{r} - \mathbf{r}_0\|^{-1}$ for $r > r_0$ (Battin, 1999, pages 387-391).

Thanks to the Legendre addition theorem that relates Legendre polynomials with associated Legendre functions (Maleček and Nádeník, 2001), equation (1.35) can be expressed in a more convenient way in terms of the terrestrial longitude, λ , and latitude, ϕ , for the vector \mathbf{r} , and λ_0 and ϕ_0 for \mathbf{r}_0 (Battin, 1999, pages 405-406):

$$V(r, \lambda, \phi) = \frac{GM}{r} \sum_{l=0}^{\infty} \left(\frac{R}{r}\right)^l \sum_{m=0}^l P_{lm}(\sin(\phi)) [C_{lm} \cos(m\lambda) + S_{lm} \sin(m\lambda)] \quad (1.36)$$

⁶This wobble is known as Chandler wobble to honor the American astronomer Seth Carlo Chandler who discovered it in the late 1800s.

⁷Recall that the Legendre polynomial of degree l , $P_l(x)$, and the associated Legendre functions of degree/order l/m , $P_{lm}(x)$, can be defined as

$$P_l(x) = \frac{1}{2^l l!} \frac{d^l}{dx^l} (x^2 - 1)^l \quad \text{and} \quad P_{lm}(x) = (1 - x^2)^{m/2} \frac{d^m}{dx^m} P_l(x),$$

and are efficiently computed using recursive relations (Battin, 1999, page 393).

where M and R are the mass and equatorial radius of the Earth, respectively, and the coefficients C_{lm} and S_{lm} :

$$C_{l0} = \frac{1}{R^l M} \int_{m_0} r_0^l P_l(\sin(\phi_0)) dm_0 \quad (1.37)$$

$$C_{lm} = \frac{2}{R^l M} \frac{(l-m)!}{(l+m)!} \int_{m_0} r_0^l P_{lm}(\sin(\phi_0)) \cos(m\lambda_0) dm_0 \quad (1.38)$$

$$S_{lm} = \frac{2}{R^l M} \frac{(l-m)!}{(l+m)!} \int_{m_0} r_0^l P_{lm}(\sin(\phi_0)) \sin(m\lambda_0) dm_0 \quad (1.39)$$

C_{l0} and C_{ll}/S_{ll} are known as zonal and sectorial coefficients, respectively. The remaining ones are named tesseral coefficients. It is common in geodesy to normalize the Legendre functions as $\bar{P}_{lm} = N_{lm}P_{lm}$, and, consequently, $\bar{C}_{lm} = C_{lm}/N_{lm}$ and $\bar{S}_{lm} = S_{lm}/N_{lm}$, with

$$N_{lm} = \sqrt{k(2l+1) \frac{(l-m)!}{(l+m)!}}, \quad k = \begin{cases} 1 & \text{if } m = 0 \\ 2 & \text{if } m \neq 0 \end{cases} \quad (1.40)$$

such that

$$\int_{-\pi/2}^{\pi/2} \bar{P}_{l_1 m}(\sin(\phi)) \bar{P}_{l_2 m}(\sin(\phi)) \cos(\phi) d\phi = 2k\delta_{l_1 l_2}, \quad \delta_{l_1 l_2} = \begin{cases} 1 & \text{if } l_1 = l_2 \\ 0 & \text{if } l_1 \neq l_2 \end{cases} \quad (1.41)$$

We see from (1.37-1.39) that the C_{lm}/S_{lm} coefficients depend on the definition of the terrestrial coordinate system upon which the vectors \mathbf{r} and \mathbf{r}_0 are projected. That connection becomes evident for the first- and second-degree coefficients, which can be written in terms of the terrestrial components of the geocenter vector, \mathbf{r}_g , and the Earth's inertia tensor \mathbf{I} , i.e.,

$$\mathbf{r}_{gT} = \begin{pmatrix} r_x \\ r_y \\ r_z \end{pmatrix} \quad \text{and} \quad \mathbf{I}_T = \begin{pmatrix} I_{xx} & I_{xy} & I_{xz} \\ I_{xy} & I_{yy} & I_{yz} \\ I_{xz} & I_{yz} & I_{zz} \end{pmatrix},$$

such that (Beutler, 2004a, equations (3.154,3.155))

$$C_{10} = \frac{r_z}{R} \quad (1.42)$$

$$C_{11} = \frac{r_x}{R} \quad (1.43)$$

$$S_{11} = \frac{r_y}{R} \quad (1.44)$$

$$C_{20} = \frac{I_{xx} + I_{yy} - 2I_{zz}}{2MR^2} \quad (1.45)$$

$$C_{21} = -\frac{I_{xz}}{MR^2} \quad (1.46)$$

$$S_{21} = -\frac{I_{yz}}{MR^2} \quad (1.47)$$

$$C_{22} = \frac{I_{yy} - I_{xx}}{4MR^2} \quad (1.48)$$

$$S_{22} = -\frac{I_{xy}}{2MR^2} \quad (1.49)$$

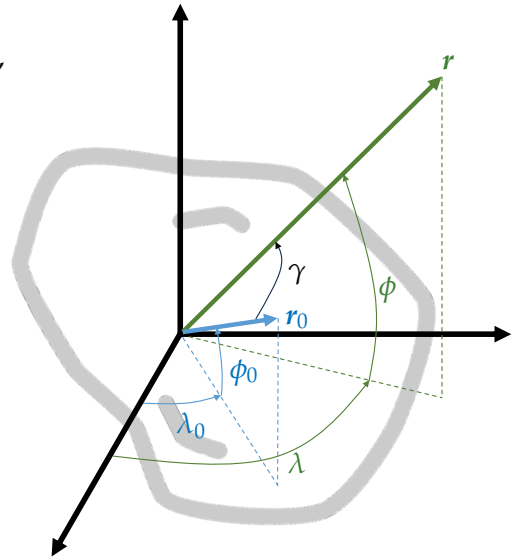


FIGURE 1.7: Definitions for the geometrical arguments of the gravitational potential as seen from a terrestrial system

Although, according to (1.42-1.44), we have access to the geocenter motion through the degree-1 Stokes coefficients, it is more conveniently modeled in GNSS analyses as a common displacement for all the ground stations involved in the geodetic solution (section 3.3.2). The GNSS-based derivation of those displacements, known as geocenter coordinates (GCC), is, along with the computation of ERP, the subject of chapter 5.

Looking now into (1.45-1.49), we first notice that C_{20} represents the Earth's oblateness. On the other hand, let us suppose that we know the value of all those degree-2 coefficients in a terrestrial system aligned with the figure axis, where the inertia tensor is $\mathbf{I}_{\mathcal{F}}$ (by definition, $I_{xz\mathcal{F}} = I_{yz\mathcal{F}} = C_{21} = S_{21} = 0$). Now, let us say that the actual terrestrial system is related to this frame by (1.22), where $p_z = 0$, and p_x and p_y are identified with the coordinates of the Earth's figure axis. Because of the tensor transformation $\mathbf{I}_{\mathcal{T}} = \mathbf{P}^T \mathbf{I}_{\mathcal{F}} \mathbf{P}$, we can show that, to first order in p_x and p_y , the only degree-2 coefficients which take on different values in the actual terrestrial system (i.e., instantaneous ITRF) are C_{21} and S_{21} , so that

$$\begin{pmatrix} C_{21} \\ S_{21} \end{pmatrix} = \begin{pmatrix} C_{20} - 2C_{22} & 2S_{22} \\ -2S_{22} & -C_{20} - 2C_{22} \end{pmatrix} \begin{pmatrix} p_x \\ p_y \end{pmatrix} \quad (1.50)$$

The potential function, $V(\mathbf{r})$, satisfies the Laplace equation, $\Delta V = 0$, for $r > R$ and hence (1.36) can also be derived from it by looking for regular solutions of the type $V_l = \frac{1}{r^{l+1}} g_l(\phi, \lambda)$ ⁸. These functions are known as spherical harmonics (the terms $g_l(\phi, \lambda)$ alone are known as surface spherical harmonics), and C_{lm} and S_{lm} are thus spherical harmonic (or Stokes) coefficients. Approaching to the problem from this perspective may establish that the $g_l(\phi, \lambda)$ functions turn out to be the two-dimensional generalization of the Fourier series, which allows them to approximate functions in the sphere (Gallier, 2009, Atkinson and Han, 2012).

Finally, we have to mention that the IERS Conventions include several models for the computation of the Stokes coefficients. On the one hand, we have an almost static part based on the Earth Gravitational Model 2008 (EGM2008, Pavlis et al., 2012), which includes drifts for C_{30} and C_{40} . This model is further complemented by a SLR-derived C_{20} and a time-dependent realization of C_{21}/S_{21} based on (1.50). Since the figure axis, Earth's pole and CIP coincide in the long-term (Wahr, 1987, Wahr, 1990), the observed mean PM coordinates are used in place of the Earth's figure axis when evaluating (1.50). On the other hand, variations in the Earth's density entail variations in the Stokes coefficients. The IERS Conventions primary provide models for those variations caused by tidal deformations due to external bodies, i.e., solid and ocean tides, as well as due to Earth's rotation irregularities, i.e., pole tides (although recent studies assert that the conventional pole tide model is flawed, Wahr et al., 2015). Moreover, other non-tidal variations originating from global mass variability in oceans and atmosphere, made available through the atmosphere and ocean de-aliasing level-1B (AOD1B) product (Dobslaw et al., 2017), may cause non-negligible variations in the Stokes coefficients. Which model should be considered or safely neglected depends on the specific application, e.g., specific considerations are necessary for time-variable gravity field estimation (chapter 6).

⁸More precisely, by looking for regular solutions of the type $V_l = r^l g_l(\phi, \lambda)$. However, it is proven that for every $r^l g_l(\phi, \lambda)$ solution there exist a $\frac{1}{r^{l+1}} g_l(\phi, \lambda)$ solution (Ferrers, 1877, pages 1-3).

1.5.2 Geoid and reference ellipsoid

Prior to introducing the geoid, we have to note that any gravity measurement collected by an instrument co-rotating with the Earth fundamentally differs from the gravitation sensed by an orbiting satellite by the fictitious centrifugal acceleration. Therefore, gravity potential, W , gravitational potential, V , and centrifugal potential, $1/2\omega^2 r^2 \cos^2(\phi)$, are related by

$$W(r, \phi, \lambda) = V(r, \phi, \lambda) + \frac{1}{2}\omega^2 r^2 \cos^2(\phi) \quad (1.51)$$

The Earth's shape is configured by gravity itself and, hence, it is very closely defined by the geoid: An equipotential gravity surface that coincides with the mean sea level. This definition establishes a clear link between the Earth's shape and gravity (and gravitation). The actual realization of the geoid from the gravitational Stokes coefficients is, however, really layered (Kaula, 2013, pages 8-10). Conceptually, it is accomplished by representing the geoid, N , as a sum of spherical harmonics:

$$N(\phi, \lambda) = R \sum_{l=0}^{\infty} \sum_{m=0}^l P_{lm}(\sin(\phi)) [\hat{C}_{lm} \cos(m\lambda) + \hat{S}_{lm} \sin(m\lambda)] \quad (1.52)$$

Replacing (1.52) in (1.51) results in a function $W(N(\phi, \lambda), \phi, \lambda)$ that can also be represented as a sum of spherical harmonics. The constant $l = m = 0$ coefficient identifies with the sought equipotential surface. The remaining coefficients, accompanying $P_{lm}(\sin(\phi)) \cos(m\lambda)$ and $P_{lm}(\sin(\phi)) \sin(m\lambda)$, must be identically zero, which gives the functional connections between the gravitational coefficients C_{lm}/S_{lm} and the geoid coefficients $\hat{C}_{lm}/\hat{S}_{lm}$.

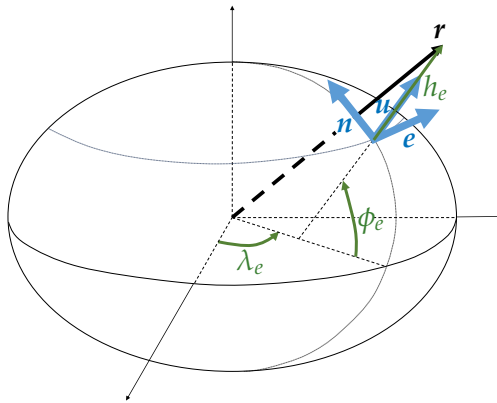


FIGURE 1.8: Ellipsoidal coordinates

Since the geoid resembles a revolution ellipsoid, it is handy to use an ellipsoidal coordinate system to locate positions in the vicinity of the Earth's surface (e.g., the location of ground stations). This coordinate system is realized by a reference ellipsoid (see Torge and Müller, 2012, section 4.1), which is defined by its semi-major and -minor axes (a and b , respectively), or any derived parameter, such as the flattening, f , or eccentricity, e :

$$f = \frac{a - b}{a}, \quad e = \frac{\sqrt{a^2 - b^2}}{a} \quad (1.53)$$

The Cartesian coordinates of a vector \mathbf{r} can thus be expressed in terms of the ellipsoidal height, longitude and latitude (h_e , λ_e and ϕ_e , respectively; see Fig. 1.8):

$$\mathbf{r}_{\mathcal{T}} = \begin{pmatrix} (N + h_e) \cos(\phi_e) \cos(\lambda_e) \\ (N + h_e) \cos(\phi_e) \sin(\lambda_e) \\ ((1 - e^2)N + h_e) \sin(\phi_e) \end{pmatrix}, \quad N = \frac{a}{\sqrt{1 - e^2 \sin^2(\phi_e)}} \quad (1.54)$$

The up, east and north directions (\mathbf{u} , \mathbf{e} and \mathbf{n} in Fig. 1.8, respectively) are well-suited to define a local Cartesian coordinate system, which is especially useful for the

description of kinematic processes within the surface of the Earth (e.g., the velocity field of the tectonic plates).

As for the gravitational potential, the IERS Conventions provide models to account for surface displacements caused by tides and loading effects. For precise geodetic applications, they have to be taken into account during the reduction of the observations (section 3.3.2).

1.5.3 Surface mass variations

Satellite-based time-variable corrections to the Stokes coefficients primary account for the variability induced by hydrological processes that occur in the vicinity of the Earth's surface. Although the GNSS-based time-variable gravity field solutions generated in chapter 6 do not qualify on their own to analyse such processes, it is still meaningful, because of its conceptual value, to introduce the surface mass representation of the Stokes coefficients. This is done in the sequel by following the discussion given by Wahr et al., 1998.

Variations in the Earth's density, $\Delta\rho$, induce variations in the Stokes coefficients $\Delta\bar{C}_{lm}/\Delta\bar{S}_{lm}$, which, according to (1.37-1.40), can be formulated as

$$\left(\frac{\Delta\bar{C}_{lm}}{\Delta\bar{S}_{lm}}\right) = \frac{3}{4\pi R\rho_E(2l+1)} \int_{-\frac{\pi}{2}}^{\frac{\pi}{2}} \int_0^{2\pi} \int_0^R \left(\frac{r_0}{R}\right)^{l+2} \bar{P}_{lm}(\sin(\phi_0)) \begin{pmatrix} \cos(m\lambda_0) \\ \sin(m\lambda_0) \end{pmatrix} \Delta\rho \cos(\phi_0) dr_0 d\lambda_0 d\phi_0 \quad (1.55)$$

where we have made use of $dm_0 = \Delta\rho r_0^2 \cos(\phi_0) dr_0 d\lambda_0 d\phi_0$ and $M = 4/3\pi R^3 \rho_E$, being ρ_E the average Earth's density.

The hydrological processes (atmosphere, oceans, ice caps and groundwater storage) occur in a thin layer of thickness H (about 10-15 km), modifying the Earth's surface mass, which, in turn, loads and deforms the underlying non-rigid Earth. The variations $\Delta\bar{C}_{lm}/\Delta\bar{S}_{lm}$ shall then account for both phenomena:

$$\left(\frac{\Delta\bar{C}_{lm}}{\Delta\bar{S}_{lm}}\right) = \left(\frac{\Delta\bar{C}_{lm}}{\Delta\bar{S}_{lm}}\right)_{\text{surface mass}} + \left(\frac{\Delta\bar{C}_{lm}}{\Delta\bar{S}_{lm}}\right)_{\text{loading}} \quad (1.56)$$

being both terms related by the load Love number of degree l , k_l , as

$$\left(\frac{\Delta\bar{C}_{lm}}{\Delta\bar{S}_{lm}}\right)_{\text{loading}} = k_l \left(\frac{\Delta\bar{C}_{lm}}{\Delta\bar{S}_{lm}}\right)_{\text{surface mass}} \quad (1.57)$$

Integrating (1.55) for $R-H \leq r_0 \leq R$, so that we only account for the surface mass contribution, and defining surface density, $\Delta\sigma$, as

$$\Delta\sigma = \int_{R-H}^R \Delta\rho dr_0 \quad (1.58)$$

equation (1.56) yields

$$\left(\frac{\Delta\bar{C}_{lm}}{\Delta\bar{S}_{lm}}\right) = \frac{3(1+k_l)}{4\pi R\rho_E(2l+1)} \int_{-\frac{\pi}{2}}^{\frac{\pi}{2}} \int_0^{2\pi} \bar{P}_{lm}(\sin(\phi_0)) \begin{pmatrix} \cos(m\lambda_0) \\ \sin(m\lambda_0) \end{pmatrix} \Delta\sigma \cos(\phi_0) d\lambda_0 d\phi_0 \quad (1.59)$$

Note that it has been assumed $(l + 2)H/R \ll 1$ (only valid for relatively small degrees, i.e., $l < 100$) and, therefore, $(r_0/R)^{l+2} \approx 1$.

By expressing the surface density as a sum of spherical harmonics

$$\Delta\sigma(\lambda_0, \phi_0) = R\rho_w \sum_{l=0}^{\infty} \sum_{m=0}^l P_{lm}(\sin(\phi_0)) [\hat{C}_{lm} \cos(m\lambda_0) + \hat{S}_{lm} \sin(m\lambda_0)] \quad (1.60)$$

where ρ_w is the density of water, and taking into account (1.41), together with the orthogonality of the $\cos(m\lambda)$ and $\sin(m\lambda)$ functions, we eventually establish the relationship between $\Delta\bar{C}_{lm}/\Delta\bar{S}_{lm}$ and $\Delta\hat{C}_{lm}/\Delta\hat{S}_{lm}$ from (1.59):

$$\begin{pmatrix} \Delta\hat{C}_{lm} \\ \Delta\hat{S}_{lm} \end{pmatrix} = \frac{\rho_E}{3\rho_w} \frac{1+2l}{1+k_l} \begin{pmatrix} \Delta\bar{C}_{lm} \\ \Delta\bar{S}_{lm} \end{pmatrix} \quad (1.61)$$

Equations (1.60, 1.61) can be used to relate the satellite-based time-variable gravity field solutions with hydrological processes, being used, for instance, to infer global freshwater trends (Rodell et al., 2018), or to quantify net ice mass loss in frigid regions (Velicogna, 2009). Consequently, the ultimate application of the gravity field solutions returns to science and, above all, society as a high-value asset.

It is worth closing this discussion by introducing the Equivalent Water Height (EWH) index, defined as the thickness of water that would produce the observed surface density variations, i.e., $\Delta\sigma = \rho_w \text{EWH}$. This index gives an alternative interpretation of (1.60).

1.6 Orbit representation

1.6.1 Equations of motion

The geocentric position, \mathbf{r} , of an Earth orbiting satellite is governed by the conservation of linear momentum, which establishes for a satellite with constant mass

$$\frac{d^2\mathbf{r}_I}{dt^2} = -\frac{GM}{r^3}\mathbf{r}_I + \mathbf{a}_p \quad (1.62)$$

where the first term on the right-hand side corresponds to the first term of the gravitational potential, and the vector \mathbf{a}_p accounts for any additional perturbing acceleration acting upon the satellite, typically several order of magnitude smaller than the central force. It may contain, for example, higher-order geopotential terms, atmospheric drag or relativistic corrections. The perturbations used in GNSS orbit modeling are outlined in section 3.3.2.

If $\mathbf{a}_p = \mathbf{0}$, equation (1.62) admits a very well-known solution: The satellite traces a conic curve, or, more specifically for our application, an ellipse, known as Keplerian orbit. The constants of integration for (1.62) are then conveniently chosen to agree with the geometrical properties of the ellipse as well as its orientation, namely, the semi-major axis, a , the eccentricity, e , the inclination, i , the right ascension of the

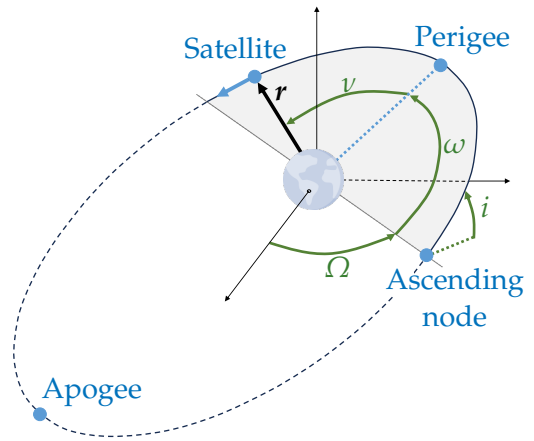


FIGURE 1.9: Keplerian orbit

ascending node, Ω , the argument of perigee, ω , and the perigee passing time, τ_p (see angles in Fig. 1.9). These constants are referred to as orbital elements and, when confined as the components of the one-dimensional array $\boldsymbol{\alpha}$, establish the functional relations $\boldsymbol{r} = \boldsymbol{r}(t, \boldsymbol{\alpha})$ and $\boldsymbol{v} = \boldsymbol{v}(t, \boldsymbol{\alpha})$ for the position and velocity vectors, respectively. Explicit expressions are given by Beutler, 2004a, equations (4.62-4.66):

$$\boldsymbol{r}_{\mathcal{I}} = \frac{a(1-e^2)}{1+e\cos(\nu)} \mathbf{R}_z(-\Omega) \mathbf{R}_x(-i) \mathbf{R}_z(-\omega) \begin{pmatrix} \cos(\nu) \\ \sin(\nu) \\ 0 \end{pmatrix} \quad (1.63)$$

$$\boldsymbol{v}_{\mathcal{I}} = \sqrt{\frac{GM}{a(1-e^2)}} \mathbf{R}_z(-\Omega) \mathbf{R}_x(-i) \mathbf{R}_z(-\omega) \begin{pmatrix} -\sin(\nu) \\ e + \cos(\nu) \\ 0 \end{pmatrix} \quad (1.64)$$

The so-called true anomaly, ν , implicitly defines the dependency with time through the eccentric anomaly, E , and Kepler's equation:

$$\tan\left(\frac{E}{2}\right) = \sqrt{\frac{1-e}{1+e}} \tan\left(\frac{\nu}{2}\right), \quad E - e \sin(E) = n(t - \tau_p) \quad (1.65)$$

where $n = \sqrt{GM/a^3}$ is the mean motion, related to the orbital period, T , by $T = 2\pi/n$. For the manipulation of these equations, it is often useful to introduce the argument of latitude, defined as $u = \nu + \omega$.

Relevant directions for the orbit analysis are the radial (unit vector in the \boldsymbol{r} direction), along-track (velocity direction) and cross-track (orthogonal to the others, resulting in a right-handed trihedron) directions.

1.6.2 Osculating elements and precession of the ascending node

As soon as the perturbing acceleration is other than zero, i.e., $\boldsymbol{a}_p \neq 0$, the orbit described by \boldsymbol{r} is no longer an ellipse. To solve (1.62), we may then use the method of variation of the constants, i.e., $\boldsymbol{r} = \boldsymbol{r}(t, \boldsymbol{\alpha}(t))$ and $\boldsymbol{v} = \boldsymbol{v}(t, \boldsymbol{\alpha}(t))$, eventually obtaining a number of equations for $\frac{d\boldsymbol{\alpha}}{dt}$. Therefore, the orbital elements are now osculating elements that define an osculating orbit and, instantaneously, \boldsymbol{r} and \boldsymbol{v} through (1.63-1.65). If \boldsymbol{a}_p can be expressed as $\boldsymbol{a}_p = \nabla W$, then $\frac{d\boldsymbol{\alpha}}{dt}$ is better described by the Lagrange's planetary equations (Battin, 1999, equation (10.31)). Otherwise, $\frac{d\boldsymbol{\alpha}}{dt}$ is described by the more general Gauss' equations (Battin, 1999, equation (10.41)).

Because of its relevance in satellite geodesy, let us only focus on the Lagrange's planetary equation for the ascending node,

$$\frac{d\Omega}{dt} = \frac{1}{na^2\sqrt{1-e^2}\sin(i)} \frac{\partial W}{\partial i} \quad (1.66)$$

and let us consider the perturbation due to the oblateness of the Earth, which manifests through the C_{20} coefficient of the gravitational potential:

$$W = \frac{\sqrt{5}}{2} GM R^2 \bar{C}_{20} \frac{(1+e\cos(\nu))^3}{a^3(1-e^2)^3} (3\sin^2(\nu+\omega)\sin^2(i) - 1) \quad (1.67)$$

The secular behavior of the orbital elements is computed by averaging the corresponding equation, in this case (1.66), within one orbital period, while keeping the orbital elements constant. The necessary integral is better performed in the variable

v , related to time by means of $\|\mathbf{r} \times \mathbf{v}\| = r^2 \frac{dv}{dt} = \sqrt{GMa(1-e^2)}$ ⁹, which eventually yields (Battin, 1999, equation (10.94))

$$\dot{\Omega}_s = \frac{3\sqrt{5}}{2} \bar{C}_{20} \left(\frac{R}{a(1-e^2)} \right)^2 n \cos(i) \quad (1.68)$$

where the secular variation of Ω has been denoted by $\dot{\Omega}_s$. Note that \bar{C}_{20} is negative (about $-4.8 \cdot 10^{-4}$), resulting in a retrograde precession of the ascending node for $i < 90^\circ$.

Because of the precession of the ascending node, the geometry between the Sun and the satellite orbital plane repeats after one draconitic period, T_d , which affects the GNSS-based geodetic solutions (see section 5.2) and can be computed for the GNSS orbits as

$$T_d = \frac{T_y}{\frac{|\dot{\Omega}_s|}{2\pi} T_y + 1} \quad (1.69)$$

being T_y one sidereal year (365.25 days).

1.6.3 Variational equations

For the reduction of the GNSS observations, we first linearize the corresponding observational model around some a priori information. During this step, we need the so-called variational equations for the orbits, whose development is introduced in the following paragraphs. The reader may complement this section with Beutler, 2004a, chapter 5.

Let us write (1.62) in the more compact form

$$\frac{d\mathbf{x}}{dt} = \mathbf{f} \quad (1.70)$$

being the state vector and the right-hand side

$$\mathbf{x} = \begin{pmatrix} \mathbf{r} \\ \mathbf{v} \end{pmatrix} \quad \text{and} \quad \mathbf{f} = \begin{pmatrix} \mathbf{v} \\ -\frac{GM}{r^3} \mathbf{r} + \mathbf{a}_p \end{pmatrix} \quad (1.71)$$

respectively, where the subscript \mathcal{I} has been dropped on purpose to alleviate the notation. The term \mathbf{f} generally depends on the time, t , the state vector, \mathbf{x} , and a number n of other dynamical parameters (e.g., Stokes coefficients) that we may confine in the one-dimensional array \mathbf{q} , i.e., $\mathbf{f} = \mathbf{f}(t, \mathbf{x}, \mathbf{q})$. The integration of (1.70) hence yields an a priori solution $\mathbf{x} = \mathbf{x}(t, \mathbf{x}_0, \mathbf{q})$, with \mathbf{x}_0 the state vector at some initial epoch, t_0 . Owing to this functional relation, we prefer to replace the total derivative operator, $\frac{d(\cdot)}{dt}$, by the partial derivative operator, $\frac{\partial(\cdot)}{\partial t}$, in (1.70). Variations in \mathbf{x} (i.e., $\delta\mathbf{x}$) are thus caused by variations in \mathbf{x}_0 ¹⁰ (i.e., $\delta\mathbf{x}_0$) and variations in \mathbf{q} (i.e., $\delta\mathbf{q}$), such that

$$\mathbf{x}(t, \mathbf{x}_0 + \delta\mathbf{x}_0, \mathbf{q} + \delta\mathbf{q}) = \mathbf{x} + \delta\mathbf{x} = \mathbf{x} + \sum_{i=1}^6 \mathbf{x}_{x_{0i}} \delta x_{0i} + \sum_{i=1}^n \mathbf{x}_{q_i} \delta q_i \quad (1.72)$$

⁹This expression is only rigorously true for $\frac{\partial v}{\partial t}$, since, according to (1.65), $v = v(t, a, e, \tau_p)$. However, $\frac{\partial v}{\partial t} = \frac{dv}{dt}$ provided that we kept fixed the orbital elements.

¹⁰Rather than variations in the initial state vector, we often use variations in the osculating elements at t_0 . This does not present any conceptual problem thanks to (1.63, 1.64).

where we have denoted the i th component of x_0 and q by the subscript i , and $x_{(\cdot)} := \frac{\partial x}{\partial (\cdot)}$. If we further apply variations to (1.70), we get

$$\delta \frac{\partial x}{\partial t} = \frac{\partial}{\partial t} \left(\sum_{i=1}^6 x_{x_{0i}} \delta x_{0i} + \sum_{i=1}^n x_{q_i} \delta q_i \right) = \delta f = \frac{\partial f}{\partial x} \left(\sum_{i=1}^6 x_{x_{0i}} \delta x_{0i} + \sum_{i=1}^n x_{q_i} \delta q_i \right) + \sum_{i=1}^n \frac{\partial f}{\partial q_i} \delta q_i \quad (1.73)$$

Since this equation must be satisfied for any δx_{0i} (with $i = 1, 2, \dots, 6$) and δq_i (with $i = 1, 2, \dots, n$), we obtain the claimed variational equations:

$$\frac{\partial x_{x_{0i}}}{\partial t} = \frac{\partial f}{\partial x} x_{x_{0i}} \quad (1.74)$$

$$\frac{\partial x_{q_i}}{\partial t} = \frac{\partial f}{\partial x} x_{q_i} + \frac{\partial f}{\partial q_i} \quad (1.75)$$

Using the so-called transition matrix, $\Phi(t, t_0)$, which results from integrating

$$\frac{\partial}{\partial t} \Phi(t, t_0) = \frac{\partial f}{\partial x} \Phi(t, t_0), \quad \text{with } \Phi(t_0, t_0) = I \quad (1.76)$$

we may verify that the solutions for the differential equations (1.74, 1.75) can be written as:

$$x_{x_{0i}} = \Phi(t, t_0) e_i \quad (1.77)$$

$$x_{q_i} = \int_{t_0}^t \Phi(t, \tau) \frac{\partial f}{\partial q_i} \Big|_{t=\tau} d\tau \quad (1.78)$$

where e_i is a one-dimensional array (column matrix) populated with zeros, except for its i th position, which is one.

We shall close this section by noting two important properties of the transition matrix:

$$\Phi(t_2, t_1) = \Phi^{-1}(t_1, t_2) \quad (1.79)$$

$$\Phi(t_3, t_1) = \Phi(t_3, t_2) \Phi(t_2, t_1) \quad (1.80)$$

1.7 Summary

As soon as we dive into the GNSS observation model in [chapter 3](#), the link to geodesy may be shadowed by the mathematical models and tools employed for the reduction of the measurements, as well as by technical implementations, numerical experiments and results. To prevent from that, this chapter has been so designed to connect the otherwise mere mathematical parameters (i.e., GCC, ERP and time-variable gravity field) to physical quantities that can actually give a profound understanding of the Earth's processes.

It was firstly introduced the current status and challenges that the geodetic community is facing, where it was pointed out the present efforts to unify the different geodetic techniques as well as the important role that global ties play in pursuit of this purpose, which is the driving element of the present dissertation. It actually justifies the analyses carried out in the following chapters: The use of undifferenced GNSS

observations (chapter 3 and chapter 4) allow to include stand-alone geodetic receivers equipped in scientific satellites into the GNSS network processing. On the other hand, the rigorous characterization of the GNSS capabilities to sense the geocenter motion, the Earth's orientation and the time-variable gravity field (chapter 5 and chapter 6) allows to detect systematics, and to identify the benefits of a common inter-technique processing. In this regard, to understand the sensitivity of GNSS solutions to the time-variable gravity field is of special interest, since this topic has received little attention in former studies.

Later, we showed how the Earth's rotation can be split into precession-nutation and polar motion from a formal point of view. This allowed to relate the kinematic parameters that can be derived with geodetic techniques to their physical meaning. We concluded the discussion of the Earth's rotation with a qualitative description of the motion.

The modeling of the Earth's gravitational potential as a sum of spherical harmonics was also introduced. Here we paid special attention to explain the meaning of the first and second degrees, which are related to the GCC and the Earth's inertia tensor. Because of its importance for society, it was also discussed the role that the time-variable gravity field plays in understanding the surface water processes.

Finally, this chapter gave an insight into orbital mechanics, where we first stressed the elliptic nature of the orbits, and how the oblateness of the Earth produces a precession in the orbital nodes. This mechanism makes the geometry between the orbital plane and the Sun repeat every one draconitic period (shorter than one sidereal year for GNSS satellites), which plays a major role in orbit modeling. This section eventually included the so-called variational equations, which results from the linearization of dynamical systems, and are necessary to parameterize the GNSS orbits.

Theory of parameter estimation for GNSS processing

2.1 Introduction

It can be advanced from [chapter 3](#) that the GNSS observations reflect a number of physical and geometrical effects, including, among others, geometrical ranges, clock errors, or signal propagation delays. To exploit these observations, we thus need to reconstruct them applying several well-known background models and parameterizing some only roughly known quantities (i.e., unknown quantities), for which we later compute corrections. The mathematical underpinning theory that we use to determine such corrections is parameter estimation (i.e., statistical inference) in linear models, and we hence refer to those corrections as estimates.

The functional relation between the observations, collected in the column matrix \mathbf{y} of dimension n , and the unknown quantities, collected in the column matrix \mathbf{x} of dimension m (for our GNSS processing, $n > m$), is simply

$$\mathbf{y} = \mathbf{f}(\mathbf{x}) \quad (2.1)$$

Linearizing around some a priori information, \mathbf{x}_0 , such that $\mathbf{x} = \mathbf{x}_0 + \delta\mathbf{x}$, we get

$$\mathbf{y} - \mathbf{f}(\mathbf{x}_0) = \left. \frac{\partial \mathbf{f}}{\partial \mathbf{x}} \right|_{\mathbf{x}=\mathbf{x}_0} \delta\mathbf{x} \quad (2.2)$$

The left-hand side term is known as the observed minus computed (O-C) term, and $\frac{\partial \mathbf{f}}{\partial \mathbf{x}}$ is named design matrix. Note that \mathbf{f} can depend on functions of the actual parameters. In particular, this is the case for the satellite coordinates, which are related to some dynamical parameters by [\(1.72\)](#). In such cases, the derivatives w.r.t. them are better computed using the chain rule, whose composition requires the solutions [\(1.77, 1.78\)](#).

The linear system of equations defined by [\(2.2\)](#) is inconsistent because of some stochastic errors that disrupt the observations. For that reason, we commonly treat the observations (and the O-C term) as normally distributed random variables characterized by the covariance matrix $\Sigma_{yy} = \sigma^2 \mathbf{P}^{-1}$, where σ and \mathbf{P} are known as root mean square (RMS) of unit weight and weight matrix, respectively. The deterministic $\delta\mathbf{x}$ parameters are then assumed to relate to the mean observations by means of the so-called Gauss-Markoff model:

$$\mathbf{E}[\mathbf{y}] = \mathbf{A}\mathbf{x}, \quad \mathbf{D}[\mathbf{y}] = \Sigma_{yy} = \sigma^2 \mathbf{P}^{-1} \quad (2.3)$$

where we have alleviated the notation with $\mathbf{y} - \mathbf{f}(\mathbf{x}_0) \rightarrow \mathbf{y}$, $\frac{\partial \mathbf{f}}{\partial \mathbf{x}} \rightarrow \mathbf{A}$ and $\delta\mathbf{x} \rightarrow \mathbf{x}$. On

the other hand, $E[\cdot]$ and $D[\cdot]$ represent the expectation and dispersion operators¹, respectively. From an algebraic point of view, $E[\mathbf{y}]$ belongs to the range (or column space) of \mathbf{A} , i.e., $E[\mathbf{y}] \in R(\mathbf{A})$, and, therefore, estimating \mathbf{x} is equivalent to estimating $E[\mathbf{y}]$.

It is generally accepted that (2.3) is not perfect due to deficiencies in the observation functional model (which includes the background models) and the stochastic model, causing systematic errors in the estimates. Such errors may become very harmful since they are often unnoticed and lead to inconsistencies between estimates from different geodetic techniques.

The whole theory of parameter estimation not only covers the estimators themselves, but a wider range of other topics, namely, algebra, probability and hypothesis testing. All these topics are rigorously covered in Koch, 1999. A more succinct discussion, yet comprehensive, can be found in Verhagen and Teunissen, 2017 and Teunissen, 2017a. In this chapter we limit ourselves to the introduction of the estimation principle (section 2.2), to the development of specific results that are of interest in the frame of this work, i.e., the equivalence principle between differenced or undifferenced GNSS processing schemes in section 2.3 and the basis for ambiguity resolution (AR) in section 2.4, to efficiently handle the resulting equations (section 2.5) and to manipulate them to generate the so-called GNSS long-arc solutions (section 2.6). A final section is left to the summary.

2.2 Estimation principles

For the Gauss-Markoff model (2.3), there are three principles that lead to the same estimate of \mathbf{x} (denoted by a hat, i.e., $\hat{\mathbf{x}}$):

- The best linear unbiased principle, meaning that (1) we require $\hat{\mathbf{x}}$ to be best in the sense that the variance of each component is minimum, (2) we require $\hat{\mathbf{x}}$ to be linear in the sense that $\hat{\mathbf{x}} = \mathbf{L}\mathbf{y}$, and (3) we require $\hat{\mathbf{x}}$ to be unbiased in the sense that $E[\hat{\mathbf{x}}] = \mathbf{x}$.
- The least squares (LS) principle, meaning that we require the norm of the residuals, i.e. $\mathbf{e} = \mathbf{y} - \mathbf{A}\mathbf{x}$, weighted by the inverse of the covariance matrix of the observations² to be minimum, i.e., $(\mathbf{y} - \mathbf{A}\mathbf{x})^\top \boldsymbol{\Sigma}_{yy}^{-1} (\mathbf{y} - \mathbf{A}\mathbf{x})$ is the objective function to be minimized.
- The maximum-likelihood principle, meaning that we require the probability of the observed data to be maximum. Since it was assumed that the observations are normally distributed³, we once more conclude that $(\mathbf{y} - \mathbf{A}\mathbf{x})^\top \boldsymbol{\Sigma}_{yy}^{-1} (\mathbf{y} - \mathbf{A}\mathbf{x})$ shall be minimized.

The sought estimate is eventually obtained from

$$\mathbf{N}\hat{\mathbf{x}} = \mathbf{b} \tag{2.4}$$

¹Commonly speaking, the expectation operator represents the mean statistic, the dispersion operator the standard deviation (STD) statistic and the square of the RMS statistic equals the square of the mean plus the square of the STD statistics.

² $\boldsymbol{\Sigma}_{yy}^{-1}$ must be by definition a positive definite matrix. Hence, $\boldsymbol{\Sigma}_{yy}^{-1}$ can be regarded as a metric, such that the dot product between \mathbf{u} and \mathbf{v} is $\mathbf{u}^\top \boldsymbol{\Sigma}_{yy}^{-1} \mathbf{v}$.

³Recall that the probability density function of a multivariate (k components) normally distributed random variable, \mathbf{x} , is $f(\mathbf{x}) = \frac{1}{\sqrt{(2\pi)^k |\boldsymbol{\Sigma}|}} \exp(-\frac{1}{2}(\mathbf{x} - \boldsymbol{\mu})^\top \boldsymbol{\Sigma}^{-1}(\mathbf{x} - \boldsymbol{\mu}))$, with $\boldsymbol{\mu} = E[\mathbf{x}]$ and $\boldsymbol{\Sigma} = D[\mathbf{x}]$.

with

$$\mathbf{N} = \mathbf{A}^\top \boldsymbol{\Sigma}_{yy}^{-1} \mathbf{A} \quad \text{and} \quad \mathbf{b} = \mathbf{A}^\top \boldsymbol{\Sigma}_{yy}^{-1} \mathbf{y} \quad (2.5)$$

It has to be pointed out that observation-specific weighting is readily made by directly modifying the components of the matrix $\boldsymbol{\Sigma}_{yy}^{-1}$.

Equations (2.4) are known as normal equations (NEQ) due to their geometrical interpretation: The estimated observations, $\hat{\mathbf{y}} = \mathbf{A}\hat{\mathbf{x}}$, and the estimated residuals, $\hat{\mathbf{e}} = \mathbf{y} - \mathbf{A}\hat{\mathbf{x}}$, are orthogonal w.r.t. the $\boldsymbol{\Sigma}_{yy}^{-1}$ metric, i.e., $\hat{\mathbf{e}}^\top \boldsymbol{\Sigma}_{yy}^{-1} \hat{\mathbf{y}} = \mathbf{0}$. It is also worth noting that (2.4) yields the same $\hat{\mathbf{x}}$ for whatever σ in (2.3). Therefore, it is preferred to use an a priori RMS of unit weight, σ_0 , when setting-up the NEQ and estimating its a posteriori value, $\hat{\sigma}$, after solving for $\hat{\mathbf{x}}$, which can be used in place of σ_0 when evaluating the formal errors of the parameters, i.e.,

$$\frac{\hat{\sigma}^2}{\sigma_0^2} = \frac{\hat{\mathbf{e}}^\top \boldsymbol{\Sigma}_{yy}^{-1} \hat{\mathbf{e}}}{n - m} = \frac{\mathbf{y}^\top \boldsymbol{\Sigma}_{yy}^{-1} \mathbf{y} - \hat{\mathbf{x}}^\top \mathbf{b}}{n - m} \quad (2.6)$$

$$\boldsymbol{\Sigma}_{\hat{\mathbf{x}}\hat{\mathbf{x}}} = \frac{\hat{\sigma}^2}{\sigma_0^2} \mathbf{N}^{-1} \quad (2.7)$$

The first equation follows from the best invariant quadratic unbiased principle used to estimate variance components (Koch, 1999, section 3.6.4), the second one from the propagation of $\boldsymbol{\Sigma}_{yy}$ ⁴. In case of considering additional unknown variance components in $\boldsymbol{\Sigma}_{yy}$, their estimator and the estimator of the parameters are no longer uncoupled and the solution has to be iteratively computed (Koch, 1999, section 3.6).

2.3 The fundamental differencing theorem

Differencing GNSS observations is useful to eliminate some parameters (e.g., satellite and receiver clock corrections) before solving the NEQ. Although this has actually been the approach followed by CODE for many years (Dach et al., 2015), the processing schemes designed in the frame of this work are based on undifferenced GNSS observations. Nonetheless, either approach leads to the same estimates, as stated by a weak version of the fundamental differencing theorem (Wells et al., 2023): “Linear biases can be accounted for either by reducing the number of observations so that the biases cancel, or by adding an equal number of unknowns to model the biases. Both approaches give identical results, under certain circumstances”. A formal proof of this theorem can be found in Schaffrin, 1986. Because of its relevance in the present work, it is the purpose of this section to use somewhat stronger assumptions (still valid for our processing) to demonstrate that theorem using an easier, yet convincing, discussion.

Let us rewrite the model (2.3) as

$$\mathbf{E}[\mathbf{y}] = \mathbf{A}\mathbf{a} + \mathbf{B}\mathbf{b}, \quad \mathbf{D}[\mathbf{y}] = \boldsymbol{\Sigma}_{yy} \quad (2.8)$$

where \mathbf{b} contains the m_b parameters that are to be eliminated by differentiation, and \mathbf{B} is a full column rank matrix (this condition is feasible since collinear parameters can always be lumped together). Let us note that for any n -dimensional column array \mathbf{v} , there exists an orthogonal decomposition w.r.t. the metric $\boldsymbol{\Sigma}_{yy}^{-1}$, such that $\mathbf{v} = \sum_i v_i \mathbf{e}_i$ and $\mathbf{e}_i^\top \boldsymbol{\Sigma}_{yy}^{-1} \mathbf{e}_j = \delta_{ij}$, being δ_{ij} the Kronecker delta. Without loss of generality, we can

⁴Recall that the covariance matrices of two multivariate random variables, x_1 and x_2 , related by $x_2 = \mathbf{M}x_1$, satisfy $\boldsymbol{\Sigma}_{x_2x_2} = \mathbf{M}\boldsymbol{\Sigma}_{x_1x_1}\mathbf{M}^\top$.

further assume that the e_i vectors, for $1 \leq i \leq m_b$, span $\mathbf{R}(\mathbf{B})$. The remaining $n - m_b$ vectors consequently span the orthogonal complement of $\mathbf{R}(\mathbf{B})$, i.e., $\mathbf{R}(\mathbf{B})^\perp$. Since $v_i = e_i^\top \Sigma_{yy}^{-1} v$, the orthogonal projection operators on $\mathbf{R}(\mathbf{B})$, i.e., \mathbf{P}_B , and $\mathbf{R}(\mathbf{B})^\perp$, i.e., \mathbf{P}_{B^\perp} , can be written as

$$\mathbf{P}_B = \mathbf{E}_B \mathbf{E}_B^\top \Sigma_{yy}^{-1} \quad (2.9)$$

$$\mathbf{P}_{B^\perp} = \mathbf{E}_{B^\perp} \mathbf{E}_{B^\perp}^\top \Sigma_{yy}^{-1} \quad (2.10)$$

with \mathbf{E}_B the $n \times m_b$ matrix whose columns contain the first m_b e_i vectors. \mathbf{E}_{B^\perp} , on the other hand, is a $n \times (n - m_b)$ matrix containing the remaining vectors.

Let us apply the LS principle to (2.8), i.e., we shall find a and b so that the following quantity is minimized

$$\begin{aligned} & (\mathbf{y} - \mathbf{A}a - \mathbf{B}b)^\top \Sigma_{yy}^{-1} (\mathbf{y} - \mathbf{A}a - \mathbf{B}b) = \\ & (\mathbf{P}_B \mathbf{y} - \mathbf{P}_B \mathbf{A}a - \mathbf{B}b + \mathbf{P}_{B^\perp} \mathbf{y} - \mathbf{P}_{B^\perp} \mathbf{A}a)^\top \Sigma_{yy}^{-1} (\mathbf{P}_B \mathbf{y} - \mathbf{P}_B \mathbf{A}a - \mathbf{B}b + \mathbf{P}_{B^\perp} \mathbf{y} - \mathbf{P}_{B^\perp} \mathbf{A}a) = \\ & (\mathbf{P}_B \mathbf{y} - \mathbf{P}_B \mathbf{A}a - \mathbf{B}b)^\top \Sigma_{yy}^{-1} (\mathbf{P}_B \mathbf{y} - \mathbf{P}_B \mathbf{A}a - \mathbf{B}b) + \\ & (\mathbf{P}_{B^\perp} \mathbf{y} - \mathbf{P}_{B^\perp} \mathbf{A}a)^\top \Sigma_{yy}^{-1} (\mathbf{P}_{B^\perp} \mathbf{y} - \mathbf{P}_{B^\perp} \mathbf{A}a) \quad (2.11) \end{aligned}$$

The first equality follows from the decomposition $v = \mathbf{P}_B v + \mathbf{P}_{B^\perp} v$ ⁵. On the other hand, the second equality holds because $\mathbf{P}_B^\top \Sigma_{yy}^{-1} \mathbf{P}_{B^\perp} = \mathbf{0}$ and $\mathbf{B}^\top \Sigma_{yy}^{-1} \mathbf{P}_{B^\perp} = \mathbf{0}$. Since Σ_{yy}^{-1} is a positive definite matrix, both terms in this second equality can be independently minimized. It is interesting to note that the first one can be steered to zero because there exists a \tilde{b} so that $\mathbf{B}\tilde{b} = \mathbf{P}_B \mathbf{y} - \mathbf{P}_B \mathbf{A}\tilde{a}$ for any \tilde{a} , implying that only the second term contributes to the numerator of (2.6). Using (2.10) and $\mathbf{E}_{B^\perp}^\top \Sigma_{yy}^{-1} \mathbf{E}_{B^\perp} = \mathbf{I}$, this second term can be written as

$$\left(\mathbf{E}_{B^\perp}^\top \Sigma_{yy}^{-1} \mathbf{y} - \mathbf{E}_{B^\perp}^\top \Sigma_{yy}^{-1} \mathbf{A}a \right)^\top \left(\mathbf{E}_{B^\perp}^\top \Sigma_{yy}^{-1} \mathbf{y} - \mathbf{E}_{B^\perp}^\top \Sigma_{yy}^{-1} \mathbf{A}a \right) \quad (2.12)$$

Let us now apply a differencing operator, \mathbf{D} , to (2.8) so that \mathbf{B} vanishes, while the remaining terms are redefined as: $\mathbf{y}^* = \mathbf{D}\mathbf{y}$, $\mathbf{A}^* = \mathbf{D}\mathbf{A}$ and $\Sigma_{y^*y^*} = \mathbf{D}\Sigma_{yy}\mathbf{D}^\top$. The most general form for this operator is $\mathbf{D} = \mathbf{M}\mathbf{E}_{B^\perp}^\top \Sigma_{yy}^{-1}$, hence $\Sigma_{y^*y^*} = \mathbf{M}\mathbf{M}^\top$. If we impose that \mathbf{M} is a $(n - m_b) \times (n - m_b)$ regular matrix, the number of reduced observations in \mathbf{y} equals the amount of eliminated b parameters, and $\Sigma_{y^*y^*}^{-1} = \mathbf{M}^{-\top} \mathbf{M}^{-1}$. For the new differenced model, the LS principle requires the following quantity to be minimized

$$\begin{aligned} & (\mathbf{y}^* - \mathbf{A}^*a)^\top \mathbf{M}^{-\top} \mathbf{M}^{-1} (\mathbf{y}^* - \mathbf{A}^*a) = \\ & \left(\mathbf{E}_{B^\perp}^\top \Sigma_{yy}^{-1} \mathbf{y} - \mathbf{E}_{B^\perp}^\top \Sigma_{yy}^{-1} \mathbf{A}a \right)^\top \left(\mathbf{E}_{B^\perp}^\top \Sigma_{yy}^{-1} \mathbf{y} - \mathbf{E}_{B^\perp}^\top \Sigma_{yy}^{-1} \mathbf{A}a \right) \quad (2.13) \end{aligned}$$

which is the same as (2.12), leading to the same estimate for a . Additionally, since the number of reduced observations is the same as the number of eliminated parameters, the denominator in (2.6) does not vary, leading also to the same estimate for σ . All in all, we have established the validity of the fundamental differencing theorem.

⁵More generally, $\mathbf{I} = \mathbf{P}_B + \mathbf{P}_{B^\perp}$, and, therefore, $\mathbf{P}_{B^\perp} = \mathbf{I} - \mathbf{P}_B$.

2.4 A posteriori parameter constraining

Additional interesting results can be derived from further developing the LS principle. In particular, this section is devoted to show how the best estimate $\hat{\mathbf{b}}$ becomes $\check{\mathbf{b}}$ when a non-optimal $\check{\mathbf{a}}$ replaces $\hat{\mathbf{a}}$ in (2.11). The penalty that the non-optimal $\check{\mathbf{a}}$ produces in the LS objective function will be discussed, too. These results are of special interest in the realm of AR, and the reader may find an alternative derivation in Teunissen and Kleusberg, 2012, section 8.2.2. Another approach is possible using probability theory, where the conditional probability distributions (Koch, 1999, section 2.5.3) yield closely related results.

In accord with the previous section, $\mathbf{R}(\mathbf{B}) = \mathbf{R}(\mathbf{E}_B)$, and, hence, $\mathbf{B} = \mathbf{E}_B \mathbf{C}$, with \mathbf{C} a $m_b \times m_b$ regular matrix. Consequently, $\mathbf{E}_B = \mathbf{B} \mathbf{C}^{-1}$, $\mathbf{B}^\top \Sigma_{yy}^{-1} \mathbf{B} = \mathbf{C}^\top \mathbf{C}$ and the orthogonal projection operators (2.9, 2.10) can be written in the better known forms

$$\mathbf{P}_B = \mathbf{B} \left(\mathbf{B}^\top \Sigma_{yy}^{-1} \mathbf{B} \right)^{-1} \mathbf{B}^\top \Sigma_{yy}^{-1} \quad (2.14)$$

$$\mathbf{P}_{B^\perp} = \mathbf{I} - \mathbf{B} \left(\mathbf{B}^\top \Sigma_{yy}^{-1} \mathbf{B} \right)^{-1} \mathbf{B}^\top \Sigma_{yy}^{-1} \quad (2.15)$$

Making use of (2.14) when steering to zero the first term in the last equality of (2.11) for the non-optimal and optimal solutions and computing the difference, we get:

$$\check{\mathbf{b}} = \hat{\mathbf{b}} - \left(\mathbf{B}^\top \Sigma_{yy}^{-1} \mathbf{B} \right)^{-1} \mathbf{B}^\top \Sigma_{yy}^{-1} \mathbf{A} (\check{\mathbf{a}} - \hat{\mathbf{a}}) \quad (2.16)$$

On the other hand, developing now the last term of (2.11) yields

$$\mathbf{y}^\top \Sigma_{yy}^{-1} \mathbf{P}_{B^\perp} \mathbf{y} + \mathbf{a}^\top \mathbf{A}^\top \Sigma_{yy}^{-1} \mathbf{P}_{B^\perp} \mathbf{A} \mathbf{a} - 2 \hat{\mathbf{a}}^\top \mathbf{A}^\top \Sigma_{yy}^{-1} \mathbf{P}_{B^\perp} \mathbf{A} \mathbf{a} \quad (2.17)$$

where we have used $\mathbf{P}_{B^\perp}^\top \Sigma_{yy}^{-1} \mathbf{P}_{B^\perp} = \Sigma_{yy}^{-1} \mathbf{P}_{B^\perp}$, and, from the application of the LS principle, $\left(\mathbf{A}^\top \Sigma_{yy}^{-1} \mathbf{P}_{B^\perp} \mathbf{A} \right) \hat{\mathbf{a}} = \mathbf{A}^\top \Sigma_{yy}^{-1} \mathbf{P}_{B^\perp} \mathbf{y}$. Using (2.15), evaluating in $\check{\mathbf{a}}$ and $\hat{\mathbf{a}}$, and computing the difference, we get:

$$(\check{\mathbf{a}} - \hat{\mathbf{a}})^\top \mathbf{A}^\top \left[\Sigma_{yy}^{-1} - \Sigma_{yy}^{-1} \mathbf{B} \left(\mathbf{B}^\top \Sigma_{yy}^{-1} \mathbf{B} \right)^{-1} \mathbf{B}^\top \Sigma_{yy}^{-1} \right] \mathbf{A} (\check{\mathbf{a}} - \hat{\mathbf{a}}) \quad (2.18)$$

From (2.7), assuming that \mathbf{N} is constructed with $\sigma_0 = \hat{\sigma}$,

$$\begin{pmatrix} \mathbf{A}^\top \Sigma_{yy}^{-1} \mathbf{A} & \mathbf{A}^\top \Sigma_{yy}^{-1} \mathbf{B} \\ \mathbf{B}^\top \Sigma_{yy}^{-1} \mathbf{A} & \mathbf{B}^\top \Sigma_{yy}^{-1} \mathbf{B} \end{pmatrix} \begin{pmatrix} \Sigma_{\hat{\mathbf{a}}\hat{\mathbf{a}}} & \Sigma_{\hat{\mathbf{a}}\hat{\mathbf{b}}} \\ \Sigma_{\hat{\mathbf{b}}\hat{\mathbf{a}}} & \Sigma_{\hat{\mathbf{b}}\hat{\mathbf{b}}} \end{pmatrix} = \begin{pmatrix} \mathbf{I} & \mathbf{0} \\ \mathbf{0} & \mathbf{I} \end{pmatrix} \quad (2.19)$$

which, after algebraic manipulation (Koch, 1999, section 1.3.4), leads to

$$\Sigma_{\hat{\mathbf{a}}\hat{\mathbf{a}}} = \left(\mathbf{A}^\top \Sigma_{yy}^{-1} \mathbf{A} \right)^{-1} + \Sigma_{\hat{\mathbf{a}}\hat{\mathbf{b}}} \Sigma_{\hat{\mathbf{b}}\hat{\mathbf{b}}}^{-1} \Sigma_{\hat{\mathbf{b}}\hat{\mathbf{a}}} \quad (2.20)$$

$$\Sigma_{\hat{\mathbf{b}}\hat{\mathbf{a}}} \Sigma_{\hat{\mathbf{a}}\hat{\mathbf{a}}}^{-1} = - \left(\mathbf{B}^\top \Sigma_{yy}^{-1} \mathbf{B} \right)^{-1} \mathbf{B}^\top \Sigma_{yy}^{-1} \mathbf{A} \quad (2.21)$$

$$\Sigma_{\hat{\mathbf{a}}\hat{\mathbf{a}}}^{-1} = \mathbf{A}^\top \left[\Sigma_{yy}^{-1} - \Sigma_{yy}^{-1} \mathbf{B} \left(\mathbf{B}^\top \Sigma_{yy}^{-1} \mathbf{B} \right)^{-1} \mathbf{B}^\top \Sigma_{yy}^{-1} \right] \mathbf{A} \quad (2.22)$$

With these expressions, we can write (2.16, 2.18) in the more compact forms

$$\check{\mathbf{b}} = \hat{\mathbf{b}} + \Sigma_{\hat{\mathbf{b}}\hat{\mathbf{a}}} \Sigma_{\hat{\mathbf{a}}\hat{\mathbf{a}}}^{-1} (\check{\mathbf{a}} - \hat{\mathbf{a}}) \quad (2.23)$$

and

$$(\check{\mathbf{a}} - \hat{\mathbf{a}})^\top \boldsymbol{\Sigma}_{\hat{\mathbf{a}}\hat{\mathbf{a}}}^{-1} (\check{\mathbf{a}} - \hat{\mathbf{a}}) \quad (2.24)$$

respectively. The term (2.24) quantifies the penalty that the LS objective function experiences when we constrain the \mathbf{a} parameters to non-optimal values. Its astonishing resemblance with the LS principle makes it especially useful to divide the optimization problem in several steps. For instance, we can estimate kinematic coordinates for a satellite (in our notation, $\hat{\mathbf{a}}$) and use them later together with their covariance information ($\boldsymbol{\Sigma}_{\hat{\mathbf{a}}\hat{\mathbf{a}}}$) to eventually estimate an orbit constrained by the laws of orbital mechanics (i.e., $\check{\mathbf{a}}$ is represented by some dynamical parameterization) minimizing the penalty (2.24) as done by Jäggi et al., 2011. The algorithms for AR, on the other hand, should keep (2.24) present, too (section 4.2). Equation (2.23) very compactly establishes how the remaining parameters of the model vary due to that constraining.

2.5 Manipulation of normal equations

2.5.1 Stacking of normal equations

If the Gauss-Markoff model can be written as

$$\mathbb{E} \left[\begin{pmatrix} \mathbf{y}_1 \\ \vdots \\ \mathbf{y}_l \end{pmatrix} \right] = \begin{pmatrix} \mathbf{A}_1 \\ \vdots \\ \mathbf{A}_l \end{pmatrix} \mathbf{x}, \quad \mathbb{D} \left[\begin{pmatrix} \mathbf{y}_1 \\ \vdots \\ \mathbf{y}_l \end{pmatrix} \right] = \begin{pmatrix} \boldsymbol{\Sigma}_1 & & \mathbf{0} \\ & \ddots & \\ \mathbf{0} & & \boldsymbol{\Sigma}_l \end{pmatrix} \quad (2.25)$$

where each \mathbf{y}_i contains n_i observations, then the NEQ become

$$\left(\sum_{i=1}^l \mathbf{N}_i \right) \hat{\mathbf{x}} = \sum_{i=1}^l \mathbf{b}_i \quad (2.26)$$

with

$$\mathbf{N}_i = \mathbf{A}_i^\top \boldsymbol{\Sigma}_i^{-1} \mathbf{A}_i \quad \text{and} \quad \mathbf{b}_i = \mathbf{A}_i^\top \boldsymbol{\Sigma}_i^{-1} \mathbf{y}_i \quad (2.27)$$

as well as

$$\frac{\hat{\sigma}^2}{\sigma_0^2} = \frac{\sum_{i=1}^l \mathbf{y}_i^\top \boldsymbol{\Sigma}_i^{-1} \mathbf{y}_i - \hat{\mathbf{x}}^\top \sum_{i=1}^l \mathbf{b}_i}{\sum_{i=1}^l n_i - m} \quad (2.28)$$

When the observations are collected in independent batches (e.g., from independent ground stations), the NEQ are more efficiently constructed through (2.26), which is popularly known as stacking of NEQ. Note that if the batch j is not sensitive to some specific set of parameters, the corresponding columns of \mathbf{A}_j are populated by zeros, and, consequently, the associated sub-matrices of \mathbf{N}_j contain zeros, too (it is said that \mathbf{N}_j is expanded to comprise all the parameters).

Constraints over the parameters are often expressed as linear equations, which can be interpreted as another set of independent observations with very tight variances. By using (2.26), those constraints can be applied at any point during the processing.

2.5.2 Linear transformations of parameters

It can be readily shown that a linear transformation of the form $\mathbf{x} = \mathbf{C}\mathbf{x}^* + \mathbf{c}$, relating the new, \mathbf{x}^* , and old, \mathbf{x} , parameterizations, leads to the equations

$$\mathbf{N}^* \hat{\mathbf{x}}^* = \mathbf{b}^* \quad (2.29)$$

$$\frac{\hat{\sigma}^{*2}}{\sigma_0^2} = \frac{\left(\mathbf{y}^\top \boldsymbol{\Sigma}_{yy}^{-1} \mathbf{y}\right)^* - \hat{\mathbf{x}}^{*\top} \mathbf{b}^*}{n - m^*} \quad (2.30)$$

where the new $(\cdot)^*$ terms can be written in terms of the old ones as:

$$\mathbf{N}^* = \mathbf{C}^\top \mathbf{N} \mathbf{C} \quad (2.31)$$

$$\mathbf{b}^* = \mathbf{C}^\top (\mathbf{b} - \mathbf{N} \mathbf{c}) \quad (2.32)$$

$$\left(\mathbf{y}^\top \boldsymbol{\Sigma}_{yy}^{-1} \mathbf{y}\right)^* = \mathbf{y}^\top \boldsymbol{\Sigma}_{yy}^{-1} \mathbf{y} + \mathbf{c}^\top \mathbf{N} \mathbf{c} - 2\mathbf{c}^\top \mathbf{b} \quad (2.33)$$

$$m^* = m - \text{number of reduced parameters} \quad (2.34)$$

A useful application of these transformations arises when the a priori information of the parameters is to be modified, for which $\mathbf{C} = \mathbf{I}$ and $\mathbf{c} = \mathbf{x}_0^* - \mathbf{x}_0$.

2.5.3 Pre-eliminating parameters

The NEQ can be block-wise divided as

$$\begin{pmatrix} \mathbf{N}_{11} & \mathbf{N}_{12} \\ \mathbf{N}_{21} & \mathbf{N}_{22} \end{pmatrix} \begin{pmatrix} \hat{\mathbf{x}}_1 \\ \hat{\mathbf{x}}_2 \end{pmatrix} = \begin{pmatrix} \mathbf{b}_1 \\ \mathbf{b}_2 \end{pmatrix} \quad (2.35)$$

Using algebraic operations, we can pre-eliminate $\hat{\mathbf{x}}_2$, so that the equations for the estimates $\hat{\mathbf{x}}_1$ and $\hat{\sigma}$ become

$$\mathbf{N}_{11}^* \hat{\mathbf{x}}_1 = \mathbf{b}_1^* \quad (2.36)$$

$$\frac{\hat{\sigma}^2}{\sigma_0^2} = \frac{\left(\mathbf{y}^\top \boldsymbol{\Sigma}_{yy}^{-1} \mathbf{y}\right)^* - \hat{\mathbf{x}}_1^\top \mathbf{b}_1^*}{n - m} \quad (2.37)$$

where

$$\mathbf{N}_{11}^* = \mathbf{N}_{11} - \mathbf{N}_{12} \mathbf{N}_{22}^{-1} \mathbf{N}_{21} \quad (2.38)$$

$$\mathbf{b}_1^* = \mathbf{b}_1 - \mathbf{N}_{12} \mathbf{N}_{22}^{-1} \mathbf{b}_2 \quad (2.39)$$

$$\left(\mathbf{y}^\top \boldsymbol{\Sigma}_{yy}^{-1} \mathbf{y}\right)^* = \mathbf{y}^\top \boldsymbol{\Sigma}_{yy}^{-1} \mathbf{y} - \mathbf{b}_2^\top \mathbf{N}_{22}^{-1} \mathbf{b}_2 \quad (2.40)$$

Note that, for the original model

$$\mathbf{E}[\mathbf{y}] = \mathbf{A}_1 \mathbf{x}_1 + \mathbf{A}_2 \mathbf{x}_2, \quad \mathbf{D}[\mathbf{y}] = \boldsymbol{\Sigma}_{yy} \quad (2.41)$$

with $\mathbf{N}_{11} = \mathbf{A}_1^\top \boldsymbol{\Sigma}_{yy}^{-1} \mathbf{A}_1$, $\mathbf{N}_{21}^\top = \mathbf{N}_{12} = \mathbf{A}_1^\top \boldsymbol{\Sigma}_{yy}^{-1} \mathbf{A}_2$ and $\mathbf{N}_{22} = \mathbf{A}_2^\top \boldsymbol{\Sigma}_{yy}^{-1} \mathbf{A}_2$, \mathbf{N}_{11}^* equals $\boldsymbol{\Sigma}_{\hat{\mathbf{x}}_1 \hat{\mathbf{x}}_1}^{-1}$ in analogy to (2.22). On the other hand, when back-substituting the previously pre-eliminated \mathbf{x}_2 parameters, we reduce $\mathbf{A}_1 \hat{\mathbf{x}}_1$ from the O-C term, resulting in

$$\left(\mathbf{A}_2^\top \boldsymbol{\Sigma}_{yy}^{-1} \mathbf{A}_2\right) \hat{\mathbf{x}}_2 = \mathbf{A}_2^\top \boldsymbol{\Sigma}_{yy}^{-1} (\mathbf{y} - \mathbf{A}_1 \hat{\mathbf{x}}_1) \quad (2.42)$$

In view of this equation, we could be tempted to state $\boldsymbol{\Sigma}_{\hat{\mathbf{x}}_2 \hat{\mathbf{x}}_2} = \left(\mathbf{A}_2^\top \boldsymbol{\Sigma}_{yy}^{-1} \mathbf{A}_2\right)^{-1}$. However, this is a mistake according to (2.20). Unfortunately, since the blocks $\boldsymbol{\Sigma}_{\hat{\mathbf{x}}_1 \hat{\mathbf{x}}_1}$ and $\boldsymbol{\Sigma}_{\hat{\mathbf{x}}_1 \hat{\mathbf{x}}_2}$ are not typically stored during the GNSS network processing to optimize the computational resources, the covariance information associated to back-substituted parameters is typically too optimistic. Particularly, this fact has conditioned the AR strategy implemented in [chapter 4](#).

2.6 Computation of long-arc solutions

Despite the fact that the GNSS observations are typically processed in daily batches, it is common to accumulate data from several consecutive sessions⁶ to generate the final geodetic solution (section 3.4). This solution benefits from continuous orbital arcs, and so it is known as long-arc solution. Mathematically, we require the same orbit parameterization in consecutive daily NEQ before stacking them, as done in section 2.5.1, which, in turn, requires the parameters of session $i + 1$ to be converted to session i through linear transformations, following the equations provided in section 2.5.2. The discussion given in the sequel is a simplified version of the more general procedure offered by Beutler et al., 1996, and so we will focus only on the subtlest parts of the development.

Let us write the NEQ of sessions i and $i + 1$ as

$$\mathbf{N}^i \mathbf{z}^i = \mathbf{b}^i \quad (2.43)$$

$$\mathbf{N}^{i+1} \mathbf{z}^{i+1} = \mathbf{b}^{i+1} \quad (2.44)$$

where \mathbf{z} is used here to denote the unknown parameters, which, for the sake of simplicity, only include the orbit parameterization, i.e., variations w.r.t. the initial state vector, $\delta \mathbf{x}_0$, variations w.r.t. physical (e.g., gravity field coefficients as for chapter 6) and empirical quantities describing the orbit modeling, $\delta \mathbf{q}$, and variations w.r.t. empirical pulses, $\delta \mathbf{p}$ (it is worth advancing from section 3.3.2 that these pulses represent instantaneous velocity changes):

$$\mathbf{z}^i = (\delta \mathbf{x}_0^{i\top} \quad \delta \mathbf{q}^\top \quad \delta \mathbf{p}^{i\top})^\top \quad (2.45)$$

$$\mathbf{z}^{i+1} = (\delta \mathbf{x}_0^{i+1\top} \quad \delta \mathbf{q}^\top \quad \delta \mathbf{p}^{i+1\top})^\top \quad (2.46)$$

The superscripts i and $i + 1$ appoint to specific quantities of the corresponding session. Here we have assumed that the parameters $\delta \mathbf{q}$ are the same for both sessions, implying that they also represent corrections about the same a priori information. Note that pulses of sessions i and $i + 1$ are applied only on days i and $i + 1$, respectively.

We see that both NEQ (2.43, 2.44) have to be expanded to account for all the pulses. In case of session i , this expansion only requires to populate the corresponding normal equation block with zeros, since the orbits are forward propagated and $\delta \mathbf{p}^{i+1}$ does not alter the satellite coordinates of session i . This no longer holds for session $i + 1$, where $\delta \mathbf{p}^i$ does modify the satellite coordinates of session $i + 1$. We thus have to find an equivalence relation between the orbit parameters defining the family of trajectories of session $i + 1$ if $\delta \mathbf{p}^i$ is, or not, considered. The linearized version of such a family of trajectories follows from (1.72, 1.77, 1.78) as⁷

$$\begin{aligned} \mathbf{x}^{i+1}(t) + \Phi^{i+1}(t, t_i) \delta \mathbf{x}_0^{i+1}(t_i) + \left[\int_{t_i}^t \Phi^{i+1}(t, \tau) \frac{\partial \mathbf{f}^{i+1}}{\partial \mathbf{q}} \Big|_{t=\tau} d\tau \right] \delta \mathbf{q} + \\ \left[\int_{t_i}^t \Phi^{i+1}(t, \tau) \frac{\partial \mathbf{f}^{i+1}}{\partial \mathbf{p}^i} \Big|_{t=\tau} d\tau \right] \delta \mathbf{p}^i + \left[\int_{t_i}^t \Phi^{i+1}(t, \tau) \frac{\partial \mathbf{f}^{i+1}}{\partial \mathbf{p}^{i+1}} \Big|_{t=\tau} d\tau \right] \delta \mathbf{p}^{i+1} \end{aligned} \quad (2.47)$$

⁶The session i contains observations from day i . However, the orbit solution can be backward and forward propagated, beyond the day i limits.

⁷The superscripts i and $i + 1$ over \mathbf{x} , Φ and \mathbf{f} indicate which trajectory has been used for the linearization, either the one from session i or the one from session $i + 1$. Additionally, the summation symbols have been exchanged by matrix multiplication to alleviate the notation.

or, equivalently,

$$\begin{aligned} \mathbf{x}^{i+1}(t) + \mathbf{\Phi}^{i+1}(t, t_{i+1})\delta\mathbf{x}_0^{i+1}(t_{i+1}) + \left[\int_{t_{i+1}}^t \mathbf{\Phi}^{i+1}(t, \tau) \frac{\partial \mathbf{f}^{i+1}}{\partial \mathbf{q}} \Big|_{t=\tau} d\tau \right] \delta\mathbf{q} + \\ \left[\int_{t_{i+1}}^t \mathbf{\Phi}^{i+1}(t, \tau) \frac{\partial \mathbf{f}^{i+1}}{\partial \mathbf{p}^{i+1}} \Big|_{t=\tau} d\tau \right] \delta\mathbf{p}^{i+1} \end{aligned} \quad (2.48)$$

depending on the epoch at which we start the orbit propagation: For (2.47), it starts at $t = t_i$, i.e., initial epoch of day i , and at $t = t_{i+1}$, i.e., initial epoch of day $i + 1$, for (2.48), being this latter the parameterization used to build the NEQ of session $i + 1$. Consequently, the initial state vector parameters represent orbit variations at different epochs, explicitly indicated in these equations by $\delta\mathbf{x}_0^{i+1}(t_i)$ and $\delta\mathbf{x}_0^{i+1}(t_{i+1})$. Likewise, and in accord with (1.71) and (3.17),

$$\frac{\partial \mathbf{f}^{(\cdot)}}{\partial p_k} = \delta(t - \tilde{t}_k) \mathbf{d}_k^{(\cdot)} = \delta(t - \tilde{t}_k) \begin{pmatrix} \mathbf{0} \\ \mathbf{e}_k^{(\cdot)} \end{pmatrix} \quad (2.49)$$

being $\delta(t - \tilde{t}_k)$ the Dirac delta function, and $\mathbf{e}_k^{(\cdot)}$ and \tilde{t}_k the direction and application time of the k th pulse, respectively (the index k here refers to any pulse disregarding if it belongs to session i or session $i + 1$).

We can force (2.47) and (2.48) to be equal for $t \geq t_{i+1}$, which leads, with the help of (1.80), to

$$\begin{aligned} \mathbf{\Phi}^{i+1}(t, t_i)\delta\mathbf{x}_0^{i+1}(t_i) = \mathbf{\Phi}^{i+1}(t, t_{i+1}) \left[\delta\mathbf{x}_0^{i+1}(t_{i+1}) - \mathbf{P}^{i+1}(t_{i+1})\delta\mathbf{p}^i \right] + \\ - \left[\int_{t_i}^{t_{i+1}} \mathbf{\Phi}^{i+1}(t, \tau) \frac{\partial \mathbf{f}^{i+1}}{\partial \mathbf{q}} \Big|_{t=\tau} d\tau \right] \delta\mathbf{q} \end{aligned} \quad (2.50)$$

where

$$\mathbf{P}^{(\cdot)}(t) = \left(\mathbf{\Phi}^{(\cdot)}(t, \tilde{t}_1) \mathbf{d}_1^{(\cdot)} \mid \mathbf{\Phi}^{(\cdot)}(t, \tilde{t}_2) \mathbf{d}_2^{(\cdot)} \mid \dots \mid \mathbf{\Phi}^{(\cdot)}(t, \tilde{t}_k) \mathbf{d}_k^{(\cdot)} \mid \dots \right) \quad (2.51)$$

for k sweeping the pulses of session i . Plugging (2.50) into (2.47) yields (for $t \geq t_{i+1}$)

$$\begin{aligned} \mathbf{x}^{i+1}(t) + \mathbf{\Phi}^{i+1}(t, t_{i+1})\delta\mathbf{x}_0^{*i+1}(t_{i+1}) + \left[\int_{t_{i+1}}^t \mathbf{\Phi}^{i+1}(t, \tau) \frac{\partial \mathbf{f}^{i+1}}{\partial \mathbf{q}} \Big|_{t=\tau} d\tau \right] \delta\mathbf{q} + \\ \mathbf{P}^{i+1}(t)\delta\mathbf{p}^i + \left[\int_{t_{i+1}}^t \mathbf{\Phi}^{i+1}(t, \tau) \frac{\partial \mathbf{f}^{i+1}}{\partial \mathbf{p}^{i+1}} \Big|_{t=\tau} d\tau \right] \delta\mathbf{p}^{i+1} \end{aligned} \quad (2.52)$$

with $\delta\mathbf{x}_0^{*i+1}(t_{i+1}) = \delta\mathbf{x}_0^{i+1}(t_{i+1}) - \mathbf{P}^{i+1}(t_{i+1})\delta\mathbf{p}^i$. Note that both (2.48) and (2.52) define, by construction, exactly the same family of trajectories for $t \geq t_{i+1}$, even if both equations are represented by different parameterizations. This holds true because of the existing collinearity between $\mathbf{\Phi}^{i+1}(t, t_{i+1})\delta\mathbf{x}_0^{*i+1}(t_{i+1})$ and $\mathbf{P}^{i+1}(t)\delta\mathbf{p}^{i8}$.

⁸Suppose that \mathbf{Aa} and \mathbf{Bb} are collinear, so that $\text{R}(\mathbf{B}) \subseteq \text{R}(\mathbf{A})$, and, therefore, $\mathbf{B} = \mathbf{AC}$. The model $\text{E}[\mathbf{y}] = \mathbf{Aa} + \mathbf{Bb}$ can thus be written as $\text{E}[\mathbf{y}] = \mathbf{A}(a + \mathbf{Cb}) = \mathbf{Ax}$. We can build the NEQ for x and then apply the linear transformation $x = a + \mathbf{Cb}$ to finally obtain the NEQ for a and b . It can be verified that the same NEQ can also be derived in one single step from the original $\text{E}[\mathbf{y}] = \mathbf{Aa} + \mathbf{Bb}$ model.

The consequence is that the linear transformation

$$\mathbf{z}^{i+1} = \begin{bmatrix} \delta \mathbf{x}_0^{i+1} \\ \delta \mathbf{q} \\ \delta \mathbf{p}^{i+1} \end{bmatrix} = \mathbf{Cz}^{*i+1} = \begin{pmatrix} \mathbf{I} & \mathbf{0} & \mathbf{P}^{i+1}(t_{i+1}) & \mathbf{0} \\ \mathbf{0} & \mathbf{I} & \mathbf{0} & \mathbf{0} \\ \mathbf{0} & \mathbf{0} & \mathbf{0} & \mathbf{I} \end{pmatrix} \begin{bmatrix} \delta \mathbf{x}_0^{*i+1} \\ \delta \mathbf{q} \\ \delta \mathbf{p}^i \\ \delta \mathbf{p}^{i+1} \end{bmatrix} \quad (2.53)$$

together with (2.31-2.34), expand the $i + 1$ NEQ as though they were initially constructed using (2.52) instead of (2.48).

Once the NEQ are expanded to account for all the pulses, we have to impose continuity between the trajectories of both sessions. In pursuit of this, we first construct the family of trajectories of session i as:

$$\begin{aligned} \mathbf{x}^i(t) + \mathbf{\Phi}^i(t, t_i) \delta \mathbf{x}_0^i(t_i) + \left[\int_{t_i}^t \mathbf{\Phi}^i(t, \tau) \frac{\partial \mathbf{f}^i}{\partial \mathbf{q}} \Big|_{t=\tau} d\tau \right] \delta \mathbf{q} + \\ \left[\int_{t_i}^t \mathbf{\Phi}^i(t, \tau) \frac{\partial \mathbf{f}^i}{\partial \mathbf{p}^i} \Big|_{t=\tau} d\tau \right] \delta \mathbf{p}^i + \left[\int_{t_i}^t \mathbf{\Phi}^i(t, \tau) \frac{\partial \mathbf{f}^i}{\partial \mathbf{p}^{i+1}} \Big|_{t=\tau} d\tau \right] \delta \mathbf{p}^{i+1} \end{aligned} \quad (2.54)$$

and evaluate it, as well as (2.52), at $t = t_{i+1}$. Dropping the $(\cdot)^*$ superscript, omitting the explicit temporal dependency of the initial state vector, i.e., $\delta \mathbf{x}_0^i = \delta \mathbf{x}_0^i(t_i)$ and $\delta \mathbf{x}_0^{i+1} = \delta \mathbf{x}_0^{*i+1}(t_{i+1})$, and equating both expressions, it is obtained

$$\begin{aligned} \delta \mathbf{x}_0^{i+1} = \mathbf{\Phi}^i(t_{i+1}, t_i) \delta \mathbf{x}_0^i + \mathbf{H}^i(t_{i+1}) \delta \mathbf{q} + \\ \left[\mathbf{P}^i(t_{i+1}) - \mathbf{P}^{i+1}(t_{i+1}) \right] \delta \mathbf{p}^i + \left[\mathbf{x}^i(t_{i+1}) - \mathbf{x}^{i+1}(t_{i+1}) \right] \end{aligned} \quad (2.55)$$

with

$$\mathbf{H}^{(\cdot)}(t) = \int_{t^{(\cdot)}}^t \mathbf{\Phi}^{(\cdot)}(t, \tau) \frac{\partial \mathbf{f}^{(\cdot)}}{\partial \mathbf{q}} \Big|_{t=\tau} d\tau \quad (2.56)$$

The term $\left[\mathbf{P}^i(t_{i+1}) - \mathbf{P}^{i+1}(t_{i+1}) \right] \delta \mathbf{p}^i = \delta \mathbf{P}(t_{i+1}) \delta \mathbf{p}^i$ is a second order term, being safely neglected provided that the trajectories used to linearize the variational equations from both sessions are “close” to each other. Eventually, we make the parameters of session $i + 1$ compatible with session i , using (2.31-2.34) and the linear transformation

$$\begin{aligned} \mathbf{z}^{i+1} = \begin{pmatrix} \delta \mathbf{x}_0^{i+1} \\ \delta \mathbf{q} \\ \delta \mathbf{p}^i \\ \delta \mathbf{p}^{i+1} \end{pmatrix} = \mathbf{Cz}^i + \mathbf{c} = \\ \begin{pmatrix} \mathbf{\Phi}^i(t_{i+1}, t_i) & \mathbf{H}^i(t_{i+1}) & \mathbf{0} & \mathbf{0} \\ \mathbf{0} & \mathbf{I} & \mathbf{0} & \mathbf{0} \\ \mathbf{0} & \mathbf{0} & \mathbf{I} & \mathbf{0} \\ \mathbf{0} & \mathbf{0} & \mathbf{0} & \mathbf{I} \end{pmatrix} \begin{pmatrix} \delta \mathbf{x}_0^i \\ \delta \mathbf{q} \\ \delta \mathbf{p}^i \\ \delta \mathbf{p}^{i+1} \end{pmatrix} + \begin{pmatrix} \mathbf{x}^i(t_{i+1}) - \mathbf{x}^{i+1}(t_{i+1}) \\ \mathbf{0} \\ \mathbf{0} \\ \mathbf{0} \end{pmatrix} \end{aligned} \quad (2.57)$$

allowing to later stack the NEQ according to section 2.5.1.

2.7 Summary

The GNSS observation model is linearized and parameterized by a number of unknown quantities, which represent geometrical contributions and physical phenomena. The computation of those quantities is the subject of estimation theory, whose

principles have been presented at the beginning of this chapter. In practice, the estimates are the solutions of a number of linear equations referred to as NEQ.

By developing the LS principle we found some conceptually profound results, which are of special interest in GNSS processing. In particular, it was shown that eliminating parameters by means of differentiation prior to building the NEQ leads to the same estimates as using the original observations, as long as the number of reduced observations equals the number of eliminated parameters. This equivalence principle is known as the fundamental differencing theorem. On the other hand, we found the expression representing the penalty that the objective function of the LS optimization problem experiences when some parameters are a posteriori constrained. The resemblance of such an expression and the LS principle makes it specially useful to divide the problem in several steps, which is the common approach to cope with the GNSS carrier phase AR problem.

The GNSS processing schemes implemented in the following chapter have to handle a huge amount of observations. An efficient processing thus requires clever manipulations of the NEQ. For instance, processing the observations within independent batches, which are later stacked, or pre-eliminating parameters so that the size of the NEQ is sequentially reduced. Those manipulations were introduced in this chapter. A useful application of those manipulations arises when accumulating observations from consecutive days, for which the particularities in the handling of orbit parameters deserve special attention in order to guarantee orbit continuity between days. The generation of these solutions (referred to as long-arc solutions) was also detailed in this chapter, stressing the most delicate parts.

Global network GNSS solutions using undifferenced observations

3.1 Introduction

The beginning of the GNSS era, as known today, dates back to the year 1978, with the launch of the first American Global Positioning System (GPS) satellite. Since the primary purpose of the GPS constellation was to strength the USA military capacities, the USSR developed its own navigation system shortly after: The *Global'naya Navigatsionnaya Sputnikovaya Sistema* (GLONASS), whose first satellite was launched in 1982. These technologies have been progressively incorporated into the people's lives, through both scientific and commercial applications, with great success and, therefore, other political communities have deployed their own navigation systems. Such is the case of the European Galileo and the Chinese BeiDou, which provide global coverage, and, for regional coverage, the Indian Regional Navigation Satellite System (IRNSS) and the Japanese Quasi-Zenith Satellite System (QZSS).

During the last decades, the scientific community has been exploiting the GNSS observations for geodetic applications, which has resulted in a variety of state-of-the-art software packages. To list a few: The Bernese GNSS Software (BSW, Dach et al., 2015), the Gravity Recovery Object Oriented Programming System (GROOPS, Mayer-Gürr et al., 2021), the Navigation Package for Earth Observation Satellites (NAPEOS, Springer et al., 2009), the GNSS-Inferred Positioning System (GIPSY, Bertiger et al., 2020), the GPS High Precision Orbit Determination Software Tools (GHOST, Wermuth et al., 2010), and GNSS Analysis at MIT (GAMIT, Herring et al., 2006), among others. We rely on the BSW for the many results computed in the frame of this dissertation. AIUB started the development of this software in the 1980s, being still maintained and operationally used by CODE in its IGS activities. Furthermore, there is a large number of BSW users spread around the world.

The GNSS network solutions derived from the BSW are commonly generated using differenced observations, i.e., differencing the measurements from two stations and two satellites (double-difference observations, or, simply, DD observations) in order to eliminate nuisance parameters, such as clock corrections. These eliminated parameters are, however, necessary for single-receiver users (e.g., for precise point positioning solutions, also known as PPP solutions) as well as for other specific applications (such as time transfer). To guarantee the integrity of the service, a second undifferenced (UD) processing (where the already estimated information is kept fixed) is thus necessary to recover those parameters. In the frame of this dissertation, we process UD observations to make all the parameters accessible at once. In pursuit of this goal, we have to design new processing schemes, as well as to implement new algorithms wherever the DD-based functionalities have to be adapted.

In theory (section 2.3), UD and DD processing schemes lead to equivalent results. However, UD strategies have some advantages lacking in their DD counterparts. To list a few:

- The UD processing schemes are more compact and offer more flexibility in the handling of the observations.
- More efficient use of the observations, since differential approaches require common tracking windows for the involved stations and satellites, which leads to the rejection of some measurements at the boundaries of the tracking interval.
- The UD strategies explicitly include all the parameters, which eases the application of new models and constraints over the otherwise eliminated parameters.
- Processing UD observations permits to easily integrate stand-alone receivers (e.g., equipped in LEO satellites) into the network processing.

Altogether, the use of UD processing schemes has become the most attractive option for GNSS analysts, justifying the effort dedicated in this dissertation to work with them in the BSW framework. It deserves a special mention, as a more general case, the raw observation approach (Strasser et al., 2019), which aims at processing undifferenced and uncombined observations¹.

Besides this introduction, this chapter consists of seven additional sections. In the following one we discuss some general aspects of the navigation systems employed in the frame of this dissertation (i.e., GPS, Galileo and GLONASS). Later (section 3.3), we dive into the GNSS observation model, where we discuss the observation model itself, the various background corrections and the parameterization. Next, the implemented processing schemes are described (section 3.4) and the derived results validated through several comparisons (section 3.5). Two additional sections analyze the impact of some important developments that have occurred in the frame of this work, namely, the transition from ITRF2014 to ITRF2020 (section 3.6), and the refinement of the Galileo orbit modeling according to the disclosed satellite metadata (section 3.7). For the sake of inquiry, we provide another observational evidence of the general relativistic effect that the Earth's oblateness has upon the Galileo clocks using SLR measurements in section 3.8. The chapter closes with the summary.

Some preliminary results included in this chapter were presented in Calero-Rodríguez et al., 2022.

3.2 General aspects of the navigation systems

The reader may find an exhaustive description of GPS, Galileo and GLONASS in Hegarty, 2017, Falcone et al., 2017 and Revnivkykh et al., 2017, respectively. A shorter description, followed in this section, is given in Sanz-Subirana et al., 2013, chapter 2.

Any navigation system consists of three segments, namely:

- The space segment, which is composed by the satellites. The main function of this segment is to transmit the signals and to store and broadcast the navigation message.

¹Note that we refer to “differenced observations” when the observations are differenced between several satellites (e.g., between-satellite observations), or stations (e.g., baseline observations) or both (e.g., double-differenced observations). The expression “combined observations” is used, on the other hand, to refer to the observations that result after applying linear combinations to the various GNSS signals.

- The ground segment, which operates the system. This segment monitors the status of the corresponding constellation, maintains the GNSS time scale and frame, and predicts ephemeris and clock corrections, which are later uplinked to the satellites.
- The user segment comprises the receivers, whose primary function is to process the received signals and to derive position and time estimates.

The various navigation systems are so designed to ensure a minimum of four satellites in view at any point within the Earth, although each constellation has its own characterization, summarized in Table 3.1. Note that the orbital eccentricities (not included in this table) are nominally close to zero and that the orbital regime, defined by the semi-major axis, is Medium Earth Orbit (MEO).

TABLE 3.1: Main aspects of the GNSS constellations

	GPS	Galileo	GLONASS
Number of nominal sat.	24	27	24
Number of planes	6	3	3
Semi-major axis	26560 km	29600 km	25510 km
Inclination	55°	56°	64.8°
Orbital period	11 h 58 min	14 h 5 min	11 h 16 min
Ground track period	1 d	10 d	8 d
Draconitic year	351.4 d	355.9 d	353.4 d

The continuous decommission and replenishment of satellites entails the modernization of the constellations with newer generations of spacecrafts. Although the satellites within the same generation are, to some extent, homogeneous, there are important inter-generation differences: Different satellite dimensions and optical properties, attitude modes, antennas and signals, among others. These generations are referred to as blocks for GPS, namely, BLOCK-I, BLOCK-II/IIA, BLOCK-IIR-A, BLOCK-IIR-B, BLOCK-IIR-M, BLOCK-IIF and BLOCK-IIIA. Regarding Galileo, only the first generation has been launched so far, which is divided in two phases: The In Orbit Validation (IOV) phase and the Full Operational Capability (FOC) phase. Incidentally, due to problems during launch, two FOC satellites were placed in eccentric orbits (eccentricity around 0.16), with non-nominal inclinations (50° instead of 56°). Since the Galileo satellites are equipped with high-performance passive hydrogen maser (PHM) clocks (Beard and Senior, 2017), this geometry allowed to carry out some general relativity tests (Kouba, 2021). The GLONASS generations are addressed as GLONASS, GLONASS-M, GLONASS-K1 and GLONASS-K2.

Fig. 3.1 shows the evolution of the number of GNSS satellites used for the solutions generated in the frame of this dissertation (July 2018 to June 2022). During this interval, the number of GPS satellites is very stable, whereas we see the incorporation of new Galileo satellites on late 2018 and on early 2022. The size of the GLONASS constellation is, however, progressively decreasing due to the decommission of malfunctioning satellites².

The GNSS signals consist of ranging codes (a sequence of bits known as pseudo-random noise sequences, or, simply, PRN sequences) and navigation data modulated on a carrier (radio) wave in the L-band (1164 MHz - 1610 MHz). The navigation data contains some ancillary information (satellite trajectories, or satellite health

²As of 2022, fifteen GLONASS satellites were working beyond their expected lifetime (<https://www.gpsworld.com/directions-2022-a-new-epoch-for-glonass/>).

status) needed to compute the navigation solution, whereas the fundamental GNSS observation (a rough station-to-satellite distance, or pseudorange observation) is derived from the ranging codes. Note that the stations also measure the phase of the carrier, which constitutes another fundamental GNSS observation.

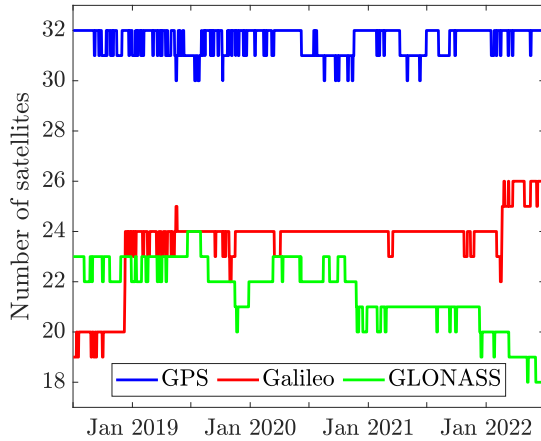


FIGURE 3.1: Evolution of number of GNSS satellites between July 2018 and June 2022

The GNSS constellations transmit different ranging codes at different frequencies, supporting various applications (e.g., civil, military, or search and rescue). To handle the many observable types and ease their usage within the different members of the GNSS community, it was developed a uniform standard format: The receiver independent exchange format (RINEX, Romero, 2020). In this format, the signals are denoted with the pattern “tna”, being “t” the observation type (C for pseudorange, L for phase), “n” refers to the frequency (from 1 to 9) and “a” is an attribute (e.g., if it is the in phase, I, or quadrature, Q, component of the ranging code).

The legacy GPS signals are transmitted in the L1 (1575.420 MHz; $n = 1$ in the RINEX format) and L2 (1227.600 MHz; $n = 2$) frequencies, although newer blocks (BLOCK-IIIF and BLOCK-IIIA) also transmit in the L5 (1176.450 MHz; $n = 5$) frequency. Additionally, the GPS constellation uses the code division multiple access (CDMA) technique, meaning that each active satellite transmits a different substream of the PRN sequence, which allows the stations to distinguish the satellites. Galileo also uses the CDMA technique, transmitting its signals at five different frequencies: E1 (1575.420 MHz; $n = 1$), E5a (1176.450 MHz; $n = 5$), E5b (1207.140 MHz; $n = 7$), E5 (1191.795 MHz; $n = 8$) and E6 (1278.750 MHz; $n = 6$).

Unlike for GPS and Galileo, the legacy GLONASS signals are transmitted in the G1 ($n = 1$) and G2 ($n = 2$) frequency bands using the frequency division multiple access (FDMA) technique, implying that each satellite broadcasts at a particular frequency, i.e.,

$$\text{Frequency at G1} = 1602 + k \times 9/16 \text{ MHz}$$

$$\text{Frequency at G2} = 1246 + k \times 7/16 \text{ MHz},$$

being $k = -7, \dots, 6$ the frequency channel number. This channel number allows the stations to identify individual GLONASS satellites. Note that antipodal satellites use the same channel number. In addition, newer GLONASS satellites (some GLONASS-M satellites and the entire GLONASS-K1 and GLONASS-K2 generations) include a new ranging code in the G3 (1202.025 MHz; $n = 3$) frequency using the CDMA technique. Likewise, the GLONASS-K2 satellites transmit, together with the legacy signals, CDMA ranging codes in the G1 and G2 frequencies.

In the BSW we process two different frequencies per satellite and station (two pseudorange observations and two phase observations). Since some stations can track a wide range of GNSS signals, the observations are selected according to some predefined priorities in order to achieve the highest possible uniformity within the network. Table 3.2 shows those priorities, referring to the signals according to the RINEX notation.

TABLE 3.2: Observation selection scheme used in BSW. The signals inside the cells are sorted in descending priority

	GPS	Galileo	GLONASS
Phase #1	L1W, L1C, L1X	L1C, L1X	L1P, L1C, L1X
Phase #2	L2W, L2C, L2D, L2P, L2X	L5Q, L5I, L5X	L2P, L2C, L2X
Pseudorange #1	C1W, C1C, C1X	C1C, C1X	C1P, C1C, C1X
Pseudorange #2	C2W, C2C, C2D, C2P, C2X, C2S, C2L	C5Q, C5I, C5X	C2P, C2C, C2X

3.3 GNSS observation model

The GNSS receivers generate replicas of the PRN sequences transmitted by the satellites. Such replicas are correlated with the actual received codes, resulting in a lag that measures the signal transfer time or, scaled by the speed of light, a rough station-to-satellite distance (code observation or, equivalently, pseudorange observation). Likewise, the receivers also align an internally generated carrier to the incoming signal. This process yields a phase shift (phase observation) that is converted to units of length when multiplied by the carrier wavelength. Note that this observation type is ambiguous in its own nature, as it represents a fractional cycle of the carrier rather than the total number of cycles separating satellite from station. Nonetheless, the receiver produces a continuous set of phase observations by counting the number of complete cycles that have occurred since the beginning of the track.

The transmitted wave is affected by several physical effects within its travel path. These effects can delay or advance the signal, ultimately altering the apparent station-to-satellite distance. Hence, we have to apply several models to cope with those effects during the processing of the observations. Likewise, some parameters shall be estimated on top of such models to mitigate their deficiencies. Both the models and parameterizations are briefly discussed in the sequel, with further insights when deemed convenient. However, it is not the purpose of this section to facilitate a “cooked” set of equations that can be directly implemented. If needed, the reader can find complementary and more exhaustive material in Hauschild, 2017a and Hauschild, 2017b; chapters 4 and 5 in Sanz-Subirana et al., 2013; chapters 5 and 6 in Strasser, 2022; or in Kouba, 2009b.

For a receiver r , a satellite s , a carrier identifier ν , and a ranging code identifier C^3 , the corresponding pseudorange, $P_{r,\nu}^{s,C}$, and phase, $L_{r,\nu}^s$, observations read as

$$P_{r,\nu}^{s,C} = \rho_r^s + \zeta_{r,\nu}^s + c(\tau_r - \tau^s) + \frac{I_r^s}{f_\nu^2} + T_r^s + c(d_r^C + d^{s,C}) + e_{r,\nu}^{s,C} \quad (3.1)$$

$$L_{r,\nu}^s = \rho_r^s + \zeta_{r,\nu}^s + c(\tau_r - \tau^s) - \frac{I_r^s}{f_\nu^2} + T_r^s + \lambda_\nu(N_{r,\nu}^s + \omega_r^s + \delta_{r,\nu} + \delta_\nu^s) + \epsilon_{r,\nu}^s \quad (3.2)$$

with constants c , λ_ν and f_ν representing the speed of light in vacuum, the corresponding carrier wavelength, and the corresponding carrier frequency, respectively (note that $c = \lambda_\nu f_\nu$). The different terms in (3.1, 3.2) refer to different contributions, namely:

- ρ_r^s is the range between the station and the satellite (section 3.3.2).

³Note that a dependency on the ranging code implicitly defines a dependency on the carrier. However, the opposite is not true.

- $\zeta_{r,\nu}^s$ accounts for the antenna phase center offset (PCO) and phase center variations (PCV), which are addressed in section 3.3.3.
- τ_r and τ^s are clock corrections on the receiver and satellite sides, respectively (section 3.3.4).
- $\frac{I_r^s}{f_v^2}$ represents the first order ionospheric delay. Although omitted in (3.1, 3.2), other higher order terms also affect the observations (section 3.3.5).
- T_r^s represents the tropospheric delay (section 3.3.6).
- ω_r^s is the phase wind-up effect (section 3.3.7).
- d_r^C and $d^{s,C}$ are hardware delays associated to the code observations (section 3.3.8). Note that they have a positive sign disregarding if they originate on the receiver or the satellite side in accord with Schaer, 2016.
- $N_{r,\nu}^s$ is the phase ambiguity (integer number in its own nature), and $\delta_{r,\nu}$ and δ_ν^s are biases associated to the phase observations (section 3.3.9). Note that they have a positive sign disregarding if they originate on the receiver or the satellite side in accord with Schaer, 2016.
- $e_r^{s,C}$ and $e_{r,\nu}^s$ represent any additional mismodeling in the pseudorange and phase observations.

The $e_r^{s,C}$ and $e_{r,\nu}^s$ terms mainly account for the multipath and the observation stochastic noise, which is in the order of meters and millimeters for pseudorange and phase observations, respectively (in practice, we down-weight the pseudorange observations by a factor of 100²). The multipath results when the transmitted signal is reflected by nearby structures, arriving to the antenna from different directions. Since it is more significant for lower elevation angles, it is common to weight the observations according to an elevation-dependent law, which, in our case, is $\sin^2(e)$, being e the elevation angle. In the sequel, no further discussion is necessary for these terms and, hence, they are omitted for brevity.

Instead of the raw observations themselves, for two ν_1 and ν_2 carrier frequencies (e.g., Galileo E1 and E5a), and their corresponding C_1 and C_2 ranging codes (e.g., C1C and C5Q), we process the ionospheric-free (IF) and the Hatch–Melbourne–Wubben (HMW; Hatch, 1983; Melbourne, 1985; Wübbena, 1985) linear combinations, defined as

$$P_{r,IF}^{s,C_1C_2} = \frac{f_{\nu_1}^2 P_{r,\nu_1}^{s,C_1} - f_{\nu_2}^2 P_{r,\nu_2}^{s,C_2}}{f_{\nu_1}^2 - f_{\nu_2}^2}, \quad L_{r,IF}^s = \frac{f_{\nu_1}^2 L_{r,\nu_1}^s - f_{\nu_2}^2 L_{r,\nu_2}^s}{f_{\nu_1}^2 - f_{\nu_2}^2} \quad \text{and} \quad (3.3)$$

$$HMW_r^s = \frac{f_{\nu_1} L_{r,\nu_1}^s - f_{\nu_2} L_{r,\nu_2}^s}{f_{\nu_1} - f_{\nu_2}} - \frac{f_{\nu_1} P_{r,\nu_1}^{s,C_1} + f_{\nu_2} P_{r,\nu_2}^{s,C_2}}{f_{\nu_1} + f_{\nu_2}}$$

Applying these linear combinations to (3.1, 3.2), we get

$$P_{r,IF}^{s,C_1C_2} = \rho_r^s + \zeta_{r,IF}^s + c(\tau_r - \tau^s) + T_r^s + c(d_{r,IF}^{C_1C_2} + d_{IF}^{s,C_1C_2}) \quad (3.4)$$

$$L_{r,IF}^s = \rho_r^s + \zeta_{r,IF}^s + c(\tau_r - \tau^s) + T_r^s + \quad (3.5)$$

$$\lambda_{NL} \left(N_{r,\nu_1}^s + \frac{\lambda_{WL}}{\lambda_2} N_{r,WL}^s + \omega_r^s + \delta_{r,NL} + \delta_{NL}^s \right)$$

$$HMW_r^{s,C_1C_2} = \zeta_{r,HMW}^s - c(d_{r,WL}^{C_1C_2} + d_{WL}^{s,C_1C_2}) + \lambda_{WL}(N_{r,WL}^s + \delta_{r,WL} + \delta_{WL}^s) \quad (3.6)$$

where we have introduced the narrow-lane (NL) and wide-lane (WL) wavelengths, i.e., $\lambda_{NL} = c/(f_{v_1} + f_{v_2})$ and $\lambda_{WL} = c/(f_{v_1} - f_{v_2})$, respectively (see table 3.3 for their numerical values). Moreover, some terms have been lumped together, namely,

$$\zeta_{r,IF}^s = \frac{f_{v_1}^2 \zeta_{r,v_1}^s - f_{v_2}^2 \zeta_{r,v_2}^s}{f_{v_1}^2 - f_{v_2}^2}, \quad \zeta_{r,HMW}^s = 2 \frac{f_{v_1} f_{v_2}}{f_{v_1}^2 - f_{v_2}^2} (\zeta_{r,v_1}^s - \zeta_{r,v_2}^s),$$

$$N_{r,WL}^s = N_{r,v_1}^s - N_{r,v_2}^s, \quad \delta_{(\cdot),WL}^{(\cdot)} = \delta_{(\cdot),v_1}^{(\cdot)} - \delta_{(\cdot),v_2}^{(\cdot)}, \quad \delta_{(\cdot),NL}^{(\cdot)} = \frac{f_{v_1} \delta_{(\cdot),v_1}^{(\cdot)} - f_{v_2} \delta_{(\cdot),v_2}^{(\cdot)}}{f_{v_1} - f_{v_2}},$$

$$d_{(\cdot),IF}^{(\cdot),C_1 C_2} = \frac{f_{v_1}^2 d_{(\cdot),v_1}^{(\cdot),C_1} - f_{v_2}^2 d_{(\cdot),v_2}^{(\cdot),C_2}}{f_{v_1}^2 - f_{v_2}^2} \quad \text{and} \quad d_{(\cdot),WL}^{(\cdot),C_1 C_2} = \frac{f_{v_1} d_{(\cdot),v_1}^{(\cdot),C_1} + f_{v_2} d_{(\cdot),v_2}^{(\cdot),C_2}}{f_{v_1} + f_{v_2}}.$$

We can refer to $N_{r,WL}^s$, $\delta_{(\cdot),WL}^{(\cdot)}$, N_{r,v_1}^s , $\delta_{(\cdot),NL}^{(\cdot)}$, $d_{(\cdot),IF}^{(\cdot),C_1 C_2}$ and $d_{(\cdot),WL}^{(\cdot),C_1 C_2}$ as WL ambiguities, WL phase biases, NL ambiguities, NL phase biases, IF code biases and WL code biases, respectively. It has to be stressed that using either the observations (3.1, 3.2) or the observations (3.4-3.6) during the GNSS processing leads to equal results by virtue of the fundamental differencing theorem (section 2.3), provided that the I_r^s terms are estimated as epoch-wise parameters. Moreover, if the biases are calibrated and the ambiguities are resolved to integers (as is typically the case during the final stages of the GNSS processing), then (3.4, 3.5) and (3.6) are uncoupled.

TABLE 3.3: Numerical values for those frequencies selected according to table 3.2 (channel number $k = 0$ for GLONASS)

	GPS $\nu_1/\nu_2 = \text{L1/L2}$	Galileo $\nu_1/\nu_2 = \text{E1/E5a}$	GLONASS $\nu_1/\nu_2 = \text{G1/G2}$
λ_{v_1}	19.0 cm	19.0 cm	18.7 cm
λ_{v_2}	24.4 cm	25.5 cm	24.1 cm
λ_{NL}	10.7 cm	10.9 cm	10.5 cm
λ_{WL}	86.2 cm	75.1 cm	84.2 cm

The geometry-free (GF) linear combination of the code observations is useful to derive ionospheric information (section 3.3.5), being computed as

$$P_{r,GF}^{s,C_1 C_2} = P_{r,v_1}^{s,C_1} - P_{r,v_2}^{s,C_2} = \zeta_{r,GF}^s + \left(\frac{1}{f_{v_1}^2} - \frac{1}{f_{v_2}^2} \right) I_r^s + c(d_{r,GF}^{C_1 C_2} + d_{GF}^{s,C_1 C_2}) \quad (3.7)$$

with

$$\zeta_{r,GF}^s = \zeta_{r,v_1}^s - \zeta_{r,v_2}^s \quad \text{and} \quad d_{(\cdot),GF}^{(\cdot),C_1 C_2} = d_{(\cdot),v_1}^{(\cdot),C_1} - d_{(\cdot),v_2}^{(\cdot),C_2}.$$

Note that the GF code biases are sometimes referred to as inter-frequency biases (IFBs) and they relate to IF and WL biases through the equation

$$d_{(\cdot),WL}^{(\cdot),C_1 C_2} = d_{(\cdot),IF}^{(\cdot),C_1 C_2} - \frac{f_{v_1} f_{v_2}}{f_{v_1}^2 - f_{v_2}^2} d_{(\cdot),GF}^{(\cdot),C_1 C_2} \quad (3.8)$$

Since the GLONASS satellites transmit their signals at slightly difference frequencies, it is not possible to separate receiver and satellite code biases, and these terms are hence considered as a single contribution (i.e., $d_r^C + d^{s,C} \rightarrow d_r^{s,C}$). Conversely, it is possible to neglect the frequency dependence for the phase biases according to Sleewaegen et al., 2012, which, in principle, still allows to separate δ_r from δ^s .

3.3.1 GNSS attitude model

Knowledge of the satellite attitude is necessary to easily describe some contributions of the GNSS observation model, as well as to precisely characterize the orbital dynamics. Nominally, GPS, Galileo and GLONASS follow the so-called yaw-steering attitude mode, which meets two requirements: The antenna boresight shall point towards the Earth (nadir direction) and the axis of the solar panels shall be orthogonal to the Sun direction, allowing them to rotate so that their entire surface is illuminated. Further imposing that one of the satellite cross-sides⁴ is always sunlit unambiguously defines the attitude.

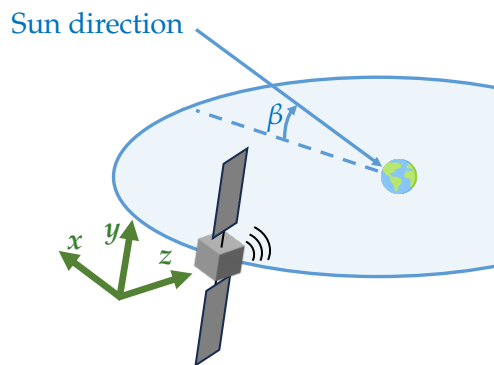


FIGURE 3.2: Orientation of the satellite body-fixed frame

Based on the yaw-steering attitude, the IGS defines a body-fixed frame uniform within the various constellations (which differs from the frames used by the manufacturers). The directions of this frame are defined as follows (Montenbruck et al., 2015a; see Fig. 3.2):

- The z -direction is the principal body axis closest to the antenna boresight direction.
- The y -direction goes through the solar panel axis. It is oriented in such a way that the satellite $+x$ -side is sunlit.
- The x -direction is chosen orthogonal to the previous directions so that the resulting xyz -trihedron is right-handed oriented.

For low β angles (angle formed between the orbital plane and the Sun's direction, Fig. 3.2), the yaw-steering mode demands high spin rates at orbit noon and orbit midnight that the attitude control system is unable to follow, being the extreme case when the Sun lies in the orbital plane (an instantaneous 180° turn is required). Additionally, some GNSS satellites cannot determine their attitude during eclipse, which also precludes the well-functioning of the control system. To cope with these difficulties, the true attitude followed by the satellites deviates from the yaw-steering mode for such low β angles. These refined models are characterized and implemented in the BSW according to Kouba, 2009a, the European GNSS Agency⁵ and Dilssner et al., 2011 for GPS, Galileo and GLONASS, respectively.

3.3.2 Range contribution

The range contribution accounts for the distance between the satellite at emission time, t_E , and the receiver at arrival time, t_A ⁶. It consists of the geometrical (Euclidean)

⁴Here we identify the satellite cross-sides with those satellite sides which do not contain either the antenna or the solar panels.

⁵The European GNSS Agency provides useful metadata information to characterize the Galileo satellites (<https://www.gsc-europa.eu/support-to-developers/galileo-satellite-metadata>).

⁶The arrival time is derived from the receiver clock reading after removing an initial estimate of the receiver clock error. This clock error comes from a coarse single-receiver navigation solution, where the satellite orbits and clock corrections are fixed to the satellite broadcast information. We refer to this process as clock synchronization.

distance and a relativistic correction owing to the space-time curvature. This latter effect (Shapiro effect) is modeled and directly removed from the observations in accord with Ashby, 2003.

The Euclidean distance is written as

$$\rho_r^s = \left| \mathbf{r}_{r\mathcal{T}}(t_A) - \mathbf{R}^\top(t_A) \mathbf{r}_I^s(t_E) \right| \quad (3.9)$$

with $\mathbf{r}_{r\mathcal{T}}(t_A)$, $\mathbf{r}_I^s(t_E)$ and $\mathbf{R}(t_A)$ the terrestrial coordinates of the ground station antenna reference point (ARP), the inertial coordinates of the satellite center of mass, and the rotation matrix that transforms terrestrial into inertial coordinates, respectively. Note that this transformation is evaluated at t_A in order to express the satellite coordinates in the same frame as the station coordinates. Moreover, emission and arrival times are related by $t_E = t_A - \Delta t$, with Δt the signal travel time, which can be approximated using the a priori information as $\Delta t = |\mathbf{r}_r(t_A) - \mathbf{r}^s(t_A)| / c$.

Equation (3.9) is the preferred representation for the geometrical range when processing the entire network, as in our case, since the satellite orbits are better described in inertial coordinates. However, those GNSS users that kept fixed the satellite orbits (e.g., for PPP applications) avoid the frame transformation by directly evaluating the GNSS orbits in the terrestrial frame, for which (3.9) becomes

$$\rho_r^s = |\mathbf{r}_{r\mathcal{T}}(t_A) - \mathbf{r}_{\mathcal{T}}^s(t_E)| + \frac{1}{c} \boldsymbol{\omega}_{\mathcal{T}} \cdot (\mathbf{r}_{\mathcal{T}}^s(t_E) \times \mathbf{r}_{r\mathcal{T}}(t_A)) \quad (3.10)$$

being $\boldsymbol{\omega}$ the angular velocity vector of the Earth. The second term in the right-hand side is known as Sagnac correction (Su, 2001).

Station coordinates

The station coordinates (here we omit the \mathcal{T} subscript for simplicity) are built by summing up several terms:

$$\mathbf{r}_r(t) = \mathbf{r}_r^{reg} + \Delta \mathbf{r}_r^{mod} + \Delta \mathbf{r}_r^{corr} \quad (3.11)$$

where

- \mathbf{r}_r^{reg} denotes regularized coordinates. In essence, these coordinates define a long-term TRF by removing high-frequency variations. They are composed of a station (constant) position vector plus a station (linear) velocity vector. After ITRF2014 (Altamimi et al., 2016), they also include post-seismic deformations, and, with the newer ITRF2020 (Altamimi et al., 2023), non-linear annual and semiannual variations. These variations are, however, not included as part of the regularized coordinates for the results generated hereafter.
- $\Delta \mathbf{r}_r^{mod}$ includes background models to capture high-frequency variations. The IERS Conventions provide such models for the Earth solid tides, ocean tides and ocean pole tides. Additionally, ocean tidal loading corrections (significant in coastal regions) are also applied based on FES2014b (Carrère et al., 2016). Likewise, atmospheric loading corrections (Boehm et al., 2009, Männel et al., 2023) can also induce variations of a few centimeters in the station coordinates. Because of the homogeneous coverage (all weather tracking) of the GNSS receivers, this effect is averaged out and, hence, we do not apply the corresponding corrections (they are, however, relevant for SLR processing due to the "blue-sky effect", as analyzed by Sošnica et al., 2013b).

Satellite coordinates

The integration of the equations of motion (1.62) leads to the trajectories traced by the center of mass of the satellites. To achieve the highest accuracy, we use advance background models for the perturbing acceleration vector, namely:

- For the gravitational accelerations:
 - Static gravity field in accord with IERS Conventions up to degree-12.
 - Solid Earth tides in accord with IERS Conventions.
 - Ocean tides based on FES2014b (Carrère et al., 2016) up to degree-8.
 - Ocean pole tides in accord with IERS Conventions (only the most significant C_{21} and S_{21} coefficients included).
 - Third body perturbations using DE421 ephemeris (Folkner et al., 2009).
 - Relativistic Schwarzschild effect in accord with IERS Conventions (from Brumberg and Kopejkin, 1989).
- For the non-gravitational accelerations:
 - Solar radiation pressure (SRP; Milani et al., 1987) model only for Galileo (optical properties disclosed by the European GNSS Agency).
 - Albedo modeling in accord with Rodriguez-Solano et al., 2012b.
 - Antenna thrust modeling in accord with Steigenberger et al., 2018.
 - Thermal radiation for Galileo in accord with Sidorov et al., 2020.

The previous list of background models has to be complemented by some empirical accelerations to mitigate their deficiencies, being the SRP mismodeling the major error source in the satellite dynamics (note that no background model is employed for GPS and GLONASS). The Empirical CODE orbit Model (ECOM; Beutler et al., 1994) was developed in the 1990s to cope with this problem. This model is very powerful in design, since it does not require any a priori satellite information (neither geometry nor optical properties, unlike those physically-driven models, Rodriguez-Solano et al., 2012a, Montenbruck et al., 2015b), and so it is equally used for the various GNSS constellations. Within the years, however, some limitations were found and several model revisions have been implemented. In the frame of this dissertation we are using the so-called ECOM2, which was developed to improve the GLONASS results (Arnold et al., 2015).

The various ECOM versions describe an empirical acceleration profile projected in a frame which is oriented towards the Sun to better capture the SRP contribution. The fundamental directions of such a frame, as given by Prange et al., 2020, are: The E_3 direction that points from the satellite to the Sun; the E_2 direction, which results from the cross product between the satellite radial direction and the E_3 direction; and the E_1 direction, orthogonal to the previous directions and forming a left-handed frame.

The mathematical representation of the ECOM2 accelerations is⁷

$$E_1(\Delta u) = E1_0 + E1_{C1} \cos(\Delta u) + E1_{S1} \sin(\Delta u) \quad (3.14)$$

$$E_2(\Delta u) = E2_0 \quad (3.15)$$

⁷The BSW also applies a scaling factor to each component proportional to the inverse of the square distance to the Sun in order to reduce the yearly variability induced by the intensity of the solar flux.

$$E_3(\Delta u) = E_{30} + E_{3C2} \cos(2\Delta u) + E_{3S2} \sin(2\Delta u) \quad (3.16)$$

where the argument Δu is the difference between the satellite and Sun latitudes (measured in the orbital plane). The notation for each parameter matches the pattern $Ei_{(0/C/S)j}$, where i defines the direction, 0, C and S define the constant, cosine and sine contributions, respectively, and j the corresponding j th harmonic. These parameters are freely estimated during the LS adjustment.

Stochastic pulses (Beutler et al., 1994), or instantaneous velocity changes, are also able to compensate mismodeling. The acceleration that they produce is represented by the Dirac delta function as

$$\mathbf{p} = p\delta(t - \tilde{t})\mathbf{e} \quad (3.17)$$

with \tilde{t} , \mathbf{e} and p the pulse application time, its direction, and its magnitude (to be estimated). We set-up pulses in the radial, along-track and cross-track directions at orbit midnight with constraining of 10^{-6} m/s, 10^{-5} m/s and 10^{-8} m/s, respectively. If the application time differs by less than six hours from any of the arc boundaries, the pulse is not estimated (Dach et al., 2021).

We shall finally note that the initial state vectors of the satellites are also estimated during the LS adjustment in the shape of orbital elements (section 1.6.1).

Rotation matrix

The rotation matrix \mathbf{R} converts terrestrial coordinates (in practice, ITRF) into inertial (or celestial) coordinates (ICRF)⁸. It is composed by three motions as discussed in section 1.4: The precession-nutation motion, the daily Earth's rotation and small departures (i.e., polar motion and universal time variations) from such a uniform rotation. The IERS Conventions provide guidelines on the implementation of the various standard background models that account for those different motions. In the case of the precession-nutation, the model is known as IAU2006A and follows from Mathews et al., 2002 and Mathews and Bretagnon, 2003. On the other hand, the recommended model for PM and UT1 has been recently updated during the realization of the ITRF2020, according to Desai and Sibois, 2016.

On top of the PM and UT1 background models we estimate piece-wise linear functions with continuity conditions, whose parameters, which we have referred to as ERP in section 1.4.3, are set-up every 24 h. However, it is not possible to estimate the absolute rotation angle of the Earth (i.e., UT1 origin) due to correlations with the orbital parameterization. More specifically, rotating the Earth around its pole can be compensated by rotating the orbital plane, through the redefinition of the ascending node, without altering the range (use Fig. 1.9 for visual aid). Consequently, one UT1 parameter is constrained to its a priori value. Likewise, a similar mechanism would occur between orbit inclination and ascending node angles and corrections over the precession-nutation model, if estimated. These correlations are analytically demonstrated in Teunissen and Kleusberg, 2012, section 14.3 by observing the collinearity of the corresponding columns of the design matrix.

Out of curiosity, we can reach the above conclusion by approaching the problem from a different analytical perspective. Specifically, we can describe the dynamics of satellite orbits in the terrestrial frame, obtaining identical solutions provided that we account for fictitious accelerations due to the Earth's rotation (namely, centrifugal and Coriolis terms). These accelerations depend on the Earth's angular velocity

⁸Whereas the ICRF origin is defined by the barycenter of the Solar System, the origin of the ITRF is defined by the center of mass of the Earth. Therefore, the \mathbf{R} matrix strictly accounts only for the rotation part of the transformation.

vector, whose precise characterization involves precession-nutation, polar motion, and universal time. Considering (1.26), it is evident that, to a first approximation, we do not have access to either the absolute value of UT1 (represented by p_z) or the absolute value of the precession-nutation angles.

3.3.3 PCO and PCV contributions

The effective station-to-satellite distance is not a direct measure between the corresponding ARPs because of the delays induced by the radiation pattern of the antennas. This effect, previously denoted by $\zeta_{r,\nu}^s$, is actually different for code and phase observations (Kersten and Schön, 2011). However, since the estimation process is driven by the phase observations due to their higher weighting, such discrepancy is not taken into account in the BSW.

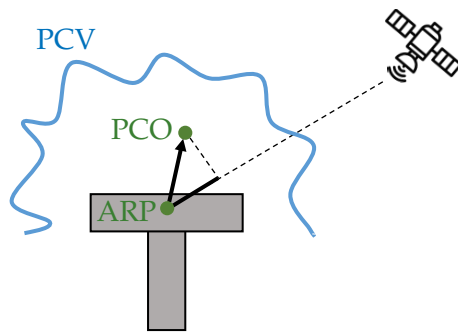


FIGURE 3.3: PCO and PCV representation

The radiation patterns are modeled as the sum of a constant offset (referred to as PCO), which must be projected in the station-to-satellite line of sight (LOS), and an azimuth-, elevation-dependent variation (referred to as PCV; see Fig. 3.3). These corrections are described in a frame attached to the antenna. In the case of the ground stations, the north-east-up directions (Fig. 1.8) are well-suited for that purpose, whereas, on the satellite side, we use the y (satellite north), x (east) and z (up) directions of the IGS satellite body-fixed frame (Fig. 3.2).

PCO and PCV values for the GNSS satellites, ground stations and different frequencies are provided by IGS in the so-called antenna exchange format (ANTEX; Rothacher and Schmid, 2010). Note that the values for the GNSS satellites are referred to their center of mass. In addition, and as noted in the preceding section, the PCO values are connected to the TRF through the scale, and, hence, it is important to consistently use the regularized IGS station coordinates together with the associated ANTEX file when realizing any specific ITRF.

3.3.4 Clock corrections

The reading of an orbiting clock does not refer to TT according to the special and general relativity theories (Ashby, 2003). On the one hand, a frequency shift occurs due to the orbit semi-major axis, being pre-launch (at the factory) calibrated in order to facilitate the maintenance of the GNSS time scales. On the other hand, the orbital eccentricities are responsible of a period clock variation that can be expressed as

$$\Delta\tau^s = -2\frac{\mathbf{r} \cdot \mathbf{v}}{c^2} \quad (3.18)$$

and is, by convention, corrected from the observations. Any other effect will be absorbed by the clock parameters, which are epoch-, station- and satellite-wise estimated because of their stochastic behavior.

The clock term appears as the difference between the station and satellite contributions and, therefore, any epoch-wise common offset cancels out. This rank defect

can be overcome by applying some epoch-wise constraints (i.e., a clock datum), for instance:

- To fix to zero the clock corrections of a particular reference station. This is the preferred option in post-processing, because some ground stations are equipped with very stable clocks. However, if that reference station has, at some point, a data gap, the associated epochs will miss the datum, hence affecting the integrity of the parameter estimation process.
- A zero mean condition over the clock corrections of several satellites. This is our preferred option during the parameter estimation process, using the GPS satellites as reference (i.e., we realize the GPS time scale).

All in all, we do not have access to the absolute clock values, but our clock estimates are shifted by an arbitrary clock offset, i.e.,

$$\tau_{(\cdot)}^{(\cdot)} + \tau \rightarrow \tau_{(\cdot)}^{(\cdot)} \quad (3.19)$$

3.3.5 Ionospheric delay

The ionosphere is a dispersive medium, meaning that the propagation speed of a wave depends on its frequency. The immediate consequence is that GNSS signals at different frequency bands experience different delays. Moreover, because of the modulation itself, the ranging code information travels at a seemingly different frequency than the carrier, resulting in a different response for the code and phase observations: The code is delayed and the phase is advanced.

In (3.1, 3.2) we have only included the first order ionospheric term, which amounts to about 99% of the total contribution (Sanz-Subirana et al., 2013, section 4.1), to emphasize that it vanishes in both the IF and MW linear combinations (3.4-3.6). However, the ionospheric effect is more precisely characterized as (IERS Conventions)

$$\Delta P = \frac{s_1}{f^2} + 2\frac{s_2}{f^3} + 3\frac{s_3}{f^4} \quad (3.20)$$

$$\Delta L = -\frac{s_1}{f^2} - \frac{s_2}{f^3} - \frac{s_3}{f^4} \quad (3.21)$$

for code and phase observations, respectively. The coefficients $s_{(\cdot)}$ depends, among others, on the total electron content (TEC) within the ray path (in particular, $s_1 = 40.3 \cdot 10^{16} \text{TEC}$), which must be known in order for us to eliminate those higher order terms (proportional to f^{-3} and f^{-4} in the the above equations) during the reconstruction of the observations.

CODE provides TEC information in the shape of global ionospheric maps (GIM; Schaer et al., 1996; Montenbruck et al., 2014). These maps represent the ionosphere as a thin layer at a given altitude (e.g., 350 km), where the (vertical) TEC is approximated by a spherical harmonics expansion. The slant TEC (i.e., TEC within the ray path) is

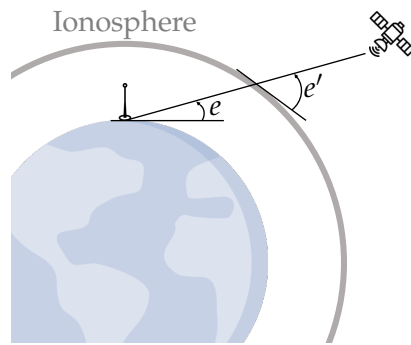


FIGURE 3.4: Ionosphere thin layer model

later computed thanks to a mapping function that uses as argument the incidence signal angle at the layer piercing point (e' in Fig. 3.4). The GF code observations (3.7) are used in this procedure, in which the GF code biases are generated as a by-product. Other studies have demonstrated that these biases can also be derived using a local (rather than global) TEC parameterization (Wang et al., 2016).

3.3.6 Tropospheric delay

The troposphere is a non-dispersive medium for frequencies below 30 GHz (Petit, Luzum, et al., 2010, section 9.2). The delay that it produces in the GNSS signals is divided into two main parts, namely, dry (or hydrostatic; subscript d) and wet (w) parts. For precise applications (as the ours), it is common to also account for the so-called tropospheric gradients (g). Therefore, the total contribution is mathematically modeled as (IERS Conventions)

$$T = m_d(e)D_d + m_w(e)D_w + m_g(e) (G_N \cos(a) + G_E \sin(a)) \quad (3.22)$$

with e and a the local elevation and azimuth angles of the received signal. The dry and wet terms are described by a mapping function $m_{(\cdot)}$ and a zenith delay $D_{(\cdot)}$. For the results generated in the frame of this dissertation, we account for them by using the information provided in the Vienna Mapping Function 1 (VMF1; Boehm and Schuh, 2004) products, which are updated in a regular basis as they assimilate methodological data. Due to uncertainties in the wet part, we also estimate piece-wise linear parameters with two-hour resolution and relative constraining of 1 m in STD on top of D_w .

The tropospheric gradients are described by another mapping function (that follows from Chen and Herring, 1997) and the two parameters G_N and G_E , which are estimated with daily resolution in our processing.

3.3.7 Phase wind-up effect

Due to the circular polarization of the GNSS signals, changes in the relative orientation between the station and the satellite produce variations in the phase observations that could be erroneously interpreted as range variations. This effect, known as wind-up effect, is corrected in the BSW according to the geometrical relationships firstly introduced by Wu et al., 1992.

3.3.8 Pseudorange biases

The pseudorange biases account for systematic effects in the code observations, which are associated to hardware delays. Such biases are modeled as station-, satellite-, frequency-, signal- and constellation-dependent linear terms (Håkansson et al., 2017), and must be estimated or calibrated. To handle them, the BSW uses the concept of observable specific bias (OSB; Villiger et al., 2019), for which these biases are set-up station-, satellite- and signal-wise (note that the signal dependency already includes the dependencies on the frequency and on the constellation). The major difficulty in deriving these biases resides on the many involved rank-defects, which require specific constraints, i.e., we have to define a OSB datum. As stated in Villiger et al., 2019, this is achieved by applying zero-mean conditions over each observable type and GNSS constellation, as well as by imposing that certain satellite and receiver IF code biases are zero. On the satellite side, the IF biases that we drive to zero are associated to the signals C1W/C2W, C1C/C5Q and C1P/C2P for GPS, Galileo and

GLONASS, respectively. On the receiver side, the corresponding signal pair, which depends on the station tracking scheme and on our signal selection priorities (table 3.3). Note that, if only IF observations are processed (as in our procedures), then another constraint imposing zero GF bias is applied. These multiple constraints have implications, not only on the biases themselves, but on the meaning of other linear parameters (in particular, clock and ionospheric corrections) of the GNSS observation model, which we shall discuss next.

Using the GF observations (3.7) we have access to $d_{r,GF}^{C_1C_2} + d_{GF}^{s,C_1C_2}$ in an absolute sense thanks to the use of ionospheric modeling (based on GIM). For GLONASS, it is one single parameter because of the FDMA technique. For GPS and Galileo we can separate receiver and satellite contributions by imposing zero-mean conditions over the satellite biases of those linearly independent C_1/C_2 pairs, which redefines the GF biases as

$$d_{GF}^{s,C_1C_2} + d_{GF}^{C_1C_2} \rightarrow d_{GF}^{s,C_1C_2}, \quad d_{r,GF}^{C_1C_2} - d_{GF}^{C_1C_2} \rightarrow d_{r,GF}^{C_1C_2} \quad (3.23)$$

These biases can be removed from the HMW observations (3.6) according to (3.8).

Let us now focus on the processing of CDMA (i.e., GPS and Galileo) IF observations. In order to separate satellite clock corrections and satellite code biases, we consistently fix to zero those satellite IF code biases pertaining to the same pair of (constellation-wise) selected signals \tilde{C}_1/\tilde{C}_2 (e.g., C1W/C2W for GPS), which results in the following redefinitions

$$\tau^s - d_{IF}^{s,\tilde{C}_1\tilde{C}_2} \rightarrow \tau^s \quad (3.24)$$

$$d_{IF}^{s,C_1C_2} - d_{IF}^{s,\tilde{C}_1\tilde{C}_2} \rightarrow d_{IF}^{s,C_1C_2} \quad (3.25)$$

$$\delta_{NL}^s - (f_1 + f_2)d_{IF}^{s,\tilde{C}_1\tilde{C}_2} \rightarrow \delta_{NL}^s \quad (3.26)$$

$$\delta_{WL}^s - (f_1 - f_2)d_{IF}^{s,\tilde{C}_1\tilde{C}_2} \rightarrow \delta_{WL}^s \quad (3.27)$$

Because of (3.25), the term d_{IF}^{s,C_1C_2} can be referred to as differential code bias (DCB). Additionally, and similar to the GF processing, we separate satellite and receiver contributions for other than the previously constrained signal pairs by applying zero-mean conditions over the satellite biases, hence

$$d_{IF}^{s,C_1C_2} + d_{IF}^{C_1C_2} \rightarrow d_{IF}^{s,C_1C_2}, \quad d_{r,IF}^{C_1C_2} - d_{IF}^{C_1C_2} \rightarrow d_{r,IF}^{C_1C_2} \quad (3.28)$$

On the other hand, to separate receiver clock corrections and receiver code biases, we fix to zero a receiver code bias per receiver and reference constellation (conventionally, GPS), resulting in

$$\tau_r + d_{r,IF}^{\tilde{C}_1\tilde{C}_2} \rightarrow \tau_r \quad (3.29)$$

$$d_{r,IF}^{C_1C_2} - d_{r,IF}^{\tilde{C}_1\tilde{C}_2} \rightarrow d_{r,IF}^{C_1C_2} \quad (3.30)$$

$$\delta_{r,NL} - (f_1 + f_2)d_{r,IF}^{\tilde{C}_1\tilde{C}_2} \rightarrow \delta_{r,NL} \quad (3.31)$$

$$\delta_{r,WL} - (f_1 - f_2)d_{r,IF}^{\tilde{C}_1\tilde{C}_2} \rightarrow \delta_{r,WL} \quad (3.32)$$

Typically the pairs C_1/C_2 and \tilde{C}_1/\tilde{C}_2 correspond to different constellations in these equations and, as a consequence, $d_{r,IF}^{C_1C_2}$ is often referred to as inter-system bias (ISB).

For other than the reference constellation, a common shift on all the associated receiver biases can be compensated by a shift on the constellation clock corrections. Hence, another zero-mean condition is applied over all the receiver biases of the same

constellation, which implies:

$$\tau^s + \tau^{GNSS} \rightarrow \tau^s \quad (3.33)$$

$$d_{r,IF}^{C_1C_2} + \tau^{GNSS} \rightarrow d_{r,IF}^{C_1C_2} \quad (3.34)$$

$$\delta_{NL}^s + (f_1 + f_2)\tau^{GNSS} \rightarrow \delta_{NL}^s \quad (3.35)$$

$$\delta_{WL}^s + (f_1 - f_2)\tau^{GNSS} \rightarrow \delta_{WL}^s \quad (3.36)$$

The term τ^{GNSS} represents a shift on the clock corrections pertaining to a specific constellation, and, consequently, acts upon its time scale. The time scale is actually an important conceptual element that has to be taken into account when manipulating clock products in post-processing. For instance, if we change the clock datum by applying an epoch-wise offset over the clock corrections of a particular clock product, we have to guarantee that those epoch-wise offsets are, in average, zero in order not to influence the underlying time scale.

Due to the FDMA technique, the GLONASS code biases are defined per satellite and receiver, i.e., $d_{r,IF}^{C_1C_2} + d_{IF}^{s,C_1C_2} \rightarrow d_{r,IF}^{s,C_1C_2}$ for the IF observations. To separate them from the GLONASS clock corrections, we have to apply a zero-mean condition over all the stations for those biases pertaining to the same satellite. This conveys a redefinition of the parameters in a similar manner as before.

3.3.9 Phase ambiguities and biases

The phase biases are linear terms that can be estimated or calibrated, and whose major difficulty lies on the rank defects that they involve, as they depend on the receiver, satellite and carrier frequency. Although omitted from (3.2) for simplicity, the phase biases also depends on the GNSS constellation (Håkansson et al., 2017), implying that $\delta_{r,\nu}$ is different for GPS L1 than for Galileo E1, even if both are the same frequency band.

In view of (3.6), we can easily recognize a one-to-one correlation between WL phase biases and ambiguity parameters. To overcome these singularities we can apply an ambiguity datum (independent for each constellation) by imposing, on the one hand, a zero-mean condition over the satellite phase biases, for which

$$\delta_{WL}^s + \delta_{WL} \rightarrow \delta_{WL}^s, \quad \delta_{r,WL} - \delta_{WL} \rightarrow \delta_{r,WL} \quad (3.37)$$

and, on the other hand, by fixing to zero as many ambiguities as satellites for a reference station (i.e., $N_{r_1,WL}^s$) and, for the remaining stations, the ambiguity of a reference satellite (i.e., $N_{r,WL}^{s_1}$). This constraining eventually yields

$$N_{r_1,WL}^s + \delta_{WL}^s \rightarrow \delta_{WL}^s \quad (3.38)$$

$$N_{r,WL}^{s_1} - N_{r_1,WL}^{s_1} + \delta_{r,WL} \rightarrow \delta_{r,WL} \quad (3.39)$$

$$\left(N_{r,WL}^s - N_{r,WL}^{s_1} \right) - \left(N_{r_1,WL}^s - N_{r_1,WL}^{s_1} \right) \rightarrow N_{r,WL}^s \quad (3.40)$$

$$\frac{\lambda_{WL}}{\lambda_2} \left(N_{r_1,WL}^s - N_{r_1,WL}^{s_1} \right) + \delta_{NL}^s \rightarrow \delta_{NL}^s \quad (3.41)$$

$$\frac{\lambda_{WL}}{\lambda_2} N_{r,WL}^{s_1} + \delta_{r,NL} \rightarrow \delta_{r,NL} \quad (3.42)$$

Proceeding in an analogous manner for the NL terms, we discover transformations equivalent to (3.37-3.40). The main advantage of this ambiguity datum is that the

redefined UD ambiguities (3.40) are actually DD ambiguities (Teunissen and Khodabandeh, 2015), preserving their integer nature.

Another option to avoid the aforementioned singularities is to lump together biases and ambiguities, such that

$$N_{r,(\cdot)}^s + \delta_{r,(\cdot)} + \delta_{(\cdot)}^s \rightarrow B_{r,(\cdot)}^s \quad (3.43)$$

Although it seemingly hampers AR, this is actually our preferred option. For the AR strategy developed in chapter 4, we implement a novel and efficient method to calibrate the phase biases as well as to recover the integer nature of the ambiguities based on the inspection of the fractional parts of $B_{r,(\cdot)}^s$.

3.4 General aspects of the processing strategy

The results generated along this work rely on the existing tools of the BSW as well as on the BSW processing engine, for which specific details and exhaustive descriptions are given in Dach et al., 2015. In this section we discuss the general aspects of the implemented processing strategies.

TABLE 3.4: Breakdown of parameters for a daily GNSS network solution assimilating observations from 200 stations at a 5-minute sampling

Parameter type	Approx. number
Station coordinates	600
Orbit parameters	1500
Earth rotation parameters	6
Satellite clock corrections	20000
Station clock corrections	60000
Ambiguity parameters	30000
Troposphere parameters	3400

Our primary processing strategy comprises four different stages: Preprocessing, computation of global parameters, computation of receiver-dependent parameters and AR. The associated flowchart is displayed in Fig. 3.5. It shall be clarified that global parameters enclose satellite orbits and clock corrections, ERP, and station coordinates (defining a global TRF as noted in section 3.3.1). Likewise, receiver-dependent parameters include receiver clock corrections, ambiguities, and tropospheric delays. In numbers, assuming a multi-GNSS (70 satellites) network made up by 200 stations, we have to solve a least-square problem with about 2000000 observations and 100000 parameters (daily sessions with code and phase observations at a 5-minute sampling). The breakdown of the parameters is given in table 3.4. Note that the OSBs (about 10000 parameters, with the largest contribution coming from GLONASS due to the FDMA technique, for which we estimate station- and satellite-dependent biases) are not included since they can be calibrated in later stages of the processing.

Preprocessing

The preprocessing aims at cleaning the observations through several steps. Firstly, we prepare the inputs, including daily batches of observations from about 300 IGS stations (more than 200 of which containing GPS, Galileo and GLONASS data) and a priori orbit and clock information. Initially, the presented processing strategy was validated with the satellite broadcast information (Calero-Rodríguez et al., 2023a),

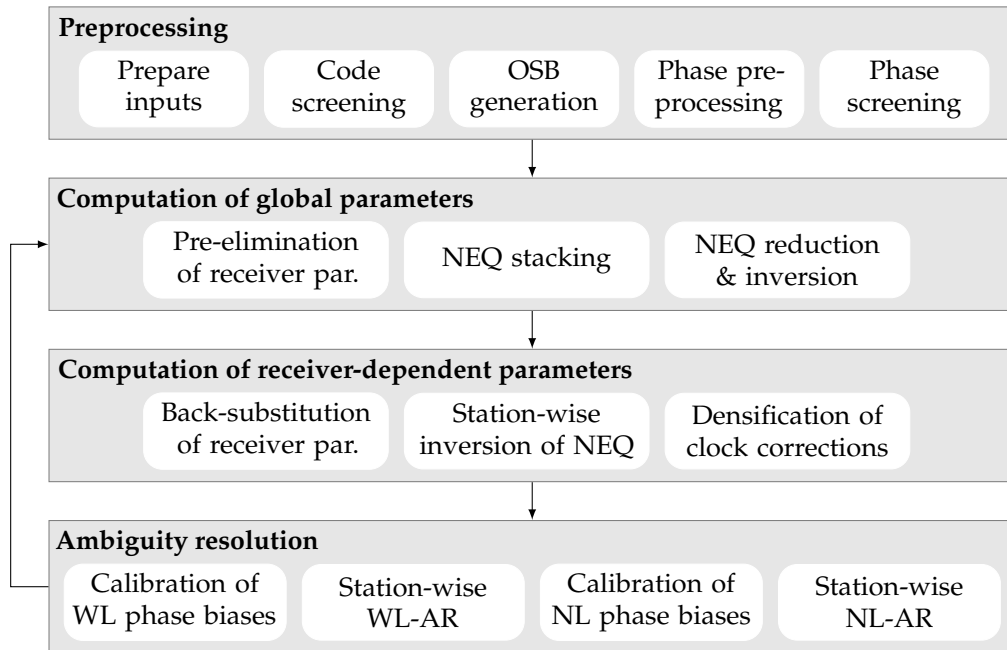


FIGURE 3.5: General flowchart of the processing strategy

although here we use the CODE Multi-GNSS Experiment (MGEX, Prange et al., 2016) products as a priori information for the sake of robustness. In this step we also select the signals that will be processed for each station (according to table 3.2), carry out a coarse screening by inspecting the observations (e.g., the HMW observations are well-suited to detect blunders), smooth the code observations (equations (2.8a,2.8b) in Schaer et al., 1996), and synchronize the receiver clocks to the GPS time scale. Note that, if it is not said otherwise, our set-up uses IF observations at a 5-minute sampling.

Secondly, code-only solutions are iteratively generated and their residuals analyzed to detect outliers. In order to perform this step more efficiently, some simplifications are considered: The stations are grouped in regional clusters, for which clock corrections and OSBs are independently pre-eliminated. Afterwards, the resulting NEQ are stacked to generate the geometric part of the solution (satellite orbits, station coordinates and troposphere parameters) that is fixed in a subsequent cluster-wise processing where the sought residuals are retrieved.

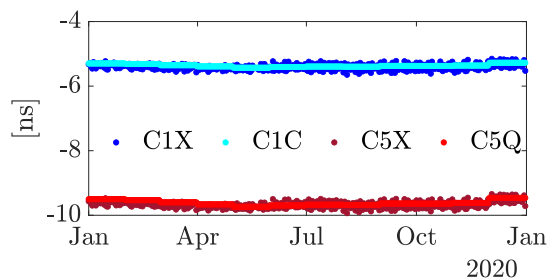


FIGURE 3.6: Code biases for satellite E33

Since OSBs and clock corrections have to be jointly estimated due to the involved rank defects, the computation of OSB parameters also requires some shortcuts to alleviate the computational burden: The observations are once more processed in regional clusters, for which the previously generated code-only orbits and station coordinates are held fixed. For these clusters we pre-eliminate other than hourly satellite

clock corrections (to get a common satellite clock inbetween the clusters) and GPS and Galileo OSBs, which are estimated after NEQ stacking and plug back into the original NEQ to retrieve the GLONASS OSBs cluster by cluster. It shall be stressed here that we are using IF observations and, consequently, we do not have access to the GF part of the biases. In order to produce a complete bias product, we hence account

for those GF biases through the a priori OSB information, directly coming from the CODE production line (particularly, GF processing), where OSBs are disseminated with monthly resolution. A remarkable fact is that biases belonging to the same frequency have similar magnitude (Sleewaegen and Clemente, 2018), which is exemplified in Fig. 3.6 by showing one year of estimated biases for the Galileo satellite E33 and code signals C1C, C1X, C5Q and C5X. Recall that the pair C1C/C5Q is used as Galileo reference in (3.28-3.26) and, therefore, the figure depicts corresponding GF contributions, whose lower dispersion is explained by their monthly resolution.

Eventually, the phase data is analyzed within several iterations too, not only to clean the observations (inspection of residuals similarly to the code data), but also to define the set of ambiguity parameters (i.e., cycle-slip detection), which is reliably done by reconstructing and examining the phase observations using the previously computed code-only solution.

The screened observations, cycle-slips and OSB information are stored and, therefore, the preprocessing stage can be skipped in any subsequent computation of geodetic solutions.

Computation of geodetic solutions

The core of the processing is based on a station-wise architecture, i.e., single stations are independently processed as far as possible, uniformly distributing the computational resources while alleviating the computational effort for large networks. Therefore, the first step to compute the global parameters (second block in Fig. 3.5) is the rigorous station-wise pre-elimination of receiver-dependent parameters, where resolved ambiguities are considered as known after the first processing loop iteration. Once all the station-dependent NEQ are generated, they are stacked, and inverted. This inversion is carried out along with a reduction of the clock parameters by sequentially splitting the stacked NEQ into smaller NEQ, each one containing 3-hour-clock batches, in order to reduce the computational time. Substituting the previously generated global solution allows to readily estimate the remaining receiver-dependent parameters during another station-wise parallelization (third block in Fig. 3.5). Optionally, the resolution of the clock product can be augmented (e.g., from 5-minute rate to 30-seconds rate) to support specific applications. We refer to this step as clock densification. It is based on the processing of inter-epoch-difference observations (in order for the ambiguity parameters to vanish) using the estimated clock corrections as anchor points (Bock et al., 2009).

In the case that additional iterations are still pending (we perform two nominal iterations with AR), it is important that the ambiguities are estimated as real numbers during the computation of receiver-dependent parameters, since their fractional parts will be the input for the subsequent AR stage.

The NEQ from the second block of Fig. 3.5 are stored to easily generate long-arc solutions (section 2.6). In particular, we retrieve and stack NEQ from three consecutive days to produce our nominal 3-day-arc global solutions, from which we extract the middle to strictly produce daily solutions. These are fed into the third block of Fig. 3.5 to consistently compute the receiver-dependent parameters.

Ambiguity resolution

Our implemented AR strategy follows a very popular approach used within the GNSS community when dual-frequency observations are available (e.g., Sanz-Subirana et al., 2013, section 6.3). It is based on the processing of HMW and IF observations in

two differentiated steps: The WL ambiguities are firstly resolved using the HMW observations, which permits to removed them from the IF observations prior to resolving for the NL in the second step. Even though this procedure is intuitive and seamless at first sight, we have to tackle conceptual and practical difficulties that arise when processing UD observations due to the phase biases, for which the DD-based algorithms have to be revisited. This topic is exhaustively addressed in the following chapter and a more detailed discussion on the ambiguity resolution strategy is given in section 4.3.

3.5 Validation of the results

We carry out several comparisons to validate the generated GNSS solutions:

- Comparisons between UD- and DD-based solutions generated under equivalent conditions (section 3.5.1).
- Comparisons between UD-based solutions and CODE MGEX products (section 3.5.2).

The comparison of (either satellite or station) coordinates belonging to two different products is performed in subsequent sections after correcting for frame misalignments, which are accounted for through the so-called Helmert transformation (Watson, 2006), which considers three translations along the coordinate axes, three rotations around the coordinate axes and one scale for all three components. This transformation is applied uniformly to all the coordinates associated with a specific product, aiming at minimizing the square norm of the differences. On the other hand, a meaningful metric that will also be employed in the sequel to compare GNSS products is the so-called signal in space (SIS, Montenbruck et al., 2018b) range. For the satellites s_1 and s_2 , an ideal station located at the center of the Earth (i.e., $r_r = \mathbf{0}$), and the products A and B , the between-satellite SIS range differences are computed as

$$SIS_{AB}^{s_1 s_2} = \rho_{AB}^{s_1 s_2} - c\tau_{AB}^{s_1 s_2} + E_{AB}^{s_1 s_2} \quad (3.44)$$

with $(\cdot)_{AB}^{s_1 s_2} := (\cdot)_A^{s_1} - (\cdot)_A^{s_2} - (\cdot)_B^{s_1} + (\cdot)_B^{s_2}$. The quantity $E_{AB}^{s_1 s_2}$ represents errors that originate at the network and leak into the satellite parameters. If the ambiguities are resolved as integers, however, the connection between receiver and satellite parameters is weak, which permits to decompose $E_{AB}^{s_1 s_2}$ in terms of WL and NL integer jumps and NL phase bias differences. This decomposition is paramount if independent products compatible with AR are to be combined (Banville et al., 2020). For the sake of simplicity, here $E_{AB}^{s_1 s_2}$ is removed as a constant bias. Note that satellite-specific SIS differences can be derived from (3.44) applying an epoch-wise zero-mean condition.

3.5.1 UD-based against DD-based solutions: Controlled test case

From March 23 to April 6, 2021, fifteen daily DD-based solutions have been generated following the standard procedures adopted by CODE, i.e., a two-fold strategy: Generation of geometry using DD observations, followed by the computation of clock corrections and associated biases through a UD processing scheme where the geometry is held fixed. To preserve to the extent possible the consistency with the corresponding UD-based solutions, the same screening has been used as well as the same a priori models and even the same ambiguity parameterization, for which the

UD ambiguities have been converted into baseline ones. The fundamental differencing theorem proven in section 2.3 states that both solutions will be identical, provided that every reduced (during differentiation) observation also reduces the number of parameters. This assumption is, however, not fully met as the baseline measurements demand equal observation windows between two stations, which generally leads to the rejection of some measurements at the boundaries of the satellite tracks.

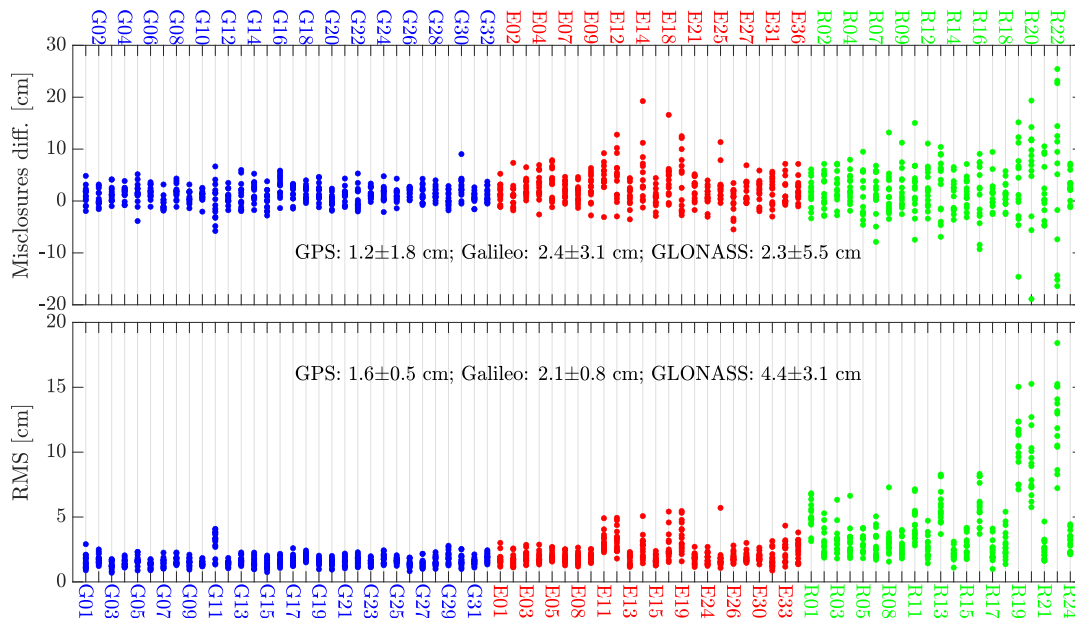


FIGURE 3.7: Comparisons between UD-based and DD-based solutions. The top panel depicts differences in the midnight misclosures (RMS of DD-based misclosure minus RMS of UD-based misclosure), whereas the bottom panel shows orbital RMS differences

The corresponding orbit comparisons are given on the bottom panel of Fig. 3.7. An excellent agreement can be seen at the level of 1.6 and 2.1 cm in (3D) RMS for GPS and Galileo, respectively. The satellite G11, which shows larger differences, is unhealthy and, hence, very poorly observed during this period, especially affecting the generation of baselines for the DD-based solution. The satellites E11, E12 and E19 (IOV satellites), and E14 and E18 (placed in eccentric orbits) are also showing larger differences than the majority of the Galileo satellites, although remain at an acceptable averaged level of about 3 cm. The GLONASS constellation, on the other hand, depicts clearly worse performance, with comparisons at the level of 4.4 cm and higher variability within the satellites. This can be largely explained by the weaker GLONASS model based on real-valued ambiguities (for both compared solutions, in this case). Likewise, the top panel of Fig. 3.7 represents differences in midnight misclosures, i.e., RMS of DD-based misclosure minus RMS of UD-based misclosure. Therefore, positive values indicate superior

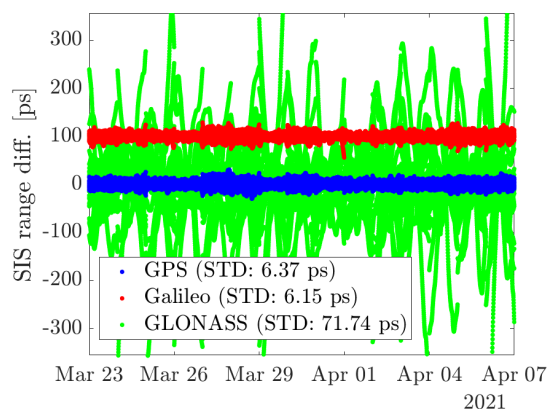


FIGURE 3.8: SIS range differences between UD-based and DD-based products

performance (smaller overlap) for the UD-based product. This is systematically the case, with average differences of 1.2, 2.4 and 2.3 cm for GPS, Galileo and GLONASS, respectively.

Fig. 3.8 compares the epoch-wise UD- and DD-based SIS range for the different constellations (Galileo comparisons shifted by 100 ps for clarity). The cloud of points is at the 6 ps level in STD for GPS and Galileo, illustrating that the UD- and DD-based solutions may be considered equivalent from both the user’s perspective and the perspective of AR. Once more, the comparison performs much worse for GLONASS, with a STD of about 70 ps (2 cm). It becomes thus evident that the term E_{AB}^{S1S2} in (3.44) cannot be regarded as a constant bias if the ambiguity parameters are not resolved.

3.5.2 UD-based solution against CODE MGEX products

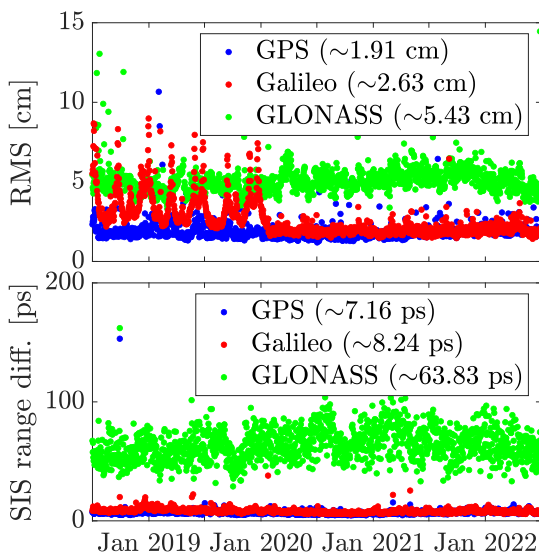


FIGURE 3.9: Comparisons between CODE MGEX products and UD-based solutions. The upper panel shows the RMS of the daily orbit comparisons, whereas the lower panel represents the STD of the daily SIS range differences

In order to adjust the set-up to the CODE MGEX solutions, long-arc UD-based products referred to ITRF2014 have been derived from stacking three individual daily NEQ for a time interval of four years (from July 2018 to June 2022). The resulting orbit comparisons are depicted in the upper panel of Fig. 3.9. The agreement between both processing lines is in line with the expectations (Griffiths and Ray, 2009), with an average RMS of 1.91, 2.63 and 5.43 cm for GPS, Galileo and GLONASS, respectively. The visible change in the pattern of the Galileo comparisons at the beginning of the year 2020 is attributed to the integration of an internally developed SRP model into the CODE production line, which has been preserved for the reprocessing of the UD-based solutions. The lower panel of Fig. 3.9, on the other hand, shows the STD of the daily SIS range differences.

Each daily comparison may contain abnormally high differences for specific satellites, which usually implies that the corresponding AR algorithm has converged to a different solution (see section 4.6.5). Such degraded satellites have been excluded from the displayed daily metrics for a fairer comparison. We see that, in average, the STD statistics are at an outstanding level of 7 and 8 ps for GPS and Galileo, respectively, whereas such comparison is at the level of 63 ps for GLONASS, which is still acceptable for solutions that do not benefit from AR.

The daily RMS of the orbit midnight misclosures for the different constellations is displayed in Fig. 3.10 for both the MGEX products (left panel) and the UD-based solutions (right panel). The UD-based solutions perform better for GPS and Galileo, with average values of 6.86 and 7.44 mm, respectively, in comparison with the 9.57 and 13.56 mm (11.86 mm, if the inconsistent period is omitted) obtained from the CODE MGEX products. This difference is not that significant if we compare with the final CODE products, whose corresponding GPS figure is 8.49 mm. In case of GLONASS, the orbit overlaps seem superior for the CODE MGEX products (15.04

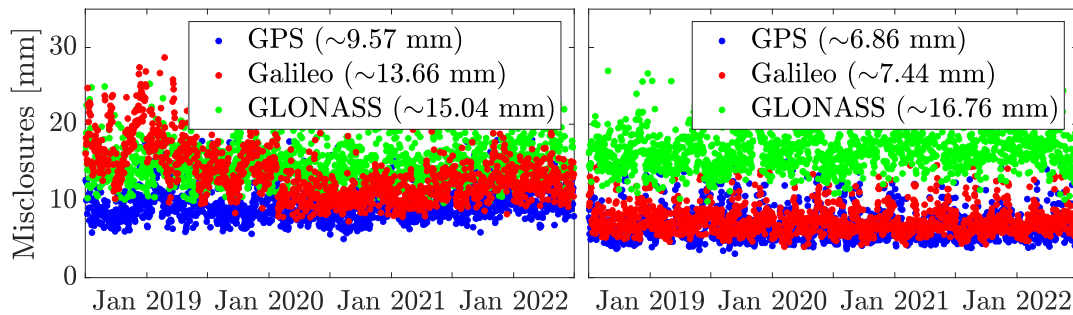


FIGURE 3.10: Orbit midnight misclosures for the CODE MGEX products (left panel) and the UD-based solutions (right panel)

mm in average, contrasting with the 16.76 mm for the UD-based solution), which very likely obeys to the use of an AR strategy (Habrigh, 2000), whose implementation is technically challenging when processing UD observations.

3.6 TRF update: From ITRF2014 to ITRF2020

It is an interesting exercise to evaluate the performance of the TRF underlying the geodetic solutions, since the quality of the derived geophysical parameters is conditioned to the stability of the frame itself. Such an exercise is the subject of the present section.

The solutions presented in the previous section are based on ITRF2014. However, the IGS transitioned from ITRF2014 to ITRF2020 at the end of 2022⁹. Therefore, we have computed analogous solutions using this newer frame along with the newer standards it conveys, namely:

- An updated mean pole used in the modeling of the ocean pole tides (Petit, Luzum, et al., 2010, v1.2.0).
- An updated version of the sub-daily polar motion model (Desai and Sibois, 2016).

The orbit midnight misclosures can be used to measure the stability of the frame. Nonetheless, the resulting figures only differ at the sub-millimeter level from the corresponding ITRF2014 values (right panel of Fig. 3.10). In order to gain further insight into the stability of the frame, we have compared the daily estimates of the station coordinates against their regularized positions. The RMS of the Helmert transformation as well as the associated Helmert parameters are given in Fig. 3.11 (rotation angles and scale multiplied by the Earth's radius) for both ITRF2014- and ITRF2020-based solutions. It can be seen that the RMS is smaller for the ITRF2020 solutions, indicating a better stability during the processed time interval. A similar conclusion yields from the smaller biases and smaller signal amplitudes observed in the translation and scaling figures for the ITRF2020 solution. Conversely, no conclusion can be drawn from the rotation parameters.

3.7 Galileo SRP model based on satellite metadata

The metadata disclosed by the European GNSS Agency for the Galileo satellites was not integrated as part of the Galileo SRP model in the CODE production line until the

⁹IGSMail-8238 <https://lists.igs.org/pipermail/igsmail/2022/008234.html>

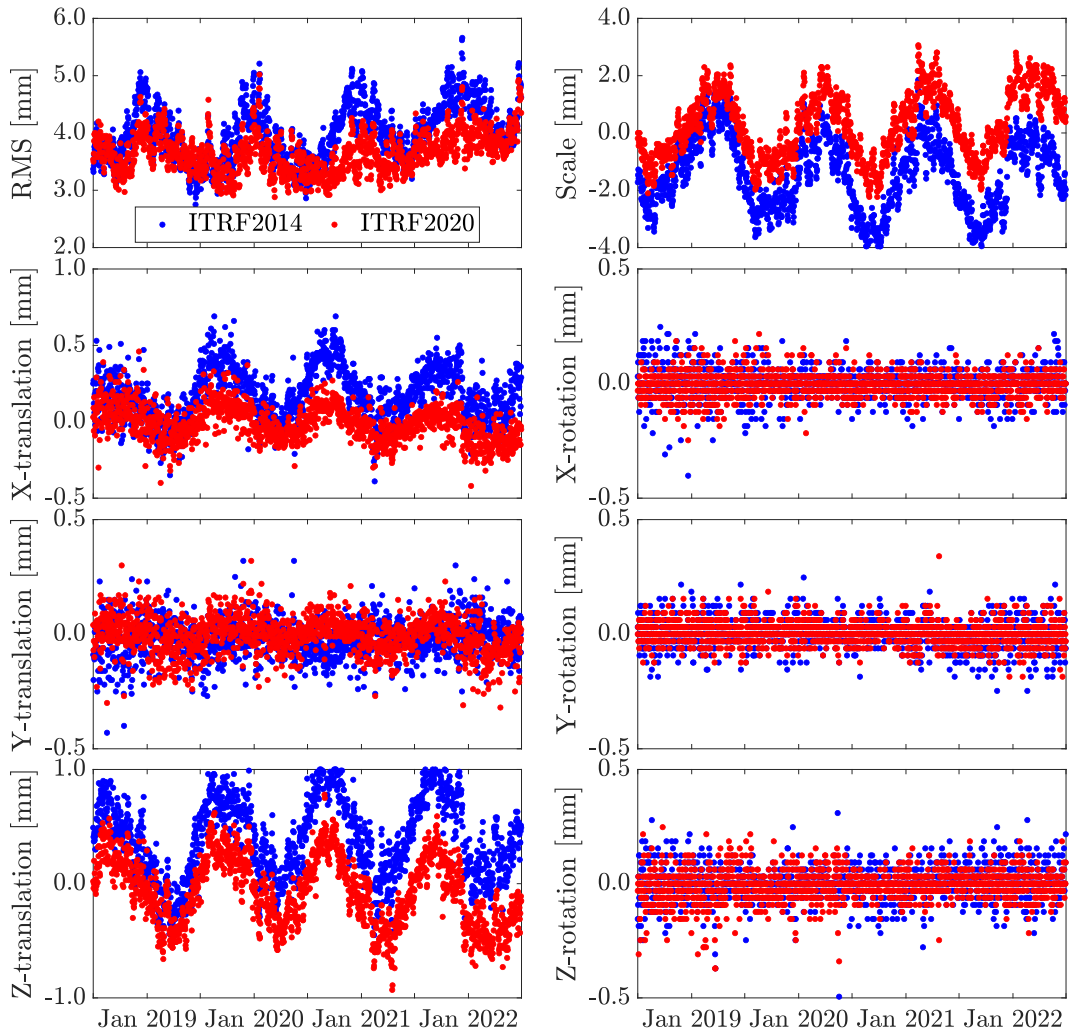


FIGURE 3.11: RMS of the Helmert transformation and Helmert parameters that result from comparing the estimated station coordinates against their regularized positions

switch to ITRF2020. Earlier solutions were using, instead, an internal characterization of the Galileo surface dimensions and optical properties derived from an in-house investigation. The performance of the new model (based on satellite metadata) was evaluated in the scope of this dissertation prior to its operational deployment. The main findings are presented herein.

The orbit misclosures are an excellent figure of merit to confirm that the in-house SRP model had a very positive impact on the Galileo solutions, as we can see on the left panel of Fig. 3.10, where the most distinct artifacts vanished after its deployment in early 2020. Upgrading the SRP model in accord with the satellite metadata has, however, a more subtle impact on the midnight misclosures: The average value turns from 7.44 to 6.42 mm. To get a more acute insight into the impact of using the satellite metadata, we also inspect the estimated Galileo ECOM2 parameters, which are devoted to compensate deficiencies in the SRP model. The estimates for the same four-year interval that we have processed so far are displayed in Fig. 3.12 as a function of the β angle (from Fig. 3.2, it represents the elevation of the Sun above the orbital plane, and, consequently, plays a vital role in SRP modeling). We can see that the new model (labeled as “Metadata”) reduces the dependency on β for every parameter (especially for low β angles), indicating that they are becoming more

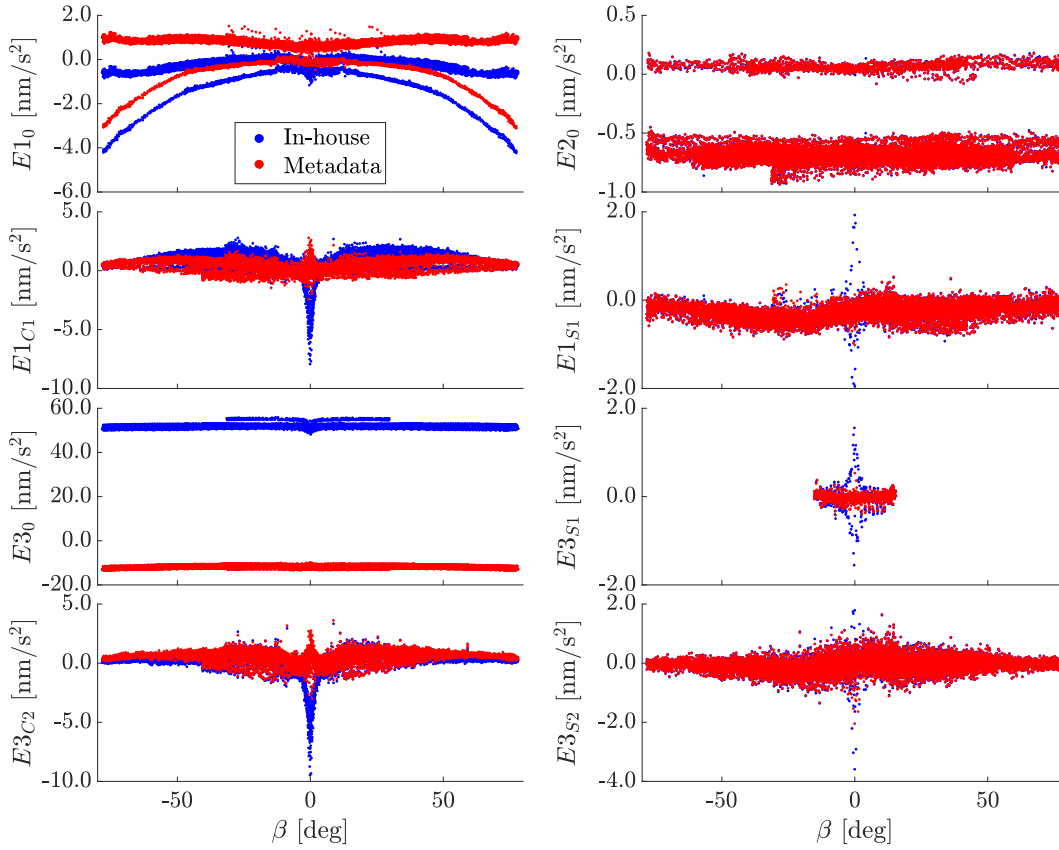


FIGURE 3.12: Comparison of estimated Galileo ECOM2 parameters for two different SRP background models

empirical than physical, as expected. Furthermore, $E3_0$, which compensates direct SRP, has a much smaller amplitude.

The interested reader may notice that the parameter $E3_{S1}$, also appearing in Fig. 3.12, is not part of the standard ECOM2 parameterization (3.14-3.16). It was included for low β angles (i.e., eclipsing satellites) in order to compensate satellite thermal radiation (Sidorov et al., 2020). Nonetheless, we can presume from Fig. 3.12 that it rather compensates mismodeling in the background SRP model, and, hence, is no longer necessary when using the Galileo metadata.

The ILRS network is able to track the Galileo constellation thanks to the laser retroreflectors arrays equipped on the satellites. The resulting SLR observations are commonly fitted to the precise orbits in post-processing, providing valuable metrics for validation purposes (the residuals can be used, for instance, to identify a variety of satellite- and station-dependent systematics, Arnold et al., 2019). Since the SRP model physically depends on the β and Δu angles, the Galileo SLR residuals are projected on a $\beta/\Delta u$ map in Fig. 3.13, where each $2^\circ \times 2^\circ$ cell represents the average value of the confined residuals. The left panel is generated with the solutions based on the in-house SRP background model, whereas the solutions based on the satellite metadata are used for the right panel. This latter panel depicts a much weaker pattern (i.e., less aggressive systematics), demonstrating an astonishing modeling improvement when the Galileo metadata is employed.

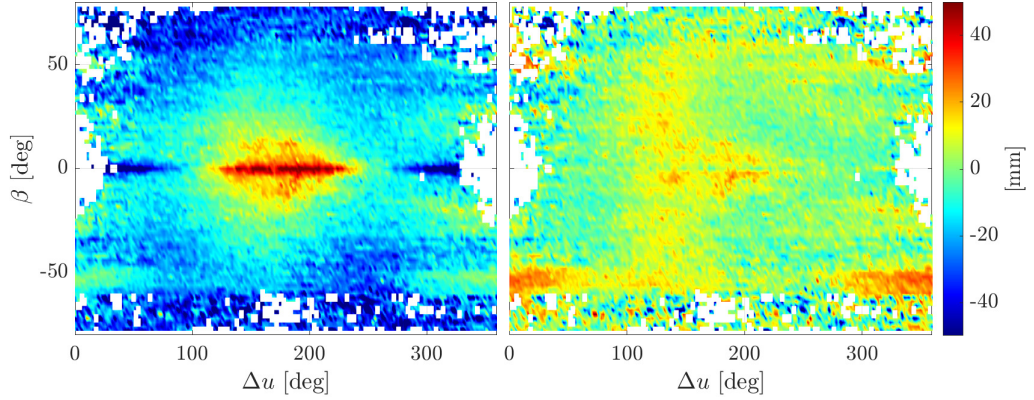


FIGURE 3.13: SLR residuals to Galileo satellites projected on a $\beta/\Delta u$ map. The residuals are averaged within a grid of $2^\circ \times 2^\circ$ cells. The left panel is associated to the Galileo solutions using the in-house SRP model, whereas the right panel corresponds to the solutions using the Galileo satellite metadata

3.8 SLR-based evidence of second-order relativistic effect on Galileo clocks

The right panel in Fig. 3.13 still hints a dependency on Δu , which is more visible in Fig. 3.14, where we show the signature that results from averaging the Galileo SLR residuals within a 2° -partition of Δu (label “SLR”). Superimposed to this signature, it is also displayed the averaged (within the same partition) residuals of the detrended Galileo clock corrections interpolated at the epochs of the SLR observations (label “CLK”). The relativistic clock correction (3.18) only accounts for the first term of the geopotential and can be extended to also account for the influence of the Earth’s oblateness by adding (Beard and Senior, 2017)

$$\Delta\tau^s = \frac{3}{2} \frac{R^2}{a^2 c^2} C_{20} \sqrt{GMa} \sin^2 i \sin^2 2u \quad (3.45)$$

where we attach to the notation of chapter 1 for the orbital elements and remaining constants. Once the correction (3.45) is applied to the Galileo clock corrections (not IGS standard), we recover the pattern labeled as “CLK_rel” in Fig. 3.14. Under the assumption that systematic effects are averaged out, only orbital radial errors (measured by the SLR observations) are mapped into the clock estimates. Hence, the remarkable correlation between the SLR and CLK_rel signatures (correlation index of 0.88, contrasting with a moderate 0.50 index between SLR and CLK) is a SLR-based observational test for general relativity (other recent studies, such as Kouba, 2021 and Formichella et al., 2021, are based solely on the inspection of Galileo clock corrections).

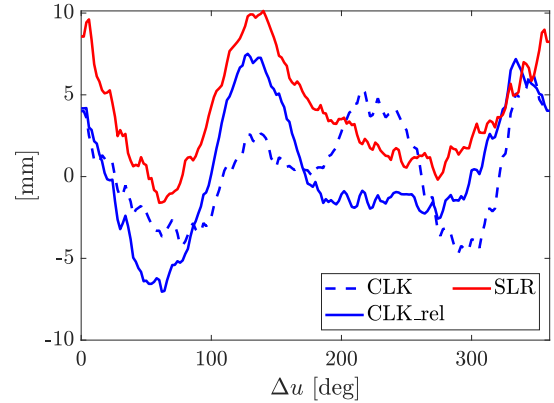


FIGURE 3.14: Galileo SLR residuals (label “SLR”) and residuals of the detrended Galileo clock estimates (“CLK”). The solution “CLK_rel” depicts the clock residuals after removing the relativistic correction (3.45)

The specific Δu -projection of the detrended clock residuals, after accounting for (3.45), can be used as a figure of merit to validate newer procedures. In particular, it becomes self-evident that the assimilation of SLR observations during the GNSS processing would have a positive impact in such a figure (Bury et al., 2021 already pointed out an improvement in the LOD estimation). The use of new models and parameterizations should be, however, the preferred option, so that the SLR observations can still be employed for independent validation. Because of the high performance of the PHM clock of Galileo (Rochat et al., 2005), some authors have proposed a stochastic model for the Galileo clock corrections based on a relative constraining of the parameters (Hackel et al., 2015, Qing et al., 2017), which is technically possible in our UD processing schemes. Since this constraining acts upon the high-frequency clock variations, we consider more interesting to apply restrictions on those frequencies proportional to the satellite orbital periods in order to uncouple orbit parameters from clock corrections. There was an attempt to implement such a concept within this dissertation. However, no conclusive results were obtained, since the clock corrections also account for other physical (unmodeled) effects that occur with orbital periodicities, such as the thermal response of the clock or attitude mismodeling (Montenbruck et al., 2012).

3.9 Summary

The main aspects of the processing of GNSS observations for geodetic applications have been presented in this chapter. We started with an introduction of the GNSS constellations used in the scope of this work, namely, GPS, Galileo and GLONASS. Here we gave a general discussion on the orbital geometries and transferred signals.

Later on, the model for the GNSS code and phase observations was addressed, with emphasis on the IF and HMW linear combinations, which are the primary observable types used to derive our GNSS solutions. Although without deep detail, every constituent of the GNSS observation model was discussed or referred to, as well as the parameterization employed to reduce the observations. We paid special attention to the involved rank defects, mainly associated to the code and phase biases, since their handling redefines the meaning of the parameters and thus have conceptual and, more importantly, practical consequences. For instance, they define the time scale of the resulting clock product or the integerness of the estimated ambiguities.

The overall view of the implemented processing schemes was also described in general terms, where we distinguished between different stages: Preprocessing, computation of geodetic solution and AR. Each stage comprises several steps, which are mostly executed by the BSW tools. For later cross-reference, we give a comprehensive compilation of the general aspects of our processing strategy in [appendix A](#).

The performance of the newly generated UD-based products was evaluated by means of comparisons against two independent DD-based solutions, one of which derives from a controlled test case where the same network, screening and parameterization as for the UD processing scheme were preserved, whereas the other comes from the official CODE MGEX production line. The findings show that the UD-based solution is at a competitive level, with STD statistics of SIS range comparisons at the level of 6-7 ps for GPS and Galileo and 70 ps for GLONASS. The (3D) RMS of the orbit comparisons, on the other hand, are in the order of 1.5-2 cm for GPS and Galileo and 5 cm for GLONASS. The GPS and Galileo UD-based solutions are apparently superior in internal consistency, measured as orbit midnight misclosures,

with averaged statistics at the level of 6.9 and 7.4 mm for GPS and Galileo, respectively. Conversely, this figure is slightly worse for the GLONASS UD-based solutions (16.8 mm) than for the CODE MGEX products (15.0 mm), presumably due to the lack of GLONASS AR in our processing schemes.

We made an exercise to evaluate the performance of the recently realized ITRF2020. GNSS solutions referred to both ITRF2014 and ITRF2020 were generated and the resulting station coordinates compared against the corresponding regularized positions. For the processed time interval, the solutions associated to the ITRF2020 frame render better in terms of RMS and stability of the estimated Helmert parameters. On the other hand, another exercise was undertaken to assess the use of the Galileo metadata in SRP modeling. A positive impact was observed in the estimated ECOM2 parameters, which reduce their dependency on the β angle, as well as on the systematics that are visible in a $\beta/\Delta u$ -mapping of the SLR residuals. Incidentally, as the clock corrections are prone to compensate radial errors, the comparison between clock and SLR residuals revealed the influence that the C_{20} geopotential coefficient has on the Galileo clocks according to the general relativity theory.

Global GNSS ambiguity resolution for undifferenced processing

4.1 Introduction

To resolve the carrier phase ambiguities of the GNSS observation model (3.1), or, equivalently, (3.5, 3.6), to their integer values is referred to as ambiguity resolution (abbreviated in this document as AR). From the parameter estimation perspective, AR largely reduces the amount of unknown parameters (the ambiguity terms represent a third of all the parameters involved in our problem in accord with table 3.4), hence increasing the strength of the geodetic solutions. In addition, since those ambiguity terms are the only parameters mutually depending on both stations and satellites, we can intuitively think that AR separates the network from the satellite side. In practice, this implies that applications based on stand-alone receivers (e.g., PPP) can attain network performance if the ambiguities are resolved as integer numbers (altogether, PPP-AR).

Despite AR has become a mature research topic supported by its own underpinning mathematical formalism (e.g., Teunissen, 2017b), different processing strategies count with different AR algorithms. These algorithms have to cope, in an efficient manner, with the high computational burdens that AR demands, especially when the amount of ambiguity parameters is sizable (as for global GNSS network solutions). Moreover, the performance of the same AR implementation can be degraded under different processing conditions. This was observed for the AR strategy employed in the CODE UD-based procedure that generates integer-cycle-conform clock products (Schaer et al., 2021). While such a strategy properly works when the algorithm is fed with GNSS orbits already compatible with AR (retrieved from a DD-based production line¹), its performance is not satisfactory if we use instead preliminary GNSS orbits based on real-valued ambiguities (first iteration in our UD-based processing strategy, Fig. 3.5). Therefore, we carried out some investigations to figure out the origin of such underperformance. The findings yielded a novel AR algorithm, which is the subject of the present chapter.

Besides CODE, various GNSS research groups have developed strategies relying on the availability of a priori geometry solutions compatible with AR (typically derived from a DD-based processing) to estimate satellite clock corrections in a dedicated UD-based processing (Geng et al., 2012, Duan et al., 2021). Other approaches, on the other hand, estimate the different contributions of the GNSS observation model within a single UD-based processing (Loyer et al., 2012, Strasser et al., 2019). Whereas the former strategies easily unveil (at station level) the integer nature of the

¹More precisely, in addition to GNSS orbits, station coordinates, troposphere delays and ERP are also retrieved from the DD-based production line.

ambiguities after calibrating phase biases at the cost of a two-fold processing scheme, the latter ones are challenged by a more complex AR stage, which must address potential errors, primarily related to the orbits, absorbed by the real-valued ambiguities, as well as confront a prohibitive computational burden for large networks due to the huge amount of ambiguity parameters. Aiming at taking the greatest advantage of both approaches, we have developed an AR strategy for UD-based processing that overcomes the restriction associated to the network size based on the inspection of real-valued ambiguities, which ultimately turns the preliminary orbit and clock solutions into integer-cycle-conform solutions that enable AR in an inexpensive station-wise parallelization.

Ge et al., 2005 integrate the DD-AR information into an UD-based processing scheme by using the resolved DD ambiguities as tight constraints in the LS adjustment, which is still computationally expensive for large networks. Likewise, similar to our approach, some authors have explored methods based on real-valued ambiguity inspection (Ge et al., 2008, Laurichesse et al., 2009). However, we address the problem from a different perspective that poses a new framework, enhancing the robustness.

From the many research groups active in this field, a number of integer-cycle-conform products are available that are actually equivalent under certain transformations, as proven by Teunissen and Khodabandeh, 2015. The authors also emphasize the essential idea stemming from (3.40), i.e., resolved UD ambiguities become DD ambiguities after properly handling the rank defects of the GNSS observation model. In the frame of this work, we use the integer-recovery clock (IRC) model presented in Laurichesse et al., 2009 and Loyer et al., 2012, which is in analogy to the decoupled satellite clock (DSC) model (Collins, 2008 and Collins et al., 2008). The IRC model is characterized by lumping together clock corrections and NL phase biases.

We avoid AR for GLONASS due to the difficulties arising from the FDMA technique. Despite the phase biases are supposed to be frequency-independent (Sleewaegen et al., 2012), there exist, however, an apparent dependency because the ambiguity parameters are multiplied by different wavelengths for each satellite, and because the code biases leak into the phase observations when coping with the rank defects of the observation model (3.25, 3.26, 3.31, 3.32). Therefore, the phase biases have to be accounted for either by using linear functions of the frequency (Chuang et al., 2013), or by resolving triple-difference ambiguities, rather than DD ones (Banville et al., 2013). Recent studies also show how to build more general integer-estimable functions for the GLONASS ambiguities (Teunissen, 2019, Teunissen and Khodabandeh, 2019). Other researchers tackle the problem using only IF phase observations, which is feasible by redefining the wavelength in such a way that the GLONASS IF ambiguities become integer numbers by construction (Banville, 2016). Finally, we shall note that the GLONASS AR approach that the BSW implements is oriented to the processing of baseline observations and makes some delicate assumptions on the magnitude of the ambiguities that are difficult to implement when processing UD observations (Habrich, 2000).

In this chapter, some theoretical notions of AR are given in section 4.2. Later, we discuss our implemented AR strategy (section 4.3) and describe the algorithm that inspects the real-valued ambiguities (section 4.4). Afterwards, the metrics used to evaluate the quality of the AR solutions are described together with some interesting technical aspects emerging from practical implementations (sections 4.5 and 4.6, respectively). A final section is dedicated to the summary.

The main ideas of this chapter can also be found in Calero-Rodríguez et al., 2023a.

4.2 Theoretical framework

A mixed-integer model is characterized by both real and integer parameters, i.e.,

$$E[\mathbf{y}] = \mathbf{A}\mathbf{a} + \mathbf{B}\mathbf{b}, \quad D[\mathbf{y}] = \boldsymbol{\Sigma}_{yy} \quad (4.1)$$

with $a_{(i)} \in \mathbb{Z}$ and $b_{(j)} \in \mathbb{R}$ (for every i and j components of \mathbf{a} and \mathbf{b} , respectively). The GNSS model (3.1, 3.2), or (3.4-3.6), qualifies as such due to the carrier phase ambiguities. To cope with (4.1), we first compute a real-valued estimate for \mathbf{a} (ambiguity vector) by using the LS principle, namely, $\hat{\mathbf{a}}$ with covariance $\boldsymbol{\Sigma}_{\hat{\mathbf{a}}\hat{\mathbf{a}}}$, which must later be mapped into a vector composed by integer numbers, i.e., $\check{\mathbf{a}}$, in such a way that the quantity

$$(\check{\mathbf{a}} - \hat{\mathbf{a}})^\top \boldsymbol{\Sigma}_{\hat{\mathbf{a}}\hat{\mathbf{a}}}^{-1} (\check{\mathbf{a}} - \hat{\mathbf{a}}) \quad (4.2)$$

is minimized (recall discussion in section 2.4). The optimization problem arising from (4.2) is known as integer least-squares (ILS) and the underlying theory is compiled in Teunissen, 2017b. In essence, ILS is solved by a search algorithm, whose efficiency decays exponentially with an increasing size of \mathbf{a} . If $\boldsymbol{\Sigma}_{\hat{\mathbf{a}}\hat{\mathbf{a}}}$ is diagonal, the solution can, however, be trivially computed as $\check{\mathbf{a}} = \lfloor \hat{\mathbf{a}} \rfloor$ (the rounding operation is denoted by $\lfloor \cdot \rfloor$). Therefore, it is preferred to solve the ILS problem in a nearly decorrelated space after applying a Z-transformation (Teunissen, 1995)

$$\check{\mathbf{z}} = \mathbf{Z}\check{\mathbf{a}}, \quad \hat{\mathbf{z}} = \mathbf{Z}\hat{\mathbf{a}}, \quad \boldsymbol{\Sigma}_{\check{\mathbf{z}}\check{\mathbf{z}}} = \mathbf{Z}\boldsymbol{\Sigma}_{\hat{\mathbf{a}}\hat{\mathbf{a}}}\mathbf{Z}^\top \quad (4.3)$$

for which (4.2) becomes

$$(\check{\mathbf{z}} - \hat{\mathbf{z}})^\top \boldsymbol{\Sigma}_{\check{\mathbf{z}}\check{\mathbf{z}}}^{-1} (\check{\mathbf{z}} - \hat{\mathbf{z}}) \quad (4.4)$$

A proper Z-transformation requires the components of \mathbf{Z} to be integer numbers and $|\det(\mathbf{Z})| = 1$, so that any integer vector \mathbf{a} maps into an integer vector \mathbf{z} and vice versa. Under these conditions, the idea behind such transformations is to find the \mathbf{Z} matrix that makes $\boldsymbol{\Sigma}_{\check{\mathbf{z}}\check{\mathbf{z}}}$ “as diagonal as possible” with the variances sorted in descending order. Indeed, the most widespread algorithm for ILS in the GNSS community, i.e., the least-squares ambiguity decorrelation adjustment (LAMBDA, Teunissen, 1995), makes extensive use of this transformation. An efficient version of LAMBDA can be implemented from the algorithms given by Chang et al., 2005.

Because of the huge amount of ambiguities when processing a dense network of GNSS stations (table 3.4), it is unfeasible to face our AR problem exclusively using a search algorithm. Consequently, other integer estimators, namely, integer rounding and integer bootstrapping, can be more appropriate options from the computational point of view. As its name suggests, integer rounding consists in rounding off the real-valued ambiguities to the nearest integers. On the other hand, integer bootstrapping resolves the ambiguities to integers one-by-one according to their formal errors: The ambiguity with the lowest error is rounded off and plugged into the NEQ so that the remaining ambiguities can be updated and resolved in subsequent iterations. The process finishes when there are no more ambiguities left. Note that both integer rounding and integer bootstrapping can implement some mechanisms to increase their robustness. For instance, resolving only those ambiguities whose fractional parts are below a certain threshold. Likewise, it is also beneficial to apply a Z-transformation prior to resolving the ambiguities with either integer estimator.

The BSW implements integer rounding, integer bootstrapping (referred to as SIGMA algorithm) and its own search algorithm (other than LAMBDA; Dach et al., 2015, section 8.3).

4.3 AR strategy based on HMW/IF observations

The AR stage implemented in our UD-based processing strategy (last block in Fig. 3.5) tries to resolve between-satellite ambiguities (i.e., single-differences per station are generated from the estimated UD ambiguities) in a two-fold procedure:

- The WL phase biases are calibrated by inspecting the fractional parts of the real-valued WL ambiguities. Those biases are later removed from the HMW observations (3.6), allowing to resolve the WL ambiguities to their integer values station-by-station using the bootstrapping integer estimator (BSW SIGMA with maximum allowed fractional part for resolvable ambiguities of 0.3 WL cycles).
- The previously resolved WL ambiguities are removed from the IF observations (3.5) and the fractional parts of the real-valued NL ambiguities are inspected to derive NL phase biases as well as other corrections. Once these biases and corrections are removed from the IF observations, we unveil the integer nature of the NL ambiguities, which are again resolved station-by-station using a bootstrapping integer estimator (BSW SIGMA with maximum allowed fractional part for resolvable ambiguities of 0.12 NL cycles). Note that we shall disregard those NL ambiguities associated with unresolved WL ambiguities, i.e., they must be estimated as real-valued numbers and cannot be used for the inspection algorithm.

Resolving ambiguities station-by-station is nothing but PPP-AR, for which integer-cycle-conform products (orbits, clock corrections and phase biases) are necessary. Because of this, the inspection of the ambiguities in the preceding steps (and the corrections thereof) is the most important and delicate part of our AR strategy, since it conceptually assumes the role of global AR.

As noted by (3.43), when the ambiguities are not resolved, their estimated real values absorb the phase biases. Conversely, if the ambiguities are resolved as integer numbers, the phase biases have to be accounted for. Since we resolve between-satellite ambiguities instead of UD ones, at least one reference real-valued ambiguity parameter per station has to be estimated, being lumped with $\delta_{r,(.)}$. Although for the HMW observations we explicitly account for the satellite phase biases (i.e., the δ_{WL}^s terms are calibrated when resolving the ambiguities), we treat the NL phase biases in a dissimilar fashion. The δ_{NL}^s parameters have a magnitude in the order of the NL wavelength (~ 10 cm from table 3.3) because of its own construction: The code observations weakly constrain the ambiguities, which, in turn, align phase and code measurements at a certain level. If they were absorbed by the satellite clock corrections, the code observations would be distorted by the same amount, which would be scarcely sensed due to their precision, leaving the remaining parameters unaltered. This is the basis for the IRC model, which lumps NL phase biases and clock corrections together (Laurichesse et al., 2009), also experimentally confirmed in Schaer et al., 2021. The final consequence is that the NL phase biases are implicitly accounted for (i.e., they are neither estimated nor calibrated, but compensated by the satellite clock corrections).

4.4 Inspection of real-valued ambiguities

As can be seen from the lower panel of Fig. 3.9, the agreement between integer-cycle-conform products (GPS and Galileo) is excellent, reaching consistencies below 10 ps in STD for the between-satellite SIS range differences. However, when we compared

for the first time our preliminary UD-based solution (i.e., unresolved ambiguities; second block, first iteration in Fig. 3.5) against the CODE Final (integer-cycle-conform) products we observed a much worse performance, at a level comparable with the GLONASS figures. In particular, the blue line in Fig. 4.1 shows such a comparison for the between-satellite pair G26/G29 on 2021/050 (the horizontal axis denotes the epoch number, stretching from 1 to 288 for daily sessions with 5-minute sampling). Far from a stability of 10 ps (0.03 NL cycles), the preliminary products may exhibit a drift with deviations larger than 1 NL cycle in the course of one day, which precludes station-wise AR. Superimposed to this curve, the red lines indicate the real-valued between-satellite ambiguities associated to the UD-based solution (resulting from third block, first iteration in Fig. 3.5), which have been shifted by integer jumps to better accommodate the clock comparison. Typically, each red line corresponds to different passes and different stations. As can be seen, there is a clear correlation between the ambiguities and the SIS range differences. This hints that, by inspecting the unresolved ambiguities, we can derive corrections to remove the drift of the preliminary products in order to make them consistent with global AR. The goal of this section is to define a systematic and rigorous way to accomplish this objective.

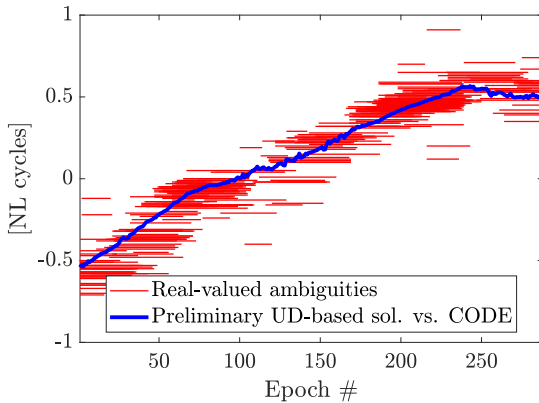


FIGURE 4.1: Between-satellite (G26/G29) SIS range comparison between the preliminary UD-based solution and the CODE Final products on 2021/050

Since the HMW observations (3.6) are GF and IF, the inspection of WL ambiguities is a moderate effort exercise. To omit redundancy in the following subsections, we thus focus only on the NL ambiguities to explain the implemented algorithm, with a final note (section 4.4.4) on how to adapt such an algorithm for WL AR.

It is worth pointing out that, although Fig. 4.1 illustrates the coupling between ambiguities and satellite-dependent parameters, some coupling could also originate on the receiver side. This mechanism is inferred in Montenbruck et al., 2018a, where the unresolved ambiguities are shown to trace signatures with a period equal to the orbital period of the LEO Sentinel-3A altimetry satellite, which is equipped with a geodetic GNSS receiver.

geodetic GNSS receiver.

4.4.1 Ambiguity parameterization

To mathematically quantify the coupling between the different parameters of the IF phase observation model (3.5)², let us start writing its linearized O-C version (with removed WL ambiguities) for the between-satellite pair s_1/s_2 in units of NL cycles:

$$L_r^{s_1 s_2} = (\mathbf{e}_r^{s_1} \cdot \mathbf{x}^{s_1} - \mathbf{e}_r^{s_2} \cdot \mathbf{x}^{s_2}) - (\tau^{s_1} - \tau^{s_2}) + (\delta^{s_1} - \delta^{s_2}) + T_r^{s_1 s_2} + \mathbf{e}_r^{s_1 s_2} \cdot \mathbf{x}_r + N_r^{s_1 s_2} \quad (4.5)$$

²Technically, what we need is nothing but the covariance matrix associated to the ambiguity parameters. However, since we fix satellite orbits and clock corrections when retrieving them (section 3.4), the resulting covariance information is overoptimistic.

where $(\cdot)_r^{s_1 s_2} := (\cdot)^{s_1} - (\cdot)^{s_2}$, e_r^s stands for the LOS pointing from station r to satellite s , and \mathbf{x}^s and \mathbf{x}_r are corrections over the a priori orbit and station coordinates, respectively. Note that the subscript NL has been dropped to alleviate the notation. This observation can be reconstructed using either the preliminary (PRE) estimates or the integer-cycle-conform (ICC) estimates, and, therefore, the following equality holds within the noise of the phase observations:

$$\begin{aligned} & [(\mathbf{e}_r^{s_1} \cdot \mathbf{x}^{s_1} - \mathbf{e}_r^{s_2} \cdot \mathbf{x}^{s_2}) - (\tau^{s_1} - \tau^{s_2}) + T_r^{s_1 s_2} + \mathbf{e}_r^{s_1 s_2} \cdot \mathbf{x}_r + B_r^{s_1 s_2}]_{\text{PRE}} = \\ & [(\mathbf{e}_r^{s_1} \cdot \mathbf{x}^{s_1} - \mathbf{e}_r^{s_2} \cdot \mathbf{x}^{s_2}) - (\tau^{s_1} - \tau^{s_2}) + (\delta^{s_1} - \delta^{s_2}) + T_r^{s_1 s_2} + \mathbf{e}_r^{s_1 s_2} \cdot \mathbf{x}_r + N_r^{s_1 s_2}]_{\text{ICC}} \end{aligned} \quad (4.6)$$

We have defined, in accord with (3.43), $N_r^{s_1 s_2} + \delta^{s_1} - \delta^{s_2} \rightarrow B_r^{s_1 s_2}$. Regrouping terms, it yields

$$\begin{aligned} B_r^{s_1 s_2} - N_r^{s_1 s_2} = \Delta N_r^{s_1 s_2} = \\ (\mathbf{e}_r^{s_1} \cdot \Delta \mathbf{x}^{s_1} - \mathbf{e}_r^{s_2} \cdot \Delta \mathbf{x}^{s_2}) - (\Delta \tau^{s_1} - \Delta \tau^{s_2}) + \Delta T_r^{s_1 s_2} + \mathbf{e}_r^{s_1 s_2} \cdot \Delta \mathbf{x}_r + (\delta^{s_1} - \delta^{s_2}) \end{aligned} \quad (4.7)$$

where Δ represents the difference between the ICC and PRE realizations of the corresponding parameter (opposite sign convention for $\Delta N_r^{s_1 s_2}$).

In the following we use the $\Delta N_r^{s_1 s_2}$ quantities as ‘‘observations’’ in a subsequent LS adjustment where the right-hand side terms are estimated as corrections for the preliminary solution. A direct implementation is, however, impossible since these observations are the (known) real-valued between-satellite ambiguities shifted by an unknown number of NL cycles. To overcome this issue, we may form ambiguity clusters. As will be detailed in the next section, their main outcome is the redefinition of the $\Delta N_r^{s_1 s_2}$ terms in such a way that they are not individually shifted, but the shift is common for a set of observations. This is, $\Delta N_r^{s_1 s_2} \rightarrow \Delta N_r^{s_1 s_2} - B_\alpha^{s_1 s_2}$, where the new realization of $\Delta N_r^{s_1 s_2}$ is unambiguously known and $B_\alpha^{s_1 s_2}$ is an unknown shift unique for every cluster (Greek letters, in this case α , designates ambiguity clusters). The unknown shifts, referred to as cluster biases, can be initially interpreted as between-satellite ambiguities and will be estimated as part of the LS adjustment.

The model (4.7) is further simplified with:

- We address the ambiguity resolution problem from a global point of view, neglecting the receiver-dependent parameters (i.e., $\Delta T_r^{s_1 s_2}$ and $\Delta \mathbf{x}_r$).
- The time-dependent orbit and clock corrections ($\Delta \mathbf{x}^s$ and $\Delta \tau^s$, respectively) are averaged over the time interval stretched by the observations $\Delta N_r^{s_1 s_2}$.
- The orbit and clock corrections are characterized by a sum of polynomials, whose coefficients are the sought parameters. In our nominal set-up, we use 9th-degree polynomials (i.e., 10 coefficients) for each orbital component (radial, cross- and along-track) and the clock-like corrections (deeper discussion in section 4.6.2).

Altogether, the simplified model eventually reads as

$$\Delta N_r^{s_1 s_2} = \left(\overline{\mathbf{e}_r^{s_1} \cdot \Delta \mathbf{x}^{s_1}} - \overline{\mathbf{e}_r^{s_2} \cdot \Delta \mathbf{x}^{s_2}} \right) - \left(\overline{\Delta \tau^{s_1}} - \overline{\Delta \tau^{s_2}} \right) + B_\alpha^{s_1 s_2} \quad (4.8)$$

The horizontal upper bars indicate temporal average of the corresponding contribution. In this equation, the phase biases are absorbed by the clock corrections, which require a dedicated datum (we apply a zero-mean condition over the satellites per clock coefficient) to give access to the ‘‘absolute’’ satellite-specific information.

There is another rank defect between cluster biases and clock corrections that can be overcome by fixing $n - 1$ (with n equal to the number of satellites) $B_\alpha^{s_1 s_2}$ parameters to zero, implying that they can now be interpreted as DD ambiguities and, as such, should converge to integer numbers. On the other hand, the radial component of the orbit corrections should be loosely constrained to mitigate the numerical instability resulting from their high correlation with the clock corrections.

The model (4.8) can be understood as a kinematic approach that refines satellite orbits and clock corrections without requiring any a priori model. However, Δx^s and $\Delta \tau^s$ compensate general error sources, and, hence, do not have a real physical interpretation. The only important aspect for a successful station-wise AR in our processing is that, when those corrections are applied over the preliminary solution (final block in Fig. 3.5), it eventually resembles an integer-cycle-conform solution.

One between-satellite observation, $\Delta N_r^{s_1 s_2}$, is obtained from two overlapping UD real-valued ambiguities belonging to the same station, whose difference and common overlap represent, respectively, the observation value and the observation time interval. The between-satellite pairs s_1/s_2 are selected from the linearly independent combinations that maximize the overall coverage. Afterwards, in order to complement potentially poorly observed periods, additional between-satellite pairs are included following the same criterion. The new pairs are appended into the set of observations until a predefined redundancy level is satisfied, which is defined as the number of occurrences of one satellite in the set of between-satellite combinations. Since no correlations between observations are considered, the larger the level of redundancy, the better. However, an increasing number of observations would compromise the computational performance of the method. Therefore, as a trade-off solution, a redundancy level of four occurrences per satellite is assumed in the frame of this work.

Although no correlations are considered, specific variances are used to weight the observations. Being σ^{s_2} the variance associated to the UD ambiguity of satellite s for a particular station, and ΔT^s its temporal length, the variance for a between-satellite combination is defined as

$$\sigma^{s_1 s_2 2} = \frac{\Delta T^{s_1} \sigma^{s_1 2} + \Delta T^{s_2} \sigma^{s_2 2}}{\Delta T^{s_1 s_2}} \quad (4.9)$$

where $\Delta T^{s_1 s_2}$ represents the common tracked time for the satellites. Note that a rejection criterion could be considered as well for those observations stretching time intervals shorter than a user-defined length (1 hour in our case). Eventually, it has to be emphasized that the model (4.8) should be separately used for different GNSS systems (i.e., independent runs for GPS and Galileo) because of the inter-system biases.

4.4.2 Ambiguity clustering

Let us recover the definition of the observations from (4.7):

$$\Delta N_r^{s_1 s_2} = B_r^{s_1 s_2} - N_r^{s_1 s_2} \quad (4.10)$$

Without loss of generality, these observations can be initialized as the fractional part of the real-valued between-satellite ambiguities. Now, let us take two observations from two different stations and same satellite pair (i.e., $\Delta N_{r_1}^{s_1 s_2}$ and $\Delta N_{r_2}^{s_1 s_2}$), and let us focus on a specific property of the definition: If the DD ambiguity formed by them can be resolved to its correct integer number using integer rounding, then the

rounding operation shall return an exact zero, i.e.,

$$M = \lfloor \Delta N_{r_1}^{s_1 s_2} - \Delta N_{r_2}^{s_1 s_2} \rfloor = \lfloor B_{r_1}^{s_1 s_2} - B_{r_2}^{s_1 s_2} \rfloor - (N_{r_1}^{s_1 s_2} - N_{r_2}^{s_1 s_2}) = 0 \quad (4.11)$$

If this outcome is other than zero, either $\Delta N_{r_1}^{s_1 s_2}$ or $\Delta N_{r_2}^{s_1 s_2}$ has to be redefined accordingly, i.e.,

$$\Delta N_{r_1}^{s_1 s_2} + M \rightarrow \Delta N_{r_1}^{s_1 s_2} \quad (4.12)$$

After this redefinition, a two-ambiguity cluster has been created. Additionally, since it is only required to preserve the underlying DD ambiguity, any common shift (i.e., the cluster bias $B_{\alpha}^{s_1 s_2}$) applied over both observations represents a valid transformation. Of course, the more the number of between-satellite ambiguities per cluster, the better. This is achieved by combining clusters. To exemplify this idea, let us consider two ambiguity clusters, namely, α and β , each composed by three observations with the following numerical values:

$$\begin{aligned} \Delta N_{r_1 \alpha}^{s_1 s_2} &= 0.3 & \Delta N_{r_2 \alpha}^{s_1 s_2} &= 0.4 & \Delta N_{r_3 \alpha}^{s_1 s_2} &= 0.5 \\ \Delta N_{r_3 \beta}^{s_1 s_2} &= -0.5 & \Delta N_{r_4 \beta}^{s_1 s_2} &= -0.4 & \Delta N_{r_5 \beta}^{s_1 s_2} &= -0.3 \end{aligned} \quad (4.13)$$

It can be seen that the two clusters are overlapping, because each cluster contains its own realization of the observation $\Delta N_{r_3}^{s_1 s_2}$. This allows to merge them by properly shifting the ambiguities of, e.g., cluster β :

$$\Delta N_{(\cdot) \beta}^{s_1 s_2} + \left(\Delta N_{r_3 \alpha}^{s_1 s_2} - \Delta N_{r_3 \beta}^{s_1 s_2} \right) \rightarrow \Delta N_{(\cdot) \alpha}^{s_1 s_2} \quad (4.14)$$

leading to one single α cluster:

$$\begin{aligned} \Delta N_{r_1 \alpha}^{s_1 s_2} &= 0.3 & \Delta N_{r_2 \alpha}^{s_1 s_2} &= 0.4 & \Delta N_{r_3 \alpha}^{s_1 s_2} &= 0.5 \\ \Delta N_{r_4 \alpha}^{s_1 s_2} &= 0.6 & \Delta N_{r_5 \alpha}^{s_1 s_2} &= 0.7 \end{aligned} \quad (4.15)$$

Note that the combination of clusters results in a set of observations whose fractional parts are not necessarily bounded by -0.5 and 0.5 cycles.

Although we use the least reliable integer rounding estimator to create the ambiguity clusters according to the rules (4.11, 4.12), the experience with DD-based network solutions demonstrates that the error sources potentially absorbed by the ambiguity parameters partially vanish when forming regional baselines (Dach et al., 2015, section 8.5). In line with this, we can establish a robust AR criteria obeying three physical-driven principles:

- The absolute value of the fractional part associated to the DD ambiguity shall be lower than a predefined threshold (we use 0.1 cycles).
- The maximum baseline length between the stations involved in the DD ambiguity shall not exceed a predefined distance (we use 4000 km).
- The overlapping factor between the observations involved in the DD ambiguity shall not be lower than a predefined ratio (we use 0.5). This ratio is computed as the overlapping time over the total time span covered by both between-satellite ambiguities.

A basic cluster associated to a particular pivot observation can be defined as the cluster containing all those observations that, when double-differentiated w.r.t. the former one, satisfy the above AR criteria for a fixed between-satellite pair (the pivot observation is part of the basic cluster, too). The combination of these basic clusters, on the other hand, leads to globally applied ambiguity clusters, which can be systematically constructed by taking into account the following cluster inter-relations (Fig. 4.2):

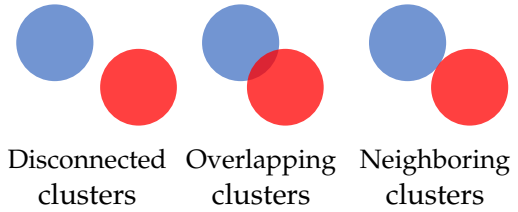


FIGURE 4.2: Abstract representation of cluster inter-relations

- We address those clusters as disconnected clusters if they are fully independent and, hence, one cluster bias needs to be estimated for each cluster.
- We address those clusters as overlapping clusters if they share at least one common observation. These clusters shall be combined.
- We address those clusters as neighboring clusters if at least one observation in cluster α is in the vicinity of at least one observation in cluster β . Such a vicinity occurs if those (at least) two observations fulfill the AR criteria. In which case, both clusters must be combined.

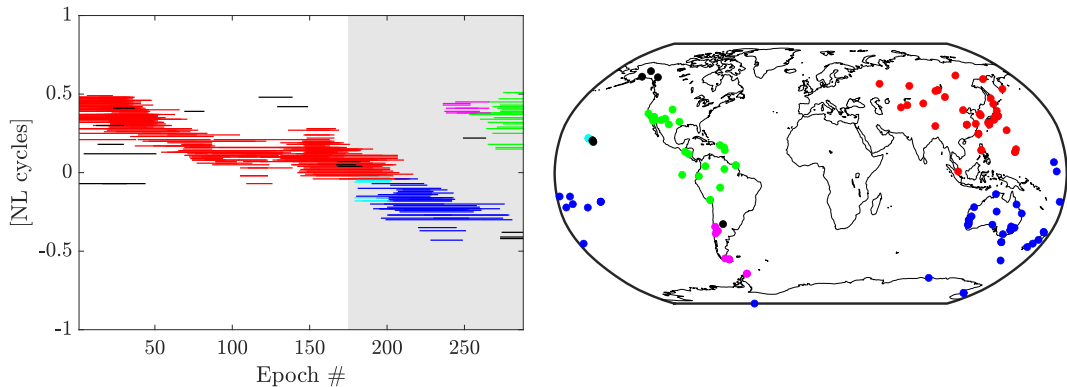


FIGURE 4.3: Between-satellite (G06/G17) ambiguity clusters on 2021/050. Each cluster is represented by a different color. The left panel displays the temporal distribution of the observations $\Delta N_r^{s_1 s_2}$ associated to each cluster. The right panel shows the corresponding tracking stations for the temporal period with gray background

Fig. 4.3 shows the temporal distribution (left panel) of some observations along with the geographical distribution for those with shaded background (right panel). The selected between-satellite pair is G06/G17 on 2021/050. As can be seen, these observations are grouped in several ambiguity clusters, which are represented by different colors. The generic black color has been designated for those containing five observations or fewer. A drift is observed, ranging up to one NL cycle once the pink and green clusters are dragged downwards, which is accomplished by the estimation of cluster biases in (4.8). It is interesting to note that each cluster is homogeneously spaced in different regions of the globe and isolated from the others. This is a consequence mainly (but not exclusively) induced by the maximum baseline length rule.

Loyer et al., 2012 and Strasser et al., 2019 define the ambiguity datum by fixing, in the most favorable case, the best observed independent ambiguities such that (3.38-3.40) holds. In the unlikely (but possible) case in which one ambiguity is individually biased, the underlying DD ambiguities will lose their integer nature, leading to an inconsistent AR stage. In contrast, the use of ambiguity clusters allows to use those $B_\alpha^{s_1 s_2}$ parameters performing best (e.g., in terms of ambiguity density, which, in turn, implies good DD-AR performance), minimizing the probability of those events to happen.

4.4.3 Mixed-integer model property

The model (4.8) features as a mixed-integer model, since $\Delta x_{(p)}^s, \Delta \tau^s \in \mathbb{R}$ and $B_\alpha^{s_1 s_2} \in \mathbb{Z}$ (where $\Delta x_{(p)}^s$ stands for the p -component of Δx^s). To make full profit of this property, it is convenient to use an integer estimator to map as integers the cluster biases determined as real numbers after a first LS adjustment.

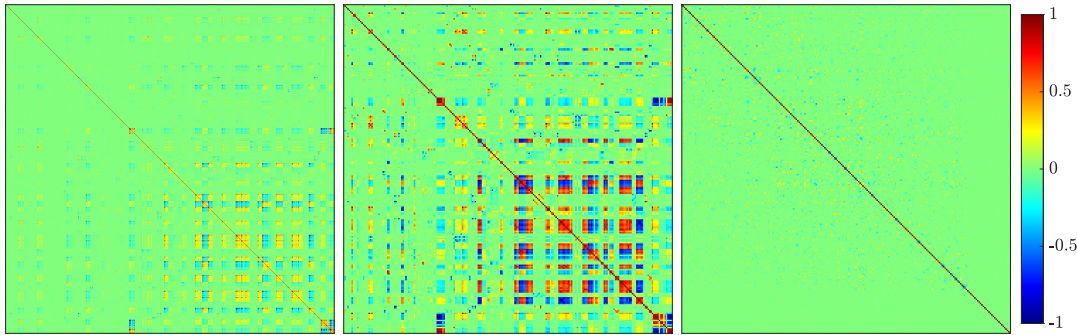


FIGURE 4.4: Correlations between $B_\alpha^{s_1 s_2}$ parameters. The left panel contains the entire set of parameters, whereas the middle and right panels contain only those related to densely populated ambiguity clusters (≥ 5 obs/clust) before and after applying a Z-transformation

The integer rounding estimator was initially tested with great success, except for a very few isolated cases, where some solutions were labeled as degraded after validation. This motivated to strive for a better estimator. Fig. 4.4 shows the correlations between the $B_\alpha^{s_1 s_2}$ parameters for a GPS run on 2021/050 from different views: The left-hand side figure depicts such correlations for the entire set of parameters, whereas the middle panel displays them only for relatively high densely populated clusters, i.e., clusters containing at least five observations. As shown, the correlations are not negligible and, thus, the integer rounding could benefit from applying a Z-transformation (right-hand side panel). Additionally, it illustrates that the majority of the correlations may be found on the set of dense clusters. Should it be small enough, then this set qualifies for ILS. Indeed, this is confirmed in table 4.1. This table contains the percentage of observations as well as the number of clusters which hold when discriminating them by their size (defined as observations per cluster, or, shorter, obs/clust) for a case study on 2021/050. If we do not consider clusters that are smaller than 5 obs/clust, a total of 233 and 204 $B_\alpha^{s_1 s_2}$ parameters remain, which is an affordable amount that LAMBDA may deal with for this problem, while retaining the 95% and 91% of the GPS and Galileo observations, respectively. All in all, the strategy to resolve the cluster biases is two-fold:

- For those cluster biases whose associated cluster size is larger or equal than a predefined value (we use 5 obs/clust), they are resolved using the LAMBDA algorithm.

TABLE 4.1: Accumulated percentage of observations and number of clusters for different cluster size levels on 2021/050

obs/clust	GPS		Galileo	
	% Obs.	# Clust.	% Obs.	# Clust.
≥ 75	83	116	58	48
≥ 15	93	184	86	134
≥ 5	95	233	91	204
≥ 3	96	289	94	278
≥ 2	97	411	95	368
≥ 1	100	1319	100	880

- The remaining cluster biases are recomputed to account for the ones previously resolved and, afterwards, they are rounded to the nearest integer as long as their fractional part is below a predefined threshold (we use 0.2 cycles). The process finishes when no more cluster biases can be resolved.

Table 4.1 also reflects a slow growing number of clusters as their size diminishes. Only the transition between the last two rows, i.e., from 2-observation lower bound for the cluster size, manifests a massive increment of about 300% for both GPS and Galileo. It can be presumed that this is caused by a number of non-integer B_{α}^{S1S2} parameters that are confined in their own single-observation clusters.

4.4.4 Inspection of WL ambiguities

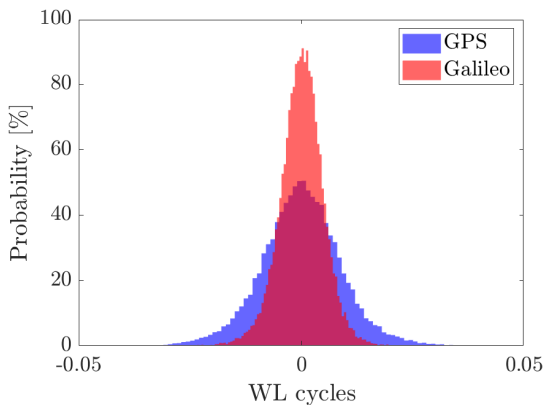


FIGURE 4.5: Histogram of the differences between WL phase biases derived with the developed tool and the CODE tool

We can parameterize the fractional parts of the WL ambiguities following the methodology of section 4.4.1. Due to the parametric simplicity of the HMW observation model (3.6), we find that the resulting observations (fractional parts of real-valued WL ambiguities) only depend on the WL phase biases and ambiguity clusters. Therefore, the same tools developed to inspect NL ambiguities can be used to inspect WL ambiguities by only setting-up zero-degree polynomials in the shape of clock-like corrections, which are identified with the sought WL phase biases. Although the criteria to generate the ambiguity clusters could also be simplified (relaxing,

e.g., the baseline length), we attach to the same configuration for simplicity.

As noted in the introduction of this chapter, the CODE UD-based procedure is fed with integer-cycle-conform information (essentially satellite orbits) coming from a DD-based processing. In this scenario, it was observed that the fractional parts of both WL and NL ambiguities can be represented by constant biases, namely, phase biases. Hence, a specific tool was developed to calibrate them. Such a tool is also based on the inspection of real-valued ambiguities, however, its robustness lies in the extensive use of the median estimator (Schaer et al., 2021), rather than in the use of ambiguity clustering. For the four-year period stretching from mid 2018 to mid 2022, we have estimated WL phase biases using both our tool and CODE's tool

under the same conditions (i.e., same observations and code biases). The results are compared and the histogram of the differences (after removing integer jumps) is shown in Fig. 4.5. We can see that both products are equivalent, since the differences are narrowed between -0.05 and 0.05 WL cycles. Interestingly, we can also see that the performance is better for Galileo (STD of 0.005 WL cycles) than for GPS (0.009).

4.5 Metrics for quality control

There is a direct connection between the overall AR performance and the number of resolved cluster biases. In fact, we define the AR rate as the percentage of observations (i.e., real-valued ambiguities) that belong to a cluster whose cluster bias has been resolved as integer. However, the unresolved cluster biases do not degrade the LS adjustment, since they are confined in their own single-ambiguity clusters (i.e., one $B_{\alpha}^{s_1 s_2}$ parameter and one $\Delta N_r^{s_1 s_2}$). We thus compute the LS residuals (ϵ) in a non-standard way:

$$\epsilon = \mathbf{y} - \mathbf{A}_x \mathbf{x}_x - \mathbf{A}_\tau \mathbf{x}_\tau - \mathbf{A}_B [\mathbf{x}_B] \quad (4.16)$$

where \mathbf{y} , \mathbf{x}_x , \mathbf{x}_τ and \mathbf{x}_B are the vectors containing the observations, the estimated orbit corrections, the estimated clock corrections, and the estimated cluster biases (including both unresolved and resolved ones), respectively. \mathbf{A}_x , \mathbf{A}_τ and \mathbf{A}_B are the corresponding parts of the design matrix. Since these residuals are actually between-satellite residuals, we generate satellite-specific errors at epoch t (e_t) as

$$e_t = \text{diag} \left(\left[\mathbf{D}_t^\top \boldsymbol{\Sigma}_t^{-1} \mathbf{D}_t \right] \right)^{1/2} \quad (4.17)$$

Here, the rows of the matrix \mathbf{D}_t contain the between-satellite differences of each s_1/s_2 pair participating at epoch t (with a final row including a zero-mean-like condition), and $\boldsymbol{\Sigma}_t$ is a covariance-like diagonal matrix whose k (diagonal) component is computed as (note that every different s_1/s_2 pair is mapped into one and the same k index)

$$d_k = N_r \frac{N_{t,max}}{N_t^{s_1/s_2}} \left(m_t^{s_1 s_2} [\epsilon]^2 + \text{IQR}_t^{s_1 s_2} [\epsilon]^2 \right) \quad (4.18)$$

with N_r , $N_r^{s_1 s_2}$ and $N_{t,max}$ being the user-defined redundancy level, the total number of s_1/s_2 observations at t , and the maximum number of observations for any s_1/s_2 pair at t , respectively. $m_t^{s_1 s_2} [\cdot]$ and $\text{IQR}_t^{s_1 s_2} [\cdot]$ are the median and inter-quartile range operators applied over all the elements belonging to the s_1/s_2 pair at t . This normalization of the residuals, yet empirically found, is very valuable to detect epoch- and satellite-dependent anomalous events.

The AR metrics described hitherto (i.e., AR rates, residuals and other specific errors) are derived as part of our real-valued ambiguity inspection procedure, which can be interpreted as global AR. Nonetheless, equivalent metrics stem from the subsequent station-by-station AR phase. In fact, these metrics give a more realistic view of the AR performance, since they are ultimately connected to the ambiguities actually resolved in the NEQ. Fig. 4.6 shows the time series of the AR metrics (AR rates and STD of ambiguity residuals) that we have derived from both steps, i.e., from the global procedure (left panels) and from the station-by-station AR phase (right panels). Since both AR steps are independent, there is not an exact correspondence between equivalent figures, specially for the NL metrics. Note that the AR rates for the NL ambiguities use the resolved WL ambiguities as reference.

We may note from Fig. 4.6 that:

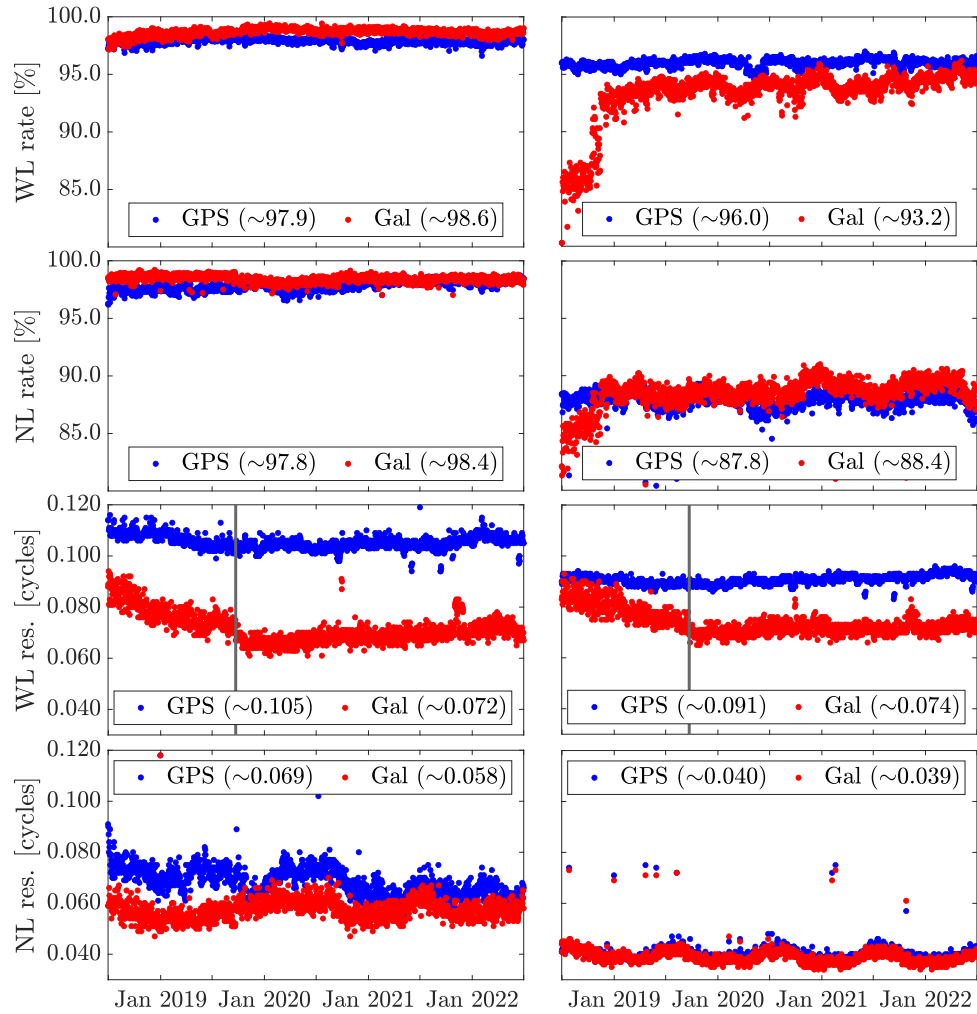


FIGURE 4.6: Time series of the AR metrics. The left panels correspond to the global AR phase, whereas the right panels to the subsequent station-wise AR phase

- The inclusion of new Galileo satellites in late 2018 (Fig. 3.1) has a very positive impact on the AR rates, which is specially noticeable in the station-by-station AR phase for both WL and NL ambiguities.
- The WL residuals are considerably poorer than the NL residuals. This is mainly due to the higher noise of the code observations, which are involved in the generation of the HMW observable. Moreover, errors coming from the calibrated code biases could also deteriorate this figure, or even the neglected PCO differences between code and phase observations (section 3.3.3).
- The WL residuals are significantly worse for GPS (~ 0.1 cycles) than for Galileo (~ 0.07 cycles), which is in line with Fig. 4.5. This fact very likely obeys to a superior quality for the Galileo code observations.
- At the beginning of the processing interval we can see higher values for the Galileo WL residuals, which might be related to wrong code bias information. Indeed, we did not account for the Galileo GF code bias information until 2019/265 (marked with vertical lines in the figures), which could lead to corrupted WL phase biases when data from stations with different tracking

schemes (commonly, C1C/C5Q and C1X/C5X) is assimilated. Nonetheless, since the Galileo signals transmitted at equal frequency bands contain similar code biases (Fig. 3.6), the overall impact is minor (no degradation is observed in the NL residuals).

- The general AR performance is outstanding, with AR residuals well below 0.1 cycles for the NL ambiguities, and AR rates around 90% after the station-wise AR phase.

4.6 Technical considerations

4.6.1 Integer-cycle-conform products for PPP-AR

Global parameters (particularly satellite orbits and clock corrections) are consistent with the integer-cycle property of the carrier phase ambiguities if they do not preserve any (between-satellite) signature that could induce arbitrary patterns on the receiver ambiguities, preventing PPP-AR applications. As a consequence, the drift observed in the real-valued ambiguities (Fig. 4.1) must eventually be compensated for as the global parameters are progressively updated in the processing loop (Fig. 3.5). This is confirmed in Fig. 4.7. In this figure, we show the temporal distribution of the estimated real-valued ambiguities (third block in Fig. 3.5) resulting from the first (left panels) and second (right panels) processing loop iterations for the Galileo satellite pair E11/E12 on 2021/069. During the second iteration, the satellite orbits and clock corrections already benefit from AR, becoming integer-cycle-conform products. Hence, as can be seen, the estimated real-valued between-satellite ambiguities tend to converge to integer numbers (zero fractional part due to the use of IRC model; otherwise, a constant bias would be observed), enabling PPP-AR (i.e., our station-wise AR phase).

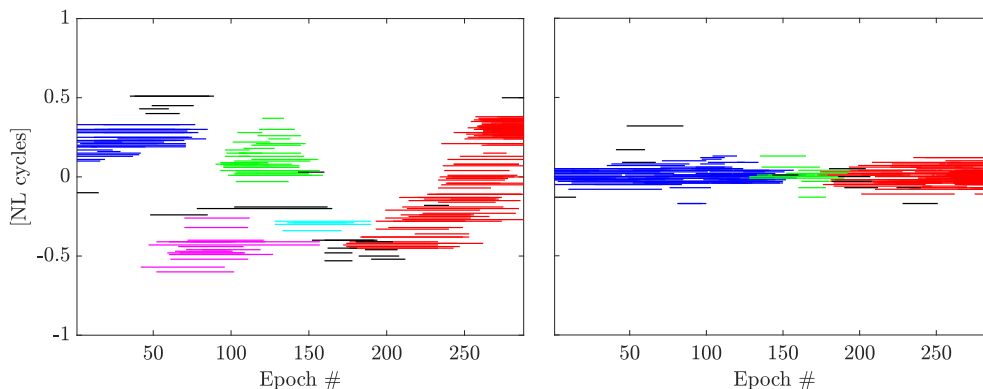


FIGURE 4.7: Temporal stability of E11/E12 real-valued ambiguities on 2021/069. The left and right panels correspond to the first and second processing loop iterations, respectively

Because of the distinct features that the real-valued ambiguities exhibit for the first and the second iterations, our ambiguity inspection procedure could benefit from independent customized setups. In particular, for the first iteration, we use 9th-degree polynomials to characterize both orbit and clock corrections (as stated in section 4.4.1). Likewise, only one constant coefficient is used to characterize the clock corrections during the second iteration, for which no orbit parameters are estimated (in line with the calibration of WL biases in section 4.4.4). The criteria for the generation of ambiguity clusters could also be different (e.g., relaxing the baseline

length limitation), but these criteria have remained the same in the frame of this work for simplicity.

4.6.2 Boundary effect

It has been noticed that the use of polynomials to approximate the orbit and clock corrections may cause a poor fit at the boundaries of the time interval. This problem is subject to the polynomial degree, becoming more evident for the higher degrees. A similar behavior originates from the polynomial interpolation problem, where convergence is not guaranteed as the number of nodes increases. This is also known as Runge's Phenomenon (Epperson, 1987).

In order to preserve the adaptability of a relatively high-degree polynomial without compromising the fitting at the boundaries, it has been empirically observed that constraining the first derivative to zero at the boundaries could partly mitigate such an effect. This is exemplified in Fig. 4.8 for the between-satellite pair E24/E31 on 2021/069. Here, the radial component of the solution (i.e., $\Delta\rho^{s_1s_2} - \Delta\tau^{s_1s_2}$, where $\Delta\rho^{s_1s_2}$ stands for the radial component of the orbit corrections) is generated from different polynomial degrees: 5th, 7th and 9th, including a version of the latter with boundary constraints. We see that the distribution of the observations (horizontal red lines) is very stable, implying that a 9th-degree polynomial overparameterizes the problem for this specific satellite pair. In fact, the 9th-degree solution exhibits some drifts at the boundaries, which are suppressed by its constrained counterpart, behaving similar to the lower degree solutions.

The boundary constraining implemented here is merely an artifice to ensure a good fit at the boundaries. However, other approaches may be better suited for this problem. Specifically, it would be interesting to employ a different parameterization to characterize the orbit- and clock-like corrections. For instance, instead of using polynomials, we could incorporate a bias, a drift, and sine and cosine functions with orbital periodicities.

4.6.3 Implications of orbit corrections

The use of orbit corrections to better inspect the real-valued ambiguities is one of the novelties of our procedure. It has been empirically observed that they really improve the reliability of the results, especially for the Galileo satellite system (probably due to its sparser constellation). Here the role of such corrections is exemplified with the between-satellite pair E11/E12 on 2021/069 (see the corresponding ambiguity cluster distribution on the left panel of Fig. 4.7). Two different solutions for this satellite pair are displayed in Fig. 4.9: We parameterize the real-valued ambiguities only with clock-like parameters for the left panel, whereas orbit- and clock-like parameters are considered for the solution on the right panel. For a fairer visualization, the averaged along- and cross-track orbit corrections (whose joint contribution is denoted by $\Delta\rho_{\perp r}^{s_1s_2}$) complement the corresponding background observations in the latter case. These

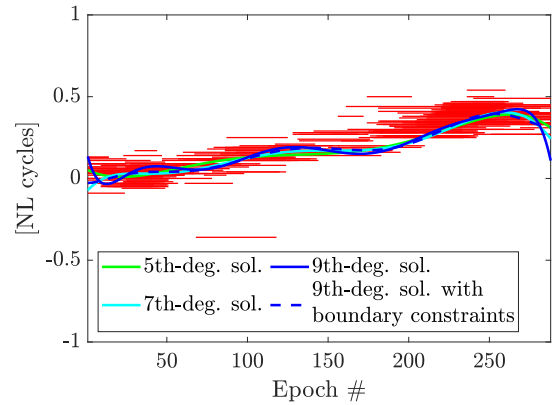


FIGURE 4.8: E24/E31 solutions characterized by different polynomial degrees

corrections may amount up to more than 2 NL cycles (20 cm), which project at the 2 cm level along the receiver-to-satellite line-of-sight. As can be seen, they manifest by shrinking the observations at the middle of the session. On the other hand, the strength of the left side solution is clearly debilitated by an apparent middle gap and a poorer fit of the observations.

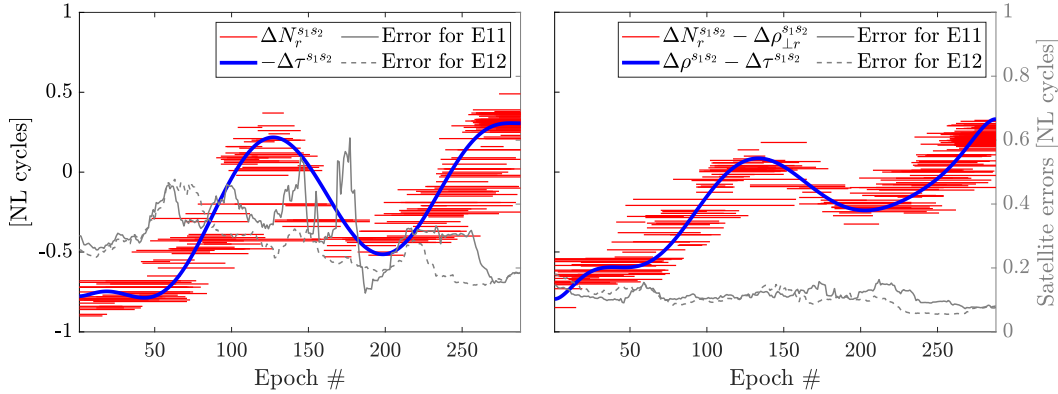


FIGURE 4.9: E11/E12 solutions on 2021/069. The one on the left-hand side uses a clock-only parameterization, whereas orbit and clock parameters are considered for the solution on the right panel

Incidentally, the corresponding epoch- and satellite-dependent errors as described by (4.16-4.18) are also displayed in the panels of Fig. 4.9 (right axis scale). They dramatically increase from about 0.15 to 0.4 NL cycles when no orbit parameters are considered, with the largest peak at the level of 0.6 NL cycles for the satellite E11. Altogether, we can state that the orbit-like parameters are statistically significant.

4.6.4 Phase jumps

In rare cases some satellites may undergo an apparent phase jump event that induces cycle slips during the preprocessing of the carrier phase measurements. It has been often, but not always, identified with unhealthy satellites. In principle, such an event should not be an issue, since it can be compensated by ambiguities and/or clock parameters.

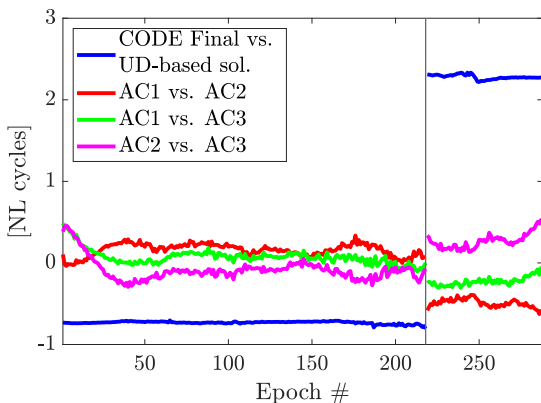


FIGURE 4.10: G01/G21 comparisons between independent AC solutions. A phase jump is commonly spotted at epoch number 218

On 2021/050, a phase jump occurs for satellite G21, illustrated in Fig. 4.10. This figure shows the between-satellite G01/G21 comparison of the newly generated UD-based solution against the CODE Final products as well as other cross-comparisons between three independent IGS ACs, which are included to confirm that this event is commonly observed at epoch number 218 (5-minute sampling; roughly 6 p.m. UTC). For these external ACs, the comparison represents a clock comparison, whereas we depict SIS range differences for our UD-based solution in order to highlight the good stability on both sides of the jump. In fact, if it is manually calibrated, the

overall stability becomes 0.02 NL cycles (or 7 ps) in STD. A more interesting point is that the jump amounts to 3 NL cycles, implying that the product still enables PPP-AR provided that such a discontinuity on the SIS range triggers a cycle slip on the station side. Nevertheless, it has to be pointed out that not every affected day exhibits integer jumps in the clock comparison. Further investigations are needed for a better understanding of this phenomenon.

Phase jumps could actually lead to inconsistencies in our AR procedure, since the cluster biases defining the datum are no longer valid for the entire session. One can argue that it is not a problem either: If one cycle slip is simultaneously detected by every station for a specific satellite, the datum is broken (the problem becomes singular) and a new parameter must unconditionally be fixed for the resulting interval. Unfortunately, any shortcoming in the cycle slip detection algorithm may translate into uncut isolated ambiguities, as shown in Fig. 4.11. It displays the ambiguity clusters

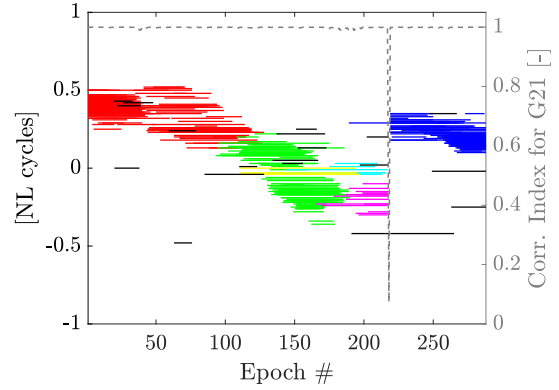


FIGURE 4.11: Correlation index example for satellite G21 on 2021/050

generated for the between-satellite pair G21/G22 on 2021/050, exemplifying that one ambiguity of the blue cluster bridges both sides of the jump. Therefore, to robustly detect these jumps, we propose the use of an inter-epoch correlation index. Let us consider the vectors \mathbf{v}_t^s and \mathbf{v}_{t+1}^s , both containing as many components as clusters overlapping epochs t and $t+1$ that include satellite s . Their components, $v_{t(\alpha)}^s$ and $v_{t+1(\alpha)}^s$, are equal to the number of observations in cluster α intersecting epochs t and $t+1$, respectively. Then, this correlation index is readily computed as

$$\frac{\mathbf{v}_t^s \cdot \mathbf{v}_{t+1}^s}{v_t^s v_{t+1}^s} \quad (4.19)$$

triggering a jump detection when it is below a user-defined threshold (e.g., 0.5). This index is also represented in Fig. 4.11 (right axis scale) for the case study.

Every time that a phase jump is detected, a new parameter (satellite-specific constant bias over the split interval) is added to our model (4.8) while a new cluster bias is accordingly fixed. The influence of this new parameter over those observations crossing the phase jump is proportional to their fraction lying on the new interval. The estimated phase jump is later combined with the corresponding clock corrections.

4.6.5 Diverging clock estimates

The SIS range comparisons are an excellent metric to evaluate the AR equivalence between independent products. In particular, we showed in Fig. 3.9 (bottom) that this metric is systematically well below 10 ps (3 mm) in STD when our UD-based solutions are compared against the CODE MGEX solutions. Therefore, processing the data of a stand-alone receiver would yield virtually the same results using either product to account for the satellite information (orbits and clock corrections).

During the computation of daily SIS range STD values for Fig. 3.9, we excluded certain satellite comparisons (potentially associated to degraded AR solutions) in order to produce representative statistics. In total, 892 out of 46322 comparisons

(1.9%) were excluded for GPS, and 121 out of 34517 (0.4%) for Galileo. Note that the rejection criterion is the satellite-specific STD being higher than three times the overall daily STD, which does not necessarily entail that the rejected solutions are degraded. Additionally, cross-comparisons against the CODE Final products often locate the potential problems on the MGEX side³. Therefore, the previous ratios are very likely upper bounds for the amount of degraded AR solutions in our UD-based processing. In any case, other GNSS research groups also report recurrent issues associated to their AR strategies (see discussion in Strasser, 2022, section 6.6.2). In particular, the CNES/CLS IGS AC provides an exhaustive list with the satellites omitted during AR⁴. In summary, the number of issues that we have identified in our processing remains within an acceptable margin.

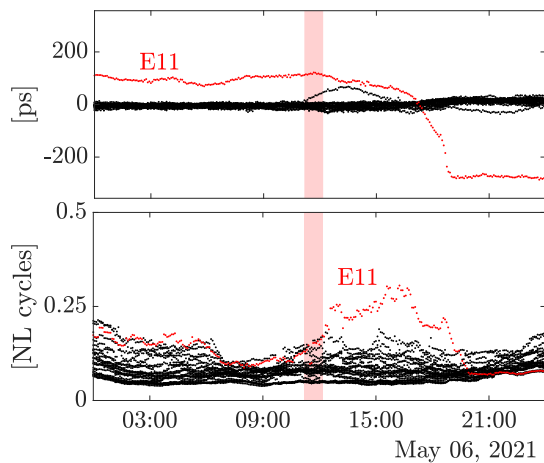


FIGURE 4.12: On top, detailed SIS range comparison (UD-based vs MGEX solutions), and, on bottom, AR errors from (4.16-4.18). E11 eclipse period pale-red shaded

As an example of degraded solution, we show epoch-by-epoch SIS range differences on the top panel of Fig. 4.12 for day 2021/126 (May 6, 2021). As can be seen, the satellite E11 (highlighted in red) exhibits suspicious variations that usually entail a damaged AR solution. This satellite experiences an eclipse period at noon on this day (pale-red shaded in the figure), which, according to Banville et al., 2020, may induce diverging clock estimates due to attitude mismodeling. Moreover, the AR satellite errors (4.17) are depicted on the lower panel of Fig. 4.12. They hint that, indeed, something probably went wrong with AR from the end of the eclipse to the lapse of the clock transition for this satellite.

4.6.6 Influence of the network size

To evaluate the robustness of our AR procedure, we have computed daily solutions on 2022/100 using three different set-ups for the size of the network: We generate a nominal solution (reference solution) with 280 stations, a more relaxed solution with 120 stations (this network size is used for the operational CODE Rapid products), and a test solution using only 30 stations (selected in such a way that global coverage is still attained) in order to assess the performance of our AR strategy under challenging conditions. Table 4.2 shows the orbit (3D) RMS comparisons as well as the STD of the SIS range differences that result from comparing the two latter set-ups with the nominal solution. For GPS and Galileo, we can see that the 120-station network produces virtually the same results as the nominal network. However, the comparisons, especially for the SIS range, blow when using the 30-station test network (30 #1 row), indicating a damaged AR phase. This is also inferred from the AR metrics. For nominal scenarios (i.e., 280- and 120-station network solutions), the RMS of the NL

³For the comparison between our UD-based solutions and the CODE Final products, the ratio of rejected GPS solutions is 1.7%, whereas this number ascends to 2.1% when comparing CODE Final against CODE MGEX products. Note that the CODE Final solutions are not used as reference within this dissertation as they do not include Galileo information for the processed interval.

⁴ftp://ftpseidr.cls.fr/pub/igsac/GRG_ELIMSAT_all.dat

residuals and AR rates (no evidence is found in the WL counterpart) for the global AR stage are about 0.06 cycles and 98%, respectively, whereas, for the 30-station network, these numbers are 0.12 cycles and 90%.

To recover nominal results from the 30-station network, our inspection algorithm has been fine-tuned with minor intuitive changes. After a few attempts, the AR metrics have become 0.07 cycles and 97% for the RMS of the residuals and AR rates. The new set-up differs from the nominal set-up in:

- Since the number of observations (real-valued ambiguities) has been significantly reduced, we have duplicated the redundancy level (recall, number of occurrences of one satellite in the between-satellite pairs) from 4 to 8.
- Since the size of the ambiguity clusters is small, the minimum number of obs/clust to try ILS decreases from 5 to 3.
- We provide extra “stiffness” to the LS adjustment by reducing the degree of the employed polynomials from 9 to 7.

A new 30-station network solution has been generated according to the above criteria and the results are also shown in table 4.2 (30 #2 row). It is observed that both orbital and SIS range comparisons are outstanding for such a small network.

TABLE 4.2: Comparisons between solutions using different network sizes and a reference solution generated from a 280-station network. The solution 30 #2 employs a different fine-tuning for the inspection the real-valued ambiguities

Num. of stations	RMS of orbit diff. [cm]			STD of SIS Range diff. [ps]		
	GPS	Gal	GLO	GPS	Gal	GLO
120	0.9	0.8	5.1	5.2	3.7	84.9
30 #1	8.7	14.5	9.7	90.1	102.5	126.1
30 #2	2.2	2.9	9.1	13.1	11.4	124.8

In table 4.2, we have also included the comparisons for GLONASS, which does not benefit from AR. It is observed that the quality of the solutions is significantly punished when the size of the network is reduced (even for the 120-station network), but it is almost insensitive to a degraded AR phase.

4.7 Summary

An AR strategy for UD-based GNSS processing has been designed and implemented to generate global GNSS solutions without the need to have precise a priori information at hand. Such a strategy follows from the usual WL and NL representation of the ambiguities, for which each contribution is independently resolved using either HMW or IF observations, respectively. In order for the ambiguities to reveal their integerness at the station level, some corrections shall be applied on the corresponding observations. The generation of those corrections is the core of our AR algorithm, which is based on the inspection of real-valued ambiguities.

The proposed AR algorithm uses a mixed-integer model to rigorously inspect the between-satellite real-valued ambiguities in a stand-alone step, which can be interpreted as global AR. The AR experience from baseline processing is implicitly considered here through the use of ambiguity clusters, which group the ambiguities

according to their fractional parts as well as the geographical distribution of the tracking stations. Those clusters complement the mixed-integer model in such a way that the number of integer parameters is reduced down to ~ 200 , which is of utmost importance because it allows LAMBDA to be used at a global scale. As a final outcome, the derived corrections modify the preliminary solution (orbits and clock information) so that it becomes compatible with the integer-cycle property of the carrier phase ambiguities, enabling between-satellite AR in an inexpensive station-wise sense (analogous to PPP-AR). We would like to also emphasize that our AR strategy employs three of the most widely recognized integer estimators. Specifically, integer rounding is utilized to generate ambiguity clusters, ILS is applied to determine the solution for the developed mixed-integer model, and integer bootstrapping is employed to ultimately resolve ambiguities in the final station-by-station phase.

The detailed view offered by our method can be exploited to define a more robust datum for the integer parameters, and to characterize other phenomena, such as apparent phase jump events. On the other hand, the resulting metrics may also reveal relevant information about the quality of the AR performance, supporting the identification of potential anomalies associated to diverging clock estimates.

The AR metrics are shown to be at an outstanding level, with ambiguity residuals well below 0.1 cycles and AR rates at the level of 95% and 88% for the WL and NL ambiguities, respectively. Additionally, cross-comparisons against the CODE products suggest that our strategy could even be more robust than classical DD-based AR strategies. Such a robustness has also been tested by processing data from a reduced 30-station network. After some fine-tuning, the results agreed with the reference solution at the 2-3 cm level for the orbit RMS and at the 10-15 ps level for the SIS range.

Review of the GNSS capabilities to derive geodynamic parameters

5.1 Introduction

Arguably, we can say that GNSS participates in virtually all the disciplines related to geodesy, since this technique densifies the ITRF, which is widely used for georeferencing measurements (including precise orbit determination of LEO satellites). Moreover, during the reduction of the GNSS observations, we access to two important sets of parameters that are directly connected to geodynamics:

- The earth rotation parameters (abbreviated in this manuscript as ERP), which are a set of kinematic parameters that represent corrections to the rotation matrix which accounts for the rotational part of the ITRF-to-ICRF transformation (section 3.3.2). From section 1.4.3, we know that these corrections are divided into polar motion (abbreviated as PM), which is the equatorial wobble of the Earth's pole, and variations in the Earth's rotation rate around the CIP, which are described by UT1 and length of day (abbreviated as LOD¹; recall that the GNSS solutions are not sensitive to the absolute rotated angle, i.e., UT1, according to the discussion given in section 3.3.2). From a physical point of view, they describe the Earth's angular velocity in accord with (1.26) and, with (1.10-1.15), can be used to understand the Earth's physical processes (Gross, 2007).
- The geocenter coordinates (abbreviated as GCC), which are a set of kinematic parameters that represent the position vector of the geocenter w.r.t. the origin of the ITRF, provided that NNT constraints are applied to the fiducial coordinates defining the frame (section 3.3.2). From a physical point of view, they relate with the degree-1 gravity coefficients according to (1.42-1.44). Since the GCC are estimated as a common offset to the coordinates of the entire network, such parameters also absorb errors emerging from higher gravity degrees if the network is not homogeneously distributed within the Earth surface (Zhang and Jin, 2014).

Over the last few decades, ERP and GCC have been derived using GNSS observations, which has led to a wealth of specialized articles covering the most prominent findings. Special mention deserves the dissertation by Zajdel, 2021², which is fully devoted to the estimation of ERP and GCC parameters in a multi-GNSS scenario (GPS, Galileo and GLONASS, as for our case) using the BSW. Therefore, rather than

¹We actually estimate variations in LOD, i.e., ΔLOD . However, for brevity, we will refer to this parameter simply as LOD in the sequel.

²See Zajdel et al., 2019, Zajdel et al., 2020, Zajdel, 2021 and Zajdel et al., 2021.

further expanding the body of knowledge, this chapter intends to provide a review of the matter, presenting some results that exemplify the achievable level of performance using the state-of-the-art GNSS processing strategy developed in previous chapters. Although this goal lacks of scientific aspiration, the present analysis is a mandatory preceding step that must be conducted prior to combining observations from diverse space techniques.

This introduction is followed by three additional sections: In section 5.2, we give a brief summary of the known difficulties associated to the GNSS-based estimation of ERP and GCC. Afterwards, the derived ERP and GCC results are presented. Here, we have carried out a number of experiments to evaluate the impact of significant changes in our GNSS processing scheme. The final section concludes the chapter.

5.2 Main difficulties estimating ERP and GCC

It is known that virtually all GNSS-based products are contaminated by spurious signals at harmonics of the draconitic year (e.g., Hugentobler, 2005, Ray et al., 2008, Griffiths and Ray, 2013), which is the repetition period of the relative geometry between the orbital plane and the Sun (section 1.6.2), equal to 351.4 d, 355.7 d and 353.4 d for GPS, Galileo and GLONASS, respectively. These artifacts have both physical and mathematical origins: From the physics, the satellite experiences some perturbations (owing to SRP) at those periodicities; if they are not perfectly modeled, then they are compensated to some extent by the estimated parameters. From the maths, on the other hand, all the co-estimated parameters correlate among themselves, and, therefore, the dependency of the empirical SRP parameterization on the draconitic year (recall that the ECOM frame is oriented towards the Sun) may induce artifacts in the whole solution matching that period. These spurious signals can be used as a figure of merit to assess the performance of new models and parameterizations (Rodríguez-Solano et al., 2014, Arnold et al., 2015). Furthermore, resonances between the orbital motion of the satellites and the Earth's rotation (Beutler, 2004b, section 3.3) could also lead to artifacts in the solution time series with periods of

$$\left| \frac{1}{n \cdot f_s + m \cdot f_E} \right|, \quad \text{for any integers } n, m \quad (5.1)$$

being f_s and f_E the periods of the satellite orbital motion and Earth's rotation, respectively. For instance, Zajdel et al., 2020 spot spurious signals in the time series of the ERP at periods of 2.5 d ($n = 2, m = -3$), 3.4 d ($n = 1, m = -2$) and 10 d ($n = 3, m = -5$) for Galileo, and, for GLONASS, 2.6 d ($n = 3, m = -6$), 3.9 d ($n = 2, m = -4$) and 7.9 d ($n = 1, m = -2$).

In relation with the GCC, there is an inferior sensitivity to the z component due to correlations with the SRP empirical model. According to Meindl et al., 2013, such correlations are associated to the ECOM2 $E3_0$ parameter and become more dangerous for high β angles. This is especially critical for the GLONASS constellation, which reach β angles as high as 88° (about 75° for GPS and Galileo). Zajdel et al., 2021 analyze different SRP parameterizations aiming at mitigating those undesirable artifacts.

The IERS Conventions provide background models for the Earth's pole. In essence, they are described by periodic motions at different frequencies (or different tides). Any error emerging from these models can be aliased into our ERP estimations (daily sampling). Indeed, this mechanism is proven in Griffiths and Ray, 2013 by means of a sensitivity analysis. For instance, it is shown that errors in the O1 (period of 25.82 d)

and $M2$ (12.42 d) tides produce alias signals of period 14.19 d and 14.76 d, respectively. A similar effect is observed in the time series of GNSS-derived coordinates due to the aliasing of tidal displacements mismodeling (Abraha et al., 2018).

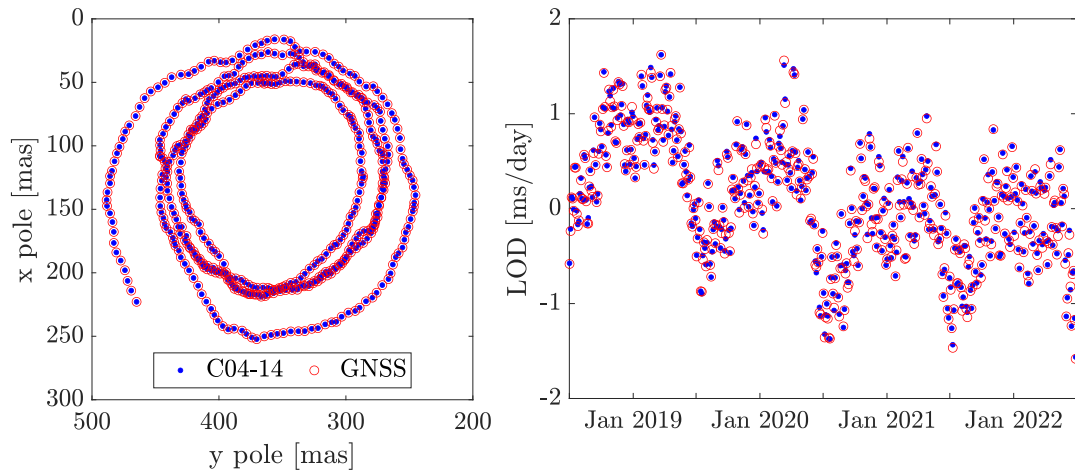


FIGURE 5.1: General view of the ERP results

5.3 GNSS-based ERP and GCC results

We have generated ERP and GCC results (four-year solution interval from mid 2018 to mid 2022) following our standard GNSS processing (appendix A) with minor modifications to conduct different exercises that exemplify the issues highlighted in the previous section. From these results, it is noteworthy to mention:

- Former studies (Lutz et al., 2016) have shown that computing 3-day-arc solutions (instead of 1-day-arc solutions) helps to attenuate long-period (more than 30 days) spurious signals. Therefore, we adhere to our nominal 3-day-arc solutions without further discussion in this regard.
- The BSW allows to easily estimate ERP and GCC in a GNSS-specific fashion (i.e., system specific parameter sets under a common run). This functionality is exploited in the solutions generated hereafter (Scaramuzza et al., 2018).
- The main features of the time series generated in accord with ITRF2014 are discussed in section 5.3.1.
- The impact of updating the sub-daily polar motion model from the IERS Conventional model (Petit, Luzum, et al., 2010) to Desai and Sibois, 2016 is evaluated in section 5.3.2.
- The main features of the time series generated in accord with ITRF2020 are discussed in section 5.3.3.
- The impact of using different fiducial sites for the TRF datum definition is evaluated in section 5.3.4.
- The impact of updating the Galileo SRP model according to the satellite metadata (recall section 3.7) is evaluated in section 5.3.5.

5.3.1 ERP and GCC solutions in accord with ITRF2014

In Fig. 5.1, we can see the GNSS-derived PM and LOD estimates on the left and right panels, respectively. These estimates are consistent with ITRF2014, and, therefore, we also include the IERS C04-14 series as reference, which are derived from a multi-technique combination and represent the most precise ERP available today (Bizouard et al., 2019). Unfortunately, both solutions are not fully independent, since the C04 series assimilate GNSS data, except for the UT1 values, mostly relying on the VLBI technique. Because of this, we generate C04 LOD values from UT1 differences, instead of directly using the C04 LOD entries.

Although the panels in Fig. 5.1 show interesting features from the physical point of view (see Gross, 2007 for a deep discussion on the matter), we cannot assess in detail the performance of our estimates. Therefore, we compute the differences between both solutions and display their amplitude spectra in Fig. 5.2 (including the single-system solutions). The associated statistics (mean and STD) are given in table 5.1. Note that we use the labels “GNSS”, “GPS”, “Gal” and “GLO” to refer to the multi-GNSS, GPS-only, Galileo-only and GLONASS-only solutions, respectively.

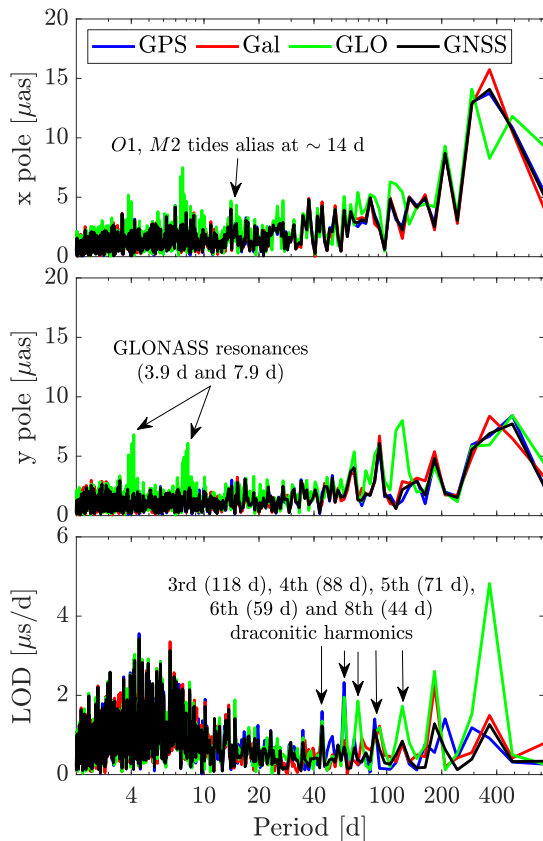


FIGURE 5.2: Amplitude spectra of the differences between GNSS-based (ITRF14) and C04-14 ERP solutions

the cumulative GNSS-based LOD series diverges from the VLBI-based UT1 solutions (Ray, 1996, Dach, 2022). All the metrics for the PM solutions show a competitive performance, being slightly better than the results presented by Zajdel et al., 2020. Our LOD statistics, on the other hand, seem a bit high. Nevertheless, when compared against the C04 LOD entries, the STD values around $20 \mu\text{s}/\text{d}$ decrease to $15 \mu\text{s}/\text{d}$.

The various panels in Fig. 5.2 depicts several spikes at particular frequencies that can be identified with some of the problems highlighted in the previous section. We speculate that the noticeable peak at around 14 d in the x coordinate of the polar motion could be related to the alias of the O1 and M2 tides into our 24-h ERP estimates. Likewise, the GLONASS-only PM solution contains visible artifacts around 3.9 d and 7.9 d, which could originate from the resonance between the orbital period and the Earth’s rotation. Regarding the LOD panel, most of the low-frequency spikes are harmonics of the draconitic year.

In view of Fig. 5.2, it can be stated that the estimates from the GLONASS-only solutions are inferior than the estimates from the other set-ups, which are at a comparable level at first glance. For a more detailed perspective, we address to table 5.1, where the mean and STD of the comparisons are included. Indeed, it is confirmed that the GLONASS solution performs the worst for all the figures, but the bias in LOD, which is seemingly worse for GPS. This bias is expected, since it has been long known that

TABLE 5.1: Statistics of the differences between GNSS-based (ITRF2014) and C04-14 ERP solutions

	x pole [μas]		y pole [μas]		LOD [$\mu\text{s/d}$]	
	mean	STD	mean	STD	mean	STD
GNSS	19	37	-12	27	-6.3	20.5
GPS	16	37	-9	27	-9.1	20.7
Gal	22	38	-14	28	-4.1	21.0
GLO	34	45	-25	36	-2.1	21.3

The corresponding time series for the GCC are displayed in Fig. 5.3, including two different scales for the z coordinate (right panels). For a better visualization, the time series are smoothed by averaging the values within a 15-day sliding window. It can be seen at naked eye that the z coordinate for the GLONASS-only solution suffers from dire artifacts, arising, as advanced in the previous section, from correlations with the ECOM2 E_{30} parameter. Likewise, the Galileo time series for the x and y coordinates are biased, probably because ITRF2014 is not compatible with the Galileo system (Specifically, no antenna calibrations are given for the Galileo E5 signals; instead, the GPS L2 calibrations are adopted).

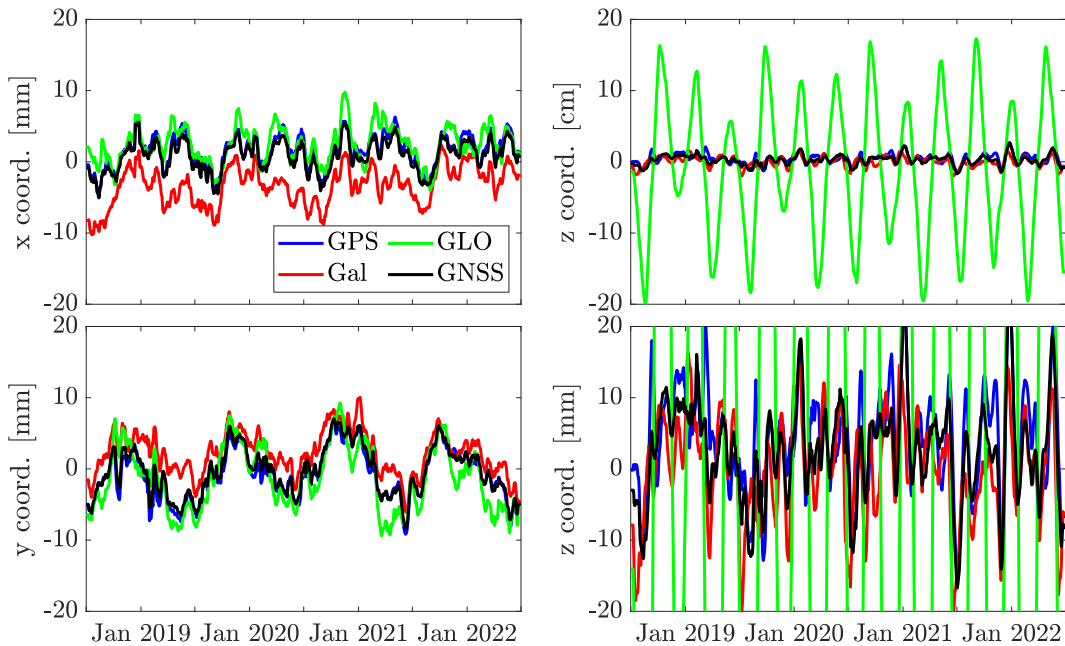


FIGURE 5.3: Time series of GNSS-based (ITRF2014) GCC solutions

A model with bias, drift, annual signal and semiannual signal is fit to the GCC time series. The resulting amplitudes and phases of the annual signals (along with the formal errors of the fit) are given in table 5.2, also including a SLR solution (Altamimi et al., 2016) for reference purposes. Whilst the GNSS, GPS and GLO solutions are consistent with each other for the x and y coordinates, with amplitudes (phases) at the level of 1.6 mm (44°) and 4.2 mm (-44°), respectively, the Gal solution seems to sense a different annual signal, which is mainly reflected in the phase component. Comparing the GNSS and SLR rows, we do not see especially different amplitudes and phases. Therefore, incorporating both GNSS and SLR data to define the long-term origin of the TRF should not compromise the integrity of the frame.

TABLE 5.2: Annual signals of the GNSS-based (ITRF2014) GCC estimates. A SLR-based solution is included for reference. The amplitudes are given in millimeters and the phases in degrees

	x coord.		y coord.		z coord.	
	Amp.	Phase	Amp.	Phase	Amp.	Phase
GNSS	1.6 ± 0.1	44 ± 3	4.2 ± 0.1	-44 ± 1	4.2 ± 0.3	17 ± 4
GPS	1.7 ± 0.1	53 ± 3	4.1 ± 0.1	-47 ± 2	4.5 ± 0.3	12 ± 4
Gal	2.3 ± 0.1	7 ± 2	3.4 ± 0.1	-35 ± 2	4.8 ± 0.3	25 ± 4
GLO	1.7 ± 0.1	53 ± 4	5.3 ± 0.1	-46 ± 2	17.0 ± 3.6	-53 ± 12
SLR	2.6 ± 0.1	46 ± 3	2.9 ± 0.1	-40 ± 2	5.7 ± 0.2	28 ± 2

5.3.2 Sub-daily polar motion background model update

The transition between ITRF2014 and ITRF2020 includes a new sub-daily PM model. According to Desai and Sibois, 2016, this newer model assimilates more altimetry and gauge observations, yielding better resolution in polar regions. Additionally, there is a higher consistency between ocean tide and libration models, as well as a better agreement with GPS observations. Consequently, it is worth evaluating its performance in an intermediate step before definitively switching to ITRF2020. This is done in this section (also investigated in Dach et al., 2021), where solutions equivalent to those of the previous section have been computed with updated sub-daily PM model. As a figure of merit, we use the overlaps of the PM estimates (note that the C04 14 series are in line with the old model), whose amplitude spectra is shown Fig. 5.4 (labels “IERS2010” and “DESAI2016” for old and new models, respectively).

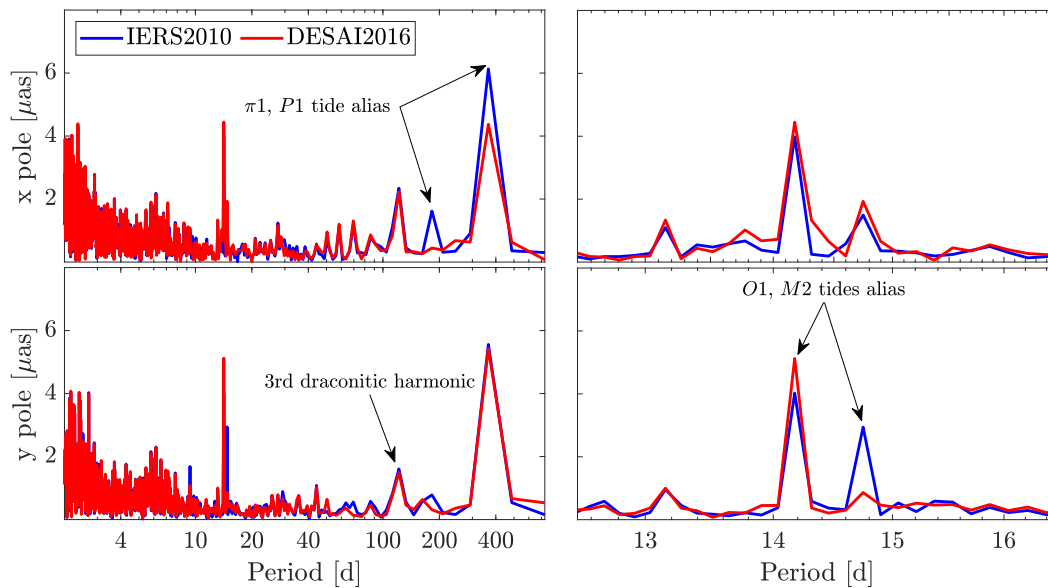


FIGURE 5.4: Amplitude spectra for the PM overlaps based on different sub-daily PM background models

The updated model reduces, on the one hand, the annual and semiannual spurious signals for the x PM coordinate (according to Griffiths and Ray, 2013, they could be related to the alias of the π_1 and P_1 tides), and, for the y PM coordinate, we see smaller amplitudes at periods about 14 d (O_1 and M_2 tides alias). All in all, this hints a superior performance for the newer model.

5.3.3 ERP and GCC solutions in accord with ITRF2020

The solutions of section 5.3.1 are repeated in full agreement with ITRF2020. This time, we use the C04-20 series (i.e., ITRF2020 realization of the C04 series³) as reference. The statistics of the ERP comparisons are given in table 5.3 (GLONASS shows, once more, the worse performance). Unexpectedly, these figures, yet lying within acceptable margins, are poorer than their ITRF2014 counterparts given in table 5.1⁴. In any case, it can be stated that the achievable ERP precision using our state-of-the-art GNSS processing scheme is about $50 \mu\text{s}$, $40 \mu\text{s}$ and $25 \mu\text{s}/\text{d}$ for the x pole coordinate, y pole coordinate and LOD, respectively. These figures should be the baseline for any future analysis combining observations from different techniques.

TABLE 5.3: Statistics of the differences between GNSS-based (ITRF2020) and C04-20 ERP solutions

	x pole [μs]		y pole [μs]		LOD [$\mu\text{s}/\text{d}$]	
	mean	STD	mean	STD	mean	STD
GNSS	19	51	-8	38	-6.8	25.3
GPS	20	51	-11	38	-9.8	25.5
Gal	16	52	1	39	-4.9	25.7
GLO	26	55	-29	45	-2.4	25.9

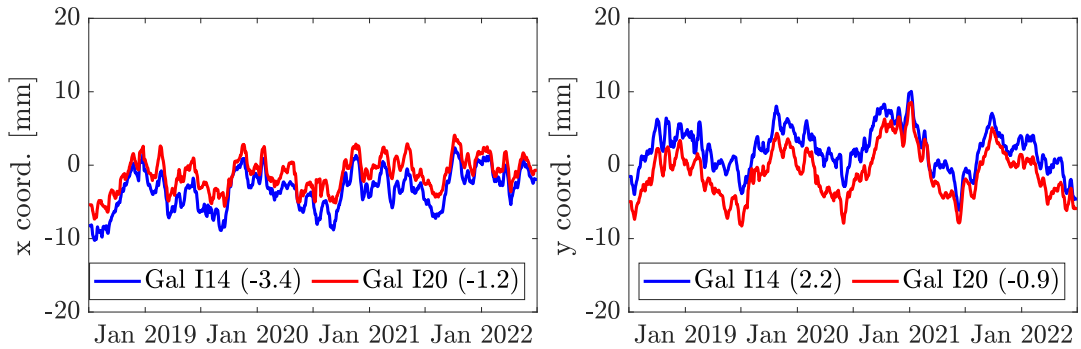


FIGURE 5.5: Time series of Galileo-based GCC x and y coordinates (bias in brackets)

The time series for the Galileo-based x and y GCC are shown in Fig. 5.5. We can see that the ITRF2020 solution reduces the magnitude of the bias for both coordinates. In particular, the x bias goes from -3.4 mm to -1.2 mm , and the y bias from 2.2 mm to -0.9 mm . This improvement is expected since Galileo observations were assimilated for the ITRF2020 realization (Altamimi et al., 2023). The main features (amplitudes and phases) of the resulting annual and semiannual signals for the multi-GNSS (GNSS row) and GNSS-specific (GPS, Gal and GLO rows) solutions are given in table 5.4 together with the corresponding SLR figures for reference (coming from Altamimi et al., 2023). There is an overall good agreement between all the GNSS-based solutions (except for the GLONASS z coordinate, which is clearly degraded) and the SLR solution for both annual and semiannual signals, with amplitude and phase differences within 1 mm and 20° , respectively. These differences are at the

³<https://hpiers.obspm.fr/iers/eop/eopc04/updateC04.txt>

⁴It has to be pointed out that these metrics not only evaluate the accuracy of the generated GNSS-based ERP but are also highly dependent on the C04 time series used as reference. On the other hand, the PM overlaps do not show significant differences between the solutions generated in both ITRF realizations.

same level as the SLR differences for two consecutive ITRF realizations (compare with table 5.2). Consequently, we further conclude that GNSS observations could be considered for the definition of the long-term ITRF origin.

TABLE 5.4: Annual signals of the GNSS-based (ITRF2020) GCC estimates. A SLR-based solution is included for reference. Solutions GNSS-b and Gal-b use an alternative datum definition (section 5.3.4) and an alternative SRP model (section 5.3.5), respectively. The amplitudes are given in millimeters and the phases in degrees

	x coord.		y coord.		z coord.	
	Amp.	Phase	Amp.	Phase	Amp.	Phase
<i>Annual signals</i>						
GNSS	1.5 ± 0.1	40 ± 4	4.4 ± 0.1	-43 ± 1	4.4 ± 0.2	24 ± 3
GPS	1.5 ± 0.1	48 ± 4	4.3 ± 0.1	-44 ± 1	4.8 ± 0.2	22 ± 3
Gal	1.8 ± 0.1	12 ± 3	4.2 ± 0.1	-38 ± 1	4.4 ± 0.3	30 ± 4
GLO	1.7 ± 0.1	44 ± 4	5.3 ± 0.1	-45 ± 1	21.1 ± 3.6	-44 ± 10
GNSS-b	1.1 ± 0.1	44 ± 5	4.3 ± 0.1	-45 ± 1	3.7 ± 0.2	18 ± 4
Gal-b	1.8 ± 0.1	12 ± 3	4.2 ± 0.1	-38 ± 1	3.7 ± 0.2	38 ± 4
SLR	1.2 ± 0.1	57 ± 7	3.5 ± 0.2	-27 ± 3	2.8 ± 0.3	40 ± 7
<i>Semiannual signals</i>						
GNSS	1.5 ± 0.1	-87 ± 4	0.5 ± 0.1	167 ± 11	1.5 ± 0.2	-118 ± 9
GPS	1.6 ± 0.1	-84 ± 3	0.5 ± 0.1	176 ± 11	0.6 ± 0.2	-144 ± 23
Gal	1.1 ± 0.1	-88 ± 5	0.5 ± 0.1	145 ± 10	2.0 ± 0.3	-148 ± 9
GLO	1.7 ± 0.1	-99 ± 4	0.7 ± 0.1	174 ± 11	25.9 ± 3.6	-119 ± 8
GNSS-b	1.4 ± 0.1	-85 ± 4	0.5 ± 0.1	167 ± 10	1.5 ± 0.2	-120 ± 9
Gal-b	1.3 ± 0.1	-88 ± 4	0.5 ± 0.1	145 ± 11	0.5 ± 0.2	-149 ± 26
SLR	0.5 ± 0.2	-73 ± 18	0.2 ± 0.2	182 ± 39	1.2 ± 0.3	-150 ± 16

5.3.4 Influence of the TRF datum definition

We have generated ERP solutions with and without co-estimating GCC, since the comparison of both time series becomes an effective way to quantify the correlation between ERP and GCC estimates. Such a comparison for the PM is represented by the blue curves in Fig. 5.7. These curves mainly depict annual variations with amplitudes up to $5\mu\text{as}$, which is not negligible in view of the amplitude spectra of the PM errors shown in Fig. 5.2. The origin of these correlations is mainly associated with the distribution of fiducial sites used to define the terrestrial datum. If these sites are homogeneously distributed within the surface of the Earth, then the coupling between ERP and GCC estimates should vanish. Conveniently, our datum definition is given by those IGS stations whose estimated coordinates deviate only within limited margins w.r.t. their regularized coordinates (section 3.3.2). Since the IGS network is denser in the northern hemisphere, this is not enough to achieve a balanced network.

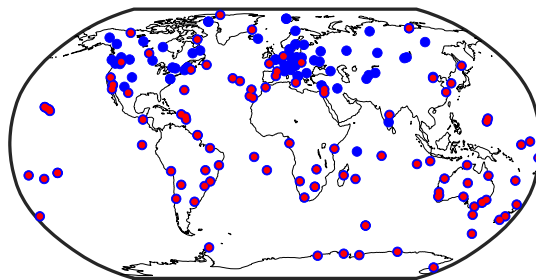


FIGURE 5.6: Original datum network (blue dots) and resulting balanced datum network (red dots) after minimizing (5.2) on 2018/190

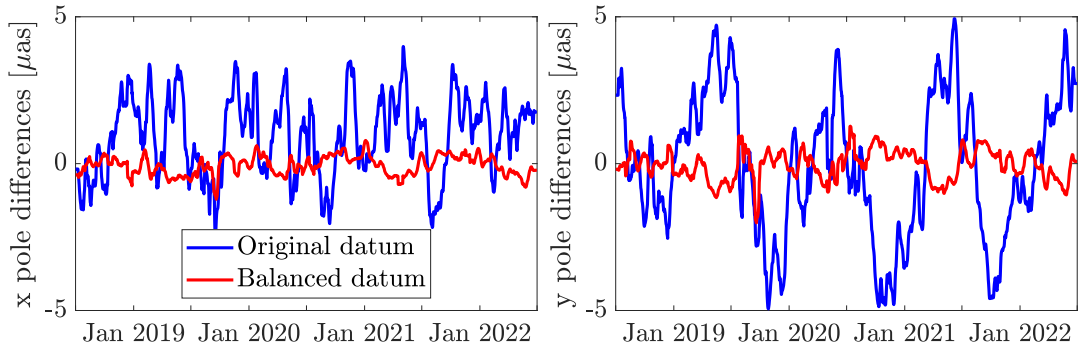


FIGURE 5.7: Comparison of PM time series generated with and without co-estimating GCC

In order to leverage these ideas, we shall find an index, b , able to measure how balanced the reference network is. An adequate option for such an index is

$$b = \left| \sum_i r_i \right| \quad (5.2)$$

where r_i is the position vector of the i th station. For an ideal network, this index should be identically zero. Hence, we aim at discriminating stations for the definition of the terrestrial datum in such a way that (5.2) is minimized. This is attained with brute computational force: We select an initial station for the datum, and then sequentially include those stations that have the least impact on b . It is observed that, at some point, including additional stations monotonically increases b . The datum is thus defined by the network with minimum b that exists before this divergence occurs and contains, at least, 100 stations to guarantee global coverage. Fig. 5.6 shows the distribution of the original datum network ($b = 338463$ km, blue dots) and the balanced datum network ($b = 523$ km, red dots) on 2018/190. It can be seen that most of the stations in Europe and the United States have been made redundant.

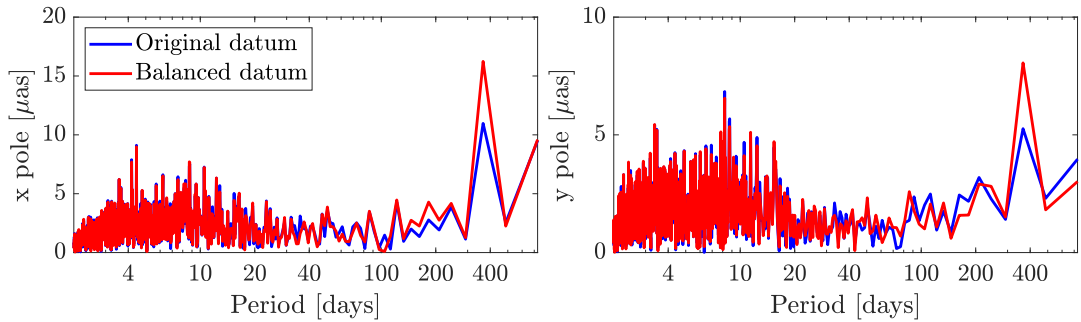


FIGURE 5.8: Amplitude spectra of the differences between GNSS-based and C04-20 PM solutions applying different terrestrial datum definitions

The comparisons of the PM results generated with and without co-estimating GCC, but applying the balanced datum, are represented by the red curves in Fig. 5.6. Because of this new datum, the coupling between ERP and GCC is now virtually zero. The main consequence in the GNSS-based GCC estimates is that the annual amplitude of the z component reduces from 4.4 mm to 3.7 mm (see GNSS-b rows in table 5.4), which can be interpreted as a good indicator. On the other hand, the new PM estimates are compared with the C04-20 series and the amplitude spectra of the

differences shown in Fig. 5.8. The annual peak becomes more aggressive for the new solution. Although this is not a good indicator, the artifact could actually be located on the reference solution. Unfortunately, the PM day boundary overlaps do not show relevant differences between both the old and the new solutions, and further studies shall be conducted to accept or rule out this new approach for the definition of the terrestrial datum.

5.3.5 Influence of the Galileo SRP model on the ERP and GCC solutions

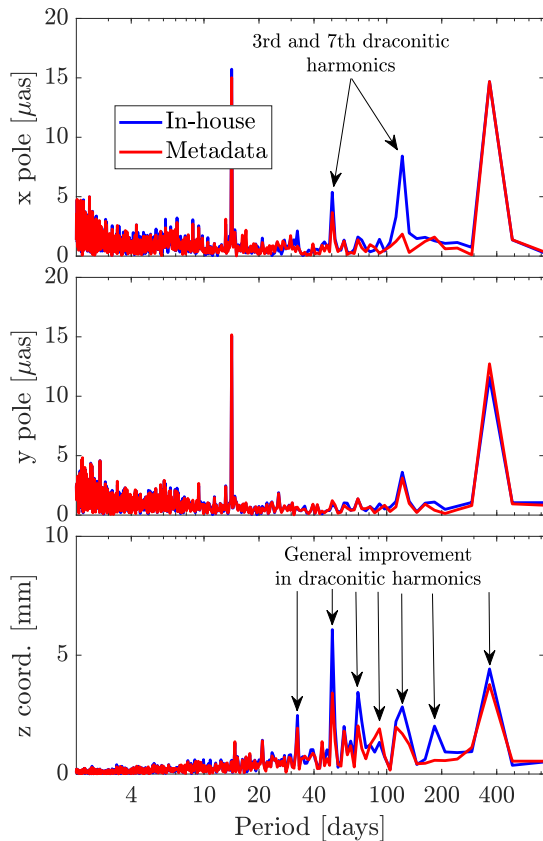


FIGURE 5.9: Amplitude spectra of the Galileo-only PM overlaps and z GCC for different SRP models

We showed in section 3.7 that updating an internally developed Galileo SRP background model with the metadata provided by the European GNSS Agency yielded better figures for both the empirical orbital parameters and the SLR residuals. This model update can also be noticed in the Galileo-only ERP and GCC estimates. The top and middle panels shown in Fig. 5.9 display the amplitude spectra of the PM overlaps, whereas the bottom panel depicts the amplitude spectra of the z GCC. It is observed that the spurious signals associated to the 3rd and 7th draconitic harmonics diminish in the x pole overlaps if the Galileo metadata is used. Likewise, for the z GCC, most of the peaks associated with draconitic harmonics also reduce their amplitude. More explicitly, table 5.4 shows that applying the updated SRP model (Gal-b rows) produce smaller amplitudes in both annual and semiannual signals for the Galileo-only z GCC solution, which change from 4.4 mm and 2.0 mm to 3.7 and 0.5 mm, respectively. Additionally, the associated formal errors are also smaller (for 0.3 mm to 0.2 mm in both cases), indicating a lower noise level in the time series.

5.4 Summary

This chapter has provided an overview of the GNSS capabilities for recovering ERP and GCC geodetic estimates. Since this topic has been covered numerous times in the specialized literature, the main issues that are encountered are known beforehand, namely, spurious signals in the time series arising from SRP mismodeling (draconitic harmonics), resonances owing to the coupling between the orbital motion and the Earth's rotation, aliasing of background models, and correlations between z GCC estimates and the orbit empirical parameterization (mainly due to $E3_0$). Just for instructive purposes, these problems were reflected within various exercises. It was explicitly exemplified how the spurious signals are reduced when updating the

background sub-daily PM model, as well as the background SRP model for Galileo. Additionally, the use of a balanced network (stations uniformly distributed within the Earth) to define the terrestrial datum has implications on the ERP and GCC annual signals. Whereas the amplitude of the z GCC annual signal became smaller, which can be interpreted as a positive indicator, the annual amplitude of the PM deviations w.r.t. the C04 series increased. This misbehavior could actually be related to the reference itself. However, further investigations are needed to accept or rule out the proposed terrestrial frame realization.

Comparing our solutions with respect to the C04 series allows to bound the ERP precision to $50 \mu\text{as}$, $40 \mu\text{as}$ and $25 \mu\text{s/d}$ for the x pole, y pole and LOD, respectively. This level of consistency should be regarded as the baseline precision for any future ERP analysis involving GNSS (e.g., in a combined GNSS and SLR processing). In addition, it was observed that the annual and semiannual signals for the GNSS- and SLR-based GCC time series agree at the level of 1 mm and 20° for the amplitudes and phases, respectively. Consequently, it seems reasonable to consider also GNSS results for the definition of the long-term ITRF origin.

The role of the time-variable gravity field in GNSS network solutions

6.1 Introduction

As pointed out in section 1.5.3, satellite-derived time-variable gravity field solutions are of special societal interest as they provide information on the surface water processes that our planet undergoes (Wahr et al., 1998). For instance, Rodell et al., 2018 and Velicogna, 2009 have used them to infer global freshwater trends and to quantify net ice mass loss in frigid regions, respectively. Likewise, these gravity solutions are also valuable for the orbit modeling of scientific LEO satellites with very stringent accuracy requirements, whose benefits have been reported by Rudenko et al., 2014 and Peter et al., 2022. It is hence not striking that the community recognized the importance of such gravity solutions with the creation of the Combination Service for Time-variable Gravity fields (COST-G, Jäggi et al., 2020) in 2019, being a new Product Center of the IAG's International Gravity Field Service (IGFS). The purpose of COST-G is to combine monthly gravity field models from various ACs, reducing the systematic errors of the individual solutions (Jean et al., 2018).

Among the dedicated satellite missions, the Gravity Recovery and Climate Experiment (GRACE, Tapley et al., 2004) and its successor GRACE-FO (Follow On, Flechtner et al., 2016) have become the most fruitful missions in this domain, providing almost persistent gravity monitoring since 2002 until the present day, except for some isolated months and an annoying gap between both missions. Nonetheless, any Earth's orbiting satellite is subject to accelerations caused by the Earth's gravity field, and so is the case for the GNSS constellations, whose capabilities to recover the Stokes' coefficients have barely been explored by the community, in spite of being at the core of the space geodetic techniques (Altamimi and Gross, 2017).

An early analysis performed by Ineichen et al., 2003 already showed the feasibility of estimating low-degree Stokes' coefficients in a multi-GNSS scenario including GPS and GLONASS. However, that analysis was not yet optimal, since precise satellite positions derived from the dynamics were used as observations instead of the original GNSS observations. Later, Sośnica et al., 2013a rigorously processed about ten years of data, where coefficients up to degree-4 were co-estimated along with other geodetic parameters. Although this study showed promising preliminary results, an important correlation between the Earth's oblateness and the variation in length of day was overlooked, which is to be addressed in the sequel. More recently, Nowak et al., 2023 used the so-called inverse method to retrieve C_{20} and C_{30} time series¹ from the

¹An upper bar is commonly used to denote normalized Stokes' coefficients (chapter 2). Although all the presented results are so normalized, that upper bar is omitted within this chapter to alleviate the notation.

solutions generated in the frame of the third IGS reprocessing campaign. By modeling the elastic response of the Earth, this method uses the displacements experienced by a network of ground stations to infer the mass redistribution that originates them (Blewitt and Clarke, 2003). In this chapter, we complement those former studies by using the direct method through the celestial mechanics approach (Beutler et al., 2010b) in order to thoroughly assess the GNSS capabilities to determine the low-degree Stokes' coefficients, with special focus on the degree-2 coefficients, as well as to evaluate the impact of applying time-variable gravity field background models to generate GNSS network solutions.

The celestial mechanics approach is an intrinsic generalization of the orbit determination process, since the corrections over the geopotential are jointly estimated with other parameters involved in the estimation process. Consequently, it has become very popular when producing gravity field solutions derived from satellite-based data (Beutler et al., 2010a, Lasser, 2022). Nevertheless, there exist other approaches (e.g., acceleration approach) that, in practice, yield equivalent results, as empirically shown by Baur et al., 2014. It is then up to the analysts to select the one that better fits their applications.

Although we have to limit ourselves to the long-wavelength gravity field when processing GNSS-based data, the relevance of these solutions go beyond their relatively small number of associated coefficients. From a conceptual point of view, Couhert et al., 2020 stress the link between low-degree Stokes' coefficients and the defining properties of a TRF: The degree-0 coefficient acts directly upon the Earth's mass, which, in turn, affects the semi-major axis of the orbits and, hence, the scale of the TRF; the degree-1 coefficients relate, as reflected by (1.42-1.44), to the geocenter coordinates, which are linked to the origin of the TRF; the degree-2 coefficients are associated, in line with (1.45-1.49), to the Earth's inertia tensor, and, indirectly, to the theoretical Earth's figure axis, which is an intuitive choice for the orientation of the TRF. These low degree terms tie the geometric frame to the gravity field and are in this sense essential for orbit determination in satellite geodesy. On the other hand, there are also practical reasons to pay extra attention to low-degree Stokes' coefficients, since it was noticed that the GRACE mission is unable to provide reliable C_{20} estimates and, in case of the GRACE-FO mission, some problems also arise for the C_{30} estimates (see Loomis et al., 2019 and Loomis et al., 2020). These issues are bypassed by replacing both coefficients by SLR-derived solutions, which results in a better characterization of some long-term geophysical processes, such as the glacial isostatic adjustment.

As inferred from the above discussion, the SLR technique is well-suited to provide long-wavelength time-variable gravity field solutions (Sośnica et al., 2015; Geisser et al., 2023). Additionally, Meyer et al., 2019 process SLR observations from geodetic satellites together with GPS observations collected by some scientific LEO satellites, successfully proving a better agreement between the resulting Stokes' coefficients and those derived from GRACE. Because of the relevance of GNSS and SLR as major geodetic techniques (recall section 1.2), it is a natural evolution in the processing standards to rigorously combine observations from they both, justifying the effort devoted in the sequel to understand the GNSS capabilities to recover time-variable gravity field solutions, which could be considered as a common tie.

This chapter includes seven additional sections. The subsequent one describes the general features of the multi-GNSS processing strategy and methodology used to generate the solutions of this chapter. Later, in section 6.3, we focus on the generation of degree-2 gravity signals exclusively using GNSS observations, which requires to address several points: The sensitivity of the GNSS orbits to time-variable gravity

signals, the handling of an emerging rank defect involving the UT1 parameters, and a deeper fine-tuning of the processing set-up and data accumulation to mitigate harmful correlations and spurious signals. Afterwards, the same time series are analyzed but using single-GNSS scenarios. In the fifth section, the parameter space is extended to include up to degree-4 coefficients. Next, we evaluate the impact of using time-variable gravity field solutions (either from the GNSS-derived solution previously computed or from COST-G) when generating global geodetic solutions. Due to the correlation between the C_{20} and LOD parameters, the C_{20} time series can be strongly influenced by those perturbing accelerations causing orbital precession, such as some otherwise neglected relativistic effects. The influence of these effects is assessed in section 6.7. As usual, the last section is left to the summary.

It is to be finally mentioned that the content presented herein has already been made available to the community through Meyer et al., 2023 and Calero-Rodríguez et al., 2023b.

6.2 Processing strategy

The baseline processing strategy follows from the schemes implemented in chapter 3, although with some particularities that require a dedicated fine-tuning. This fine-tuning is conducted in subsequent sections so that the newly generated GNSS-based gravity field solutions resemble some state-of-the-art references, namely, SLR-derived C_{20} and C_{30} coefficients extracted from the Technical Note 14 (TN-14, Loomis et al., 2020), and, for the remaining coefficients, GRACE-derived solutions provided by COST-G (Jäggi et al., 2020).

The general processing aspects from appendix A are still valid, except for some specific points which are relevant throughout this chapter:

- The fine-tuning employed for the generation of GNSS-based gravity field solutions considers (section 6.3):
 - Orbit arc length (Beutler et al., 1996).
 - Amount of accumulated data.
 - Constraining of stochastic pulses (Beutler et al., 1994).
- Multi-GNSS (GPS, Galileo and GLONASS) or, for section 6.4, single-GNSS processing.
- Estimated Stokes' coefficients up to degree-2 or, for the experiments of section 6.5, up to degree-4.
- If the gravity field is to be estimated, the a priori static gravity field follows from the IERS Conventions (Petit, Luzum, et al., 2010), based on EGM2008 (Pavlis et al., 2012). When we evaluate the impact of using time-variable gravity fields in GNSS network solutions (Stokes' coefficients not estimated; section 6.6), several background models are tested: IERS Conventions, the generated GNSS-based time-variable degree-2 solutions (complemented by the IERS Conventions up to degree-12) and a fitted signal model (FSM, which includes bias, drift, annual signal and semiannual signal) to the COST-G monthly solutions.
- To keep consistency with the reference solutions, the AOD1B product (Dobslaw et al., 2017; not IGS standard) is used as a background model, too. Additionally, although it suffices to model only the C_{21} and S_{21} contributions of the ocean

pole tides when processing GNSS data, we apply this model up to degree-8 for this chapter.

- The relativistic accelerations due to the Lense–Thirring and de Sitter effects as specified in the IERS Conventions (not IGS standards) are applied for the study presented in section 6.7.

6.3 Estimability of degree-2 Stokes’ coefficients using GNSS orbits

6.3.1 Sensitivity to the time-variable gravity field

The signals of the observed time-variable gravity field have amplitudes that range from hundreds to thousands ppb w.r.t. the static part in the corresponding coefficients (table 6.1). Such small variations are scarcely sensed by the GNSS satellites placed at altitudes of about 20200 km, 23200 km and 19100 km for GPS, Galileo and GLONASS, respectively. In order to get an insight into the estimability of these signals through the dynamics of those GNSS satellites, we carry out a sensitivity analysis in this section. It consists in comparing a set of GNSS reference orbits against other two sets for which we have induced degree- and order-specific perturbations to the background static gravity field according to the amplitudes of the expected time-variable signals. The first of these sets (case #1 in table 6.2) results from the direct propagation of the initial state vectors of the reference orbits. The second set (case #2 in table 6.2) fits the satellite dynamics to the reference satellite coordinates, where, besides initial state vectors, empirical ECOM2 parameters are estimated. The first comparison quantifies the net impact that gravity signals have on the dynamics itself, whilst the second one reflects the sensitivity to those parameters during the estimation process.

TABLE 6.1: Degree- and order-specific amplitudes of the time-variable gravity field derived from the COST-G FSM. Each value accounts for the sum of the amplitudes of the semiannual and annual signals for the sine and cosine harmonic terms. The “abs” (absolute) rows give the net value scaled by 10^{10} , whereas the “rel” (relative) ones give the ratio w.r.t. the static part in ppb

Degree		Order						
		0	1	2	3	4	5	6
2	abs	0.98	0.38	0.97				
	rel	$2 \cdot 10^1$	$93 \cdot 10^6$	$56 \cdot 10^3$				
3	abs	1.00	0.63	0.63	1.40			
	rel	$11 \cdot 10^4$	$2 \cdot 10^5$	$98 \cdot 10^3$	$15 \cdot 10^4$			
4	abs	0.32	0.61	0.88	0.44	1.40		
	rel	$6 \cdot 10^4$	$12 \cdot 10^4$	$16 \cdot 10^4$	$15 \cdot 10^4$	$64 \cdot 10^4$		
5	abs	1.00	0.40	0.52	0.60	0.56	0.42	
	rel	$15 \cdot 10^5$	$47 \cdot 10^4$	$98 \cdot 10^3$	$18 \cdot 10^4$	$9 \cdot 10^5$	$11 \cdot 10^4$	
6	abs	0.44	0.61	0.56	0.47	0.40	0.47	0.49
	rel	$29 \cdot 10^4$	$11 \cdot 10^5$	$81 \cdot 10^4$	$36 \cdot 10^5$	$23 \cdot 10^4$	$98 \cdot 10^3$	$3 \cdot 10^6$

Table 6.2 shows the outcome of the aforementioned comparisons by using the overall (i.e., including all the satellites) 3D-RMS as representative metric. Note that the chosen day for the experiment is 2022/100 (year/day of year). We can see that, except for the case #1 and degree-2 values, the 3D-RMS of the comparisons is well below 1

TABLE 6.2: Comparison between reference GNSS orbits and test orbits computed with perturbed static gravity field (according to the amplitudes of table 6.1). For the case #1, the test orbits are propagated, whereas they are fitted to the reference coordinates for case #2. Note that the values are in mm and represent overall 3D-RMS

Degree		Order						
		0	1	2	3	4	5	6
2	#1	3.163	1.230	3.925				
	#2	0.416	0.090	0.114				
3	#1	0.682	0.542	1.086	1.947			
	#2	0.042	0.035	0.068	0.206			
4	#1	0.088	0.102	0.227	0.094	1.242		
	#2	0.009	0.012	0.007	0.010	0.059		
5	#1	0.059	0.014	0.050	0.033	0.040	0.066	
	#2	0.002	0.002	0.003	0.003	0.002	0.003	
6	#1	0.009	0.007	0.007	0.007	0.009	0.014	0.014
	#2	0.002	0.002	0.000	0.002	0.002	0.002	0.002

mm, suggesting that the GNSS-based estimation of Stokes' coefficients is extremely challenging because of the accuracy of the GNSS orbits themselves, which is reported to be at the centimeter level (Griffiths and Ray, 2009). The degree-2 comparisons, on the other hand, could be statistically significant since the midnight misclosures hint that the internal orbit precision is at the millimeter level (Fig. 3.10). Nonetheless, the estimability of degree-2 coefficients is still hampered by the co-estimation of empirical parameters (degree-2, case #2) and, hence, the orbit parameterization plays a vital role in determining true gravity signals.

Incidentally, we can also see from table 6.2 that the sensitivity increases with the order as a result of the relatively big polar gap of the GNSS orbital planes (Gelderen and Koop, 1997).

6.3.2 Collinearity between length of day and Earth's oblateness

The same mechanism that explains the collinearity between the orbit ascending nodes and the universal time parameters (representing deviations w.r.t. UTC), as discussed in section 3.3.2, makes the time derivatives of these quantities correlate, too. Equation (1.68) tells how the secular variation of the orbit ascending node relates to the Earth's oblateness, which, complemented by (1.34), shows how its variations (i.e., ΔC_{20}) can be compensated with variations in universal time or length of day parameters ($\Delta UT1$ or ΔLOD , respectively) during the LS adjustment:

$$\Delta \dot{\Omega}_s = \frac{3\sqrt{5}}{2} \Delta C_{20} \left(\frac{R}{a(1-e^2)} \right)^2 n \cos(i) = \Omega \frac{d\Delta UT1}{dt} = -\Omega \frac{\Delta LOD}{LOD} \quad (6.1)$$

In view of this equation, these parameters could be decorrelated if the involved orbital geometries were sufficiently different. Unfortunately, this is not the case for the included GNSS constellations, whose eccentricities are near zero, whose mean motions are about two revolutions per day, and whose inclinations are about 55° for GPS and Galileo and 64° for GLONASS. Therefore, we expect that length of day and Earth's oblateness contaminate each other during the LS adjustment, losing their physical meaning.

The previous discussion is confirmed with numerical experiments by simply looking into the corresponding block of the correlation matrix obtained from a LS adjustment. This block, extracted from a 7-day-arc solution on 2022/100, is displayed on top of Fig. 6.1 (the UT1 parameters are referred to the day boundaries). The parameter UT1₄ is constrained to its a priori value, hence defining the origin (anchor point) from which the other universal time parameters are measured. According to (6.1), a positive ΔC_{20} leads to a positive $\Delta UT1$ if $\cos(i) > 0$ (as for the GNSS orbits) and, therefore, a positive correlation for UT1_{*i*} with $i > 4$. For $i < 4$, the origin is advanced w.r.t. reference epoch of the UT1_{*i*} parameters, inverting the sign of the correlation.

C_{20}	-0.98	-0.97	-0.94	-0.00	0.94	0.97	0.98	0.98
C_{20}	0.06	-0.06	-0.01	-0.03	0.00	0.02	0.06	-0.05
	UT1 ₁	UT1 ₂	UT1 ₃	UT1 ₄	UT1 ₅	UT1 ₆	UT1 ₇	UT1 ₈

FIGURE 6.1: Correlation blocks between C_{20} and UT1 parameters for a 7-day-arc solution. The upper block results from a standard processing, whereas the lower one includes zero-mean conditions applied to the UT1 parameters

zero-mean condition w.r.t. the slope directly acts upon the average length of day. In analogy to the minimum constraints (3.12) that define the TRF, these new constraints are formulated as

$$(\mathbf{A}^\top \mathbf{A})^{-1} \mathbf{A}^\top \mathbf{u} = \mathbf{0} \quad (6.2)$$

where \mathbf{u} is a vector containing the UT1_{*i*} parameters, and \mathbf{A} is a $n \times 2$ matrix (with n equal to the number of UT1_{*i*} parameters) whose first column is populated with ones and whose second column contains the epochs associated to the UT1_{*i*} parameters. After applying this constraining, the correlations vanish as shown on the lower block of Fig 6.1. Note that, since the universal time values provided by the IERS C04 series are based on VLBI observations, our GNSS-based C_{20} estimates are arguably steered by the VLBI technique.

It has to be pointed out that the correlations between the C_{21} and S_{21} coefficients and PM coordinates are fully negligible. This seems in conflict with (1.50). Nonetheless, these equations give a theoretical realization of the (mean) PM, associated to the mass distribution of the Earth, whereas its practical realization relies on a kinematic principle, subject to the coordinates of a set of fiducial ground stations. It is probably, on the other hand, that such correlations manifest if, instead of the celestial mechanics approach, the inverse method is used to determine the gravity field.

6.3.3 Arc length selection

The length of the orbital arcs (section 2.6) is a defining variable of the orbit modeling. Longer arcs help to decorrelate the orbit parameters at the cost of increasing the effect of mismodeling, hence, the best compromise depends on the parameters of interest. In this section we evaluate the impact of the orbital arc length on the C_{20} estimates. Time series of the GNSS-derived gravity field have been computed using different arc lengths, namely, 1-day-arc, 3-day-arc, 5-day-arc, 7-day-arc and 9-day-arc solutions. In particular, the temporal evolution of the estimated C_{20} parameters is shown in Fig. 6.2.

In order to get rid of this rank defect, we include a more restrictive constraining over the universal time parameters in the shape of zero-mean conditions w.r.t. the bias and slope of the a priori values (for these solutions we are using the IERS C04-14 series, Bizouard et al., 2019, that contains VLBI-based UT1 information). The zero-mean condition w.r.t. the bias replaces the standard constraining (i.e., $UT1_4 = 0$), whereas the

As expected from the sensitivity analysis of section 6.3.1, the various solutions of Fig. 6.2 present a very high level of noise, which precludes the detection of the physical signal traced by the reference solution. We thus compute the RMS of the differences w.r.t. such a reference to evaluate the performance of the individual solutions, which yield $11.68 \cdot 10^{-10}$, $6.55 \cdot 10^{-10}$, $4.26 \cdot 10^{-10}$, $3.62 \cdot 10^{-10}$ and $3.68 \cdot 10^{-10}$ for the 1-day-arc, 3-day-arc, 5-day-arc, 7-day-arc and 9-day-arc solutions, respectively. This metric suggests the use of 7-day-arc solutions as baseline. However, due to its low statistical significance, the main motivation for us to definitively choose the 7-day-arc set-up is to better agree with the arc lengths employed in SLR processing (Geisser et al., 2023), facilitating a later joint analysis.

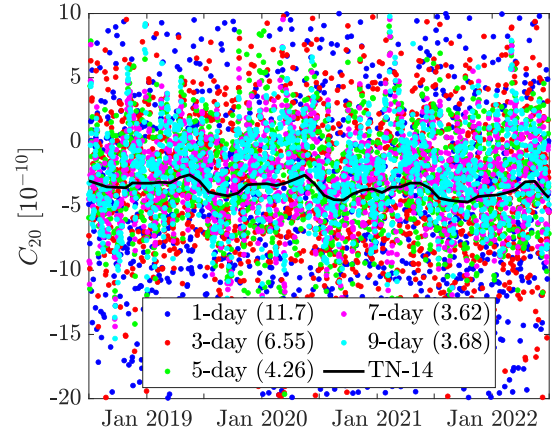


FIGURE 6.2: GNSS-derived C_{20} time series for different arc lengths (the EGM2008 constant value is subtracted from all the series). The RMS differences w.r.t. the reference are given in brackets with a scaling of 10^{10}

6.3.4 Data accumulation

In view of Fig. 6.2, to unveil time-variable gravity signals requires to assimilate larger batches of data. The common approach followed by the existing solutions consists in accumulating one month of data. For GRACE, daily NEQ are stacked (Meyer et al., 2012), whereas weekly NEQ are combined by SLR analysts (Geisser et al., 2023). In this section we test four different strategies to stack our weekly solutions (note that at this point the NEQ only contain Stokes' coefficients and UT1 parameters to impose the zero-mean conditions):

- Accumulation of 4 non-overlapping NEQ, amounting to 28 days of assimilated data (solution labeled as “NonOve30”).
- Accumulation of 24 overlapping NEQ, amounting to 30 days of assimilated data (solution labeled as “Ove30”).
- Accumulation of 9 non-overlapping NEQ, amounting to 63 days of assimilated data (solution labeled as “NonOve60”).
- Accumulation of 54 overlapping NEQ, amounting to 60 days of assimilated data (solution labeled as “Ove60”).

Note that the accumulated NEQ contain Stokes' coefficients and, additionally, ERP so that one single set of minimum constraints 6.2 is applied for the entire interval. Moreover, the window used to accumulate the data slides with daily steps, resulting in time series with daily resolution.

Figure 6.3 depicts the generated time series. To exemplify the role of using (6.2), the left panel includes an auxiliary solution labeled as “Ove60_Aux” that follows the same set-up as Ove60, but applying the standard constraining to the universal time parameters (recall, simply $UT1_4 = 0$). It clearly exhibits much larger spurious signals. The panel on the right-hand side excludes this degraded solution for a better visualization. It has to be pointed out that the strategy NonOve30 is in line with the

SLR processing standards and so it is the one that should be used in a joint processing. However, it is ruled out here because of its higher noise. On the other hand, the strategies NonOve60 and Ove60 seem to attenuate more spurious signals than their monthly counterparts, being Ove60 our preferred option due to its lower noise (the non-rigorous stacking of overlapping NEQ acts as a smoothing).

We refuse to further increase the time window of accumulated NEQ because that could leak important signals. In particular, the limiting theoretical sampling to capture semiannual signals equals three months according to the Nyquist theorem.

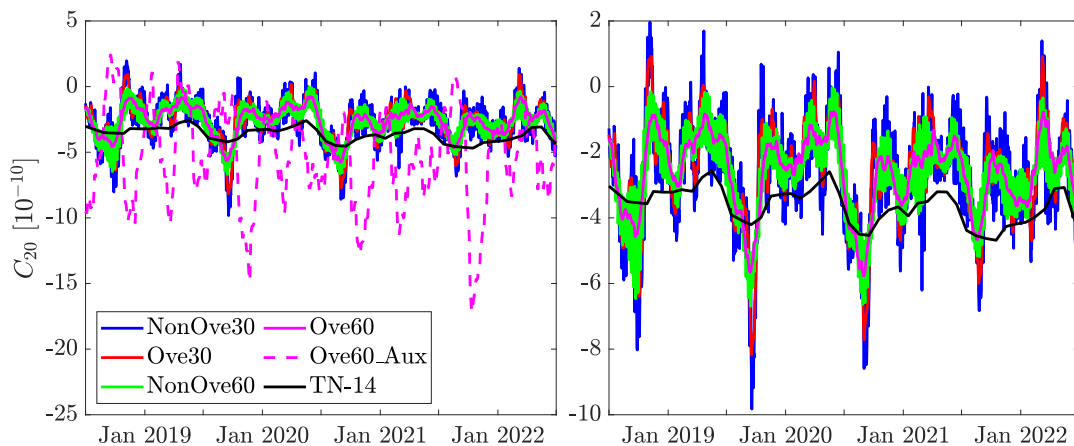


FIGURE 6.3: Different data accumulation strategies for the GNSS-derived C_{20} time series (w.r.t. EGM2008). The left panel shows the impact, through Ove60_Aux, of not applying (6.2), whereas the right panel omits this solution for a better visualization

6.3.5 Constraining of stochastic pulses

Because of the limited sensitivity to the gravity signals, small correlations between the parameters might significantly affect the gravity solutions. Correlation blocks between the estimated Stokes' coefficients and the orbit parameterization for a 7-day-arc solution on 2022/100 are shown in Fig. 6.4. These figures depict the extreme cases, i.e., maximum or minimum correlation index within all the parameters of the same type. Note that the orbit parameterization includes the initial state vector represented by orbital elements (section 1.6.1), the ECOM2 parameters, and stochastic pulses in the radial (p_R), along-track (p_S) and cross-track (p_W) directions. It is worth recalling from section 3.3.2 that the notation for the ECOM2 parameters matches the pattern $Ei_{(0/C/S)j}$, where i defines the direction ($E3$, $E2$ and $E1$ are the satellite-to-Sun direction, the axial direction of the satellite solar panels and a mutually orthogonal direction resulting in a left-handed frame), 0, C and S define the constant, cosine and sine contributions, respectively, and j the corresponding j th harmonic. The set-ups used to generate the panels of this figure only differ in the constraining of the stochastic pulses: The top panel agrees with our standard constraining, i.e., pulses constrained to zero with a STD of 10^{-6} m/s, 10^{-5} m/s and 10^{-8} m/s for p_R , p_S and p_W , respectively; the middle solution adds a more restrictive constraining of 10^{-7} m/s over p_S ; the bottom solution also includes this constraining along with a tight constraint of 10^{-7} m/s for p_R .

Theoretically, the reduction of the number of parameters produces stronger solutions, which is the motivation to test different empirical models. In particular, if a background SRP model is applied, the omission of the $E3_{C2}$ and $E3_{S2}$ parameters

might benefit some figures of the ERP and GCC geodetic estimates (Zajdel et al., 2020, Zajdel et al., 2021). However, since their correlations seem to be the least harmful (Fig. 6.4, top panel), and we only model SRP for Galileo, these parameters are not considered here for further analysis. Conversely, the most dangerous correlations appear between C_{20} and the $E1_0$ and $E2_0$ terms. These terms are paramount in orbit modeling and it was empirically verified that the solution is degraded as soon as one of them is excluded from the LS adjustment.

In another attempt to reduce the correlations between C_{20} and the ECOM2 parameters, a tailor-made empirical model was developed. To generate this model, we evaluated the projection of the acceleration caused by the Earth's oblateness onto the ECOM2 directions and created, from the original ECOM2 functions and the Gram-Schmidt orthogonalization, a set of functions orthogonal to such an acceleration profile. These functions were later used instead of the original ECOM2 functions. The outcome of this exercise was, however, unsuccessful since the mismodeling dominated the solution. Additionally, the original purpose, i.e., to mitigate the C_{20} correlations, was not satisfactory either because intermediate estimated parameters indirectly connect the new empirical parameters with C_{20} .

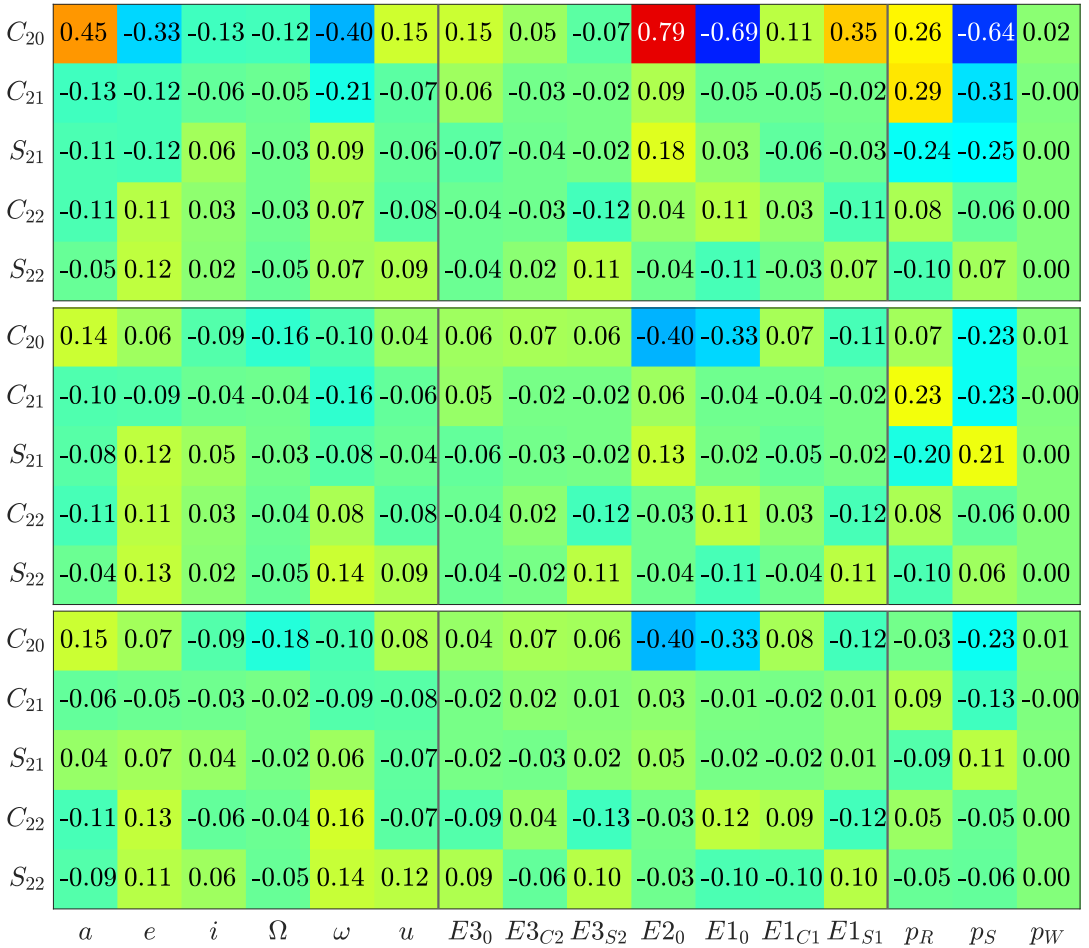


FIGURE 6.4: Correlation blocks between Stokes' coefficients and orbital parameters. Each panel uses a different constraining for the pulses p_R , p_S and p_W : 10^{-6} m/s, 10^{-5} m/s and 10^{-8} m/s for the upper panel; 10^{-6} m/s, 10^{-7} m/s and 10^{-8} m/s for the middle panel; and 10^{-7} m/s, 10^{-7} m/s and 10^{-8} m/s for the lower panel

Within the panels of Fig. 6.4 it is noticed that the stochastic pulses play a decisive

role in controlling the correlations. In the middle panel it can be seen that the more stringent constraining over p_S (10^{-7} m/s instead of 10^{-5} m/s) reduces not only its own correlation with C_{20} , but also the correlations arising from the orbital elements (especially for the semi-major axis), which hints that the pulses convey information between the parameters. Likewise, we have also observed that constraining the p_R parameters to 10^{-7} m/s (lower panel) turns out to be positive for the estimability of C_{21} and S_{21} . The overall impact that this constraining of p_S and p_R has in the gravity solutions is illustrated in the following section.

6.3.6 GNSS-based degree-2 gravity solutions

By applying the fine-tuning developed in previous sections, the time series of the GNSS-derived degree-2 coefficients have been generated and displayed in Fig. 6.5 with the label “GNSS”, whose average formal errors (considering 1 mm STD for the carrier phase observations) are depicted on the top right panel. The panels of this figure also show the reference solution for comparison purposes and an auxiliary solution (labeled “GNSS_Ini”) that follows from the initial constraining for the stochastic pulses. The direct inspection of these panels exemplifies the positive impact that the new constraining has over C_{20} , C_{21} and S_{21} , heavily alleviating spurious signals. The impact over C_{22} and S_{22} is, on the other hand, insignificant, as could be inferred from their much lower correlation indexes (Fig. 6.4).

In general, there is a good agreement between the GNSS and reference solutions, with correlation factors of 0.85, 0.78, 0.62, 0.83 and 0.89 for C_{20} , C_{21} , S_{21} , C_{22} and S_{22} , respectively, indicating that it is possible to estimate true gravity signals using the dynamics of GNSS orbits. Nonetheless, we can still see some discrepancies that deserve special mention. First, the GNSS-based C_{20} coefficient is biased w.r.t. the reference by $1.18 \cdot 10^{-10}$. The origin of this bias is uncertain as it could be a mixture of VLBI (owing to the minimum constraining of section 6.3.2), GNSS (through the orbital dynamics) and SLR (because of the reference solution) systematics. We shed further light on this in section 6.7. Secondly, the C_{21} and, above all, S_{21} coefficients contain suspicious signals, which are most probably artifacts. This poorer performance is indicated by their comparatively larger formal errors. The sectoral coefficients, on the other hand, perform the best, which can be explained by the polar gap rule-of-thumb (Gelderen and Koop, 1997).

In order to have a quantitative insight into the performance, bias, drift, annual and semiannual signals have been extracted from the time series, whose values are given in table 6.3. Except for the C_{20} bias, the GNSS signal components, and, particularly, the bias and drift, are in agreement with those of the reference solution, which indicates a good long-term estimability and increases the confidence in the solutions.

6.4 GNSS-specific estimation of degree-2 gravity signals

The fine-tuning and results presented so far are based on a multi-GNSS processing including GPS, Galileo and GLONASS. To evaluate the individual performance of each constellation, single-GNSS solutions are generated in this section, where the set-up developed in former analyses is inherited. To guarantee the consistency between the different solutions, the network of ground stations is reduced (from ~ 300 to ~ 200 stations) such that only multi-GNSS receivers simultaneously tracking the three systems are included. This reduced network was proven to produce multi-GNSS gravity solutions equivalent to the ones in section 6.3.6 (RMS differences in the order

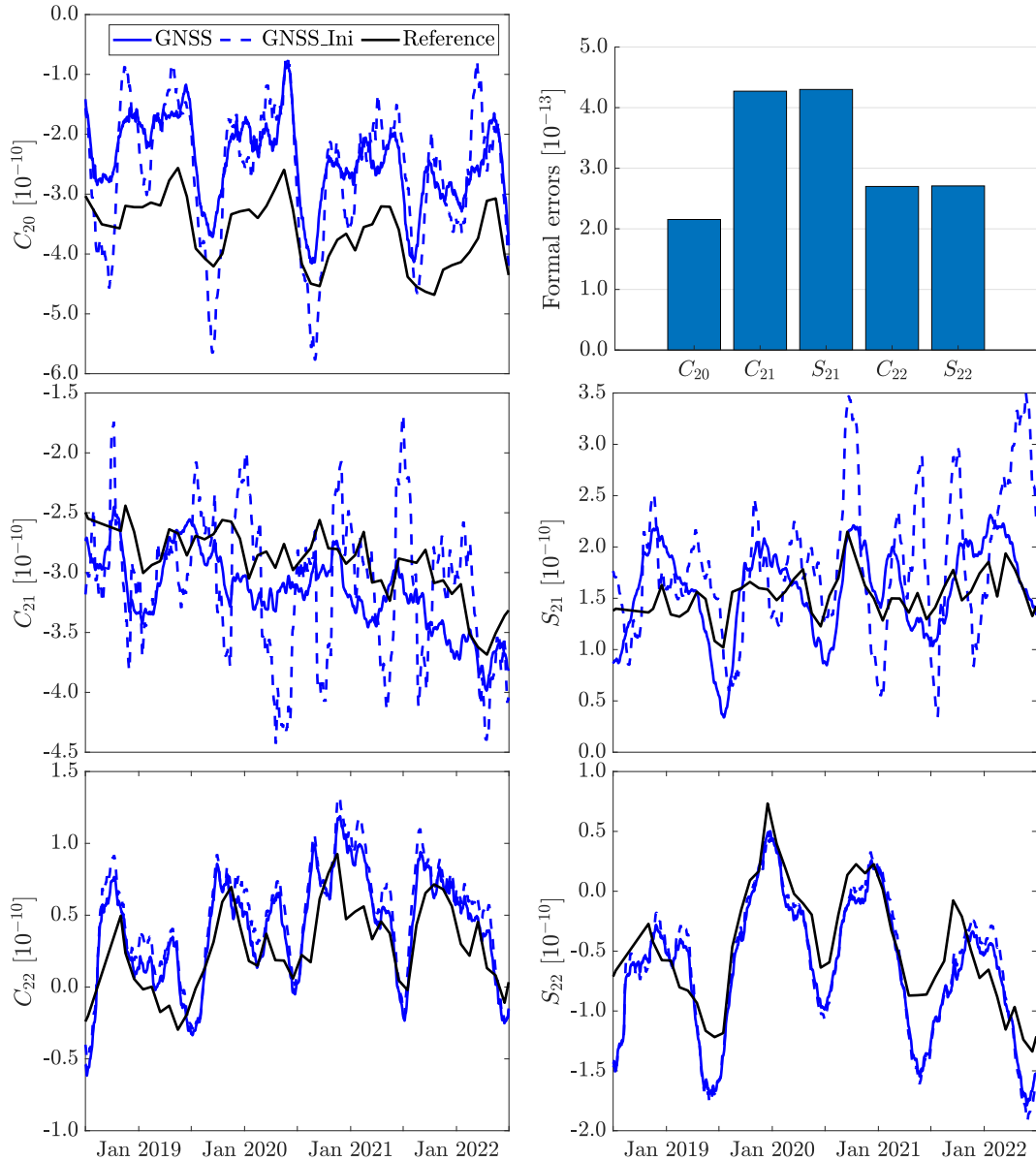


FIGURE 6.5: Time series of GNSS-derived degree-2 Stokes' coefficients (w.r.t. EGM2008) using the final set-up ("GNSS") and a preliminary set-up based on the standard constraining over the pulses ("GNSS_Ini"). The reference solutions follow from TN-14 or COST-G for C_{20} or the other coefficients, respectively. The top right panel shows the average formal errors of the GNSS solution

of 10^{-12}). Likewise, since we only apply a SRP background model for Galileo, it was also proven that disabling it does not lead to crucial variations in the Galileo-specific Stokes' coefficients (RMS differences in the order of 10^{-11}).

The correlation blocks between Stokes' coefficients and orbital parameters for GPS, Galileo and GLONASS are shown on the top, middle and bottom panels of Fig. 6.6, respectively. Likewise, the time series of the estimated solutions and their formal errors are given in Fig. 6.7, where the previously generated multi-GNSS solution is kept as reference.

The most meaningful feature that can be observed from Fig. 6.6 is the comparatively higher correlation numbers associated to the GPS-only C_{22} and S_{22} coefficients,

TABLE 6.3: Bias (w.r.t. EGM2008), drift, annual and semiannual signals for the degree-2 Stokes' coefficients resulting from multi-GNSS and single-GNSS solutions, along with the corresponding reference values. The bias, drift and signal amplitudes are scaled by 10^{10} , the drift represents yearly variations and the signal phases are given in degrees

		Bias	Drift	Annual Amp.	Annual Phase	Semi. Amp.	Semi. Phase
C_{20}	GNSS	-1.85	-0.30	0.60	-101.63	0.49	-83.55
	GPS	-1.76	-0.36	0.52	-104.18	0.25	-95.06
	Gal	-2.04	-0.18	1.01	-111.13	1.29	-97.42
	GLO	-1.60	-0.27	0.90	-76.23	0.69	-34.85
	TN-14	-3.03	-0.30	0.57	-89.09	0.30	-86.78
C_{21}	GNSS	-2.79	-0.19	0.17	37.57	0.06	-97.34
	GPS	-2.80	-0.15	0.12	75.40	0.14	-58.05
	Gal	-3.01	-0.14	0.49	-2.78	0.18	-145.35
	GLO	-2.16	0.14	1.13	159.18	0.20	-246.50
	COST-G	-2.57	-0.17	0.15	85.82	0.00	-92.69
S_{21}	GNSS	1.39	0.10	0.50	171.49	0.20	195.11
	GPS	1.36	0.11	0.63	183.24	0.20	211.62
	Gal	1.34	0.03	0.43	188.51	0.39	145.59
	GLO	0.87	0.33	1.06	139.21	0.26	254.02
	COST-G	1.38	0.08	0.10	140.57	0.12	170.65
C_{22}	GNSS	0.18	0.12	0.33	143.52	0.20	-178.01
	GPS	-0.06	-0.16	0.91	124.13	0.69	-136.74
	Gal	0.49	0.14	0.51	142.64	0.14	-243.86
	GLO	-0.06	0.12	0.26	136.95	0.30	-169.39
	COST-G	0.03	0.12	0.28	131.71	0.12	-158.78
S_{22}	GNSS	-0.57	-0.03	0.63	160.19	0.12	124.99
	GPS	-1.11	0.20	3.22	315.09	0.63	152.14
	Gal	-0.38	0.00	1.00	170.26	0.26	132.02
	GLO	-0.56	-0.09	0.51	146.71	0.10	137.24
	COST-G	-0.39	-0.04	0.43	140.37	0.07	164.32

which turn out to be resonant terms due to the 2:1 ratio between the GPS orbital period and the Earth's rotation (Kaula, 2013, section 3.6). This coupling debilitates the estimability of such coefficients, which also manifests in the corresponding formal errors, given on the top right panel of Fig. 6.7. The bottom panels of this figure definitively confirm that the GPS-only C_{22} and S_{22} solutions are clearly polluted. In contrast, the corresponding multi-GNSS solution is mainly driven by the GLONASS constellation. This behavior was already explained by Ineichen et al., 2003. The remaining C_{20} , C_{21} and S_{21} solutions are steered by the GPS constellation, being the C_{21} and S_{21} coefficients especially badly estimated with the GLONASS orbits. This poor performance is reflected in the corresponding formal errors, although, at the time of writing, the reason is not known.

In relation with the Galileo solutions, these are not outstanding for any coefficient. It can be speculated that the main reason for this misbehavior is its higher orbital altitude (more than 3000 km higher than the altitude for GPS and GLONASS). The interested reader may still claim that this should be reflected in the formal errors, which are comparatively better than for the GLONASS constellation. However, unlike for Galileo, phase ambiguities are not resolved during the GLONASS-only

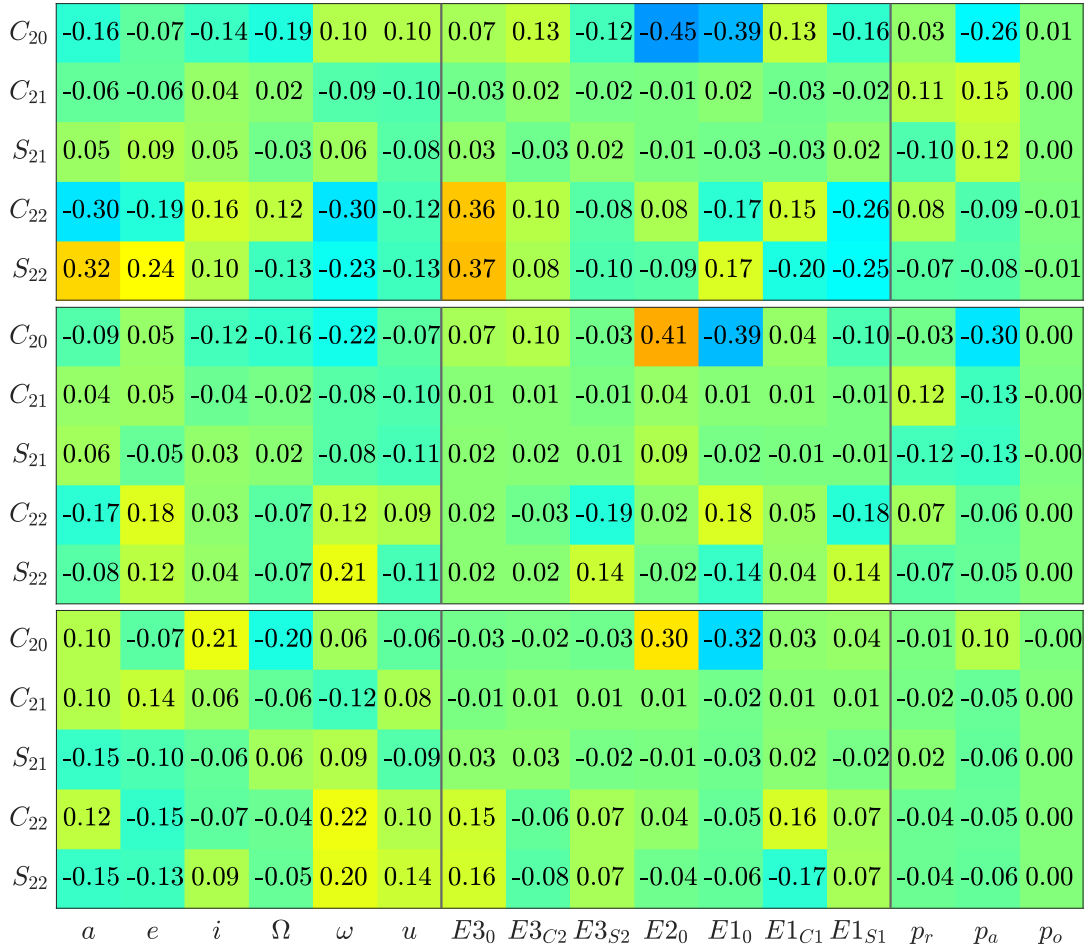


FIGURE 6.6: Correlation blocks between Stokes' coefficients and orbital parameters for GPS- (top), Galileo- (middle) and GLONASS-only (bottom) solutions

processing, resulting in a weaker model that can ultimately increase the formal errors of the various parameters above the ones of Galileo.

The bias, drift, annual and semiannual signals of these solutions are also given in table 6.3. Although single-GNSS solutions can show better metrics (w.r.t. the reference) than the multi-GNSS solution for some specific components (e.g., see annual signal for the GLONASS-only C_{22} coefficient), the multi-GNSS solution has the best overall performance.

6.5 Higher order GNSS-derived gravity signals

We have extended the gravity field parameterization up to degree-4 for the present exercise. The average formal errors of the resulting coefficients are shown in Fig. 6.8. For comparison reasons, this figure also includes the corresponding metrics from the degree-2 solutions (i.e., Fig. 6.5, top right panel). It is observed that the errors for the second-degree coefficients get worse due to new correlations: The parameters C_{20} , C_{21} , S_{21} , C_{22} and S_{22} correlate with C_{40} , C_{41} , S_{41} , C_{42} and S_{42} , respectively, with correlation indexes of about 0.8. This order- and parity-wise coupling is well-known, being its underlying mechanism explained by the so-called lumped coefficient approach

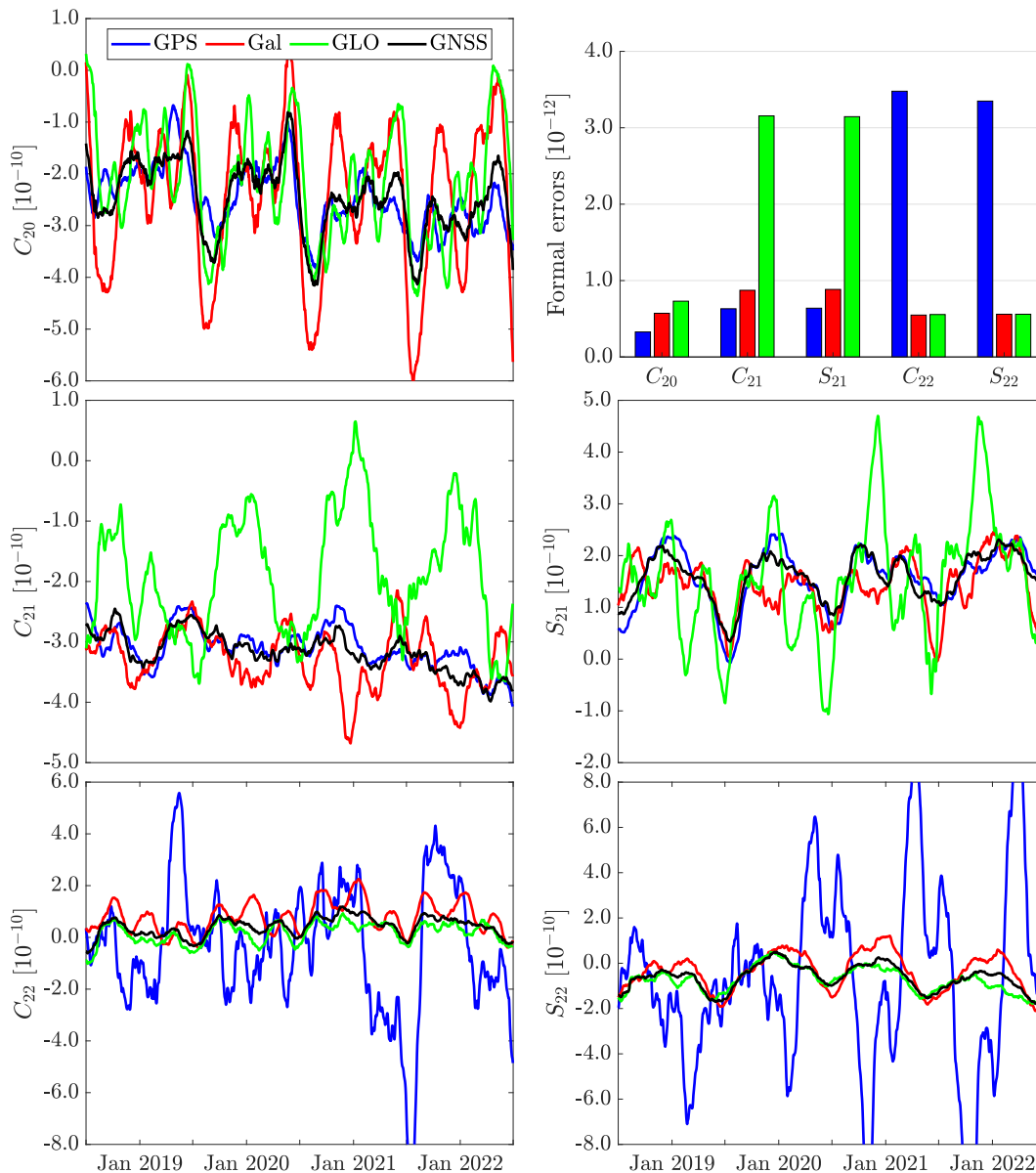


FIGURE 6.7: Time series of degree-2 Stokes' coefficients (w.r.t. EGM2008) derived from single-GNSS solutions. The top right panel shows their average formal errors

(Sneeuw, 2000), which allows to formulate the gravity recovery problem by means of order-wise equations.

Because of the existing difficulties found when estimating degree-2 coefficients, the comparatively higher formal errors for the new higher degree coefficients hint that these are very poorly estimated. Indeed, this is confirmed in table 6.4, which includes the bias, drift, annual and semiannual signals extracted from the freshly computed time series, as well as the corresponding values for the reference solutions. We have to firstly highlight the worse performance observed for the new degree-2 signal components in comparison with the previously computed values, which better fitted the reference figures (recall table 6.3). Moreover, the degree-3 and degree-4 estimated signals are mostly spoiled by the presence of artifacts, as can be presumed from their unrealistically big annual amplitudes. From these amplitudes (and in line with the formal errors), we deduce that the sectoral C_{33} and S_{33} terms are best

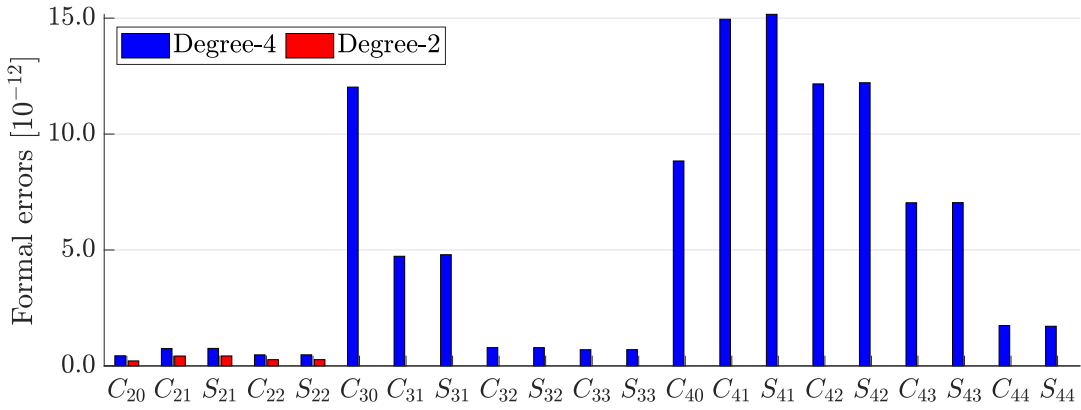


FIGURE 6.8: Average formal errors for the GNSS-based Stokes' coefficients estimated up to degree-4. The corresponding degree-2 metrics are included for the sake of comparison

estimated, yet still containing pervasive spurious signals, as become evident from Fig. 6.9.

We finally conclude that other than degree-2 gravity coefficients are very weakly estimated, debilitating also the degree-2 time series. Nonetheless, these coefficients could be included into the GNSS-derived NEQ in a multi-technique processing, as long as the weighting scheme makes those higher order coefficients steer by the most capable technique (e.g., SLR).

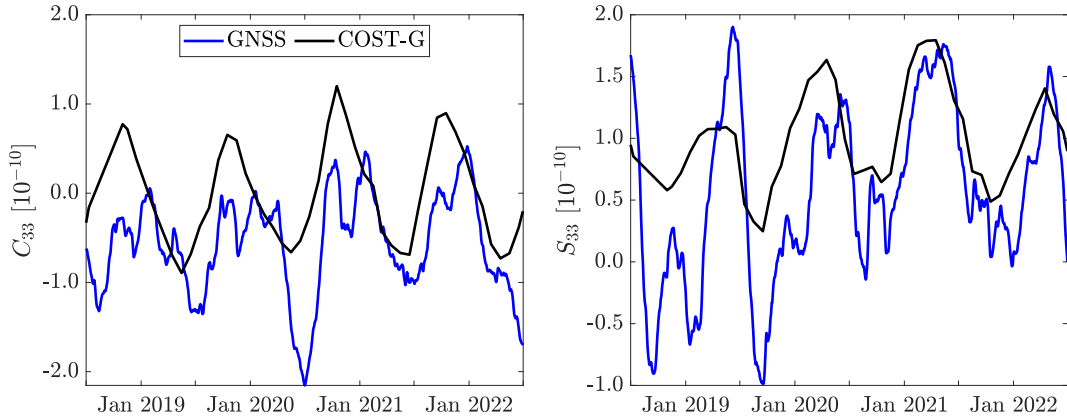


FIGURE 6.9: Time series of GNSS-derived C_{33} and S_{33} coefficients (w.r.t. EGM2008)

6.6 GNSS network solutions based on time-variable gravity field models

We do not recommend to co-estimate gravity field parameters during the generation of geodetic GNSS network solutions, since the relatively small amount of assimilated observations employed by the different ACs in their regular products (e.g., 3-day-arc solutions for the CODE final products, Dach et al., 2020) do not allow to retrieve realistic gravity signals (Fig. 6.2). Consequently, these parameters would mostly absorb noise, losing their statistical significance and weakening the model. Nonetheless, the use of time-variable gravity background models, if available, might still benefit the geodetic solution itself, which is evaluated herein.

TABLE 6.4: Bias (w.r.t. EGM2008), drift, annual and semiannual signals for the degree-4 Stokes' coefficients. The bias, drift and signal amplitudes are scaled by 10^{10} , the drift represents yearly variations and the signal phases are given in degrees

		Bias	Drift	Annual Amp.	Annual Phase	Semi. Amp.	Semi. Phase
C_{20}	GNSS	-2.00	-0.27	0.80	-113.52	0.66	-116.96
	TN-14	-3.03	-0.30	0.57	-89.09	0.30	-86.78
C_{21}	GNSS	-2.86	0.05	0.41	66.92	0.14	-103.19
	COST-G	-2.57	-0.17	0.15	85.82	0.00	-92.69
S_{21}	GNSS	1.57	0.07	0.66	192.80	0.38	183.33
	COST-G	1.38	0.08	0.10	140.57	0.12	170.65
C_{22}	GNSS	0.22	0.16	0.31	170.67	0.09	-121.56
	COST-G	0.03	0.12	0.28	131.71	0.12	-158.78
S_{22}	GNSS	-0.59	-0.01	0.66	170.17	0.10	211.49
	COST-G	-0.39	-0.04	0.43	140.37	0.07	164.32
C_{30}	GNSS	-3.14	0.03	8.35	-184.28	6.75	-70.55
	TN-14	-0.12	-0.07	0.71	-85.88	0.06	-55.23
C_{31}	GNSS	0.45	0.64	2.15	-315.72	2.60	137.75
	COST-G	-0.08	-0.17	0.11	-177.60	0.03	58.22
S_{31}	GNSS	-0.61	0.39	3.37	-29.59	1.35	-153.27
	COST-G	0.60	0.06	0.42	-58.85	0.03	19.83
C_{32}	GNSS	-1.85	-0.15	1.64	56.87	0.27	132.59
	COST-G	-0.72	-0.03	0.02	-6.52	0.04	42.48
S_{32}	GNSS	0.22	-0.64	0.65	-172.98	0.39	-4.99
	COST-G	-0.36	-0.17	0.52	-82.94	0.03	-151.19
C_{33}	GNSS	-0.69	0.06	0.62	165.62	0.18	161.77
	COST-G	-0.10	0.05	0.74	119.93	0.08	178.48
S_{33}	GNSS	0.30	0.13	0.67	-59.00	0.28	-74.98
	COST-G	0.91	0.04	0.43	-92.45	0.02	-158.98
C_{40}	GNSS	4.10	-0.37	5.64	35.36	8.71	12.27
	COST-G	-0.43	0.03	0.17	-5.52	0.11	-84.68
C_{41}	GNSS	2.16	-5.52	6.95	-100.16	2.16	84.36
	COST-G	-1.02	-0.18	0.40	-68.90	0.01	127.13
S_{41}	GNSS	-4.22	0.42	6.50	49.54	4.29	-9.39
	COST-G	-0.32	-0.05	0.15	-99.62	0.02	-52.39
C_{42}	GNSS	1.34	1.34	4.36	-96.16	4.98	-24.19
	COST-G	-0.53	0.05	0.11	54.68	0.08	32.07
S_{42}	GNSS	-0.06	0.75	4.04	-118.98	4.26	-95.13
	COST-G	0.12	-0.05	0.64	-67.91	0.03	82.03
C_{43}	GNSS	-8.86	0.32	2.57	54.58	4.31	37.47
	COST-G	0.20	-0.05	0.13	-103.65	0.03	44.39
S_{43}	GNSS	12.60	-4.12	3.72	-135.25	2.63	153.98
	COST-G	0.56	0.00	0.18	-113.55	0.09	-57.64
C_{44}	GNSS	0.51	-0.39	1.03	97.39	1.02	-51.08
	COST-G	0.60	-0.05	0.81	105.30	0.06	-96.52
S_{44}	GNSS	-0.53	0.20	1.90	32.30	0.55	129.88
	COST-G	0.27	0.08	0.39	-64.49	0.04	-6.12

The impact of modeling the time-variable gravity field during the GNSS network processing is assessed by comparing three solutions generated from the same standard procedure (in particular, 3-day-arc solutions with nominal pulses constraining of 10^{-6} m/s, 10^{-5} m/s and 10^{-8} m/s in the radial, along-track and cross-track directions), but varying the “static” part of the geopotential, namely, a first solution in accord with the model from the IERS Conventions up to degree-12 (label “IERS”), a second solution using the estimated degree-2 gravity signals (Fig. 6.5) complemented by the IERS Conventions for the higher degrees (label “GNSS”), and a third solution using the COST-G FSM (label “FSM”). The choice of the FSM rather than the original COST-G gravity fields is not arbitrary, since the FSM can be used during the generation of IGS operational products (even for real time applications) without the latency associated to the regular COST-G monthly solutions (Peter et al., 2022).

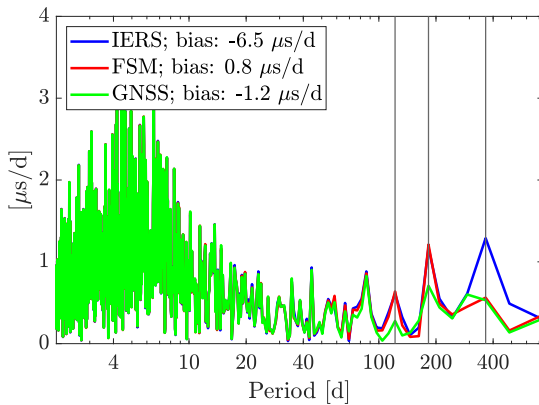


FIGURE 6.10: Amplitude spectra of the differences between GNSS-based LOD solutions and the C04-14 series. Annual, semiannual and triannual periods marked with vertical lines

The midnight orbit misclosures show identical internal consistency (only sub-millimeter discrepancies between the figures), whereas the cross-comparisons of the resulting orbits depict differences of 2-3 mm in 3D-RMS, with a better synergy between the GNSS and FSM solutions, which indicates, as expected from table 6.1, that other than degree-2 gravity signals are almost negligible for GNSS orbit modeling. In any case, these metrics do not permit to make any strong statement about the quality of the orbits, or, equivalently, the associated realization of the terrestrial frame. If we inspect, on the other hand, the estimated time series for the PM coordinates, we do not see a significant impact either (RMS differences below $1 \mu\text{s}$). On the contrary, the various time series for the LOD estimates do have fine distinctions that manifest when they are compared against the C04-14 series, as expected from (6.1). The amplitude spectra of these comparisons is given in Fig. 6.10. The IERS solution contains the largest bias ($-6.5 \mu\text{s}/\text{d}$), which is moved close to zero for the FSM and GNSS solutions ($0.8 \mu\text{s}/\text{d}$ and $-1.2 \mu\text{s}/\text{d}$, respectively). This is a very meaningful finding, since we know that the cumulative GNSS-based LOD series diverges from the VLBI-based UT1 solutions (tables 5.1 and 5.3). We can now explain such an excursion, to a certain extent, by deficiencies in C_{20} . However, system-specific differences are still expected because of the different C_{20} biases and drifts recovered by GPS, Galileo and GLONASS (table 6.3). At the middle epoch of the processing interval, their corresponding C_{20} shifts w.r.t. the multi-GNSS solution amount to $-0.03 \cdot 10^{-10}$, $0.05 \cdot 10^{-10}$ and $0.31 \cdot 10^{-10}$, which, by using (6.1), are expressed in LOD variations of $0.06 \mu\text{s}/\text{d}$, $-0.06 \mu\text{s}/\text{d}$ and $-0.52 \mu\text{s}/\text{d}$, respectively. A further insight into Fig. 6.10 also reveals a reduction of the annual harmonic when a time-variable gravity field is used (from $1.29 \mu\text{s}/\text{d}$ for IERS to $0.56 \mu\text{s}/\text{d}$ for both FSM and GNSS), as well as improvements for the semiannual (from $1.21 \mu\text{s}/\text{d}$ to $0.70 \mu\text{s}/\text{d}$) and triannual (from $0.63 \mu\text{s}/\text{d}$ to $0.28 \mu\text{s}/\text{d}$) signals for the GNSS solution. The better performance of this solution is expected by construction, since it is a direct consequence of the application of a zero-mean condition w.r.t. the slope of the universal time parameters.

The midnight orbit misclosures show identical internal consistency (only sub-millimeter discrepancies between the figures), whereas the cross-comparisons of the resulting orbits depict differences of 2-3 mm in 3D-RMS, with a better synergy between the GNSS and FSM solutions, which indicates, as expected from table 6.1, that other than degree-2 gravity signals are almost negligible for GNSS orbit modeling. In any case, these metrics do not permit to make any strong statement about the quality of the orbits, or, equivalently, the associated realization of the terrestrial frame. If we inspect, on the other hand, the estimated time series for the PM coordinates, we do not see a significant impact either (RMS differences below $1 \mu\text{s}$).

6.7 Mapping of the relativistic orbit precession into the Earth's oblateness

General relativity effects acting upon the orbits of artificial satellites in the vicinity of the Earth can be accounted for by applying three main acceleration terms when propagating the equations of motion (Brumberg and Kopejkin, 1989): The Schwarzschild term, the Lense-Thirring effect and the de Sitter effect. Disregarding these effects results in 3D-RMS orbital errors for the GNSS satellites of about 20 cm, 1 mm and 1 cm, respectively, over the course of one day. Consequently, only the most notable Schwarzschild term has become part of the IGS processing standards, being the others safely neglected.

Sośnica et al., 2021 thoroughly assess the impact of these relativistic effects on the Galileo orbits. It is stressed that both the Lense-Thirring and de Sitter effects cause a precession in the orbit ascending nodes. The latter contributes by $53 \mu\text{s}/\text{d}$ to the total precession (independent of the orbital geometry), whereas the secular contribution of the former is given by

$$\Delta\dot{\Omega}_s = 2 \frac{GMJ}{c^2 a^3 (1 - e^2)^{3/2}} \quad (6.3)$$

where G , M , a , e and c are, in line with the notation followed so far, the gravitational constant, the Earth's mass, the orbit semi-major axis, the orbit eccentricity and the speed of light in vacuum. The new J symbol represents the magnitude of the Earth's angular momentum per unit mass ($\approx 9.8 \cdot 10^8 \text{ m}^2/\text{s}$). Evaluating (6.3), it is obtained a secular precession of $8 \mu\text{s}/\text{d}$, $6 \mu\text{s}/\text{d}$ and $9 \mu\text{s}/\text{d}$ for GPS, Galileo and GLONASS, respectively, being mapped into total (i.e., Lense-Thirring plus de Sitter) C_{20} variations of $2.1 \cdot 10^{-10}$, $3 \cdot 10^{-10}$ and $2.4 \cdot 10^{-10}$, according to (6.1). If we average these numbers using the square inverse of the GNSS-specific C_{20} formal errors ($0.32 \cdot 10^{-12}$, $0.57 \cdot 10^{-12}$ and $0.73 \cdot 10^{-12}$ from Fig. 6.7) as weights, we then recover a theoretical C_{20} variation of $2.3 \cdot 10^{-10}$ for the multi-GNSS solution.

The degree-2 gravity field results of section 6.3.6 have been repeated, but including the Lense-Thirring and de Sitter effects as part of the orbit modeling. This new solution ("GNSS_Rel") is shown in Fig. 6.11. It differs from the previous solution mainly by a $2.3 \cdot 10^{-10}$ shift, which perfectly matches our theoretical expectation. Note that this new GNSS-based C_{20} solution no longer compensates the relativistic precession and, therefore, it is dragged downwards. Although the bias w.r.t. the reference exhibited by the GNSS_Rel solution is similar in magnitude to the bias of the GNSS solution, the new solution better fits our internal SLR realization of C_{20} (labeled as "SLR" in Fig. 6.11), which follows from Geisser et al., 2023. Therefore, those relativistic corrections should be modeled in a combined GNSS-SLR processing.

We shall close this section by highlighting some truly profound implications that stem from the good agreement between the GNSS_Rel and SLR C_{20} time series:

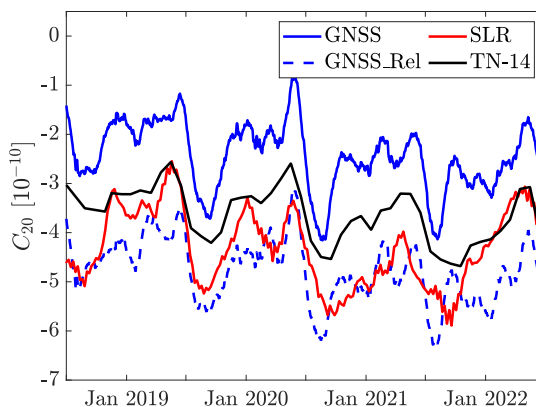


FIGURE 6.11: GNSS- and SLR-derived C_{20} time series (w.r.t. EGM2008)

Since our GNSS realization is steered by a new constraint based on VLBI-derived universal time information, that agreement actually indicates a good GNSS-SLR-VLBI consistency. Additionally, the necessity to apply the otherwise neglected Lense-Thirring and de Sitter effects is another observational evidence supporting the general relativity theory.

6.8 Summary

In this chapter we have analyzed the GNSS capabilities to sense and estimate the long-wavelength time-variable gravity field (with special focus on degree-2 coefficients) applying the celestial mechanic approach, as well as its impact over the geodetic solutions. The motivation to conduct this study is two-fold: On the one hand, the community has paid very little attention to this topic and so new results can be highly appreciated; on the other hand, any rigorous GNSS-SLR combined analysis shall consider as many common parameters as possible, for which the Stokes' coefficients may act as common global ties.

The GNSS sensitivity to time-variable gravity signals is really discouraging since accounting for such signals was found to only produce millimeter (for the degree-2 coefficients) or sub-millimeter (for the remaining coefficients) orbit variations, which is beyond the GNSS orbital accuracy. Additionally, the estimation of C_{20} is hampered by a rank defect involving this quantity and the LOD. Therefore, to separate both contributions, we included a zero-mean condition w.r.t. the slope of the universal time parameters given by the C04-14 series. The conceptual consequence of this constraint is that our GNSS C_{20} estimate is arguably defined by VLBI observations.

Our standard GNSS processing was fine-tuned so that the estimated degree-2 gravity coefficients eventually represented actual gravity signals as inferred from the direct comparisons with some state-of-the-art references (correlation factors of 0.85, 0.78, 0.62, 0.83 and 0.89 for C_{20} , C_{21} , S_{21} , C_{22} and S_{22} , respectively). In particular, the orbital arc length was broadened to one week, the resulting NEQ were accumulated to assimilate two months of observations and the stochastic pulses were applied with a tighter constraining. This constraining is necessary to decorrelate along-track pulses and C_{20} parameters, as well as radial pulses and C_{22} and S_{22} parameters. Interestingly, it was observed that GPS contributes the most to the estimation of C_{20} , C_{21} and S_{21} , whereas the contribution to the C_{22} and S_{22} terms, which are resonant terms for the GPS constellation, mainly comes from GLONASS. The Galileo constellation does not play an important role for any coefficient, presumably due to its higher altitude.

A further effort to expand the gravity field parameterization to degree-4 turned out to be pointless, since only artifacts were observed in the resulting time series. Therefore, if these coefficients are considered in a multi-technique processing, we have to ensure that the observations are so weighted that those coefficients stem from the more capable technique (e.g., SLR).

The influence that the time variable gravity field has on the GNSS network solutions was evaluated by using the previously generated GNSS-based degree-2 estimates as well as the COST-G FSM as background models that replace the IERS Conventions for the static part of the geopotential. The only geodetic parameter that experienced a significant impact was the LOD, which reduced its bias and some annual harmonics when compared against the C04-14 series. This observed enhancement is enough to recommend the use of the COST-G FSM for the generation of IGS products (already implemented in the operational CODE processing).

Due to the connection between the orbit ascending nodes and C_{20} , any perturbation affecting the precession of the orbits can be mapped into the C_{20} parameter. In particular, this was observed for the Lense–Thirring and de Sitter effects, which are two relativistic contributions typically neglected in GNSS processing. When these accelerations were applied, the GNSS C_{20} series were shifted by $2.3 \cdot 10^{-10}$, placing them close to an internally generated SLR-based solution. This good agreement has a very profound meaning because, all in all, it can be interpreted as a consistency measure between GNSS, SLR, VLBI and the general relativity theory.

Summary, conclusions and outlook

This dissertation has covered methods and algorithms for undifferenced multi-GNSS global network processing and applications to satellite geodesy. Conceptually, the six core chapters over which the content has been exposed can be grouped into two parts:

- An introductory part (encompassing the first three chapters) has been devoted to elaborating on basic principles and fundamentals. Initially, we discussed the physical interpretation of the quantities derived when reducing the GNSS observations (i.e., the connection between ERP, GCC, and the time-variable gravity field with Earth's angular velocity and surface water processes), aiming to provide an attractive introduction to the geodetic results that are at the core of this dissertation.

The topic of parameter estimation was also covered from an atypical perspective, where we mostly focused on specific results that are not usually treated in general literature. Namely, the equivalence between our undifferenced processing scheme and the legacy differenced processing schemes, the mathematical idea underlying the AR algorithms, and the methodology to generate long-arc orbital solutions from daily NEQ. In our context, these results are of conceptual interest and hence, grant extra value to the dissertation overall.

This introductory part concludes with an overview of the models employed to generate our GNSS solutions. Although the scope of this dissertation precludes an in-depth analysis of the GNSS observation model, our discussion remains comprehensive, and every contribution of the model is discussed or referenced. Additionally, the implemented processing strategy used to derive global GNSS solutions is presented. Here, it was stressed that the stations are processed in parallel as much as possible to reduce the computational burden. During the validation of the results, we observed that our solutions are at a competitive level when compared against the state-of-the-art solutions produced by CODE (satellite orbits and SIS range precision superior to 3 cm and 10 ps, respectively), which serves as a starting point to focus on other geodetic results.

- The central part comprises the three remaining chapters and presents the geodetic results and innovations. We began developing a novel AR algorithm specifically designed for our undifferenced processing strategy, which could prove beneficial when processing sizable GNSS networks. The algorithm is based on the inspection of real-valued ambiguities while considering the theoretical foundations of AR. This allowed us to properly apply integer rounding, integer bootstrapping, and ILS estimators at different stages of the algorithm, enhancing both efficiency and robustness. The general AR metrics were at a

competitive level, with ambiguity residuals and rates around 0.1 cycles and 90%, respectively.

By means of several exercises, we provided an instructive view on the GNSS capabilities to derive ERP and GCC, where several known problems related to spurious signals in the time series were exemplified. It was shown that the current precision for the PM and LOD estimates is about 40 – 50 μs and 25 $\mu\text{s}/\text{d}$, respectively. Furthermore, annual and semiannual signals of GNSS- and SLR-based GCC differ by about 1 mm.

We finally evaluated the role that the time-variable part of the gravity field has in GNSS processing. This topic poses a nearly virgin scenario, since it has received very little attention in the specialized literature. We firstly observed that, after a thorough fine-tuning, the derived GNSS-based degree-2 gravity solutions correlate above 80% with state-of-the-art SLR-based solutions. More importantly, it was found that the known bias between the GNSS- and VLBI-based LOD estimates is mainly explained by C_{20} mismodeling: Using the COST-G solutions as background static gravity field reduces the bias from $-6.5 \mu\text{s}/\text{d}$ to $0.8 \mu\text{s}/\text{d}$. Additionally, the otherwise neglected relativistic perturbations due to the Lense-Thirring and the de Sitter effects become noticeable by the C_{20} estimates.

The work carried out in this dissertation could be complemented or extended in many regards. Three major lines of research as a natural continuation are:

- Although we have successfully generated undifferenced GNSS global solutions using the BSW for the first time, our processing method still has certain limitations. Primarily, we are currently processing IF observations and only utilizing two frequencies per constellation and ground station. Apart from technical constraints, this prevents us from accessing to the entire set of OSB, which has to be complemented by an independent solution based on GF observations. The current trends in the GNSS community circumvent this issue by employing undifferenced and uncombined observations, which represent the natural strategy for processing every available GNSS signal. Incorporating this approach into our procedures stands as an important pending task for the future.
- There is a strong coupling between the orbits and the clock corrections, which may produce systematic errors of about 1 cm in the orbital radial direction, as became obvious from Fig. 3.14. Over the years, huge efforts have been dedicated to improve the quality of the orbits (and, by extension, the quality of the geodetic solutions) through novel modelings and parameterizations. However, improvements could also be achieved by modeling the clock corrections instead, which is technically possible when processing undifferenced observations. This is a very challenging task, since it requires to process all the clock parameters together, very badly affecting the computational burden. Additionally, the clock corrections not only absorb the stochastic behaviour of the satellite oscillators, but also other physical effects (such as deviations from nominal attitude or thermal effects). Nevertheless, properly constraining the clock parameters (e.g., by reducing those signals occurring with orbital period) could lead to an important breakthrough in future GNSS-based solutions.
- Geodetic solutions of superior quality could be generated by combining observations from different scenarios, so that the estimability of the parameters is improved. For instance, as part of the Space Tie Project, it was shown that

including LEO satellites (some of which placed in polar orbits) into the global GNSS processing helps to decorrelate the z GCC. Similarly, improvements are also expected if observations from the main geodetic techniques (i.e., SLR, VLBI and DORIS) are jointly processed. The implementation and standardization of procedures combining an eclectic variety of observations is another important milestone that could be achieved in the near future as a continuation of the present work.

GNSS processing strategy

Solution interval	<p>Four-year time series: July 2018 to June 2022.</p> <p>When consecutive days (e.g., for 3-day arc solutions) of data are accumulated, the middle day gives the effective epoch of the time series and, hence, the interval of the assimilated observations is somewhat wider than the interval of the time series.</p>
Observations	<p>UD pseudorange and phase measurements from a network with about 300 stations.</p> <p>Multi-GNSS (i.e., GPS, Galileo and GLONASS) processing.</p> <p>GPS signals: IF L1/L2; Galileo signals: IF E1/E5a; GLONASS signals: IF G1/G2.</p> <p>Pseudorange measurements down-weighted by a factor of 100^2 w.r.t. phase measurements.</p> <p>Cut-off angle of 5° with elevation-dependent weighting ($\sin^2(e)$ law, being e the elevation angle).</p> <p>Observations processed with a 300 s sampling.</p>
Observation nuisance terms	<p>Resolved phase ambiguities for GPS and Galileo removed from the observations (chapter 4).</p> <p>Calibrated OSB removed from the observations (Villiger et al., 2019).</p> <p>Estimated unresolved ambiguities.</p> <p>Estimated epoch-wise receiver and satellite clock corrections. The relativistic clock correction originating from the orbital eccentricity is removed from the satellite clock estimates in accord with Ashby, 2003.</p>
Signal propagation delays	<p>First order ionospheric delays eliminated by using IF observations.</p> <p>Applied corrections to eliminate higher order ionospheric delays and ray-bending (Brunner and Gu, 1991 and Bassiri and Hajj, 1993) based on GIM (Schaer et al., 1996).</p> <p>Applied corrections to eliminate the Shapiro effect (Ashby, 2003).</p> <p>Applied corrections to eliminate the phase wind-up effect (Wu et al., 1992).</p> <p>Estimated VMF1 (Boehm and Schuh, 2004) piece-wise linear troposphere parameters with 2-hour sampling and loose relative constraints of 1 m in STD.</p> <p>Estimated tropospheric gradients (Chen and Herring, 1997) with daily resolution.</p>

Terrestrial reference frame	<p>IGS realization of ITRF2020 (Altamimi et al., 2023) and corresponding antenna model. The nonlinear seasonal signals are not applied.</p> <p>Estimated station coordinates.</p> <p>Datum defined by NNT and NNR constraints over fiducial sites, after their verification: Maximum allowed deviation in horizontal and up displacements equal to 1 cm and 3 cm, respectively.</p> <p>Solid Earth tides, pole tides and ocean pole tides in agreement with IERS Conventions.</p> <p>Ocean tidal loading corrections based on FES2014b (Carrère et al., 2016).</p>
Attitude modeling	<p>GPS: Kouba, 2009a; Galileo: Galileo satellite metadata^a GLONASS: Dilssner et al., 2011.</p>
Earth's orientation	<p>Precession and nutation: IAU2006A (Mathews et al., 2002, Mathews and Bretagnon, 2003).</p> <p>Sub-daily polar motion originating from ocean tides and libration according to Desai and Sibois, 2016.</p> <p>Estimated piece-wise linear ERP with continuity condition and daily resolution.</p>
Orbit modeling	<p>3-day-arc orbital solutions (Beutler et al., 1996).</p> <p>Static gravity field up to degree-12: IERS Conventions; solid Earth tides: IERS Conventions; ocean tides up to degree-8: FES2014b (Carrère et al., 2016); ocean pole tides up to degree-8: IERS Conventions; Atmospheric and ocean de-aliasing up to degree-8: AOD1B (Dobslaw et al., 2017); third body perturbations using DE421 ephemeris (Folkner et al., 2009).</p> <p>SRP modeling only for Galileo according to Galileo satellite metadata^a</p> <p>Albedo modeling according to Rodriguez-Solano et al., 2012b.</p> <p>Antenna thrust (Steigenberger et al., 2018).</p> <p>Thermal radiation for Galileo (Sidorov et al., 2020).</p> <p>Relativistic corrections to the satellite accelerations according to IERS Conventions: Schwarzschild term applied.</p> <p>Estimated orbit initial state vector.</p> <p>Estimated ECOM2 empirical parameters (Arnold et al., 2015).</p> <p>Estimated stochastic pulses (Beutler et al., 1994) at orbit midnight in radial, along-track and out-of-plane directions with 10^{-6} m/s, 10^{-5} m/s and 10^{-8} m/s constraining. The pulses are only applied if the application time differs by more than six hours from the orbital arc boundaries.</p>

^a <https://www.gsc-europa.eu/support-to-developers/galileo-satellite-metadata>

Bibliography

- Abraha, Kibrom Ebuy, Felix Norman Teferle, Addisu Hunegnaw, and Rolf Dach (2018). "Effects of unmodelled tidal displacements in GPS and GLONASS coordinate time-series". In: *Geophysical journal international* 214.3, pp. 2195–2206.
- Altamimi, Zuheir, Claude Boucher, and Patrick Sillard (2002). "New trends for the realization of the international terrestrial reference system". In: *Advances in Space Research* 30.2, pp. 175–184.
- Altamimi, Zuheir, Xavier Collilieux, and Laurent Métivier (2011). "ITRF2008: an improved solution of the international terrestrial reference frame". In: *Journal of Geodesy* 85, pp. 457–473.
- Altamimi, Zuheir and Richard Gross (2017). "Geodesy". In: *Springer Handbook of Global Navigation Satellite Systems*, pp. 1039–1061.
- Altamimi, Zuheir, Paul Rebischung, Xavier Collilieux, Laurent Métivier, and Kristel Chanard (2023). "ITRF2020: An augmented reference frame refining the modeling of nonlinear station motions". In: *Journal of Geodesy* 97.5, p. 47.
- Altamimi, Zuheir, Paul Rebischung, Laurent Métivier, and Xavier Collilieux (2016). "ITRF2014: A new release of the International Terrestrial Reference Frame modeling nonlinear station motions". In: *Journal of geophysical research: solid earth* 121.8, pp. 6109–6131.
- Arnold, Daniel, Michael Meindl, Gerhard Beutler, Rolf Dach, Stefan Schaer, Simon Lutz, Lars Prange, Krzysztof Sośnica, Leos Mervart, and Adrian Jäggi (2015). "CODE's new solar radiation pressure model for GNSS orbit determination". In: *Journal of geodesy* 89, pp. 775–791.
- Arnold, Daniel, Oliver Montenbruck, Stefan Hackel, and Krzysztof Sośnica (2019). "Satellite laser ranging to low Earth orbiters: orbit and network validation". In: *Journal of geodesy* 93.11, pp. 2315–2334.
- Ashby, Neil (2003). "Relativity in the global positioning system". In: *Living Reviews in relativity* 6.1, pp. 1–42.
- Atkinson, Kendall and Weimin Han (2012). *Spherical harmonics and approximations on the unit sphere: an introduction*. Vol. 2044. Springer Science & Business Media.
- Bambi, Cosimo (2018). *Introduction to General Relativity: A Course for Undergraduate Students of Physics*. Springer.
- Banville, Simon (2016). "GLONASS ionosphere-free ambiguity resolution for precise point positioning". In: *Journal of Geodesy* 90.5, pp. 487–496.
- Banville, Simon, Paul Collins, and François Lahaye (2013). "GLONASS ambiguity resolution of mixed receiver types without external calibration". In: *GPS solutions* 17, pp. 275–282.
- Banville, Simon, Jianghui Geng, Sylvain Loyer, Stefan Schaer, Tim Springer, and Sebastian Strasser (2020). "On the interoperability of IGS products for precise point positioning with ambiguity resolution". In: *Journal of geodesy* 94, pp. 1–15.

- Bassiri, Sassan and George A Hajj (1993). "Higher-order ionospheric effects on the global positioning system observables and means of modeling them". In: *Manuscripta geodaetica* 18, pp. 280–280.
- Battin, Richard H (1999). *An introduction to the mathematics and methods of astrodynamics*. Aiaa.
- Baur, Oliver, Heike Bock, Eduard Höck, Adrian Jäggi, Sandro Krauss, Torsten Mayer-Gürr, Tilo Reubelt, Christian Siemes, and Norbert Zehentner (2014). "Comparison of GOCE-GPS gravity fields derived by different approaches". In: *Journal of geodesy* 88, pp. 959–973.
- Beard, Ron and Ken Senior (2017). "Clocks". In: *Springer handbook of global navigation satellite systems*, pp. 121–164.
- Bertiger, Willy, Yoaz Bar-Sever, Angie Dorsey, Bruce Haines, Nate Harvey, Dan Hemberger, Michael Heflin, Wenwen Lu, Mark Miller, Angelyn W Moore, et al. (2020). "GipsyX/RTGx, a new tool set for space geodetic operations and research". In: *Advances in space research* 66.3, pp. 469–489.
- Beutler, Gerhard (2004a). *Methods of Celestial Mechanics: Volume I: Physical, Mathematical and Numerical Principles*. Springer Science & Business Media.
- (2004b). *Methods of Celestial Mechanics: Volume II: Application to Planetary System, Geodynamics and Satellite Geodesy*. Springer Science & Business Media.
- Beutler, Gerhard, E Brockmann, W Gurtner, U Hugentobler, L Mervart, M Rothacher, and A Verdun (1994). "Extended orbit modeling techniques at the CODE processing center of the international GPS service for geodynamics (IGS): theory and initial results". In: *Manuscripta geodaetica* 19.6, pp. 367–386.
- Beutler, Gerhard, E Brockmann, U Hugentobler, L Mervart, M Rothacher, and R Weber (1996). "Combining consecutive short arcs into long arcs for precise and efficient GPS orbit determination". In: *Journal of Geodesy* 70, pp. 287–299.
- Beutler, Gerhard, Adrian Jäggi, Leoš Mervart, and Ulrich Meyer (2010a). "The celestial mechanics approach: application to data of the GRACE mission". In: *Journal of geodesy* 84, pp. 661–681.
- (2010b). "The celestial mechanics approach: theoretical foundations". In: *Journal of Geodesy* 84, pp. 605–624.
- Beutler, Gerhard, Arturo Villiger, Rolf Dach, Andreas Verdun, and Adrian Jäggi (2020). "Long polar motion series: Facts and insights". In: *Advances in space research* 66.11, pp. 2487–2515.
- BI, PM (2006). "The international system of units". In.
- Bizouard, Christian, Sébastien Lambert, César Gattano, Olivier Becker, and Jean-Yves Richard (2019). "The IERS EOP 14C04 solution for Earth orientation parameters consistent with ITRF 2014". In: *Journal of Geodesy* 93.5, pp. 621–633.
- Blewitt, Geoffrey and Peter Clarke (2003). "Inversion of Earth's changing shape to weigh sea level in static equilibrium with surface mass redistribution". In: *Journal of Geophysical Research: Solid Earth* 108.B6.
- Bock, Heike, Rolf Dach, Adrian Jäggi, and Gerhard Beutler (2009). "High-rate GPS clock corrections from CODE: support of 1 Hz applications". In: *Journal of Geodesy* 83, pp. 1083–1094.
- Boehm, Johannes, Robert Heinkelmann, Paulo Jorge Mendes Cerveira, Andrea Pany, and Harald Schuh (2009). "Atmospheric loading corrections at the observation level in VLBI analysis". In: *Journal of Geodesy* 83, pp. 1107–1113.
- Boehm, Johannes and Harald Schuh (2004). "Vienna mapping functions in VLBI analyses". In: *Geophysical research letters* 31.1.

- Brumberg, VA and Sergei M Kopejkin (1989). "Relativistic reference systems and motion of test bodies in the vicinity of the Earth". In: *Nuovo Cimento B* 103.1, pp. 63–98.
- Brunner, Fritz K and Min Gu (1991). "An improved model for the dual frequency ionospheric correction of GPS observations". In: *Manuscripta geodaetica* 16.3, pp. 205–214.
- Bury, Grzegorz, Krzysztof Sośnica, Radosław Zajdel, Dariusz Strugarek, and Urs Hugentobler (2021). "Determination of precise Galileo orbits using combined GNSS and SLR observations". In: *GPS Solutions* 25.1, p. 11.
- Calero-Rodríguez, Emilio J, Arturo Villiger, Stefan Schaer, Rolf Dach, and Adrian Jäggi (2023a). "Between-satellite ambiguity resolution based on preliminary GNSS orbit and clock information using a globally applied ambiguity clustering strategy". In: *GPS solutions* 27.3, p. 125.
- Calero-Rodríguez, Emilio J., Rolf Dach, and Adrian Jäggi (2023b). "Estimation of degree-2 gravity field solutions using GNSS observations". In: *XXVIII General Assembly of the International Union of Geodesy and Geophysics (IUGG), Berlin, Germany*.
- Calero-Rodríguez, Emilio J., Arturo Villiger, Stefan Schaer, Rolf Dach, and Adrian Jäggi (2022). "Combined orbit and clock zero-difference solution at CODE: ambiguity resolution strategy". In: *EGU General Assembly Conference Abstracts*, EGU22–11628.
- Carrère, Loren, F Lyard, M Cancet, A Guillot, N Picot, et al. (2016). "FES 2014, a new tidal model—Validation results and perspectives for improvements". In: *Proceedings of the ESA living planet symposium*, pp. 9–13.
- Chang, X -W, X Yang, and T Zhou (2005). "MLAMBDA: A modified LAMBDA method for integer least-squares estimation". In: *Journal of Geodesy* 79, pp. 552–565.
- Chen, G and Thomas A Herring (1997). "Effects of atmospheric azimuthal asymmetry on the analysis of space geodetic data". In: *Journal of Geophysical Research: Solid Earth* 102.B9, pp. 20489–20502.
- Chuang, Shi, Yi Wenting, Song Weiwei, Lou Yidong, Yao Yibin, and Zhang Rui (2013). "GLONASS pseudorange inter-channel biases and their effects on combined GPS/GLONASS precise point positioning". In: *GPS solutions* 17, pp. 439–451.
- Collins, Paul (2008). "Isolating and estimating undifferenced GPS integer ambiguities". In: *Proceedings of the 2008 national technical meeting of the institute of navigation*, pp. 720–732.
- Collins, Paul, Francois Lahaye, Pierre Heroux, and Sunil Bisnath (2008). "Precise point positioning with ambiguity resolution using the decoupled clock model". In: *Proceedings of the 21st international technical meeting of the satellite division of the Institute of Navigation (ION GNSS 2008)*, pp. 1315–1322.
- Couhert, A, C Bizouard, F Mercier, K Chanard, M Greff, and P Exertier (2020). "Self-consistent determination of the Earth's GM, geocenter motion and figure axis orientation". In: *Journal of Geodesy* 94, pp. 1–16.
- Dach, Rolf (2022). "Dependency of satellite geodesy on UT1-UTC from VLBI". In: *International VLBI Service for Geodesy and Astrometry*, pp. 3–9.
- Dach, Rolf, Daniel Arnold, Christian Baumann, Stefano Bertone, Heike Bock, Yoomin Jean, Adrian Jäggi, Simon Lutz, Andrea Grahl, Michael Meindl, et al. (2015). "Bernese GNSS software". In.
- Dach, Rolf, Stefan Schaer, Daniel Arnold, Elmar Brockmann, Maciej Sebastian Kalarus, Lars Prange, Pascal Stebler, and Adrian Jäggi (2020). "CODE final product series for the IGS". In.

- Dach, Rolf, Inga Selmke, Arturo Villiger, Daniel Arnold, Lars Prange, Stefan Schaer, Dmitry Sidorov, Pascal Stebler, Adrian Jäggi, and Urs Hugentobler (2021). "Review of recent GNSS modelling improvements based on CODEs Repro3 contribution". In: *Advances in space research* 68.3, pp. 1263–1280.
- Delva, Pacôme, Zuheir Altamimi, Alejandro Blazquez, Mathis Blossfeld, Johannes Böhm, Pascal Bonnefond, Jean-Paul Boy, Sean Bruinsma, Grzegorz Bury, Miltiadis Chatzinikos, et al. (2023). "GENESIS: co-location of geodetic techniques in space". In: *Earth, Planets and Space* 75.1, p. 5.
- Desai, Shailen D and Aurore E Sibois (2016). "Evaluating predicted diurnal and semidiurnal tidal variations in polar motion with GPS-based observations". In: *Journal of Geophysical Research: Solid Earth* 121.7, pp. 5237–5256.
- Dilssner, F, T Springer, G Gienger, and J Dow (2011). "The GLONASS-M satellite yaw-attitude model". In: *Advances in Space Research* 47.1, pp. 160–171.
- Dobslaw, H, I Bergmann-Wolf, R Dill, L Poropat, M Thomas, Christoph Dahle, Saskia Esselborn, R König, and Frank Flechtner (2017). "A new high-resolution model of non-tidal atmosphere and ocean mass variability for de-aliasing of satellite gravity observations: AOD1B RL06". In: *Geophysical Journal International* 211.1, pp. 263–269.
- Duan, Bingbing, Urs Hugentobler, Inga Selmke, and Ningbo Wang (2021). "Estimating ambiguity fixed satellite orbit, integer clock and daily bias products for GPS L1/L2, L1/L5 and Galileo E1/E5a, E1/E5b signals". In: *Journal of Geodesy* 95, pp. 1–14.
- Epperson, James F (1987). "On the Runge example". In: *The American Mathematical Monthly* 94.4, pp. 329–341.
- Falcone, Marco, Jörg Hahn, and Thomas Burger (2017). "Galileo". In: *Springer handbook of global navigation satellite systems*, pp. 247–272.
- Ferrers, Norman Macleod (1877). *An elementary treatise on spherical harmonics and subjects connected with them*. Macmillan and Company.
- Flechtner, Frank, Karl-Hans Neumayer, Christoph Dahle, Henryk Dobslaw, Elisa Fagiolini, Jean-Claude Raimondo, and Andreas Güntner (2016). "What can be expected from the GRACE-FO laser ranging interferometer for earth science applications?" In: *Remote sensing and water resources*, pp. 263–280.
- Folkner, William M, James G Williams, and Dale H Boggs (2009). "The planetary and lunar ephemeris DE 421". In: *IPN progress report* 42.178, p. 1.
- Formichella, Valerio, Lorenzo Galleani, Giovanna Signorile, and Ilaria Sesia (2021). "Time–frequency analysis of the Galileo satellite clocks: looking for the J2 relativistic effect and other periodic variations". In: *GPS Solutions* 25, pp. 1–14.
- Gallier, Jean (2009). "Notes on spherical harmonics and linear representations of Lie groups". In: *preprint*.
- Ge, Maorong, Gerd Gendt, Galina Dick, and FP Zhang (2005). "Improving carrier-phase ambiguity resolution in global GPS network solutions". In: *Journal of Geodesy* 79, pp. 103–110.
- Ge, Maorong, Gerd Gendt, Met al Rothacher, C Shi, and J Liu (2008). "Resolution of GPS carrier-phase ambiguities in precise point positioning (PPP) with daily observations". In: *Journal of geodesy* 82, pp. 389–399.
- Geisser, Linda, Ulrich Meyer, Daniel Arnold, and Adrian Jäggi (2023). "Contribution of LARES SLR Data to Co-estimated Earth Geopotential Coefficients". In: Springer.
- Gelderen, Martin van and Radboud Koop (1997). "The use of degree variances in satellite gradiometry". In: *Journal of Geodesy* 71, pp. 337–343.
- Geng, Jianghui, Chuang Shi, Maorong Ge, Alan H Dodson, Yidong Lou, Qile Zhao, and Jingnan Liu (2012). "Improving the estimation of fractional-cycle biases

- for ambiguity resolution in precise point positioning". In: *Journal of Geodesy* 86, pp. 579–589.
- Griffiths, J and Jim R Ray (2013). "Sub-daily alias and draconitic errors in the IGS orbits". In: *GPS solutions* 17, pp. 413–422.
- Griffiths, Jake and Jim R Ray (2009). "On the precision and accuracy of IGS orbits". In: *Journal of Geodesy* 83.3-4, pp. 277–287.
- Gross, Richard (1992). "Correspondence between theory and observations of polar motion". In: *Geophysical Journal International* 109.1, pp. 162–170.
- (2007). "Earth rotation variations-long period". In: *Treatise on geophysics* 3, pp. 239–294.
- Habrigh, Heinz (2000). *Geodetic applications of the global navigation satellite system (GLONASS) and of GLONASS/GPS combinations*. Verlag des Bundesamtes für Kartographie und Geodäsie.
- Hackel, Stefan, Peter Steigenberger, Urs Hugentobler, Maik Uhlemann, and Oliver Montenbruck (2015). "Galileo orbit determination using combined GNSS and SLR observations". In: *GPS solutions* 19, pp. 15–25.
- Håkansson, Martin, Anna BO Jensen, Milan Horemuz, and Gunnar Hedling (2017). "Review of code and phase biases in multi-GNSS positioning". In: *GPS Solutions* 21, pp. 849–860.
- Hatch, Ron (1983). "The synergism of GPS code and carrier measurements". In: *International geodetic symposium on satellite doppler positioning*. Vol. 2, pp. 1213–1231.
- Hauschild, André (2017a). "Basic observation equations". In: *Springer handbook of global navigation satellite systems*, pp. 561–582.
- Hauschild, Andre (2017b). "Combinations of observations". In: *Springer handbook of global navigation satellite systems*, pp. 583–604.
- Hegarty, Christopher J (2017). "The global positioning system (GPS)". In: *Springer handbook of global navigation satellite systems*, pp. 197–218.
- Herrera Pinzón, Ivan Dario (2023). "Methods for an Enhanced Co-Location of Space Geodetic Techniques". PhD thesis. ETH Zurich.
- Herring, TA, RW King, and SC McClusky (2006). "Gamt". In: *Reference Manual. GPS Analysis at MIT. Release 10*, pp. 1–182.
- Hofmann-Wellenhof, Bernhard and Helmut Moritz (2006). *Physical geodesy*. Springer Science & Business Media.
- Hugentobler, Urs (2005). "Models in GNSS data analysis". In: *Presentation at "Advances in GPS data processing and modelling for geodynamics" held at University College London*, pp. 9–10.
- Ineichen, D, Gerhard Beutler, and U Hugentobler (2003). "Sensitivity of GPS and GLONASS orbits with respect to resonant geopotential parameters". In: *Journal of Geodesy* 77, pp. 478–486.
- Jäggi, Adrian, Ulrich Meyer, Martin Lasser, Barbara Jenny, Teodolina Lopez, Frank Flechtner, Christoph Dahle, Christoph Förste, Torsten Mayer-Gürr, Andreas Kvas, et al. (2020). "International combination service for time-variable gravity fields (COST-G) start of operational phase and future perspectives". In: *Beyond 100: The Next Century in Geodesy: Proceedings of the IAG General Assembly, Montreal, Canada, July 8-18, 2019*. Springer, pp. 57–65.
- Jäggi, Adrian, Lars Prange, and Urs Hugentobler (2011). "Impact of covariance information of kinematic positions on orbit reconstruction and gravity field recovery". In: *Advances in space research* 47.9, pp. 1472–1479.
- Jean, Yoomin, Ulrich Meyer, and Adrian Jäggi (2018). "Combination of GRACE monthly gravity field solutions from different processing strategies". In: *Journal of Geodesy* 92, pp. 1313–1328.

- Johnston, Gary, Anna Riddell, and Grant Hausler (2017). "The international GNSS service". In: *Springer handbook of global navigation satellite systems*, pp. 967–982.
- Kaula, William M (2013). *Theory of satellite geodesy: applications of satellites to geodesy*. Courier Corporation.
- KC, Shanker and Tri Acharya (June 2023). "A Brief History of Advances in Geodesy with National Cases". In: 5, pp. 16–26.
- Kersten, Tobias and Steffen Schön (2011). "GNSS Group Delay Variations-Potential for improving GNSS based Time and Frequency Transfer?" In: *Proceedings of the 43rd Annual Precise Time and Time Interval Systems and Applications Meeting*, pp. 255–270.
- Koch, Karl-Rudolf (1999). *Parameter estimation and hypothesis testing in linear models*. Springer Science & Business Media.
- Kouba, J (2009a). "A simplified yaw-attitude model for eclipsing GPS satellites". In: *GPS solutions* 13, pp. 1–12.
- (2021). "Testing of general relativity with two Galileo satellites in eccentric orbits". In: *GPS Solutions* 25.4, p. 139.
- Kouba, Jan (2009b). *A guide to using International GNSS Service (IGS) products*.
- Lasser, Martin (2022). "Noise Modelling for GRACE Follow-On Observables in the Celestial Mechanics Approach". PhD thesis. Universität Bern.
- Laurichesse, Denis, Flavien Mercier, JEAN-Paul Berthias, Patrick Broca, and Luca Cerri (2009). "Integer ambiguity resolution on undifferenced GPS phase measurements and its application to PPP and satellite precise orbit determination". In: *Navigation* 56.2, pp. 135–149.
- Loomis, Bryant D, Kenneth E Rachlin, and Scott B Luthcke (2019). "Improved Earth oblateness rate reveals increased ice sheet losses and mass-driven sea level rise". In: *Geophysical Research Letters* 46.12, pp. 6910–6917.
- Loomis, Bryant D, Kenneth E Rachlin, David N Wiese, Felix W Landerer, and Scott B Luthcke (2020). "Replacing GRACE/GRACE-FO with satellite laser ranging: Impacts on Antarctic Ice Sheet mass change". In: *Geophysical Research Letters* 47.3, e2019GL085488.
- Loyer, Sylvain, Félix Perosanz, Flavien Mercier, Hugues Capdeville, and Jean-Charles Marty (2012). "Zero-difference GPS ambiguity resolution at CNES–CLS IGS Analysis Center". In: *Journal of Geodesy* 86, pp. 991–1003.
- Lutz, Simon, Michael Meindl, Peter Steigenberger, Gerhard Beutler, Krzysztof Sośnica, Stefan Schaer, Rolf Dach, Daniel Arnold, Daniela Thaller, and Adrian Jäggi (2016). "Impact of the arc length on GNSS analysis results". In: *Journal of geodesy* 90, pp. 365–378.
- Maleček, Kamil and Zbyněk Nádeník (2001). "On the inductive proof of Legendre addition theorem". In: *Studia Geophysica et Geodaetica* 45, pp. 1–11.
- Männel, Benjamin, Andre Brandt, Susanne Glaser, and Harald Schuh (2023). "Correcting Non-Tidal Surface Loading in GNSS repro3 and Comparison with ITRF2020". In: Springer.
- Mathews, PM and Pierre Bretagnon (2003). "Polar motions equivalent to high frequency nutations for a nonrigid Earth with anelastic mantle". In: *Astronomy & Astrophysics* 400.3, pp. 1113–1128.
- Mathews, PM, Thomas A Herring, and Bruce Allen Buffett (2002). "Modeling of nutation and precession: New nutation series for nonrigid Earth and insights into the Earth's interior". In: *Journal of Geophysical Research: Solid Earth* 107.B4, ETG–3.
- Mayer-Gürr, Torsten, Saniya Behzadpour, Annette Eicker, Matthias Ellmer, Beate Koch, Sandro Krauss, Christian Pock, Daniel Rieser, Sebastian Strasser, Barbara Süsner-Rechberger, et al. (2021). "GROOPS: A software toolkit for gravity field recovery and GNSS processing". In: *Computers & geosciences* 155, p. 104864.

- Meindl, Michael, Gerhard Beutler, Daniela Thaller, Rolf Dach, and Adrian Jäggi (2013). "Geocenter coordinates estimated from GNSS data as viewed by perturbation theory". In: *Advances in Space Research* 51.7, pp. 1047–1064.
- Melbourne, William G (1985). "The case for ranging in GPS-based geodetic systems". In: *Proceedings of the first international symposium on precise positioning with the Global Positioning System*. US Department of Commerce Rockville, Maryland, pp. 373–386.
- Meyer, Ulrich, Adrian Jäggi, and Gerhard Beutler (2012). "Monthly gravity field solutions based on GRACE observations generated with the Celestial Mechanics Approach". In: *Earth and planetary science letters* 345, pp. 72–80.
- Meyer, Ulrich, Heike Peter, Linda Geisser, Emilio Calero, Rolf Dach, and Adrian Jäggi (2023). *COST-G models of time-variable gravity for precise orbit determination*. Tech. rep. Copernicus Meetings.
- Meyer, Ulrich, Krzysztof Sośnica, Daniel Arnold, Christoph Dahle, Daniela Thaller, Rolf Dach, and Adrian Jäggi (2019). "SLR, GRACE and SWARM gravity field determination and combination". In: *Remote sensing* 11.8, p. 956.
- Milani, Andrea, Anna Maria Nobili, and Paolo Farinella (1987). *Non-gravitational perturbations and satellite geodesy*.
- Montenbruck, Oliver, Eberhard Gill, and Fh Lutze (2002). "Satellite orbits: models, methods, and applications". In: *Appl. Mech. Rev.* 55.2, B27–B28.
- Montenbruck, Oliver, Stefan Hackel, and Adrian Jäggi (2018a). "Precise orbit determination of the Sentinel-3A altimetry satellite using ambiguity-fixed GPS carrier phase observations". In: *Journal of geodesy* 92.7, pp. 711–726.
- Montenbruck, Oliver, André Hauschild, and Peter Steigenberger (2014). "Differential code bias estimation using multi-GNSS observations and global ionosphere maps". In: *Navigation: Journal of the Institute of Navigation* 61.3, pp. 191–201.
- Montenbruck, Oliver, Urs Hugentobler, Rolf Dach, Peter Steigenberger, and André Hauschild (2012). "Apparent clock variations of the Block IIF-1 (SVN62) GPS satellite". In: *GPS solutions* 16, pp. 303–313.
- Montenbruck, Oliver, Ralf Schmid, Flavien Mercier, Peter Steigenberger, Carey Noll, Roman Fatkulin, Satoshi Kogure, and Aiylam S Ganeshan (2015a). "GNSS satellite geometry and attitude models". In: *Advances in Space Research* 56.6, pp. 1015–1029.
- Montenbruck, Oliver, Peter Steigenberger, and André Hauschild (2018b). "Multi-GNSS signal-in-space range error assessment—Methodology and results". In: *Advances in Space Research* 61.12, pp. 3020–3038.
- Montenbruck, Oliver, Peter Steigenberger, and Urs Hugentobler (2015b). "Enhanced solar radiation pressure modeling for Galileo satellites". In: *Journal of Geodesy* 89, pp. 283–297.
- Nothnagel, A, T Artz, D Behrend, and Z Malkin (2017). "International VLBI Service for Geodesy and Astrometry: Delivering high-quality products and embarking on observations of the next generation". In: *Journal of Geodesy* 91.7, pp. 711–721.
- Nowak, Adrian, Radosław Zajdel, and Krzysztof Sośnica (2023). "Determination of low-degree gravity field coefficients based on inverse GNSS methods from the IGS Repro3 data". In: *XXVIII General Assembly of the International Union of Geodesy and Geophysics (IUGG)*. GFZ German Research Centre for Geosciences.
- Pavlis, Nikolaos K, Simon A Holmes, Steve C Kenyon, and John K Factor (2012). "The development and evaluation of the Earth Gravitational Model 2008 (EGM2008)". In: *Journal of geophysical research: solid earth* 117.B4.
- Pearlman, Michael R, Carey E Noll, Erricos C Pavlis, Frank G Lemoine, Ludwig Combrink, John J Degnan, Georg Kirchner, and Ulrich Schreiber (2019). "The

- ILRS: approaching 20 years and planning for the future". In: *Journal of Geodesy* 93, pp. 2161–2180.
- Peter, Heike, Ulrich Meyer, Martin Lasser, and Adrian Jäggi (2022). "COST-G gravity field models for precise orbit determination of Low Earth Orbiting Satellites". In: *Advances in Space Research* 69.12, pp. 4155–4168.
- Petit, Gérard, Brian Luzum, et al. (2010). "IERS technical note no. 36". In: *IERS conventions* 179.
- Plag, Hans-Peter and Michael Pearlman (2007). "The global geodetic observing system: meeting the requirements of a global society on a changing planet in 2020 the reference document". In: *Int. Assoc. Geod.*
- Prange, Lars, Gerhard Beutler, Rolf Dach, Daniel Arnold, Stefan Schaer, and Adrian Jäggi (2020). "An empirical solar radiation pressure model for satellites moving in the orbit-normal mode". In: *Advances in space research* 65.1, pp. 235–250.
- Prange, Lars, Rolf Dach, Simon Lutz, Stefan Schaer, and Adrian Jäggi (2016). "The CODE MGEX orbit and clock solution". In: *IAG 150 Years: Proceedings of the IAG Scientific Assembly in Postdam, Germany, 2013*. Springer, pp. 767–773.
- Qing, Yun, Yidong Lou, Xiaolei Dai, and Yang Liu (2017). "Benefits of satellite clock modeling in BDS and Galileo orbit determination". In: *Advances in Space Research* 60.12, pp. 2550–2560.
- Ray, J, Z Altamimi, X Collilieux, and Tonie van Dam (2008). "Anomalous harmonics in the spectra of GPS position estimates". In: *GPS solutions* 12, pp. 55–64.
- Ray, JR (1996). "Measurements of length of day using the Global Positioning System". In: *Journal of Geophysical Research: Solid Earth* 101.B9, pp. 20141–20149.
- Rebischung, Paul and Ralf Schmid (2016). "IGS14/igs14.atx: a new framework for the IGS products". In: *AGU fall meeting 2016*.
- Revnivykh, Sergey, Alexey Bolkunov, Alexander Serdyukov, and Oliver Montenbruck (2017). "Glonass". In: *Springer Handbook of Global Navigation Satellite Systems*, pp. 219–245.
- Rochat, P, F Droz, P Mosset, G Barmaverain, Q Wang, D Boving, L Mattioni, M Belloni, M Gioia, U Schmidt, et al. (2005). "The onboard galileo rubidium and passive maser, status & performance". In: *Proceedings of the 2005 IEEE International Frequency Control Symposium and Exposition, 2005*. IEEE, pp. 26–32.
- Rodell, Matthew, Jay S Famiglietti, David N Wiese, JT Reager, Hiroko K Beaulieu, Felix W Landerer, and M-H Lo (2018). "Emerging trends in global freshwater availability". In: *Nature* 557.7707, pp. 651–659.
- Rodriguez-Solano, CJ, U Hugentobler, and P Steigenberger (2012a). "Adjustable box-wing model for solar radiation pressure impacting GPS satellites". In: *Advances in Space Research* 49.7, pp. 1113–1128.
- Rodriguez-Solano, CJ, U Hugentobler, P Steigenberger, M Bloßfeld, and M Fritsche (2014). "Reducing the draconitic errors in GNSS geodetic products". In: *Journal of Geodesy* 88.6, pp. 559–574.
- Rodriguez-Solano, CJ, U Hugentobler, P Steigenberger, and Simon Lutz (2012b). "Impact of Earth radiation pressure on GPS position estimates". In: *Journal of geodesy* 86, pp. 309–317.
- Romero, Ignacio (2020). "The receiver independent exchange format version 3.05". In: *International GNSS Service Files*, <https://files.igs.org/pub/data/format/rinex305.pdf>.
- Rothacher, Markus and Ralf Schmid (2010). "ANTEX: The antenna exchange format, version 1.4". In: *Document available at igs.cb.jpl.nasa.gov/igs/cb/station/general/antex14.txt*. Search in.

- Rudenko, Sergei, Denise Dettmering, Saskia Esselborn, Tilo Schöne, Christoph Förste, Jean-Michel Lemoine, Michaël Ablain, David Alexandre, and Karl-Hans Neumayer (2014). "Influence of time variable geopotential models on precise orbits of altimetry satellites, global and regional mean sea level trends". In: *Advances in Space Research* 54.1, pp. 92–118.
- Sanz-Subirana, Jaume, JM Juan-Zornoza, and M Hernández-Pajares (2013). "GNSS data processing". In: *Volume I: Fundamentals and algorithms*, pp. 145–161.
- Scaramuzza, Stefano, Rolf Dach, Gerhard Beutler, Daniel Arnold, Andreja Sušnik, and Adrian Jäggi (2018). "Dependency of geodynamic parameters on the GNSS constellation". In: *Journal of Geodesy* 92, pp. 93–104.
- Schaer, Stefan (2016). "SINEX BIAS—Solution (software/technique) INdependent EXchange format for GNSS BIASes version 1.00". In: *IGS workshop on GNSS biases, Bern, Switzerland*.
- Schaer, Stefan, Gerhard Beutler, Markus Rothacher, and Timon A Springer (1996). "Daily global ionosphere maps based on GPS carrier phase data routinely produced by the CODE Analysis Center". In: *Proceedings of the IGS Analysis Center Workshop 1996*.
- Schaer, Stefan, Arturo Villiger, Daniel Arnold, Rolf Dach, Lars Prange, and Adrian Jäggi (2021). "The CODE ambiguity-fixed clock and phase bias analysis products: generation, properties, and performance". In: *Journal of Geodesy* 95, pp. 1–25.
- Schaffrin, B (1986). "Generating classes of equivalent linear models by nuisance parameter elimination". In: *Manus. Geod.* 11, pp. 262–271.
- Seeber, Günter (2003). *Satellite geodesy*. Walter de gruyter.
- Sidorov, Dmitry, Rolf Dach, Bernard Polle, Lars Prange, and Adrian Jäggi (2020). "Adopting the empirical CODE orbit model to Galileo satellites". In: *Advances in space research* 66.12, pp. 2799–2811.
- Sleewaegen, Jean-Marie, Andrew Simsky, Wim De Wilde, FRANK Boon, and Tom Willems (2012). "Demystifying GLONASS inter-frequency carrier phase biases". In: *Inside GNSS* 7.3, pp. 57–61.
- Sleewaegen, JM and F Clemente (2018). "Quantifying the pilot-data bias on all current GNSS signals and satellites". In: *IGS Workshop*.
- Sneeuw, Nicolaas (2000). "A semi-analytical approach to gravity field analysis from satellite observations". PhD thesis. Technische Universität München.
- Sośnica, K, G Bury, R Zajdel, K Kazmierski, J Ventura-Traveset, R Prieto-Cerdeira, and L Mendes (2021). "General relativistic effects acting on the orbits of Galileo satellites". In: *Celestial Mechanics and Dynamical Astronomy* 133, pp. 1–31.
- Sośnica, Krzysztof, Adrian Jäggi, Gerhard Beutler, Ulrich Meyer, Rolf Dach, Daniela Thaller, and Leos Mervart (2013a). "Time variable Earth's gravity field from SLR and GNSS satellites". In: *Journal of Geodesy* 87, pp. 945–960.
- Sośnica, Krzysztof, Daniela Thaller, Rolf Dach, Adrian Jäggi, and Gerhard Beutler (2013b). "Impact of loading displacements on SLR-derived parameters and on the consistency between GNSS and SLR results". In: *Journal of Geodesy* 87, pp. 751–769.
- Springer, T, Rene Zandbergen, and A Águeda Maté (2009). "NAPEOS mathematical models and algorithms". In: *Document № DOPS-SYS-TN-0100-OPS-GN* 1.5, p. 150.
- Steigenberger, Peter and Oliver Montenbruck (2023). "Consistency of Galileo satellite antenna phase center offsets". In: *Journal of Geodesy* 97.6, p. 58.

- Steigenberger, Peter, Steffen Thielert, and Oliver Montenbruck (2018). "GNSS satellite transmit power and its impact on orbit determination". In: *Journal of Geodesy* 92.6, pp. 609–624.
- Strasser, Sebastian (2022). "Reprocessing multiple GNSS constellations and a global station network from 1994 to 2020 with the raw observation approach". PhD thesis. Graz University of Technology Graz, Austria.
- Strasser, Sebastian, Torsten Mayer-Gürr, and Norbert Zehentner (2019). "Processing of GNSS constellations and ground station networks using the raw observation approach". In: *Journal of Geodesy* 93.7, pp. 1045–1057.
- Su, Ching-Chuan (2001). "Reinterpretation of the Michelson-Morley experiment based on the GPS Sagnac correction". In: *Europhysics Letters* 56.2, p. 170.
- Tapley, Byron D, Srinivas Bettadpur, John C Ries, Paul F Thompson, and Michael M Watkins (2004). "GRACE measurements of mass variability in the Earth system". In: *science* 305.5683, pp. 503–505.
- Teunissen, Peter JG (1995). "The invertible GPS ambiguity transformations". In: — (2017a). "Batch and recursive model validation". In: *Springer handbook of global navigation satellite systems*, pp. 687–720.
- (2017b). "Carrier phase integer ambiguity resolution". In: *Springer handbook of global navigation satellite systems*, pp. 661–685.
- (2019). "A new GLONASS FDMA model". In: *GPS Solutions* 23.4, p. 100.
- Teunissen, Peter JG and Amir Khodabandeh (2015). "Review and principles of PPP-RTK methods". In: *Journal of Geodesy* 89.3, pp. 217–240.
- (2019). "GLONASS ambiguity resolution". In: *GPS Solutions* 23.4, p. 101.
- Teunissen, Peter JG and Alfred Kleusberg (2012). *GPS for Geodesy*. Springer Science & Business Media.
- Teunissen, PJG (1995). "The least-square ambiguity decorrelation adjustment: a method for fast GPS integer ambiguity estimation". In: *J. Geodesy* 70.1, pp. 65–82.
- Torge, Wolfgang and Jürgen Müller (2012). "Geodesy". In: *Geodesy*. de Gruyter.
- Velicogna, Isabella (2009). "Increasing rates of ice mass loss from the Greenland and Antarctic ice sheets revealed by GRACE". In: *Geophysical Research Letters* 36.19.
- Verhagen, S., B. Li, and Peter JG Teunissen (2012). "LAMBDA - Matlab implementation, version 3.0. Delft University of Technology and Curtin University". In: — (2017). "Least-squares estimation and Kalman filtering". In: *Springer handbook of global navigation satellite systems*, pp. 639–660.
- Villiger, Arturo, Rolf Dach, Stefan Schaer, Lars Prange, Florian Zimmermann, Heiner Kuhlmann, Gerhard Wübbena, Martin Schmitz, Gerhard Beutler, and Adrian Jäggi (2020). "GNSS scale determination using calibrated receiver and Galileo satellite antenna patterns". In: *Journal of geodesy* 94, pp. 1–13.
- Villiger, Arturo, Stefan Schaer, Rolf Dach, Lars Prange, Andreja Sušnik, and Adrian Jäggi (2019). "Determination of GNSS pseudo-absolute code biases and their long-term combination". In: *Journal of geodesy* 93, pp. 1487–1500.
- Wahr, John M (1987). "The Earth's C21 and S21 gravity coefficients and the rotation of the core". In: *Geophysical Journal International* 88.1, pp. 265–276.
- (1990). "Correction and update to 'The earth's C 21 and C 21 gravity coefficients and the rotation of the core'". In: *Geophysical Journal International* 101.3, pp. 709–711.
- Wahr, John M, Mery Molenaar, and Frank Bryan (1998). "Time variability of the Earth's gravity field: Hydrological and oceanic effects and their possible detection using GRACE". In: *Journal of Geophysical Research: Solid Earth* 103.B12, pp. 30205–30229.

- Wahr, John M, R Steven Nerem, and Srinivas V Bettadpur (2015). "The pole tide and its effect on GRACE time-variable gravity measurements: Implications for estimates of surface mass variations". In: *Journal of Geophysical Research: Solid Earth* 120.6, pp. 4597–4615.
- Wang, Ningbo, Yunbin Yuan, Zishen Li, Oliver Montenbruck, and Bingfeng Tan (2016). "Determination of differential code biases with multi-GNSS observations". In: *Journal of Geodesy* 90, pp. 209–228.
- Watson, GA (2006). "Computing helmert transformations". In: *Journal of computational and applied mathematics* 197.2, pp. 387–394.
- Wells, DE, W Lindlohr, B Schaffrin, and E Grafarend (2023). "GPS design: undifferenced carrier beat phase observations and the fundamental differencing theorem". In.
- Wermuth, Martin, Oliver Montenbruck, and Tom Van Helleputte (2010). "GPS high precision orbit determination software tools (GHOST)". In.
- Willis, Pascal, Frank G Lemoine, Guilhem Moreaux, Laurent Soudarin, Pascale Ferrage, John Ries, Michiel Otten, Jerome Saunier, Carey Noll, Richard Biancale, et al. (2016). "The International DORIS Service (IDS): Recent developments in preparation for ITRF2013". In: *IGAG 150 Years: Proceedings of the IAG Scientific Assembly in Postdam, Germany, 2013*, pp. 631–640.
- Wu, Jiun-Tsong, Sien C Wu, George A Hajj, Willy I Bertiger, and Stephen M Lichten (1992). "Effects of antenna orientation on GPS carrier phase". In: *Astrodynamics* 1991, pp. 1647–1660.
- Wübbena, Gerhard (1985). "Software developments for geodetic positioning with GPS using TI-4100 code and carrier measurements". In: *Proceedings of the first international symposium on precise positioning with the global positioning system*. Vol. 19. US Department of Commerce Rockville, Maryland, pp. 403–412.
- Zajdel, Radosław (2021). "Determination of global geodetic parameters using the gps, glonass, and galileo satellite systems". PhD thesis. Doctoral dissertation, Wrocław University of Environmental and Life Sciences . . .
- Zajdel, Radosław, Krzysztof Sośnica, and Grzegorz Bury (2021). "Geocenter coordinates derived from multi-GNSS: a look into the role of solar radiation pressure modeling". In: *GPS Solutions* 25.1, p. 1.
- Zajdel, Radosław, Krzysztof Sośnica, Grzegorz Bury, Rolf Dach, and Lars Prange (2020). "System-specific systematic errors in earth rotation parameters derived from GPS, GLONASS, and Galileo". In: *GPS solutions* 24.3, p. 74.
- Zajdel, Radosław, Krzysztof Sośnica, Rolf Dach, G Bury, L Prange, and Adrian Jäggi (2019). "Network effects and handling of the geocenter motion in multi-GNSS processing". In: *Journal of Geophysical Research: Solid Earth* 124.6, pp. 5970–5989.
- Zhang, Xinggang and Shuanggen Jin (2014). "Uncertainties and effects on geocenter motion estimates from global GPS observations". In: *Advances in Space Research* 54.1, pp. 59–71.

Emilio José CALERO RODRÍGUEZ

PERSONAL DATA

PLACE AND DATE OF BIRTH:

PHONE:

EMAIL:

WORK EXPERIENCE

<i>Current</i>	GNC Engineer at GMV AEROSPACE AND DEFENCE S.A., Tres Cantos, Madrid, Spain
MARCH 2024	<i>Defense and Security</i> GNC engineer working in various defense programs and projects.
FEB 2020 - JAN 2024	PhD candidate at ASTRONOMICAL INSTITUTE OF THE UNIVERSITY OF BERN, Bern, Switzerland <i>Satellite Geodesy Group</i> Researcher in the SPACE TIE Project to rigorously develop multi-GNSS solutions based on undifferenced processing schemes. The major achievements include the development of a novel ambiguity resolution algorithm applicable to the processing of global networks, where a large number of ground stations is involved. On the other hand, it has been thoroughly evaluated the capability of the GNSS constellations to recover geodynamical parameters, i.e., geocenter coordinates, Earth rotation parameters and long-wavelength time-variable gravity field. Teaching assistant in the master's course Modeling Techniques in Physics , in charge of the practical lectures on numerical integration of ordinary differential equations. Assistant in the Bernese GNSS Software Introduction Course , in charge of the PPP (Precise Point Positioning) lecture.
OCT 2016 - JAN 2020	Project Engineer at GMV AEROSPACE AND DEFENCE S.A., Tres Cantos, Madrid, Spain <i>Flight Dynamics and Operations Business Unit</i> Service Operator of the Operational Copernicus Precise Orbit Determination (POD) Service running at GMV in Tres Cantos, Madrid, Spain. This operational service provides very accurate orbital and attitude products to the Sentinel-1, -2 and -3 missions. Although the tasks involved in an operational service are focused on the maintenance and upgrade of operational chains to meet and improve the accuracy and latency of the different products, the POD team struggles to keep their algorithms and tools aligned to the state-of-the-art standards, diving into the GNSS and physical fundamentals. Additionally, active participation has been dedicated to other related activities, such as the POD for the satellite Paz (supporting the set-up and fine-tune of its POD system) and the development of the scene generator module for the System Performance Simulator and Ground Processor Prototype for the GNSS instrument of the upcoming Sentinel-3C, -3D and -6 satellites.
MAR-SEP 2016	Internship at GMV AEROSPACE AND DEFENCE S.A., Tres Cantos, Madrid, Spain <i>Optimization of Low-Thrust Orbit Transfers at Flight Dynamics and Operations Department</i> Internship in a researching project relative to the optimization of Low-Thrust trajectories, learning about its fundamentals and working with state-of-the-art optimization tools (IPOPT, WORHP and an in-house tool) in order to assess their suitability and performance solving large-scale optimization problems.

FEB-JUL 2014 | Internship at E-USOC (SPANISH USER SUPPORT AND OPERATIONS CENTRE), Pozuelo de Alarcón, Madrid, Spain
Development of the On-Board Computer for a Nanosatellite (double Cube-Sat)
 During this internship, it was developed the core of the communications between the on-board computer of a nanosatellite (named QBITO) and its main payload (an instrument able to measure the properties of the lower thermosphere), as part of the 7FP project QB50, lead by the Von Karman Institute (VKI) in Belgium. The software was written in C, making use of the multi-tasking and real-time capabilities of freeRTOS, an operative system devoted to fulfil, among others, the stringent requirements of low-cost embedded systems.

EDUCATION

2020-2024 | Doctor of Philosophy in SATELLITE GEODESY
University of Bern, Bern, Switzerland
 Thesis: "Methods and algorithms for undifferenced multi-GNSS global network processing and applications to satellite geodesy"
 Supervisor: Prof. Adrian JÄGGI

2014-2016 | Master of Science in AERONAUTICAL ENGINEERING
Technical University Of Madrid, Madrid, Spain
 Thesis: "Optimization of Low-Thrust Earth-Mars Trajectories Using the Relative Motion Theory"
 Advisor: Prof. Claudio BOMBARDELLI

2010-2014 | Bachelor Degree in AEROSPACE ENGINEERING
Technical University Of Madrid, Madrid, Spain
 Thesis: "Design and Implementation of the Real-Time On-Board SW for a Nanosatellite"
 Advisor: Prof. Ana LAVERÓN

PUBLICATIONS AND CONGRESSES

DEC 2017 | **Deflection of fictitious asteroid 2017 PDC: Ion beam vs. kinetic impactor PDC 2017**
 Bombardelli C., Calero E.J., Gonzalo J.L.

APR 2019 | **Single-receiver ambiguity resolution for Copernicus Sentinel Satellites EGU 2019**
 Calero E.J., Fernández J., Peter H., Féménias P.

APR 2019 | **Reprocessing of the Copernicus Sentinel-1, -2, -3 orbits EGU 2019**
 Fernández J., Calero E.J., Peter H., Féménias P.

MAY 2019 | **Copernicus Sentinel-1 Orbits - Results of an Offline Reprocessing LPS 2019**
 Peter H., Fernández J., Calero E.J., Féménias P.

MAY 2019 | **Single-receiver ambiguity resolution for Copernicus Sentinel satellites LPS 2019**
 Fernández J., Peter H., Calero E.J., Féménias P.

OCT 2019 | **Single-receiver ambiguity resolution for Sentinel-3 Precise Orbit Determination at the Copernicus POD Service OSTST 2019**
 Calero E.J., Peter H., Fernández J., Féménias P.

OCT 2019 | **Copernicus POD Service - Model updates and validation of Sentinel-3 orbit determination OSTST 2019**
 Peter H., Calero E.J., Fernández J., Féménias P.

- DEC 2019 **Model Updates and Reprocessing of the Copernicus Sentinel-1, -2, -3 orbits**
AGU 2019
Peter H., Calero E.J., Berzosa J., Fernández M., Pastor R., Fernández J., Féménias P.
- DEC 2019 **Single-receiver ambiguity resolution for Copernicus Sentinel Satellites using different GNSS products**
AGU 2019
Calero E.J., Peter H., Berzosa J., Fernández M., Pastor R., Fernández J., Féménias P.
- DEC 2019 **Simulation of GNSS POD scenarios**
AGU 2019
Fernández J., Guindal A., Pastor R., Calero E.J., Berzosa J.
- MAY 2022 **Combined orbit and clock zero-difference solution at CODE: ambiguity resolution strategy**
EGU 2022
Calero E.J., Villiger A., Schaer S., Dach R., Jäggi A.
- APR 2023 **COST-G models of time-variable gravity for precise orbit determination**
EGU 2023
Meyer, U., Peter, H., Geisser, L., Calero, E.J., Dach, R., and Jäggi, A.
- MAY 2023 **Between-satellite ambiguity resolution based on preliminary GNSS orbit and clock information using a globally applied ambiguity clustering strategy**
GPS Solutions
Calero, E.J., Villiger, A., Schaer, S., Dach, R., Jäggi, A.
- JUL 2023 **Estimation of degree-2 gravity field solutions using GNSS observations**
IUGG 2023
Calero, E.J., Dach, R., and Jäggi, A.

LANGUAGES

SPANISH: Mothertongue

ENGLISH: Professional working proficiency

COMPUTER SKILLS

Prog. Languages: FORTRAN, C/C++, Bash, TCL, Perl, mysql, Java, Python, \LaTeX

Platforms: LINUX, Windows, Mac OS

Tools: Docker, MatLab&Simulink, Visual Studio, Eclipse, Subversion (SVN), MS Office

INTERESTS AND ACTIVITIES

Technology, Programming, GNSS, Applied Mathematics and Physics, Space Research, Cycling

List of publications

The research conducted in the scope of this dissertation has been made available to the scientific community through the publication of peer-review articles:

- **Calero-Rodríguez, E.J.**, Villiger, A., Schaer, S., Dach, R., Jäggi, A. Between-satellite ambiguity resolution based on preliminary GNSS orbit and clock information using a globally applied ambiguity clustering strategy. *GPS Solut* **27**, 4.12 125 (2023). <https://doi.org/10.1007/s10291-023-01435-3>

as well as the participation in international congresses:

- **Calero-Rodríguez, E.J.**, Villiger, A., Schaer, S., Dach, R., Jäggi, A.: Combined orbit and clock zero-difference solution at CODE: ambiguity resolution strategy, EGU General Assembly 2022, Vienna, Austria, 23–27 May 2022, EGU22-11628, <https://doi.org/10.5194/egusphere-egu22-11628>, 2022.
- Meyer, U., Peter, H., Geisser, L., **Calero-Rodríguez, E.J.**, Dach, R., and Jäggi, A.: COST-G models of time-variable gravity for precise orbit determination, EGU General Assembly 2023, Vienna, Austria, 24–28 Apr 2023, EGU23-6553, <https://doi.org/10.5194/egusphere-egu23-6553>, 2023.
- **Calero Rodríguez, E. J.**, Dach, R., Jäggi, A. (2023): Estimation of degree-2 gravity field solutions using GNSS observations, XXVIII General Assembly of the International Union of Geodesy and Geophysics (IUGG) (Berlin 2023). <https://doi.org/10.57757/IUGG23-1948>

Declaration of Originality

Last name, first name: Calero Rodríguez, Emilio José

Matriculation number: 19-131-374

I hereby declare that this thesis represents my original work and that I have used no other sources except as noted by citations.

All data, tables, figures and text citations which have been reproduced from any other source, including the internet, have been explicitly acknowledged as such.

I am aware that in case of non-compliance, the Senate is entitled to withdraw the doctorate degree awarded to me on the basis of the present thesis, in accordance with the "Statut der Universität Bern (Universitätsstatut; UniSt)", Art. 69, of 7 June 2011.

Bern, July 8, 2024

A handwritten signature in blue ink, appearing to read "Emilio José Calero Rodríguez", with a large, stylized flourish at the end.

Emilio José Calero Rodríguez